Sculpting a quasi one-dimensional Bose-Einstein condensate to generate calibrated matter waves

Javed Akram

am Fachbereich Physik
der Freien Universität Berlin eingereichte Dissertation

This dissertation is submitted for the degree of
Doktor der Naturwissenschaften

Institute für Theoretische Physik

18 March 2016

Die in vorliegender Dissertation dargestellte Arbeit wurde in der Zeit zwischen Oktober 2011 und Februar 2016 am Fachbereich Physik der Freien Universität Berlin unter Betreuung von Priv.-Doz. Dr. Axel Pelster durchgeführt.

Erstgutachter: Priv.-Doz. Dr. Axel Pelster

Zweitgutachter: Prof. Dr. Jürgen Bosse

Tag der Disputation: 18 March 2016

I would like to dedicate this thesis to my loving family and friends

&

To the people of Pakistan

※※※※※※※※※※※※※※※※※※※※

※※※※※※※※※※※※※※※※

※※※※※※※※※※※

※※※※※※※

Declaration

I hereby declare that, except where specific reference is made to the work of others, the contents of this dissertation are original and have not been submitted in whole or in part for consideration for any other degree or qualification in this, or any other university. This dissertation is my own work and contains nothing which is the outcome of work done in collaboration with others, except as specified in the text and acknowledgements. This dissertation have not been accepted or rejected as insufficient within the context of previous doctoral studies.

Javed Akram
18 March 2016

Abstract

The ability to trap and manipulate atoms at lower dimensions with laser light has had a tremendous development in generating coherent matter waves in the realm of the emerging field of atomtronics. The present thesis provides a detailed theoretical investigation of different quasi one-dimensional traps in view of how to sculpt both static and dynamic properties of confined Bose-Einstein condensates (BECs). Apart from the introductory part, this thesis is divided into three parts, which gradually follow on from one to another.

In the second part of the thesis, we focus on studying ^{87}Rb atoms in a quasi one-dimensional trap geometry, which consists of a harmonic trap together with a red- or blue-detuned Gaussian or Hermite-Gaussian dimple trap (dT or HGdT). This represents an advanced confinement, which has recently been used in Innsbruck to obtain quantum degeneracy for the first strontium BEC without the traditional evaporating cooling technique. After outlining the system geometry, we compare analytical with numerical equilibrium results and show that the dT or HGdT yields either a bump or a dip upon the condensate depending on whether the laser-beam mode is either red- or blue-detuned, respectively. Following the time-of-flight (TOF) dynamics we obtain that the bump upon the condensate does not decay, but the dip decreases. Furthermore, after having switched off the red- or blue-detuned optical dipole trap (ODT) potential, shock-waves or gray(dark) pair-soliton bi-trains emerge, which oscillate with a characteristic frequency in the remaining harmonic trap. It turns out that the generation of gray/dark pair-solitons bi-trains represents a generic phenomenon stemming from collisions of the moderately/fully fragmented BEC. It is astonishing to find that the special shape of the generated solitons in the harmonically trapped BEC can be sculptured by imposing a specific ODT geometry.

With this we continue to part III of our thesis, where we analyze a quasi one-dimensional BEC in a nonlinear gravito-optical surface trap. In order to solve such a nonlinear boundary value problem, we apply the mirror principle, which is usually used to deal with linear boundary value problems in the realm, for instance, of electrostatics. Combining analytical and numerical results we show that the condensate wave function changes from a Gaussian to a triangular shape for increasing the atom number. Later, we numerically analyze in detail two non-ballistic expansions of the BEC cloud due to gravity, when the confining evanescent laser beam is shut off. In the first case we assume that particles are lost when they hit the prism, yielding a decrease of the particle number, which quantitatively agrees with previous Innsbruck experimental results. In the second case we consider the reflection of the BEC cloud from a hard-wall mirror, which we model by using a blue-detuned far-off resonant sheet of light, and obtain qualitative agreement with experimental results from Hanover.

In the final part, we investigate the sculpting of a trapped ^{87}Rb BEC due to the presence of a single ^{133}Cs impurity. To this end, we determine the equilibrium phase diagram, which is spanned by the intra- and interspecies coupling strengths. Furthermore, we show that a localized impurity at the trap center induces a bump or dip in the condensate in case of an attractive or repulsive interspecies interaction strength, respectively. Conversely, we obtain due to the condensate environment an effective mass of the impurity, which increases quadratically for small interspecies interaction strength. During the resulting TOF expansion it turns out that the bump in the condensate starts decreasing marginally, whereas the dip starts decaying after a characteristic time scale, which decreases with increasing repulsive impurity-BEC interaction. In addition, once the attractive or repulsive interspecies coupling strength is switched off we find that white shock-waves or bi-solitons emerge, which oscillate within the remaining harmonic confinement with a characteristic frequency. This is a phenomenon similar to the above discussed BEC in an ODT, although this time we have not seen bi-soliton trains but only bi-solitons. Presumably, the reason behind the generation of bi-solitons instead of bi-soliton trains is that the width of the sculpted portion of the BEC is smaller in the impurity than in the ODT case.

All our findings show that in special circumstances a BEC can be recognized as an atom laser which represents one of the key ingredients for experiments in quantum atom optics, much like the laser is central to the field of a quantum optics.

Zusammenfassung

Die Fähigkeit, Atome in niedrigen Raumdimensionen mit Laserlicht fangen und manipulieren zu können, hat zu einer gewaltigen Entwicklung in der Erzeugung kohärenter Materiewellen im Bereich des aufkommenden Atomtronik-Gebietes geführt. Die vorliegende Doktorarbeit beinhaltet eine detaillierte theoretische Untersuchung von verschiedenen quasi-eindimensionalen Fallen im Hinblick darauf, wie sowohl statische als auch dynamische Eigenschaften gefangener Bose-Einstein-Kondensate (BEK) beeinflusst werden können. Abgesehen vom einleitenden Teil ist die Doktorarbeit in drei Teile gegliedert, die sukzessive aufeinander aufbauen.

Im zweiten Teil der Doktorarbeit beschränken wir uns darauf, ^{87}Rb-Atome in einer quasi-eindimensionalen Fallengeometrie zu untersuchen, die aus einer harmonischen Falle sowie einer rot- oder blau-verstimmten Gaußschen oder Hermite-Gaußschen Dimpelfalle besteht. Es handelt sich hierbei um eine erweiterte Falle, die kürzlich in Innsbruck verwandt wurde, um die Quantenentartung des ersten Strontium Bose-Einstein-Kondensates ohne die traditionelle Verdampfungskühlung zu erreichen. Nach der Erläuterung der Systemgeometrie vergleichen wir analytische und numerische Gleichgewichtsresultate und zeigen, dass die Falle entweder zu einer Beule oder einer Delle im Kondensat führt, abhängig davon, ob die Lasermode entweder rot- oder blau-verstimmt ist. Verfolgt man die Expansionsdynamik des Kondensates, so zeigt sich, dass die Beule erhalten bleibt, während sich die Delle mit der Zeit verkleinert. Nachdem das rot- bzw. blau-verstimmte optische Dipolfallenpotential ausgeschaltet wird, entstehen Schockwellen bzw. graue (dunkle) Bi-Soliton-Züge, die mit einer charakteristischen Frequenz in der verbleibenden harmonischen Falle oszillieren. Es stellt sich heraus, dass die Erzeugung der Bi-Soliton-Züge ein generisches Phänomen darstellt, das auf Kollisionen des teilweise oder vollständig fragmentierten Bose-Einstein-Kondensates zurückzuführen ist. Es ist erstaunlich, dass die Form der erzeugten Solitonen in dem harmonisch gefangenen Bose-Einstein-Kondensat durch ein bestimmtes optischen Dipolfallenpotential bestimmt werden kann.

Anschließend analysieren wir im zweiten Teil der Doktorarbeit ein quasi-eindimensionales Bose-Einstein-Kondensat in einer gravito-optischen Oberflächenfalle. Um solch ein nichtlineares Randwertproblem zu lösen, wenden wir das Spiegelprinzip an, das üblicherweise verwendet wird, um lineare Randwertprobleme zum Beispiel im Bereich der Elektrostatik zu behandeln. Durch Kombination analytischer und numerischer Resultate zeigen wir, dass sich die Kondensatwellenfunktion von einer Gauß- zu einer Dreiecksform verändert, wenn man die Atomzahl erhöht. Außerdem untersuchen wir numerisch im Detail zwei nicht-ballistische Expansionen einer BEK-Wolke unter dem Einfluß der Gravitation, wenn das evaneszente Fallenpotential ausgeschaltet wird. Im ersten Falle nehmen wir an, dass die Teilchen verloren gehen, wenn sie auf das Prisma auftreffen, so dass die Teilchenzahl in quantitativer Übereinstimmung mit einem früheren Innsbruck-Experiment abnimmt. Im zweiten Falle betrachten wir die Reflektion einer BEK-Wolke an einem Spiegel, den wir durch eine blau-verstimmten Laserlichtschnitt modellieren, und reproduzieren damit qualitativ frühere experimentelle Resultate von Hannover.

Im letzten Teil untersuchen wir, wie ein gefangenes ^{87}Rb Bose-Einstein-Kondensat in Anwesenheit einer einzelnen ^{133}Cs Verunreinigung verformt werden kann. Hierzu bestimmen wir das Gleichgewichtsphasendiagramm, das von der Wechselwirkungsstärke zwischen den Rb-Atomen sowie zwischen den Rb-Atomen und dem Cs-Atom aufgespannt wird. Außerdem zeigen wir, dass eine im Fallenzentrum lokalisierte Verunreinigung eine Beule oder Delle im Kondensat erzeugt, falls eine attraktive oder repulsive Rb-Cs Wechselwirkung vorliegt. Umgekehrt erhalten wir aufgrund des Kondensatumgebung eine effektive Masse der Verunreinigung, die quadratisch mit der Rb-Cs-Wechselwirkungsstärke anwächst. Während der Expansion zeigt sich, dass sich die Beule im Kondensat marginal verkleinert, während sich die Delle mit einer charakteristischen Zeitskala verringert, die mit zunehmend repulsiver Rb-Cs-Wechselwirkungsstärke abnimmt. Wenn die attraktive oder repulsive Rb-Cs-Wechselwirkungsstärke ausgeschaltet wird, finden wir weiße Schockwellen oder Bi-Solitonen, die mit einer charaktieristischen Frequenz in der verbleibenden Falle oszillieren. Es handelt sich hierbei um ein

ähnliches Phänomen wie bei dem zuvor diskutierten Bose-Einstein-Kondensat in einer optischen Dipolfalle, obwohl dieses Mal keine Bi-Soliton-Züge sondern nur Bi-Solitonen auftreten. Vermutlich liegt die Ursache für die Erzeugung von Bi-Solitonen anstelle von Bi-Soliton-Zügen darin, dass die Breite der Verformung des Bose-Einstein-Kondensates im Falle der Verunreinigung viel kleiner als im Falle des optischen Dipolpotentials ist.

All unsere Ergebnisse zeigen, dass unter speziellen Umständen ein Bose-Einstein-Kondensat als ein Atomlaser angesehen werden kann, der genau so ein Schlüsselelement für Experimente im Bereich der Quantenatomoptik darstellt, wie der Laser für die Quantenoptik zentral ist.

Acknowledgements

This thesis is indeed the accomplishment of many years of learning. I speak not only of my studies here in the Department of Physics at the Free University of Berlin, but also of my Master and M.Phil. studies at the Quaid-i-Azam University Islamabad. Looking back over the years, I recall with sincere gratitude to teachers, family, friends, and colleagues, who have inspired and encouraged me along my journey.

First of all, I want to thank my PhD supervisor Priv.-Doz. Dr. Axel Pelster. Axel has many enormous qualities which make him such a great scientist: his capability to see ways around a research problem, his attention to analyze every detail about the research topic, and most particularly, his love and enthusiasm for his research work. Axel has taught me many great things about theoretical physics and I am forever indebted to him for his compassionate commitment to ensuring his students succeed. I am also grateful for his suggestions during my studies, including his comments, critics and corrections on the manuscripts of this thesis. Although this thesis features the end of my time as one of Axel's students, I am confident that our association will last a lifetime.

Secondly, to my co-advisor Prof. Dr. Jürgen Bosse, thank you for truly teaching me to be a better theoretical scientist, and for all the critical discussions. I will always look back passionately at all our interactions. In particular, I would like to mention his critical reading of this thesis, which improved its readability, as well as the support letters for extending the PhD fellowship.

I would also like to gratefully thank Prof. Dr. Dr. h.c. mult. Hagen Kleinert, for providing an outstanding scientific atmosphere in his research group. I have greatly benefited from him during many lunch-time discussions on the range of general physics. I will miss such dialogues in the future.

I am excited to acknowledge the financial support from the German Academic Exchange Service (DAAD) in form of a PhD fellowship. From the DAAD organization, particularly, I want to acknowledge Ms. Dagmar Beerwerth from DAAD-Section 442, with whom I exchanged numerous emails. She was always patient with all of my questions and concerns and was always there to answer in a friendly mood.

During my PhD thesis, I got the opportunity to stay at the Institute of Physics Belgrade, Serbia, under a German-Serbian DAAD exchange program. At the Institute of Physics Belgrade, I did research work with Prof. Dr. Antun Balaž on the numerical simulations of

my thesis. I really enjoyed the hospitality and scientific exchange with his working group. Moreover I would like to express my gratitude to Prof. Dr. Vanderlei Salvador Bagnato and Prof. Dr. Ednilson Santos, for inviting me at the Universidade de São Paulo, Sao Carlos, Brazil under a German-Brazilian DAAD-CAPES exchange program. I benefited a lot from this scientific exchange program and remembered many scientific discussions with Prof. Dr. Vanderlei Bagnato during his weekly research group meetings, his company was always very friendly. Further, I would like to thank Prof. Dr. Ednilson Santos for his invaluable conversations.

I am pleased to acknowledge Benjamin James Girodias, an undergraduate student from Pomona College Tucson, Arizona in Claremont, California USA, who spent 2014 summer in our group under the RISE-DAAD program. Chapter 5 of this thesis has been done as a collaborated work with Ben. I hope our collaboration will continue in future. Here, I am pleased to acknowledge my colleagues at the Free University of Berlin, Mahmoud Ghabour, Tama Khellil, Muhammad Mobarak, and Mathias May.

To my friends both near and far, thanks for all the good times we have had together, which came as a lifesaver for a busy PhD student like myself. It is a long list but I am excited to gratitude particularly few names from Berlin, Dr. Jürgen Dietel, Dr. Christine Gruber, Dr. Robert Brandt, Victor Bezerra, Václav Zatloukal, Jana Hradilová, Anna Trepka, Branko Nikolić, Christiane Hoyer, Anna Dell'aversana, Sagi Rotfogel, Martin Bonkhoff, Bernhard Irsigler and Tatjana Salmen. Tatjana, you and your family get a special thanks, while over the years I have the best memories with all of you. And I hope that life brings you everything you deserve and more. Now I want to add thanks to Bazm-e-Berlin group (a Pakistani student community in Berlin), where I met with few amazing people like, Dr. Muhammad Yasar Razzaq, Farhan Chaudhary, Yousaf Khan Jazab, Wajid Ali and Zia ur Rehman. We always enjoyed to discuss on philosophy, religion and politics, I hope that we have gained a lot from each other over this period of time. Here, I also want to thank the entire open-source community for providing us with wonderful software like Ubuntu, Open-Office, Kile, Lyx, KolourPaint, JabRef, Python, arXiv.org and gnuplot.

Last, but most certainly not least, I want acknowledge to my family in Pakistan. Thank you for your unconditional love and for supporting me through all the ups and downs of my life. My mother's belief on me is second to none, her company is always gratifying for me. I am pleased to put my special thanks to my uncles/aunts, specially, Muhammad Akbar, Muhammad Safdar and Shabir Hussian. They always push me to achieve my goals in life, without their help, ceaseless love and support I could not have kept up. I am pleased to thank my brothers, sisters and all other members of my family, who have been a constant source of encouragement and support for me during my PhD thesis.

List of Publications

Previous Publications

Engineering CNOT gate in cavity QED scenario
J. Akram and F. Saif, **J. Russ. Las. Res. 29, 519 (2008)**.
DOI:"10.1007/s10946-008-9045-y"

Controlled acceleration of modulated quantum bouncer
J. Akram, K. Nasser, and F. Saif, **J. Russ. Las. Res. 30, 157 (2009)**.
DOI:"10.1007/s10946-009-9063-4"

Acceleration of material waves in Fermi accelerator
J. Akram, K. Nasser, I. U. Rehman, and F. Saif, **Math. Prob. in Eng. 8, 246438 (2009)**.
DOI:"10.1155/2009/246438"

Thesis Publications

Statics and dynamics of quasi one-dimensional BEC in harmonic and dimple trap
J. Akram and A. Pelster, **arXiv:1508.05482 (2015)**.
http://arxiv.org/abs/1508.05482

Sculpting a quasi one-dimensional BEC to generate calibrated matter-waves
J. Akram and A. Pelster, **Phys. Rev. A 93, 023606 (2016)**.
DOI:"10.1103/PhysRevA.93.023606"

Quasi one-dimensional BEC in gravito-optical surface trap
J. Akram, B. Girodias, and A. Pelster,
J. Phys. B: At., Mol. Opt. Phys. 49, 075302 (2016).
DOI:"10.1088/0953-4075/49/7/075302"

Numerical study of localized impurity in a Bose-Einstein condensate
J. Akram and A. Pelster, **Phys. Rev. A 93, 033610 (2016)**.
DOI:"10.1103/PhysRevA.93.033610"

Pinning a single excited-impurity in a Bose-Einstein condensate
J. Akram (In preparation).

Contents

Chapter 1

Introduction to Bose-Einstein condensates

1.1 Historical importance of Bose-Einstein condensate

The story of the Bose-Einstein condensate (BEC) starts back in 1900. In this special year, Planck obtained the formula for describing black-body radiation by assuming the discretization of energy and introducing the idea of photons. Two decades later, in 1924, while working at the Physics Department of the University of Dhaka, Satyendra Nath Bose wrote a paper rederiving Planck's quantum radiation formula by proposing a new distribution for identical particles with integer spin. Initially, the distribution was applied to massless bosonic particles only, in which the number of particles is unconstrained. Though, that paper was not accepted at once for publication, he sent the article precisely to Albert Einstein. Einstein, recognizing the value of that paper, translated it into German and submitted on Bose's behalf to the prestigious Zeitschrift für Physik [3]. Later, Einstein generalized the idea to massive bosonic atoms by introducing the chemical potential, and predicted the existence of a new phase for matter, which is known as Bose-Einstein condensate, that applies to all particles with integer spin [4].

70 years later[1], atomic BEC was created experimentally in dilute vapors of ^{87}Rb [2], which triggered an explosion of related research activities. In the BEC state, all atoms in the bosonic gas fall into a single quantum-mechanical ground state. For the 3D homogeneous case, the transition to the BEC occurs if the atomic density n, and the deBroglie wavelength λ_{th}, corresponding to the characteristic velocity of the thermal motion of the atoms, satisfy the following condition [6]:

---

[1] Historical note: world's first BEC consisted of about 2000 ^{87}Rb atoms and was achieved at 10:54 AM on June 5, 1995 in a laboratory at JILA (Boulder, USA) as shown in Fig. 1.1 [5].

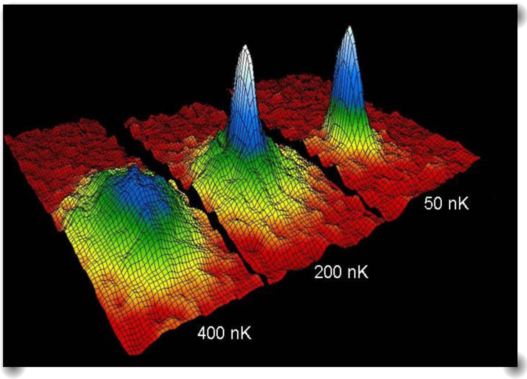

Figure 1.1: Images of velocity distributions for trapped rubidium atoms taken from [1]. On the left is the distribution for the thermal cloud, taken when the system is at a larger temperature of about 400 nK than the critical temperature for BECs, the center frame shows partly condensate and partly a thermal cloud at about 200 nK, and the final image is purely a condensate within the density peak at the temperature 50 nK. The physical size of each image amounts to 200 μm × 270 μm and is taken after a period of about 0.04 s. The color represents density, with red as low density and white as high density and the lower the peak the more the atoms have moved since being released from the trap [2].

$$n\lambda_{\text{th}}^3 \approx 1, \tag{1.1}$$

here, $\lambda_{\text{th}} = \sqrt{\hbar^2/3mk_{\text{B}}T}$ is the thermal deBroglie wavelength[2] for particles of mass m at a temperature T, and k_{B} is Boltzmann's constant. Equation (1.1) implies that the deBroglie wavelength is comparable to the mean distance between atoms, thus making the gas a macroscopic degenerate quantum state. This condition is only realizable at temperatures less than milli-Kelvin (mK)[3], hence, as a matter of fact, the atomic BECs are the coldest objects existing in labs. BEC's creation became only possible after the development of appropriate experimental techniques needed to reach the necessary ultra-low temperatures. Mainly, we can divide the cooling procedure of atoms into two main steps. **First**: the method of laser cooling is applied to the gas loaded into a magneto-optical trap, this method was rewarded with the Nobel Prize in Physics for 1997 [7–9]. This method makes it possible to create a moderately cool state, at temperature $\sim 100\,\mu$K. **Second**: this step undergoes forced evaporative cooling, where about 90% of atoms are lost, and the remaining atomic cloud

---

[2] The deBroglie wavelength connects classical particle physics and quantum mechanical wave physics via the Heisenberg uncertainty relation $\lambda_{\text{th}} = \frac{\hbar}{mv}$. We can determine the mean velocity of a particle in a gas from the temperature of the gas via the equipartition theorem of thermodynamics: $\frac{m}{2} < v >^2 = < E_{\text{kin}} > = \frac{3}{2}k_{\text{B}}T$ yields $< v > = \sqrt{\frac{3k_{\text{B}}T}{m}}$. Comparing both relations determines the deBroglie wavelength of a particle $< \lambda_{\text{th}} > = \sqrt{\hbar^2/3mk_{\text{B}}T}$.

[3] The mean distance between particles in a gas at room temperature is of the order of 10 nm. In order to observe quantum mechanical effects in a gas of similar density, we have to reduce the temperature drastically. Roughly, we can calculate this temperature by demanding that the thermal deBroglie wavelength has to become equal to the mean particle distance, i.e. $\lambda_{\text{th}} \approx 10$ nm, yielding $T \approx 0.002$ K.

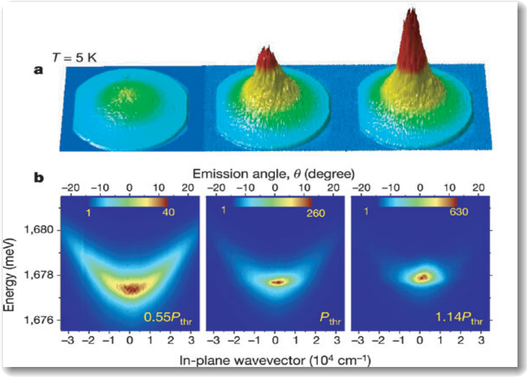

Figure 1.2: (a) Pseudo-3D images of the angular distribution of the spectrally integrated emission of polaritons. With increasing excitation power, a sharp and intense peak is formed in the center of the emission distribution, corresponding to the lowest momentum state $k_{||} = 0$. b) Same data as in (a) but resolved in energy. The polariton thermal cloud is found to be at 19 K without significant changes when increasing the excitation to twice the threshold power. The low-energy part of the polariton occupancy cannot usually be properly fitted by a Bose-Einstein distribution function, as expected for a BEC of interacting particles. Results are taken from Ref. [10].

spontaneously forms the BEC.

Just as a reminder of the relevant parameter regime: the total number of atoms can range from a few hundred to about 10^8, although in principle, both smaller and larger numbers of atoms are possible and the size of the domain in which the gas is trapped is of the order of 100 μm in diameter, the maximal density ranges from 10^{11} cm^{-3} to 5×10^{15} cm^{-3} and the temperatures required to achieve the BEC phase range typically from 10^{-7} K to 10^{-5} K, which means that the atomic velocities in the BEC phase can be as low as 1 mm/s [11]. Certainly, for longer times the BEC phase of atoms is unstable against recombination processes and it will ultimately go into a solid state, but in practice, with a suitable selection of the hyperfine states, the lifetime of the condensate can be raised to the order of minutes [11].

The advanced technology of the laser-cooling methods has made it possible to achieve the Bose-Einstein condensation in alkali metals, for example, rubidium [2], sodium [12], lithium [13], hydrogen [14], potassium [15], cesium [16], in alkaline-earth metals such as calcium [17] and strontium [18, 19], rare-earth elements like ytterbium atoms in optical trap is done in 2003 [20] and BEC in a dilute gas of helium was observed in 2001 [21, 22]. Furthermore, strong dipolar BECs were observed in chromium [23], erbium [24], and dysprosium [25]. Macroscopic phase coherence of the BEC is one of the most remarkable manifestations of quantum mechanics. In the last decade, engineering of optical microcavities make use of the mixing of electronic excitations with photons to create a composite boson called a polariton that has a very light mass, and recent experiments provide good evidence for a high-temperature Bose-Einstein condensate as shown in Fig. 1.2 [10]. Polariton [26] and magnon [27] systems also offer an opportunity to study quantum dynamics of non-equilibrium states of many-body systems, which turn out to be a new kind of cold atoms laboratory.

1.2 Optical dipole trap

The ability to manipulate and trap atoms with laser light has had a tremendous development in many fields of physics. The very first experimental success of trapping 500 sodium atoms for several seconds in the tight focus of a Gaussian red-detuned laser beam occurred in 1986 [28]. The physical mechanism behind such an optical dipole trap is the electric dipole interaction of the trapped atoms with the intense laser light, which is far detuned from the nearest optical transition of the atoms. They are hence largely independent from magnetic sublevels of the confined atoms, in contrast to a magneto-optical trap (MOT), which can only trap atoms with a certain internal state [29, 30]. The so called dimple trap (dT) or Hermite-Gaussian dimple trap (HGdT) is nothing but a small tight optical dipole trap [31–33]. Cooling and trapping of atoms with these dT's has a strong impact on the study of Bose-Einstein condensates [34, 35], the observation of long decay times for atoms in their ground state [36], and the research of trapping other atomic species or molecules [37].

A straightforward method for realizing a dT is to rely on the potential created by a freely propagating laser beam. The detuning of the laser frequency versus the atomic resonances determines, whether the atoms are red/blue-detuned, i.e. the laser frequency is below/above the atomic resonance frequency, respectively [29]. The red-detuned dT was particularly used for realizing matter wave traps in the focus of a Gaussian laser beam [38–40]. On the other hand, the blue-detuned Gaussian laser beam was used in optical waveguides [41–46], where the creation of repulsive potentials was demonstrated by using a Laguerre-Gaussian laser beam [47–52]. A focused or well-collimated Gaussian laser beam with a large red-detuning [53] or a dark hollow laser beam with a large blue-detuning [51] has been used to form 3D optical dipole trap's, which can be widely applied to the accurate, non-contact manipulation and control of cold atoms [33, 54, 55].

A more recent application of an optical dipole trap is the optical tweezer. Adam Kaufman and his colleagues demonstrated an assembling of quantum matter one atom at a time. Actually they controlled two atoms of ^{87}Rb by using an optical tweezer trap, which was created by using two separate far-detuned laser beams [56]. This experiment is the first step in engineering a brand new quantum system. It may well open the door to systematically using single-trapped atoms to assemble BECs or other quantum systems. Such designer quantum systems have exciting future prospects, including highly sensitive nanoscale force detection, tiny optical devices based on the control of neutral atoms, and quantum simulators based on laser-cooled atoms in arrays of optical tweezers.

Another state-of-the-art application of optical dipole traps is to attain to quantum degeneracy without the traditional evaporating colling technique used for bosonic alkali-metal

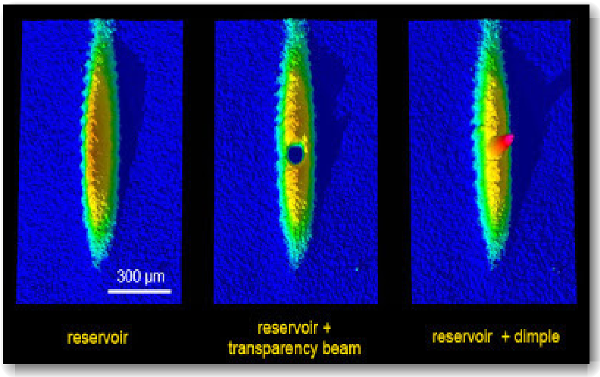

Figure 1.3: Three absorption images of 10 million strontium atoms trapped in a dipole trap and cooled to about 800 nK by laser light. The left image shows the reservoir of atoms, which is used to dissipate heat. For the central image, a transparency beam was applied, such that atoms located within this beam cannot absorb photons from the cooling light. The density in this region is greatly enhanced by a dimple beam, as can be seen on the right image, where the transparency beam has been turned off. This image is taken from Ref. [35].

gases. The first steps have been taken at the institute for quantum optics and quantum information (IQOQI) in Innsbruck, where they used a dimple trap to create the first ^{84}Sr BEC as shown in Fig. 1.3. This scheme has two main regions: the outside “reservoir” region, in which atoms are gently cooled by laser light and a central dimple region, in which the BEC is formed. This simple technique paves a relatively simple path towards a truly continuous atom laser. Here, a thermal source of atoms would be converted into a coherent beam of atoms, constantly out-coupled from the dimple region. The dimple would be continuously fed by the reservoir region, which in turn would be refilled by pre-cooled atoms from a MOT. Such truly continuous atom lasers are highly desired in various schemes of precision measurements [35].

1.3 Gravito-optical surface trap

From the physical point of view, all known experimental techniques for trapping neutral atoms can be classified with few basic methods. These basic methods are: **optical trapping** of atoms, which can be implemented by using electric dipole interaction between atoms and laser fields, **magnetic trapping** of atoms, which is based on magnetic dipole interaction of atoms and external magnetic-field, combined **magneto-optical** trapping, which can be achieved by using the interaction between atoms, magnetic and laser fields, and also mixed **gravito-optical** and **gravito-magnetic** trapping.

Gravito-optical trapping idea, was first introduced by Cook and Hill in 1982, which greatly influenced the development of the methods of trapping cold atoms near to a surface. The idea was to use an evanescent laser wave propagating along a dielectric–vacuum

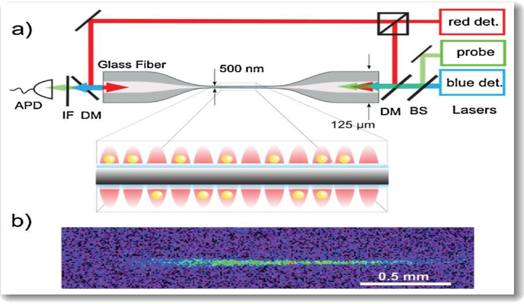

Figure 1.4: (a) Experimental setup of fiber-based atom trap. The blue-detuned running wave in combination with the red-detuned standing wave creates the trapping potential. A resonant laser is used for probing the atoms via the evanescent field. (b) Fluorescence image of the trapped atomic ensemble. This image is copied from [57].

interface as a reflecting mirror for atoms [58]. Since the evanescent light wave penetrates into the vacuum to a distance of the order of the optical wavelength, the high gradient of the evanescent wave field produces a substantial dipole gradient force on the atom. In the case of a large blue detuning, the gradient force produces in the vacuum region a repulsive barrier, which reflects atoms. This barrier is not very high, but it is quite sufficient to reflect cold atoms [59]. The first experiment on the reflection of a thermal beam of sodium atoms [60, 61] and on the reflection of normally incident cold atoms [62, 63] confirmed that an evanescent wave can effectively reflect atoms. It was also shown that the reflection coefficient of the atom mirror may be high even at a low intensity of the laser wave. It was found that, introducing metal coatings of additional dielectric layers in the vicinity of the dielectric–vacuum interface, substantially enhanced the evanescent wave field as a consequence of exciting surface plasmons [64] or on account of the formation of a dielectric waveguide [65].

The interaction of ultra-cold atoms at low dimensions with surfaces has attracted much attention in the past few years, as there enhanced quantum and thermal fluctuations have turned out to play an important role for various technological applications [67–69]. Under such circumstances also the influence of gravity has to be taken into account, therefore atomic mirrors were constructed in the presence of the gravitational field by using repulsive evanescent waves, at which both atomic beams and cold atomic clouds are reflected [70]. The trapping of atoms in a gravitational cavity, which consists of a single horizontal concave mirror placed in the gravitational field, is discussed in detail in Refs. [71, 72]. The inherent losses of atoms in a gravitational cavity can be reduced by using a higher detuning between the evanescent wave and the atomic resonance frequency in a gravitational trap [63]. In 1996, Marzlin and Audretsch studied the trapping of three-level atoms in a gravito-optical trap by using the trampolining technique without trampoline [73]. Another approach is proposed by Saif et al., where a spatially periodic modulated atomic mirror yields either a localization [74, 75] or a coherent acceleration [76, 77] of material wave packets depending on the chosen initial conditions and the respective system parameters. In 2002, Nesvizhevsky et al.

reported the evidence of gravitational quantum bound states of neutrons in a gravitational cavity [78]. A good trap geometry is not the only issue in trapping and observing the dynamics of atoms but an efficient loading scheme is also necessary. The experimental group of Rudi Grimm from Innsbruck demonstrated both the loading of cesium atoms [79, 80] and the subsequent creation of a BEC in a 2D gravito-optical surface trap (GOST) [81, 82]. More recently, Colombe et al. studied the scheme for loading a ^{87}Rb BEC into a 2D evanescent light trap and for observing the diffraction of a BEC in the time domain [83, 84]. Afterwards Perrin et at. studied the diffuse reflection of a BEC from a rough evanescent wave mirror [85].

Neutral cesium atoms have been trapped in a one-dimensional optical lattice created by a two-color evanescent field surrounding an optical nanofiber a shown in Fig. 1.4 [57]. Because the atoms are with a distance of 230 nm quite close to the nano fiber surface, the atoms efficiently interface with resonant light sent through the nanofiber. This experimental work not only provides a platform to study the collective states of light and matter but also paves the way towards nonlinear optics and quantum communication applications with fiber-coupled atomic ensembles.

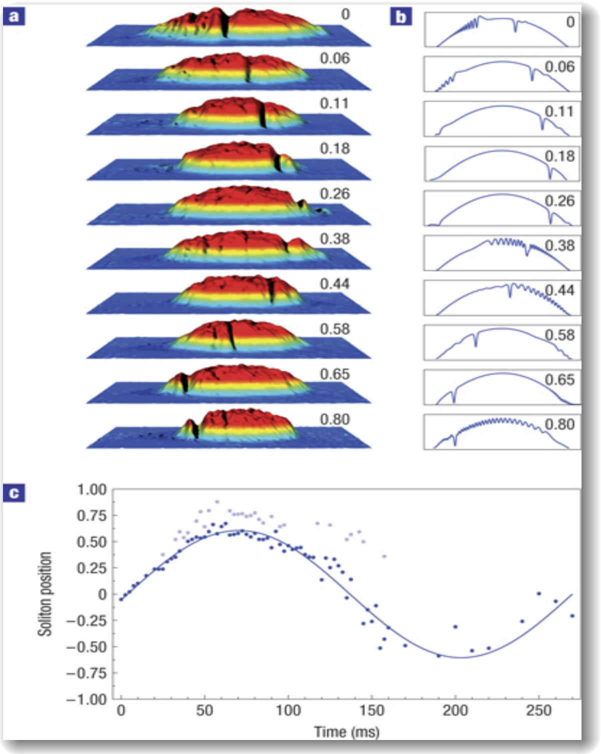

Figure 1.5: a) A set of absorption images showing the dark soliton position at various times after phase imprinting. b) Results of a numerical calculation solving the 1D Gross–Pitaevskii equation. c) Axial positions of the soliton (dark blue dots) with respect to the center of mass and normalized to the width of the condensate. Results are taken from Ref. [66].

1.4 From simple to complex: nonlinear dynamics of sculpted BEC

The state-of-the-art BEC experiments provide the freedom to control and manipulate a BEC easily and efficiently by means of external magnetic and optical laser fields. This circumstance facilitates various experiments, and provides a foundation for quite accurate theoretical models. As a result, ultra-cold gases can be used to establish many phenomena, which originate, e.g., in condensed-matter physics, but turn out to be too complex in the original settings [86]. From a theoretical point of view, the static and dynamic properties of a BEC can be described by

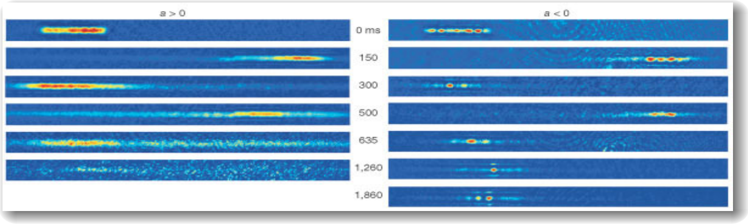

Figure 1.6: The condensate spreads for $a > 0$, while for $a < 0$ non-spreading occurs and localized structures (solitons) are formed. Such bright solitons have been observed for times exceeding 3 s. The images are copied from [91].

means of an effective mean-field equation, known as the Gross-Pitaevskii equation [6, 87], which is also recognized in literature as the nonlinear Schrödinger equation (NLSE). The GPE became a universal model to describe the evolution of complex field envelopes in nonlinear dispersive media [88–90].

One miraculous property of a BEC is its coherence similar to laser light, which makes it a leading candidate for the realization of "atom lasers". In this manner, BEC is recognized as one of the key ingredients for experiments on nonlinear and quantum atom optics, much like the laser is central to the fields of nonlinear and quantum optics [92, 93]. Dispersion and diffraction cause localized wave packets to spread as they propagate. Solitons may be formed when a nonlinear interaction produces a self-focusing of the wave packet that compensates for dispersion [91]. The term 'soliton' is used to describe any solution of a nonlinear equation or system which (i) represents a wave of permanent form; (ii) is localized, decaying or becoming constant at infinity; and (iii) may interact strongly with other solitons so that after the interaction it retains its form, almost as if the principle of superposition were valid [94]. A weakly interacting BEC obeys GPE that supports dark solitons, in the case of repulsive intrinsic interaction of atoms, which were predicted theoretically [95] and created experimentally [66, 96–98] as shown in Fig. 1.5 and multiple dark solitons were created in [97], while their interactions and collisions were also studied theoretically [99] and experimentally [100]. For an attractive intrinsic interaction of atoms, coherent matter waves are called bright solitons as shown in Fig. 1.6 [91]. In experiment [91, 101] bright solitons have been created by magnetically tuning the interactions in a stable ^{7}Li Bose–Einstein condensate from repulsive to attractive for a quasi one-dimensional optical trap, the creation of bright solitons for ^{87}Rb BEC has been also experimentally observed [102, 103]. The creation of dark–bright solitons by filling the dark soliton with atoms in another hyperfine state were predicted theoretically for binary BEC [104] and observed in experiments [66] as well as shown in Fig. 1.7.

In this thesis, we will focus on studying neutral ^{87}Rb atoms within a quasi one-dimensional harmonic trap with an additional dimple trap. Experimentally, a highly elongated quasi-1D regime can be reached by tightly confining the atoms in the radial direction, effectively freezing-out the transverse dynamics [6, 105–112]. It is worth mentioning that, when the transverse length scales are of the order of or less than the atomic interaction length, the one-dimensional system can only be described within the Tonks-Girardeau or within the super-Tonks-Girardeau regime [113–115], which is experimentally realizable near a confinement-induced resonance [116–118].

On the other hand, when the transverse confinement is larger than the atomic interaction strength, the GPE can be reduced to an effective quasi 1D model [119]. In one spatial dimension (1D), this equation is well-known to feature bright and dark solitons for attractive and repulsive s-wave scattering lengths, respectively [86, 120–122]. Many experiments investigate the collision of two Bose-Einstein condensates, where the celebrated matter-wave interference pattern appears [123] or shock-waves are generated [124]. For lower collisional energies, the repulsive interaction energy becomes significant, and the interference pattern evolves into an array of gray solitons [91, 101, 125–129]. Dark solitons can be created by manipulating the condensate density using external potentials [66, 96, 130, 131].

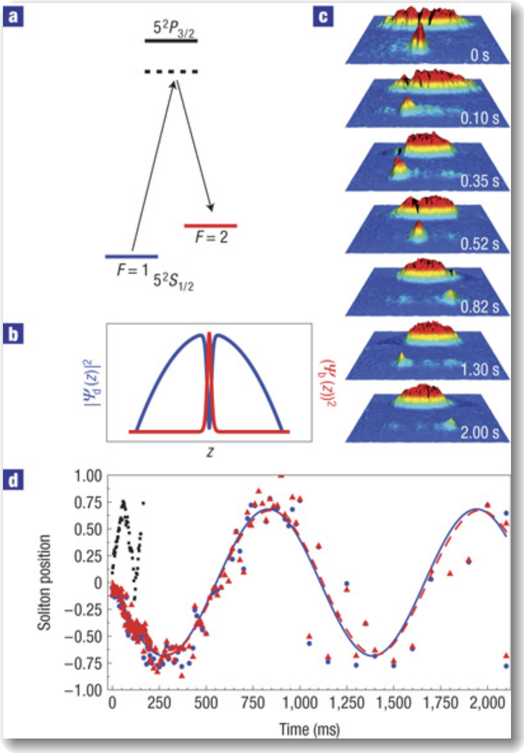

Figure 1.7: a) Cartoon picture shows the hyperfine states of ^{87}Rb BEC. b) Density profile of two BECs at $t = 0$. c) A set of double-exposure absorption images showing the density distributions of the two components that undergo slow oscillations in the axial direction. d) Time series of the axial positions of the dark (blue circles) and bright (red triangles) components of the soliton in addition to corresponding sinusoidal fits to the position. Results are taken from Ref. [66].

1.5 BECs with impurities

Until this section, we have discussed properties of the quasi one-dimensional GPE describing a condensate consisting of alike atoms, i.e. atoms of the same species in the same internal state. In this section we briefly discuss the case of a BEC with impurities, where a single impurity in a BEC can consist of a different bosonic atom or alike atom but in a different internal hyperfine state. Recent developments in theoretical and experimental research focus on controlling a single or few particle impurities in an ultra-cold quantum gas in view of detecting and engineering strongly correlated quantum states [132–135]. This research direction paths the way for a huge number of proposals for novel applications. For example, a well-localized single spin atom impurity allows to study the Kondo effect [136]. Dressed spin-down impurities in a spin-up Fermi sea of ultra-cold atoms in balanced or imbalanced mixtures even offer to investigate the quantum transport of spin impurity atoms through a strongly interacting Fermi gas [137, 138]. Furthermore, realizations of a single trapped ion impurity in a BEC features a spatial resolution on the micrometer scale, which is advantageous in comparison with absorption imaging [139, 140]. Atomtronics applications are envisioned with single atoms acting as switches for a macroscopic system in an atomtronic circuit [141]. Two impurity atoms immersed in a quantum gas can entangle by an effective long-range interaction mediated by the gas [142], or individual qubits can be cooled preserving internal state coherence [142, 143]. By adding impurities one by one, experimentalists can track, in principle, the transition from the one-body to the many-body regime, which ultimately yields information about cluster formation [144]. By implementing a single atom within a Bose-Einstein condensate also fundamental questions of quantum mechanics can be addressed with remarkable precision, for instance, to which extent a single impurity can act as a local and nondestructive probe for a strongly correlated quantum many-body state [145, 146]. In addition, the experimental achievement to trap a single impurity within a BEC [147–149] allows for investigating polaronic physics within the realm of ultracold quantum gases. Polarons can be defined as the excitations created through the interaction of the impurity with the BEC atoms [150, 151].

1.6 Structure of the thesis

This thesis consists of four parts, which practically succeed from one to another. **Part I** gives a detailed summary of optical-dipole traps and outlines the second quantization formalism to calculate the zero-temperature Gross-Pitaevskii mean-field equation. A professional reader in ODT and in mean-field theory can frankly skip **part I**, and simply use it as a reference. **Part II** covers the physics of the creation of complex coherent matter waves in a harmonically trapped BEC by assuming a specific geometrical configuration of the external ODT. **Part III** presents results of a BEC in a gravito-optical surface trap including an experimental comparison. And **part IV** exhibits how to control a single impurity atom in a BEC cloud. With this general overview, we introduce the reader to the outline of the particular chapters.

In **Chapter 2** we start with the introduction of optical dipole traps. Due to the presence of the electric field of the laser, the positive and negative charges in the atom experience opposing forces. The dipole potentials and the scattering rate depend on the intensity of the laser beam $I(\mathbf{r})$ and the atomic polarizability $\alpha(\omega)$. To derive the atomic polarizability we use a classical Abraham–Lorentz model and compare its results with the semi-classical model. Furthermore, we describe how to trap atoms near to dielectric surfaces with the help of the evanescent wave potential. Afterwards, we formulate many-particle systems, and consider the second quantization formalism to calculate the free energy and the number of particles for a homogeneous and a trapped BEC. Later on, we work out a D-dimensional Gross-Pitaevskii equation (DGPE) for the harmonically confined Bose-Einstein condensation within a semi-classical frame work. At the end of this chapter, as a special case, we briefly discuss the dynamics of quasi one-dimensional Bose-Einstein condensates, which display many distinctive nonlinear features as solitons or shock-waves.

After a brief introduction, in **Chapter 3** we start with the fact that the underlying Gross-Pitaevskii equation for a condensate wave function can be formulated as the Hamilton principle of least action with a corresponding action functional. In particular, we will focus on a quasi one-dimensional trapping of neutral ^{87}Rb atoms in a harmonic trap with an additional ODT, which can be generated by a red/blue-detuned Gaussian laser beam. Within a zero-temperature Gross-Pitaevskii mean-field description we provide a one-dimensional physical intuitive model, which we solve by both a time-independent variational approach and numerical calculations. With this we obtain at first equilibrium results for the emerging condensate wave function, which reveal that a dimple trap (dT) potential induces a bump or a dip in case of a red- or a blue-detuned Gaussian laser beam, respectively. Afterwards, we investigate how this dT induced bump/dip-imprint upon the condensate wave function evolves for two quench scenarios. At first we consider the generic case that the harmonic confinement is released. During the resulting time-of-flight expansion it turns out that the dT induced bump in the condensate wave function remains present, whereas the dip starts decaying after a characteristic time scale, which decreases with increasing blue-detuned dT depth. Secondly, once the red- or blue-detuned dT is switched off, we find that white shock-waves or gray/dark bi-soliton trains emerge, which oscillate within the harmonic confinement with a characteristic frequency. The outcome of this chapter has been summarized in a manuscript with the title **Statics and dynamics of quasi one-dimensional Bose-Einstein condensate in harmonic and dimple trap** [152].

Then in **Chapter 4** we explore sculpting the dynamics of a quasi one-dimensional harmonically trapped Bose-Einstein condensate (BEC) due to an additional red- and blue-detuned Hermite-Gaussian dimple trap (HGdT). Our system is modeled by a time-dependent Gross-Pitaevskii equation, which is numerically solved by the Crank-Nicolson method in both imaginary and real time. For equilibrium, we obtain a condensate with two bumps/dips, which are induced by the chosen TEM_{01} mode for the red/blue-detuned HGdT, respectively. Afterwards, in time-of-flight dynamics, we examine the adherence/decay of the two bumps/dips in the condensate, which are induced by the still present red/blue-detuned HGdT, respectively. On the other hand, once the red/blue HGdT potential is switched off, white shock-waves or bi-trains of gray/dark pair-solitons are created. During this process it is found that the generation of gray/dark pair-solitons bi-trains are generic phenomena of collisions of moderately/fully fragmented BEC. Additionally, it turns out that the special shape of generated solitons in the harmonically trapped BEC firmly depends upon the geometry of the HGdT. The results of this chapter will soon be published as a regular article with the title **Sculpting a quasi one-dimensional Bose-Einstein condensate to generate calibrated matter-waves** [153].

Chapter 5 describes both static and dynamic properties of a weakly interacting Bose-Einstein condensate in a quasi one-dimensional gravito-optical surface trap, where the downward pull of gravity is compensated by the exponentially decaying potential of an evanescent wave. At first we work out approximate solutions to the Gross-Pitaevskii equation for small number of atoms using a variational Gaussian ansatz and for larger number of atoms using the Thomas-Fermi limit. Then we confirm the accuracy of these analytic solutions by comparing them to numerical results. From there, we numerically analyze how the BEC cloud expands non-ballistically when the confining laser beams are turned off, showing agreement between our theoretical and previous experimental results. Furthermore, we analyze how the BEC cloud expands non-ballistically due to gravity after switching off the evanescent laser field in the presence of a hard-wall mirror. There we find that the BEC shows significant self-interference patterns for a large number of atoms, whereas for a small number of atoms, a revival of the BEC wave packet with few matter-wave interference patterns is observed. This chapter is based on a manuscript with the title **Quasi one-dimensional Bose-Einstein condensate in gravito-optical surface trap** [154], which is currently refereed.

Later in **Chapter 6** we investigate a single ^{133}Cs impurity in the center of a trapped ^{87}Rb Bose-Einstein condensate. Within a zero-temperature mean-field description we solve numerically two coupled quasi one-dimensional differential equations (1DDEs) for the condensate and the impurity wave function, and plot the resulting phase diagram, which is spanned by inter- and intra-species coupling strengths. With this we obtain at first equilibrium results for the emerging condensate wave function, which reveals an impurity-induced bump or dip in case of an attractive or a repulsive Rb-Cs interaction strength. Afterwards, we investigate how the impurity imprint upon the condensate wave function evolves for two quench scenarios. At first we consider the case that the harmonic confinement is released. During the resulting time-of-flight expansion it turns out that the impurity imprint marginally decreases for an attractive s-wave coupling but considerably decreases for a repulsive s-wave scattering. Secondly, once the interspecies coupling strength is switched off, we find that bi-solitons emerge, which oscillate within the harmonic confinement with a characteristic frequency. The results of this chapter have been sent to a journal as a regular article, under the title **Numerical study of localized impurity in a Bose-Einstein condensate** [155].

Lastly, in **Chapter** 7, we conclude with a summary of the key results of this thesis and indicate future possible research directions.

Chapter 2

Theoretical foundations

At low temperatures, when the two-particle interactions are weak, the lowest energy level of a Bose gas is macroscopically occupied, yielding a Bose–Einstein condensate. It is described by a condensate wave function, which solves a nonlinear Schrödinger equation (NLSE) known as the Gross–Pitaevskii equation (GPE). The GPE model has proven to be a good description of many static and dynamic properties for both single condensate systems and condensate mixtures [6, 87], even though thermal contributions and quantum fluctuations are not taken into account.

In order to cool down a Bose gas to quantum degeneracy, one has to isolate it via a trapping confinement from its laboratory environment, which has room temperature. To this end this chapter starts with introducing the optical dipole trap (ODT) in Sec. 2.1. Furthermore, we describe how to trap atoms near to dielectric surfaces with the help of the evanescent wave potential in Sec. 2.2. Subsequently, in Sec. 2.3 we determine the semi-classical free energy and the number of particles for D dimensions and, as a special case, we calculate the critical temperature for a three-dimensional and for a one-dimensional Bose gas both for the homogeneous and the trap case. Furthermore, we derive the Gross–Pitaevskii equation for D dimensions in Sec. 2.4. For weak interactions we solve it by using a Gaussian variational ansatz for the condensate wave function, where we determine the equations of motion for the respective variational parameters for the D-dimensional harmonic trap. For strong interactions GPE is solved with the Thomas-Fermi (TF) approximation. At the end of this chapter in Sec. 2.5, we then discuss the time-independent quasi one-dimensional GPE as a special case, where we compare Gaussian variational ansatz, as well as Thomas-Fermi and numerical solution of the 1DGPE. And finally, as a non-trivial example for the condensate dynamics, we describe the physics of a black and a gray soliton.

2.1 Optical dipole trap

To build an optical dipole trap, a laser beam, which represents an intensity gradient in the light field, is focused on a cloud of cold atoms. Due to the presence of the electric field of the laser, the positive and negative charges in the atom experience opposing forces. This causes a separation of the charges, which induces an atomic dipole moment. The interaction of this atomic dipole moment with the intensity gradient of the laser beam creates an optical dipole force, which is conservative, i.e. it can be written as the negative gradient of the potential. In the following we derive that ODT potential as well as the scattering rate first in a classical and then in a semi-classical approach. Note that, in view of experiments, the scattering rate should be low in an ODT, as scattering leads to heating.

2.1.1 Classical model

To start the quantitative analysis, suppose a laser beam flashes on an atom. Here, the electric field $\mathbf{E}(\mathbf{r},t)=\hat{\mathbf{j}}\,[E(\mathbf{r})exp(-i\omega t)+E^{\star}(\mathbf{r})exp(i\omega t)]$ induces due to charge separation an atomic dipole electric moment $\mathbf{d}(\mathbf{r},t)=\hat{\mathbf{j}}\,[d(\mathbf{r})exp(-i\omega t)+d^{\star}(\mathbf{r})exp(i\omega t)]$, which oscillates at the driving frequency ω. The unit polarization vector is $\hat{\mathbf{j}}$ and the magnitude of the electric field and dipole moment are denoted by $E(\mathbf{r})$ and $d(\mathbf{r})$, respectively. The atomic dipole moment and the electric field are related via $\mathbf{d}(\mathbf{r},\omega)=\alpha(\omega)\mathbf{E}(\mathbf{r},\omega)$, with $\alpha(\omega)$ being the complex atomic polarizability. The interaction potential of the dipole moment is [29],

$$\mathrm{U_{dip}}(\mathbf{r})=-\frac{1}{2}<\mathbf{d}\cdot\mathbf{E}>=-\mathrm{Re}[\alpha]|\mathbf{E}|^2=-\frac{1}{2\varepsilon_0 c}\mathrm{Re}[\alpha]I(\mathbf{r})\,. \tag{2.1}$$

Here $I(\mathbf{r})=2\varepsilon_0 c|\mathbf{E}|^2$ represents the field intensity in vacuum, $<\bullet>=\frac{1}{T}\int_0^T\bullet dt$ denotes the time average over the period $T=2\pi/\omega$, c is the speed of light, and ε_0 stands for the vacuum permittivity. The factor 1/2 in Eq. (2.1) arises from the fact that the dipole moment is induced by the field and is not permanently there.

The second important quantity, the scattering rate, is proportional to the amount of power that is absorbed from the driving field. As the imaginary part of the polarizability is the component, that is out of phase with the driving field, it is responsible for the absorption. The absorbed power is given by the average change in the dipole potential over time [29],

$$P_{\mathrm{abs}}=<\frac{d\mathbf{d}}{dt}\cdot\mathbf{E}>=2\omega\mathrm{Im}[\alpha]|\mathbf{E}|^2=\frac{\omega}{\varepsilon_0 c}\mathrm{Im}[\alpha]I(\mathbf{r})\,. \tag{2.2}$$

In order to obtain the scattering rate, this power needs to be divided by the energy of one photon. With $\hbar\omega$ denoting the energy of a photon, the scattering rate results in

$$\Gamma_{\mathrm{sc}}(\mathbf{r})=\frac{P_{\mathrm{abs}}}{\hbar\omega}=\frac{\mathrm{Im}[\alpha]I(\mathbf{r})}{\hbar\varepsilon_0 c}\,. \tag{2.3}$$

The dipole potential (2.1) and the scattering rate (2.3) depend upon the position dependent intensity of the laser-beam $I(\mathbf{r})$ and the atomic polarizability $\alpha(\omega)$. To derive the atomic polarizability one can use a classical Lorentz-oscillator approach.

In the late nineteenth century, when quantum mechanics had not yet been established, Hendrik Antoon Lorentz modelled atom-field interactions with the help of classical mechanics and electromagnetic theory. To this end, he defined the question of atom-field interactions in these terms. Lorentz thought that an atom mainly consists of two masses, the heavy nucleus mass which is connected to the electron mass by a spring. The spring can be set into motion with the help of an external electric field, which is interacting with the charge of the electron. The external field would either attract or repel the electron, which causes a stretching or a compressing of the spring. In this classical model an electron is bound elastically to the nucleus of the atom and oscillates with the eigenfrequency ω_A. With keeping above scenario in mind, the classical equation of motion of an electron reads according to Ref. [156]

$$m_{\mathrm{e}}\ddot{\mathbf{r}}(t) = -\,m_{\mathrm{e}}\Gamma\dot{\mathbf{r}}(t) - m_{\mathrm{e}}\omega_{\mathrm{A}}^2\mathbf{r}(t) - e\mathbf{E}(\mathbf{r},t)\,. \tag{2.4}$$

The first term on the right-hand-side is a damping term, with Γ representing the classical damping rate and m_{e} the mass of the electron. It represents the rate at which the polarization decays after the electric field has been removed. The second term on the right-hand-side is the restoring force of the electron. The third term on the right-hand-side is the driving force, originating from the external electric field $\mathbf{E}(\mathbf{r},t)$, where e stands for the elementary charge.

Later in 1902, Max Abraham connected the radiated power to the damping term in the Lorentz model. When a charged particle such as an electron accelerates, it radiates away energy in form of electromagnetic waves. For velocities, that are small relative to the speed of light, the total power radiated is given by the Larmor formula $P_{\mathrm{Lr}} = e^2\left(\ddot{\mathbf{r}}\right)^2/6\pi\varepsilon_0 c^3$ [157, p. 489] and [158, p. 748]. The average work by the radiation-reaction force $\mathbf{F}_{\mathrm{rr}}$ must balance the energy emitted into the field [159]

$$\begin{aligned}\int_{t_0}^{t}\mathbf{F}_{\mathrm{rr}}\dot{\mathbf{r}}\left(t'\right)dt' &= -\int_{t_0}^{t}P_{\mathrm{Lr}}dt' = -\frac{e^2}{6\pi\varepsilon_0 c^3}\int_{t_0}^{t}\ddot{\mathbf{r}}\left(t'\right)\ddot{\mathbf{r}}\left(t'\right)dt' \\ &= -\frac{e^2}{6\pi\varepsilon_0 c^3}\left[\dot{\mathbf{r}}\left(t'\right)\ddot{\mathbf{r}}\left(t'\right)\Big|_{t_0}^{t} - \int_{t_0}^{t}\dot{\mathbf{r}}\left(t'\right)\dddot{\mathbf{r}}\left(t'\right)dt'\right] = \int_{t_0}^{t}\left[\frac{e^2}{6\pi\varepsilon_0 c^3}\dddot{\mathbf{r}}\left(t'\right)\right]\dot{\mathbf{r}}\left(t'\right)dt'\,.\end{aligned} \tag{2.5}$$

If we pick $t-t_0$ to be an integer multiple of the optical period, the boundary term $\dot{\mathbf{r}}\left(t'\right)\ddot{\mathbf{r}}\left(t'\right)$ vanishes. Note that it is also negligible for large $t-t_0$. Thus, we conclude from (2.5) that the radiation-reaction force is given by

$$\mathbf{F}_{\mathrm{rr}} = \frac{e^2}{6\pi\varepsilon_0 c^3}\dddot{\mathbf{r}}\left(t\right). \tag{2.6}$$

For most atoms the spontaneous decay rate is best obtained from experimental data, but this classical approach nevertheless provides a good approximation in certain cases, and is accurate to within a few percent for the D lines of the alkali atoms. The on-resonance damping rate Γ, which results from radiative energy loss in the classical harmonic oscillator approach, is defined as

$$\Gamma = \frac{e^2 \omega_{\mathrm{A}}^2}{6\pi\varepsilon_0 m_{\mathrm{e}} c^3}\,. \tag{2.7}$$

In the classical approach, the decay rate (2.7) can be determined by calculating the absorption and emission of an atomic oscillator radiation [160]. Therefore we can rewrite the radiation-reaction force (2.6) as

$$F_{\mathrm{rr}} = \frac{m_{\mathrm{e}}\Gamma}{\omega_{\mathrm{A}}^2}\dddot{\mathbf{r}}(t). \tag{2.8}$$

The Abraham–Lorentz model of radiation reaction amounts now to replace the damping term in Eq. (2.4) with the radiation-reaction force (2.8). With this the equation of motion (2.4) reads [161, 162]

$$m_{\mathrm{e}}\ddot{\mathbf{r}}(t) = -\frac{m_{\mathrm{e}}\Gamma}{\omega_{\mathrm{A}}^2}\dddot{\mathbf{r}}(t) - m_{\mathrm{e}}\omega_{\mathrm{A}}^2\mathbf{r}(t) - e\mathbf{E}(\mathbf{r},t)\,. \tag{2.9}$$

By inserting $\mathbf{E}(\mathbf{r},t) = \hat{\mathbf{j}}\left[E(\mathbf{r})exp(-i\omega t) + E^*(\mathbf{r})exp(i\omega t)\right]$ and $\mathbf{r}(t) = \hat{\mathbf{j}}\left[r_0 exp(-i\omega t) + r_0^* exp(i\omega t)\right]$ in Eq. (2.9), we obtain the position amplitude to be

$$r_0 = \frac{-eE(\mathbf{r})}{m_{\mathrm{e}}\left[\omega_{\mathrm{A}}^2 - \omega^2 - i\left(\omega^3/\omega_{\mathrm{A}}^2\right)\Gamma\right]}\,. \tag{2.10}$$

The polarization of the atom is nothing but the density (per volume) of the dipole moment, which is defined as the product of the charge and the displacement vector from the negative to the positive charge, that is, from the electron to the nucleus $\mathbf{d}(\mathbf{r}) = -e\mathbf{r} = \alpha(\omega)\mathbf{E}(\mathbf{r})$. Therefore, we obtain for the atomic polarizability

$$\alpha(\omega) = \frac{e^2}{m_{\mathrm{e}}\left[\omega_{\mathrm{A}}^2 - \omega^2 - i\left(\omega^3/\omega_{\mathrm{A}}^2\right)\Gamma\right]}\,. \tag{2.11}$$

With the polarizability (2.11), the final expressions for the dipole potential and the scattering rate can be found, by separating the real part and the imaginary part of the polarizability

$$\mathrm{Re}[\alpha] = 6\pi\varepsilon_0 c^3 \frac{\Gamma/\omega_{\mathrm{A}}^2\left(\omega_{\mathrm{A}}^2 - \omega^2\right)}{\left(\omega_{\mathrm{A}}^2 - \omega^2\right)^2 + \left(\omega^3/\omega_{\mathrm{A}}^2\right)^2\Gamma^2}, \tag{2.12}$$

$$\mathrm{Im}[\alpha] = 6\pi\varepsilon_0 c^3 \frac{\left(\omega^3/\omega_{\mathrm{A}}^4\right)\Gamma^2}{\left(\omega_{\mathrm{A}}^2 - \omega^2\right)^2 + \left(\omega^3/\omega_{\mathrm{A}}^2\right)^2\Gamma^2}\,. \tag{2.13}$$

In the above equation, we used again (2.7). By inserting $\mathrm{Re}[\alpha]$ into equation (2.1), we find that, within a classical approach, the dipole potential is

$$\mathrm{U_{dip}}(\mathbf{r}) = -\frac{3\pi c^2}{\omega_\mathrm{A}^2} \frac{\Gamma\left(\omega_\mathrm{A}^2-\omega^2\right)}{\left[\left(\omega_\mathrm{A}^2-\omega^2\right)^2+\left(\omega^3/\omega_\mathrm{A}^2\right)^2\Gamma^2\right]} I(\mathbf{r})\,. \tag{2.14}$$

This can be rewritten as follows:

$$\mathrm{U_{dip}}(\mathbf{r}) = -\frac{3\pi c^2}{\omega_\mathrm{A}^2} \frac{\Gamma}{\left(\omega_\mathrm{A}+\omega\right)\left(\omega_\mathrm{A}-\omega\right)\left[1+\frac{\left(\omega^3/\omega_\mathrm{A}^2\right)^2\Gamma^2}{\left(\omega_\mathrm{A}+\omega\right)^2\left(\omega_\mathrm{A}-\omega\right)^2}\right]} I(\mathbf{r})\,. \tag{2.15}$$

For simplification we assume that the absolute value of the detuning $\Delta = \omega - \omega_\mathrm{A}$ is much larger than the natural line width of the transition i.e. $|\Delta| \gg \Gamma$, so we have $\omega_\mathrm{A}^2\left(\omega+\omega_\mathrm{A}\right)\Delta \gg \omega^3\Gamma$ and the expression reduces to

$$\mathrm{U_{dip}}(\mathbf{r}) = -\frac{3\pi c^2}{2\omega_\mathrm{A}^3}\left(\frac{\Gamma}{\omega_\mathrm{A}-\omega}+\frac{\Gamma}{\omega_\mathrm{A}+\omega}\right) I(\mathbf{r})\,. \tag{2.16}$$

By using the same procedure we obtain for the scattering rate from (2.3) and (2.13)

$$\Gamma_\mathrm{sc}(\mathbf{r}) = \frac{3\pi c^2}{2\hbar\omega_\mathrm{A}^3}\left(\frac{\omega}{\omega_\mathrm{A}}\right)^3\left(\frac{\Gamma}{\omega_\mathrm{A}-\omega}+\frac{\Gamma}{\omega_\mathrm{A}+\omega}\right)^2 I(\mathbf{r})\,. \tag{2.17}$$

To understand the physics of ODT's, these equations can be simplified even further by using the rotating wave approximation (RWA) [163]. This approximation is valid when the frequency of the beam is relatively close to the resonance frequency of the atomic transition, i.e. $\omega \approx \omega_\mathrm{A}$. Then the second term on the right-hand side of equations (2.16) and (2.17) becomes much smaller than the first term due to $\omega+\omega_\mathrm{A} \gg \Delta$, and can therefore be neglected. Note that this approximation can be used as the ODT in the experiment is relatively far from resonance. By using the rotating wave approximation, we write the dipole potential (2.16)

$$\mathrm{U_{dip}}(\mathbf{r}) = \frac{3\pi\Gamma c^2}{2\omega_\mathrm{A}^3\Delta} I(\mathbf{r}), \tag{2.18}$$

and the scattering rate (2.17) becomes

$$\Gamma_\mathrm{sc}(\mathbf{r}) = \frac{3\pi c^2}{2\hbar\omega_\mathrm{A}^3}\left(\frac{\Gamma}{\Delta}\right)^2 I(\mathbf{r})\,. \tag{2.19}$$

For negative detuning Δ, i.e. light frequencies ω below the atomic resonance frequency ω_A, the ODT potential is negative and atoms are attracted into the light field (red-detuned trap). For positive detuning, i.e. light frequencies above the atomic resonance frequency, the ODT potential is positive and atoms are repelled from the light field (blue-detuned trap) as shown

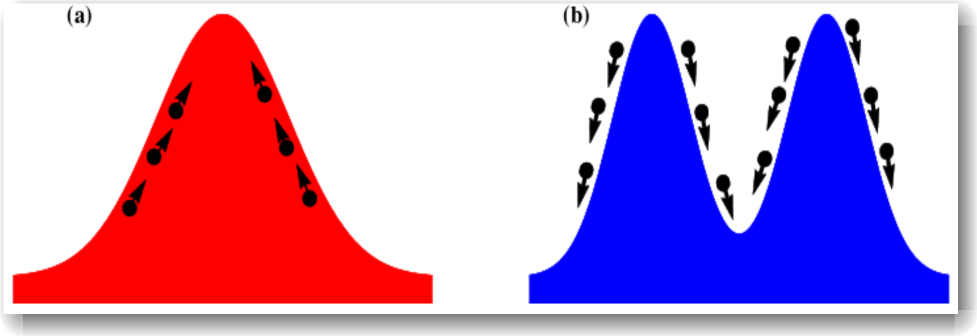

Figure 2.1: A cartoon illustration the dipole trap with (a) red- and (b) blue-detuning [29].

in Fig. 2.1. Traps operating within the validity of the RWA are called far-off-resonant optical traps (FORT). The dipole potential scales as $I(\mathbf{r})/\Delta$, whereas the scattering rate scales as $I(\mathbf{r})/\Delta^2$, therefore it is favorable to choose in an experiment a large detuning of the laser beam. In order to compensate for the decrease in the dipole potential, the intensity of the laser beam can be increased.

2.1.2 Semi-classical two-level atomic model

A quantum description of an optical dipole trap involves the complex energy level structure of atoms. At the beginning, to avoid the complexity of the problem, we introduce a simplified two-level atom model, which consists of a ground state $|e>$ and an excited state $|g>$ with the excitation frequency ω_A. Note that, in order to treat a real atom as a two-level atom with all its complex energy level structure, a large detuning as compared to the natural line width of the transition, i.e. $|\Delta| \gg \Gamma$, is required, so that the hyperfine structure of the atom cannot be distinguished. Nevertheless, the incident laser light frequency ω must be close enough to a specific resonance to ensure that we are in the region of the particular two-level approximation. This is same kind of physical analogy which was used to derive equation (2.18).

The effect of laser light on the energy levels of the atomic system can be evaluated using time-independent perturbation theory [29]. The Hamiltonian of the system for the perturbed case is given by $\mathscr{H} = \mathscr{H}_0 + \mathscr{H}_1$, where $\mathscr{H}_1$ describes the perturbation from the unperturbed Hamiltonian $\mathscr{H}_0$. In our special case we have $\mathscr{H}_1 = -\hat{\mathbf{d}}\mathbf{E}$, where $\hat{\mathbf{d}} = -e\mathbf{r}$ is the electric dipole operator. As a general result of second-order time-independent perturbation theory for non-degenerate states, an interaction Hamiltonian leads to an energy shift of the i-th state that is given by [29]

$$\Delta E_i = \sum_{i \neq j} \frac{|<i|\mathscr{H}_1|j>|^2}{\Xi_i - \Xi_j}. \tag{2.20}$$

Note that the first-order perturbation $< i|\mathscr{H}_1|i >$ vanishes due to symmetry reasons. Here, Ξ_i represents the unperturbed energies of the atom plus the electromagnetic field [29]. For a two-level system, the ground state level has zero internal energy and the light field energy is $n\hbar\omega$, according to the number of photons n, so the total energy of the unperturbed ground state is $\Xi_i = n\hbar\omega$. On the other hand, when an atom absorbs a photon and gets into an excited state, the sum of its internal energy $\hbar\omega_\mathrm{A}$ and the field energy $\Xi_i = (n-1)\hbar\omega$ yields $\Xi_j = \hbar\omega_\mathrm{A} + (n-1)\hbar\omega = -\hbar\Delta + \Xi_i$. Thus (2.20) reduces to

$$\Delta E = \pm\frac{|< i|\hat{\mathbf{d}}|j >|^2}{\hbar\Delta}|\mathbf{E}|^2 . \tag{2.21}$$

Here, the ± signs correspond to the ground (+) and excited state (−) shifts, respectively. From the Weisskopf-Wigner theory of the atomic spontaneous emission [164, Eq. 6.3.14], the decay rate is defined according to

$$\Gamma = \frac{\omega_\mathrm{A}^3 \left|< e|\hat{\mathbf{d}}|g >\right|^2}{3\pi\varepsilon_0\hbar c^3}, \tag{2.22}$$

where $< e|\hat{\mathbf{d}}|g >$ is the dipole matrix element between the ground and the excited state. Note that the semi-classical result (2.22) goes over into the classical one (2.7) by identifying $\left|< e|\hat{\mathbf{d}}|g >\right|$ with $e\sqrt{\hbar/2m\omega_\mathrm{A}}$. Taking into account (2.22), we can rewrite (2.21) as

$$\Delta E = \pm\frac{3\pi\varepsilon_0\Gamma c^3}{\omega_\mathrm{A}^3\Delta}|\mathbf{E}|^2 . \tag{2.23}$$

The energy shift ΔE for the ground (excited) state is either positive (negative) for blue or negative (positive) for red detuning, which is also known as 'light shift' or 'Stark shift'. And the corresponding scattering rate is calculated due to $|\mathbf{E}|^2 = I(\mathbf{r})/(2c\varepsilon_0)$ by using the linear dielectric susceptibility of a two-level atom [161, Eq. 2.178] and [165, Eq. 3.2.23]:

$$\Gamma_\mathrm{sc} = \frac{3\pi\varepsilon_0 c^3}{\hbar\omega_\mathrm{A}^3}\left(\frac{\Gamma}{\Delta}\right)^2|\mathbf{E}|^2 . \tag{2.24}$$

This result coincides with the classical one in Eq. (2.19).

AC Stark Shift: If the incident light is defined by an oscillating electric field, then it can be drafted as $|\mathbf{E}|^2 = I(\mathbf{r})/(2c\varepsilon_0)$ and the energy shift in Eq. (2.23) gets

$$\Delta E = \pm\frac{3\pi\Gamma c^2}{2\omega_\mathrm{A}^3\Delta}I(\mathbf{r}) . \tag{2.25}$$

This result, coincides with the one in Eq. (2.18) which was derived with the help of classical model for the rotating wave approximation. For red-detuning $\Delta < 0$ or blue-detuning $\Delta > 0$, the atom interacts with the external light and shifts the ground state energy downwards or

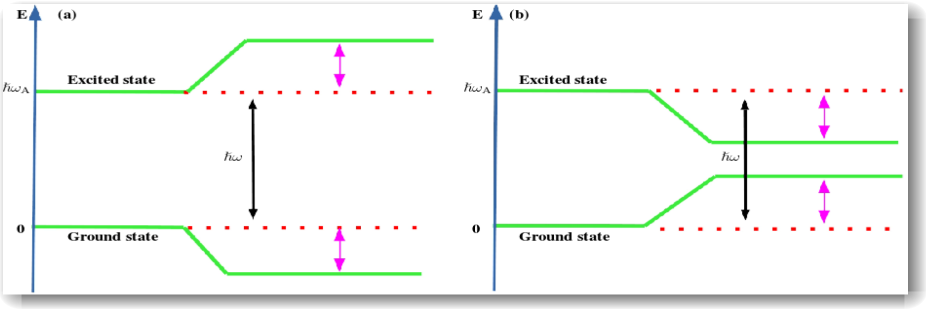

Figure 2.2: A cartoon diagram of AC Stark shift in a two-level atom. (a) For red-detuned light i.e. $\Delta < 0$, the ground state is shifted down and the excited state is shifted up by the same amount ΔE. (b) For blue-detuned light i.e. $\Delta > 0$, the ground state is shifted up and the excited state is shifted down by the same amount ΔE.

upwards, respectively, as shown in Fig. 2.2.

DC Stark Shift: If the incident light is described by a DC electric field, which amounts to the limit $\omega \to 0$, and the light intensity takes the form $|\mathbf{E}|^2 = \mathrm{I}(\mathbf{r})/(\varepsilon_0 c)$, so we obtain from Eq. (2.23)

$$\Delta E = \mp \frac{3\pi\Gamma c^2}{\omega_A^4} I(\mathbf{r}) \,. \tag{2.26}$$

Note that the sign changed because of the detuning term $\Delta \approx -\omega_A$.

2.1.3 Multi-level atomic model

Extending the previous results from a two-level to a multi-level atomic system only requires a slight modification. For the two-level system, we assumed the rotating wave approximation, which is naturally not valid anymore for the multi-level atomic system. Defining the dipole moment matrix elements $\mathbf{D}_{mn} =< m|\hat{\mathbf{d}}|n >$ between states m and n of the atom, the decay rate for a two-level atom in (2.22) is generalized for the multi-level system according to [29]

$$\Gamma_{mn} = \frac{\omega_{mn}^3}{3\pi\varepsilon_0\hbar c^3} |\mathbf{D}_{mn}|^2 \,. \tag{2.27}$$

By summing the energy shifts from all the transitions of the atom, the dipole trapping potential can be calculated from the semi-classical result (2.25),

$$\mathrm{U_{dip}} = -\sum_{m\neq n} \frac{3\pi c^2}{2\omega_{mn}^3} \left(\frac{\Gamma_{mn}}{\omega_{mn}-\omega} + \frac{\Gamma_{mn}}{\omega_{mn}+\omega} \right) I(\mathbf{r}) \,. \tag{2.28}$$

Following the same steps, we get instead of the semi-classical results (2.24)

$$\Gamma_{\mathrm{sc}} = \sum_{m\neq n} \frac{3\pi c^2}{2\hbar\omega_{mn}^3} \left(\frac{\omega}{\omega_{mn}}\right)^3 \left(\frac{\Gamma_{mn}}{\omega_{mn}-\omega} + \frac{\Gamma_{mn}}{\omega_{mn}+\omega}\right)^2 I(\mathbf{r})\,. \tag{2.29}$$

The multi-level atom results (2.28) and (2.29) are the true results to measure the accurate trap depth and the scattering rate for the optical dipole traps. But on the other hand the two-level approximated semi-classical results (2.23) and (2.24) are helpful to understand the basic physics of the optical dipole traps.

2.2 Evanescent wave

The manipulation of ultra-cold atoms with optical or magnetic fields close to dielectric surfaces is broadly explored in the context of constructing atom optics devices. An evanescent wave has the special aspect that its electromagnetic field decays exponentially with increasing distance from the dielectric boundary. Under a special circumstance, an evanescent field allows to reflect and to cool atoms near to dielectric surfaces. To create the evanescent wave, experimentalists use a fused silica prism, where the laser beam undergoes a total internal reflection at the surface of the prism [79]. This reflection follows Snell's law $n_i \sin\Theta_i = n_r \sin\Theta_r$, with n_i and n_r denoting the respective refractive indices as well as Θ_i and Θ_r being the angle of incidence and the angle of refraction. All the light is reflected internally, if the angle between the incident wave vector and the surface normal exceeds the critical angle, which is given according to Snell's law by $\Theta_c = \arcsin\left(n_r/n_i\right)$. As a result of the total internal reflection of the light and because the electric field must be continuous at the boundary of dielectric surface, some amount of the field "leaks out" into the vacuum region which is known as the evanescent wave. The strength of this field is larger at the boundary of the surface and falls off exponentially as it penetrates into the vacuum. The transmitted electric field vector reads

$$\mathbf{E}_t\left(\mathbf{r},t\right) = E_t \mathbf{e}_t e^{-i\left(k_{tx}x + k_{tz}z - \omega t\right)}\,, \tag{2.30}$$

where, E_t denotes the amplitude of the electric field, $\mathbf{e}_t$ stands for the polarization of the electric field, k_{tx} and k_{tz} are the wave vectors as shown in Fig. 2.3. Note that the wave vector along the y-axis is zero, while it is perpendicular to the electric field. Due to the boundary condition between the dielectric media and the air, the transversal components of the respective wave vectors coincide:

$$k_{ix} = k_{rx} = k_{tx}. \tag{2.31}$$

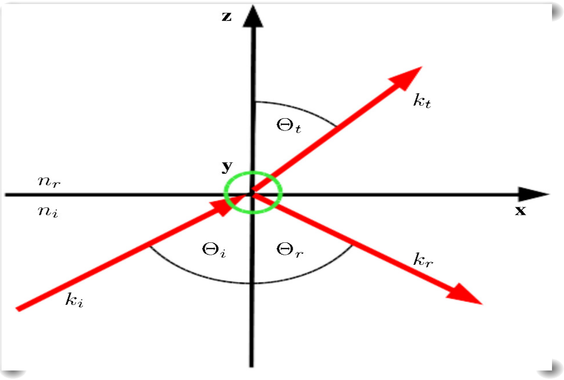

Figure 2.3: A picture description of Snell's law. An evanescent wave occurs for a total internal reflection at the dielectric interface, i.e. when $\Theta_r = \pi/2$.

This can be rewritten according to

$$k_i \sin\Theta_i = k_r \sin\Theta_r = k_t \sin\Theta_t, \tag{2.32}$$

with the wave vectors

$$k_i = \frac{\omega}{c} n_i \, , \; k_r = \frac{\omega}{c} n_i \, , \; k_t = \frac{\omega}{c} n_r \, . \tag{2.33}$$

After some algebra, the wave vectors are rewritten as

$$k_{tx} = \frac{\omega}{c} n_i \sin\Theta_i, \tag{2.34}$$

$$k_{tz} = i\frac{\omega}{c} n_r \sqrt{\left(\frac{n_i}{n_r}\sin\Theta_i\right)^2 - 1}\, . \tag{2.35}$$

By putting these values in equation (2.30), the expression for the evanescent wave field reads [79, 80, 82]

$$\mathbf{E}_t\left(\mathbf{r},t\right) = E_t \mathbf{e_t} e^{-z/\Lambda} e^{-i(k_{tx}x-\omega t)}\, . \tag{2.36}$$

where

$$\Lambda = \lambda / \left[2\pi \sqrt{\left(\frac{n_i}{n_r}\sin\Theta_i\right)^2 - 1} \right] \tag{2.37}$$

represents the decay length of the evanescent wave. Ovchinnikov et al. in experiment [79] used $n_i = 1.45$ and $n_r = 1$, which represents the index of refraction of the fused silica medium and the air, respectively.

Trapping of atoms near to dielectric surfaces has some disadvantages, for example, some unwanted forces start to play a vital role, when the distance between atoms and the surface becomes about 100 nm [166], these forces are known as van-der-Waals (vdW) forces. The attractive vdW force is based upon the electromagnetic interaction of an atomic dipole with its mirror image on the dielectric surface. We will not describe the complex calculation of this effect, because we assume that atoms are trapped far away from the prism surface, therefore for more detailed analysis, please see Ref. [167]. The van-der-Waals potential can be divided into two special cases, which differ depending on the distance of the atoms from the surface. The regime, where the atoms are close to the dielectric surface, i.e. $z \ll \lambda_{\text{eff}}/2\pi$, is called the Lennard-Jones regime [168, 169], here λ_{eff} is the effective transition wave length for the two-level atom. In the other case, where the atoms are far away from the surface, i.e. $z \gg \lambda/2\pi$, the regime is called Casimir-Polder regime [166, 170].

2.3 Free energy

Although the second quantization is a representation of a system but not a solution, its application often leads to a considerable simplification of the analysis of many-particle systems. Somehow, second quantization provides a basic and efficient language in which we formulate many-particle systems. The description of bosons starts from defining the second-quantized Hamiltonian operator [6, 87, 171],

$$\mathscr{H}_{\text{S}} = \int d^3\mathbf{x}\hat{\Psi}^{\dagger}(\mathbf{x})\, h(\mathbf{x})\, \hat{\Psi}(\mathbf{x}) + \frac{1}{2}\int d^3\mathbf{x}\hat{\Psi}^{\dagger}(\mathbf{x}) \int d^3\mathbf{x}'\hat{\Psi}^{\dagger}(\mathbf{x})\, U(\mathbf{x},\mathbf{x}')\, \hat{\Psi}(\mathbf{x}')\, \hat{\Psi}(\mathbf{x}), \tag{2.38}$$

where the first-quantized Hamiltonian operator $h(\mathbf{x}) = -\hbar^2\Delta/(2m_{\text{B}}) + V(\mathbf{x})$ contains the kinetic term plus an external potential $V(\mathbf{x})$ and $U(\mathbf{x},\mathbf{x}')$ denotes the interaction potential between bosons. In the above expression, the field operators $\hat{\Psi}^{\dagger}(\mathbf{x})$ and $\hat{\Psi}(\mathbf{x})$ obey the usual commutator relations for bosonic particles, i.e.

$$\begin{aligned} \left[\hat{\Psi}^{\dagger}(\mathbf{x}), \hat{\Psi}^{\dagger}(\mathbf{x}')\right]_{-} &= \left[\hat{\Psi}(\mathbf{x}), \hat{\Psi}(\mathbf{x}')\right]_{-} = 0, \\ \left[\hat{\Psi}(\mathbf{x}'), \hat{\Psi}^{\dagger}(\mathbf{x})\right]_{-} &= \delta(\mathbf{x}-\mathbf{x}') . \end{aligned} \tag{2.39}$$

The many-body Hamiltonian can be generalized according to the grand-canonical ensemble

$$\mathscr{H} = \int d^3\mathbf{x}\hat{\Psi}^{\dagger}(\mathbf{x})\,[h(\mathbf{x})-\mu]\,\hat{\Psi}(\mathbf{x}) + \frac{1}{2}\int d^3\mathbf{x}\hat{\Psi}^{\dagger}(\mathbf{x}) \int d^3\mathbf{x}'\hat{\Psi}^{\dagger}(\mathbf{x})\, U(\mathbf{x},\mathbf{x}')\, \hat{\Psi}(\mathbf{x}')\, \hat{\Psi}(\mathbf{x}), \tag{2.40}$$

where μ represents the chemical potential. The grand-canonical formalism defines the partition function Z as

$$Z = e^{-\beta F} = \text{Tr}\left[e^{-\beta\mathscr{H}}\right], \tag{2.41}$$

where F is the free energy of the system, $\beta = 1/k_\mathrm{B}T$ is the inverse temperature and the trace in the expression has to be taken over all states of the Fock space. We introduce a one-particle basis, which is characterized by discrete quantum numbers n, and write the field operator as an expansion with respect to these functions $\Psi_n(\mathbf{x})$ as

$$\hat{\Psi}(\mathbf{x}) = \sum_n \hat{a}_n \Psi_n(\mathbf{x}), \qquad \hat{\Psi}^\dagger(\mathbf{x}) = \sum_n \hat{a}_n^\dagger \Psi_n^*(\mathbf{x}). \tag{2.42}$$

The one-particle basis is chosen to be orthonormal

$$\int d^3\mathbf{x} \Psi_n(\mathbf{x})\Psi_m^*(\mathbf{x}) = \delta_{nm}, \tag{2.43}$$

and complete

$$\sum_n \Psi_n(\mathbf{x})\Psi_n^*(\mathbf{x}') = \delta\left(\mathbf{x}-\mathbf{x}'\right). \tag{2.44}$$

The expansion coefficients $\hat{a}_n^\dagger = \int d^3\mathbf{x}\Psi_n(\mathbf{x})\hat{\Psi}^\dagger(\mathbf{x})$ and $\hat{a}_n = \int d^3\mathbf{x}\Psi_n^*(\mathbf{x})\hat{\Psi}(\mathbf{x})$ represent the creation and annihilation operators of a particle with the quantum number n as they obey the canonical commutator relations

$$\left[\hat{a}_n^\dagger, \hat{a}_m^\dagger\right]_- = [\hat{a}_n, \hat{a}_m]_- = 0, \qquad \left[\hat{a}_n, \hat{a}_m^\dagger\right]_- = \delta_{nm}. \tag{2.45}$$

2.3.1 Non-interacting particles

For simplicity reason we assume at the moment that the bosons are non-interacting particles, i.e. $U(\mathbf{x},\mathbf{x}') = 0$. Without loss of generality we can choose the one-particle basis such that $h(\mathbf{x})\Psi_m(\mathbf{x}) = E_m\Psi_m(\mathbf{x})$, therefore we insert (2.42) into the Hamiltonian operator (2.40) and get

$$\hat{\mathscr{H}} = \int d^3\mathbf{x} \underbrace{\left[\sum_n \hat{a}_n^\dagger \Psi_n^*(\mathbf{x})\right] \underbrace{\left[h(\mathbf{x}) - \mu\right]\left[\sum_m \hat{a}_m \Psi_m(\mathbf{x})\right]}_{\sum_m \hat{a}_m (E_m-\mu)\Psi_m(\mathbf{x})}}_{\sum_n\sum_m \hat{a}_n^\dagger\hat{a}_m(E_n-\mu)\delta_{nm}}. \tag{2.46}$$

We rewrite the Hamiltonian in terms of these creation and annihilation operators as

$$\hat{\mathscr{H}} = \sum_n (E_n - \mu)\,\hat{a}_n^\dagger \hat{a}_n. \tag{2.47}$$

Here, we formulated our system in terms of one-particle energies E_n. A basis in Fock space is provided by the occupation number basis $\prod_n |N_n>_n$ with the property

$$\hat{a}_n^{\dagger}|N_n>_n = \sqrt{N_n+1}|N_n+1>_n, \qquad \hat{a}_n|N_n>_n = \sqrt{N_n}|N_n-1>_n\,. \tag{2.48}$$

Because we have a large number of particles in the ground state, we obtain $\hat{a}_0^{\dagger}|N_0>_0 \approx \sqrt{N_0}|N_0>_0$ and $\hat{a}_0|N_0>_0 \approx \sqrt{N_0}|N_0>_0$ or $\hat{a}_0 \approx \hat{a}_0^{\dagger} \approx \sqrt{N_0} = \Psi_0$. As T decreases, more and more bosons occupy the ground state, as it has the lowest energy. Thus we should take into account the ground state separately. Therefore, we divide the Hamiltonian into two parts, one for the ground state and one for the excited states

$$\hat{\mathscr{H}} = (E_0-\mu)\,\Psi_0^2 + \sum_{n\neq 0}(E_n-\mu)\,\hat{a}_n^{\dagger}\hat{a}_n\,. \tag{2.49}$$

Using (2.49), the partition function (2.41) can be written as

$$Z = \mathrm{Tr}\left[e^{-\beta\left[(E_0-\mu)\Psi_0^2+\sum_{n\neq 0}(E_n-\mu)\hat{a}_n^{\dagger}\hat{a}_n\right]}\right], \tag{2.50}$$

here the trace in Fock space is defined as

$$\mathrm{Tr}\hat{\mathscr{O}} = \left(\prod_{n\neq 0}\sum_{N_n=0}^{\infty}\right) < ......,N_n,....|\hat{\mathscr{O}}|......,N_n,.... > . \tag{2.51}$$

With this, we rewrite the partition function

$$Z = < N_0|e^{-\beta\left[(E_0-\mu)\Psi_0^2\right]}|N_0 > \underbrace{\left(\prod_{n\neq 0}\sum_{N_n=0}^{\infty}\right) < ......,N_n,....|e^{-\beta\sum_{n\neq 0}^{\infty}(E_n-\mu)\hat{a}_n^{\dagger}\hat{a}_n}|......,N_n,.... >}_{\prod_{n\neq 0}\sum_{N_n=0}^{\infty}e^{-\beta\sum_{n\neq 0}^{\infty}(E_n-\mu)N_n}}, \tag{2.52}$$

or more simplified

$$Z = e^{-\beta\left[(E_0-\mu)\Psi_0^2\right]}\prod_{n\neq 0}\frac{1}{1-e^{-\beta(E_n-\mu)}}\,. \tag{2.53}$$

By evaluating the geometric series we have to impose

$$E_n > \mu \qquad \text{for all } n\neq 0\,. \tag{2.54}$$

After some algebra, the free energy of the system takes the form

$$F=-\frac{1}{\beta}\ln Z=(E_0-\mu)\Psi_0^2+\frac{1}{\beta}\sum_{n\neq 0}\ln\left[1-e^{-\beta(E_n-\mu)}\right]. \tag{2.55}$$

Following Landau [87] the physically realized order parameter follows from extremizing the free energy F:

$$2(E_0-\mu)\Psi_0=0 \qquad \Rightarrow \qquad \begin{cases} \Psi_0=0\equiv N_0 & \text{Gas phase, } E_0\neq\mu \\[2ex] E_0=\mu & \text{BEC phase, } N_0\neq 0\,. \end{cases} \tag{2.56}$$

Here, the first case describes the high-temperature phase, wherein the bosons do not occupy the ground state macroscopically, while the second case represents the low-temperature phase, wherein a Bose-Einstein condensate is present. We see the fact that in the grand-canonical ensemble one has to investigate the thermodynamic properties of the respective phases separately.

With the use of the thermodynamic relation $N\equiv-\partial F/\partial\mu$, we calculate from Eq. (2.55) the Bose-Einstein distribution for the excited states:

$$N=N_0+\sum_{n\neq 0}\frac{1}{e^{\beta(E_n-\mu)}-1}\,. \tag{2.57}$$

2.3.2 Semi-classical limit

In this section, we show how the properties of a trapped cloud of non-interacting particles may be described semi-classically. This approximation holds, provided that the typical de-Broglie wave lengths of particles are small compared with the length scales over which the trapping potential and the particle density vary significantly. Locally, the gas may then be treated as quasi-uniform. Properties of non-condensed particles may be calculated using a semi-classical distribution function F_{th}. In a semi-classical limit, when $\hbar\to 0$, $T\to\infty$ and (2.54), we determine for the thermal part of the free energy (2.55)

$$F_{\text{th}}=\frac{1}{\beta}\underbrace{\sum_{n\neq 0}\ln\left(1-e^{-\beta(E_n-\mu)}\right)}_{-\sum_{m=1}^{\infty}\frac{e^{-m\beta(E_n-\mu)}}{m}}=-\frac{1}{\beta}\sum_{m=1}^{\infty}\frac{e^{m\beta\mu}}{m}\sum_{n\neq 0}e^{-m\beta E_n}. \tag{2.58}$$

Here $\sum_{n\neq 0}e^{-m\beta E_n}=Z_1(m\beta)-e^{-m\beta E_0}$, and $Z_1(\beta)$ represents the one-particle partition function. In a semi-classical approximation, we identify the quantum number n with a point in phase space

$$\begin{aligned} & n \to \mathbf{x}, \mathbf{p}, && (2.59) \\ & \sum_{n \neq 0} \to \int_{-\infty}^{\infty} d^D \mathbf{x} \int_{-\infty}^{\infty} \frac{d^D \mathbf{p}}{(2\pi\hbar)^D}, \\ & E_n \to E_0 + H(\mathbf{x}, \mathbf{p}), \end{aligned}$$

where D represents the number of dimensions. By using above mentioned approximations we write the semi-classical free energy (2.55)

$$F = (E_0 - \mu)\Psi_0^2 + \frac{1}{\beta}\int_{-\infty}^{\infty} d^D\mathbf{x} \int_{-\infty}^{\infty} \frac{d^D\mathbf{p}}{(2\pi\hbar)^D} \ln\left\{1 - e^{-\beta[H(\mathbf{x},\mathbf{p}) + E_0 - \mu]}\right\}. \tag{2.60}$$

Thus, the first term describes the contribution of those bosons, which are in the ground state. This condensate contribution depends on the number $N_0 = \Psi_0^2$, which defines the condensed bosons. The second term describes the contribution of the non-condensed bosons within the semi-classical approximation. Finally, using the thermodynamic relation $N \equiv -\partial F/\partial\mu$, we obtain for the number of particles

$$N = N_0 + \int_{-\infty}^{\infty} d^D\mathbf{x} \int_{-\infty}^{\infty} \frac{d^D\mathbf{p}}{(2\pi\hbar)^D} \frac{1}{e^{\beta[H(\mathbf{x},\mathbf{p}) + E_0 - \mu]} - 1}. \tag{2.61}$$

2.3.3 Ideal Bose gas

As an example of the Bose-Einstein distribution, let us consider an ideal Bose gas. An ideal Bose gas consists of a large number of identical non-interacting bosons in a box with rigid walls and fixed volume V. We consider an ideal Bose gas in a three-dimensional box with length L in the thermodynamic limit $L \to \infty$, with the Hamiltonian $H(\mathbf{x}, \mathbf{p}) = \mathbf{p}^2/2m_\mathrm{B} + V(\mathbf{x})$. For this ensemble, obviously a homogeneous Bose gas is considered $V(\mathbf{x}) = 0$, $E_0 = 0$ with dimensions $D = 3$, with this we write free energy of the system from Eq. (2.60)

$$F = (E_0 - \mu)\Psi_0^2 + \frac{1}{\beta}\int_{-\infty}^{\infty} d^3\mathbf{x} \int_{-\infty}^{\infty} \frac{d^3\mathbf{p}}{(2\pi\hbar)^3} \ln\left[1 - e^{-\beta\left(\mathbf{p}^2/2m_\mathrm{B} - \mu\right)}\right]. \tag{2.62}$$

By using the Taylor series expression $\ln(1 - e^{-\mathbf{y}}) = -\sum_{m=1}^{\infty} e^{-m\mathbf{y}}/m$ and the Gaussian integral $\int_{-\infty}^{\infty} d^3\mathbf{p} e^{-m\beta\left(\mathbf{p}^2/2m_\mathrm{B}\right)} = 2\sqrt{2}\left(\pi m_\mathrm{B}/m\beta\right)^{3/2}$, we simplify above relation as

$$F = (E_0 - \mu)\Psi_0^2 - \frac{V}{\beta\lambda^3}\xi_{5/2}\left(e^{\beta\mu}\right). \tag{2.63}$$

Herein, $\lambda = \sqrt{2\pi\hbar^2\beta/m_{\mathrm{B}}}$ denotes thermal deBroglie wave length and $\xi_\nu(z) = \sum_{m=1}^{\infty} z^m/m^\nu$ is the polylogarithm function, which has the important identity

$$\frac{d}{dz}\xi_\nu(z) = \frac{\xi_{\nu-1}(z)}{z}. \tag{2.64}$$

Thus, the number of atoms in an ideal Bose gas turns out to be

$$N = N_0 + \frac{V}{\lambda^3}\xi_{3/2}\left(e^{\beta\mu}\right). \tag{2.65}$$

At a critical temperature T_c in a uniform 3D system, we have due to (2.56) $N_0 = 0$ and $\mu = 0$. To derive a relation between the density $n = N/V$ and the critical thermal deBroglie wave length, we use the Robinson formula [172]

$$\xi_\nu(e^a) = (-a)^{\nu-1}\Gamma(1-\nu) + \sum_{k=0}^{\infty}\frac{(a)^k}{k!}\xi(\nu-k) \tag{2.66}$$

with $\nu = 3/2$

$$\xi_{3/2}\left(e^{\beta\mu}\right) = -2\sqrt{-\pi\beta\mu} + \xi(3/2) + \beta\mu\xi(1/2) + \ldots, \tag{2.67}$$

which yields

$$\lim_{\mu\uparrow 0}\xi_{3/2}\left(e^{\beta\mu}\right) = \xi(3/2). \tag{2.68}$$

Thus we conclude from (2.65)

$$N = \frac{V}{\lambda_{T_c}^3}\xi_{3/2}(1), \tag{2.69}$$

which gives us the critical point with density $n = N/V$,

$$n\lambda_{T_c}^3 = 2.612, \tag{2.70}$$

as was already calculated qualitatively in (1.1). At lower temperatures than T_c, the thermal population is

$$N_T = \frac{V}{\lambda_T^3}\xi_{3/2}(1). \tag{2.71}$$

Taking the ratio of last two equations $\lambda_T^3/\lambda_{T_c}^3 = N/N_T$, we write the number of particles in the condensate for a homogeneous Bose gas as

$$N_0 = N - N_T = N\left[1 - \left(\frac{T}{T_c}\right)^{\frac{3}{2}}\right]. \tag{2.72}$$

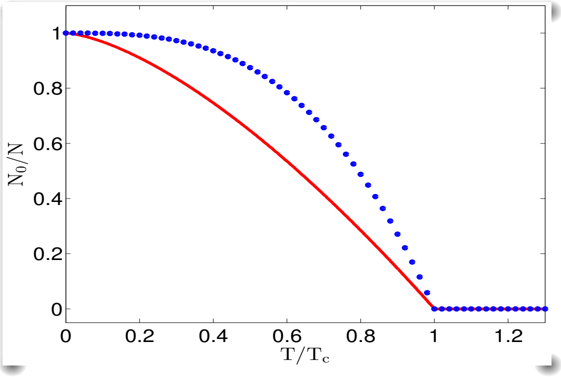

Figure 2.4: Homogeneous (solid red-line) and three-dimensional harmonic trapped (blue-circles) condensate fraction N_0/N versus normalized temperature T/T_c. Here, T_c represents the respective critical temperatures.

Figure 2.4 shows the condensate fraction N_0/N versus normalized temperature T/T_c. We encounter here a "two-fluid" system for which the total particle density splits into a condensed fraction N_0 and a normal fraction N_T.

2.3.4 3D harmonically trapped Bose gas

We now consider a non-interacting Bose gas in a three-dimensional harmonic trap $V(\mathbf{x}) = m_\mathrm{B}\sum_{i=1}^{3}\omega_i^2 x_i^2/2$, which is described by the Hamiltonian $H(\mathbf{x},\mathbf{p}) = \mathbf{p}^2/2m_\mathrm{B} + V(\mathbf{x})$. We write the free energy of the system from Eq. (2.60) as

$$F = (E_0-\mu)\Psi_0^2 - \frac{1}{\beta}\sum_{m=1}^{\infty}\frac{e^{m\beta(\mu-E_0)}}{m}\int_{-\infty}^{\infty} d^3\mathbf{x}\int_{-\infty}^{\infty}\frac{d^3\mathbf{p}}{(2\pi\hbar)^3}e^{-m\beta\left[\mathbf{p}^2/2m_\mathrm{B}+m_\mathrm{B}\sum_{i=1}^{3}\omega_i^2x_i^2/2\right]}. \tag{2.73}$$

Evaluating the Gaussian phase space integral and using the polylogarithm function, we derive the following expression for the free energy

$$F = (E_0-\mu)\Psi_0^2 - \frac{\xi_4\left(e^{\beta(\mu-E_0)}\right)}{\beta\left(\hbar\beta\tilde{\omega}\right)^3}, \tag{2.74}$$

where $\tilde{\omega} = (\omega_1\omega_2\omega_3)^{1/3}$ expresses the geometric mean of the trap frequencies. With this we obtain the relation for the number of atoms in a 3D harmonic trap Bose gas

$$N = N_0 + \frac{\xi_3\left(e^{\beta(\mu-E_0)}\right)}{\left(\hbar\beta\tilde{\omega}\right)^3}. \tag{2.75}$$

To determine the relation for number of atoms at $T = T_c$, we use the condition $\mu = E_0$ and $N_0 = 0$, which yields

$$N = \left(\frac{k_\mathrm{B} T_c}{\hbar\tilde{\omega}}\right)^3 \xi(3)\,. \tag{2.76}$$

Furthermore, we read off from (2.75) that for $T \leq T_c$ the thermal population is given by

$$N_T = \left(\frac{k_\mathrm{B} T}{\hbar\tilde{\omega}}\right)^3 \xi(3)\,. \tag{2.77}$$

By taking the ratio of the last two equations $N_T/N = (T/T_c)^3$, we write the number of particles in the condensate as

$$N_0 = N - N_T = N\left[1 - \left(\frac{T}{T_c}\right)^3\right]. \tag{2.78}$$

The condensate fraction as shown in Fig. 2.4 was confirmed by experimental results [173].

2.3.5 1D homogeneous and harmonic trapped Bose gas

According to the Mermin–Wagner theorem [174] a BEC does not exist in the two-dimensional (2D) or in the one-dimensional (1D) homogeneous case. As we will restrict ourselves to the 1D system we show in this section that the BEC transition can happen for the trapped case but not for the homogeneous case. With this, first we discuss the homogeneous case by redefining the free energy of the system (2.60) for the one-dimensional scenario

$$F = (E_0 - \mu)\Psi_0^2 - \frac{L}{\beta}\sum_{m=1}^{\infty}\frac{e^{m(\mu - E_0)}}{m}\int_{-\infty}^{\infty}\frac{dp}{2\pi\hbar}e^{-m\beta\left(p^2/2m_\mathrm{B}\right)}. \tag{2.79}$$

By using the polylogarithm function, we write the simplified expression for the free energy of the system as

$$F = (E_0 - \mu)\Psi_0^2 - L\frac{\xi_{3/2}\left(e^{\beta(\mu - E_0)}\right)}{\beta\hbar\sqrt{2\pi}\left(\beta/m_\mathrm{B}\right)^{1/2}}\,. \tag{2.80}$$

With this we yield the relation for the number of atoms $N \equiv -\partial F/\partial\mu$ in a 1D homogeneous Bose gas

$$N = N_0 + L\frac{\xi_{1/2}\left(e^{\beta(\mu - E_0)}\right)}{\hbar\sqrt{2\pi}\left(\beta/m_\mathrm{B}\right)^{1/2}}\,. \tag{2.81}$$

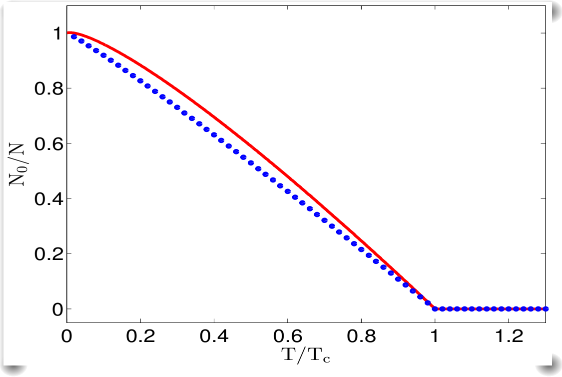

Figure 2.5: Condensate fraction N_0/N versus normalized temperature T/T_c, for $N = 10^2$ (solid red-line) and $N = 10^6$ (blue-circles) harmonically trapped bosons in 1D. Here, T_c represents the respective critical temperatures.

To determine the relation for the number of atoms at the $T = T_c$, we use the condition $\mu = E_0$ and $N_0 = 0$, yielding

$$N = L\frac{\xi_{1/2}(1)}{\hbar\sqrt{2\pi}\left(\beta_c/m_{\mathrm{B}}\right)^{1/2}}. \tag{2.82}$$

We know that the polylogarithm function $\xi_{1/2}(1)$ diverges, therefore we cannot see the transition for the 1D homogeneous case. For the critical temperature Eq. (2.82) can be rewritten $T_c = 2\pi\hbar^2\left[N/L\xi_{1/2}(1)\right]^2/k_{\mathrm{B}}m_{\mathrm{B}}$, so we derive the Mermin–Wagner theorem, which states that $T_c = 0$ for the 1D homogeneous case [174].

Now let's calculate the transition temperature for the trapped one-dimensional BEC starting from (2.60):

$$F = (E_0-\mu)\Psi_0^2 - \frac{1}{\beta(2\pi\hbar)}\sum_{m=1}^{\infty}\frac{e^{m(\mu-E_0)}}{m}\underbrace{\int_{-\infty}^{\infty}dx\int_{-\infty}^{\infty}dp e^{-m\beta\left[p^2/2m_{\mathrm{B}}+m_{\mathrm{B}}\omega^2x^2/2\right]}}_{2\pi/m\beta\omega}. \tag{2.83}$$

The simplified free energy is

$$F = (E_0-\mu)\Psi_0^2 - \frac{\xi_2\left(e^{\beta(\mu-E_0)}\right)}{\hbar\beta^2\omega}. \tag{2.84}$$

By using the above relation, we define the number of atoms $N \equiv -\partial F/\partial\mu$ in a 1D trapped Bose gas

$$N = N_0 + \frac{\xi_1\left(e^{\beta(\mu-E_0)}\right)}{\hbar\beta\omega}. \tag{2.85}$$

In order to evaluate (2.85) at the initial point, we use the specialized Robinson formula $\xi_1(e^a) = -\ln(-a) + \sum\limits_{k=1}^{\infty} a^k\xi(1-k)/k!$ [171], and get $\xi_1(1) = \infty$. From this we conclude that, by using the semi-classical approach, we can not find the particle number for the one-dimensional trapped case. Therefore we need to calculate the number of particles with an advanced technique [175], which takes into account finite-size effects and yields for the one-dimensional condensate fraction

$$N_0 = N\left[1-\frac{T}{T_c}\left(1+\frac{\ln\left(T/T_c\right)}{\gamma-\ln\left(\hbar\omega\beta_c\right)}\right)\right]+\ldots., \tag{2.86}$$

Here the critical temperature is approximately defined as $T_c = \left\{N/\left[\gamma-\ln\left(\hbar\omega\beta_c\right)\right]\right\}\hbar\omega/k_{\mathrm{B}}$ with $\gamma = 0.5772$ being Euler's constant [175]. For the different number of atoms, we plot the one-dimensional condensate fraction versus the normalized critical temperature as shown in Fig. 2.5. For the harmonic oscillator frequency $\omega = 2\pi\times 100\,\mathrm{Hz}$, the critical temperature for $N = 10^2$ and $N = 10^6$ particles are $T_c = 0.124\,\mu\mathrm{K}$ and $T_c = 0.402\,\mathrm{mK}$, respectively.

2.4 Gross-Pitaevskii equation

At zero temperature for weak two-particle interaction, one can consider the Bose gas to be governed by a single wave function. In the following we sketch its derivation starting from the Heisenberg picture formulation $\hat{\Psi}_{\mathrm{H}}\left(\mathbf{r},t\right) = e^{-i\hat{\mathscr{H}}_{\mathrm{S}}t/\hbar}\hat{\Psi}_{\mathrm{S}}\left(\mathbf{r}\right)e^{i\hat{\mathscr{H}}_{\mathrm{S}}t/\hbar}$ where $\hat{\Psi}_{\mathrm{S}}\left(\mathbf{r}\right)$ defines the Schrödinger state and $\hat{\mathscr{H}}_{\mathrm{S}}$ describes the second-quantization Hamiltonian (2.38). In the following we restrict ourselves to a contact interaction, i.e. $U\left(\mathbf{r},\mathbf{r}'\right) = G_{\mathrm{B}}^{D}\delta\left(\mathbf{r}-\mathbf{r}'\right)$, where the two-particle contact interaction strength G_{B}^{D} depends on the D dimensions of the system. We rewrite the second-quantization Hamiltonian (2.38) by using the Heisenberg picture formulation $\hat{\mathbb{H}} = e^{-i\hat{\mathscr{H}}_{\mathrm{S}}t/\hbar}\hat{\mathscr{H}}_{\mathrm{S}}e^{i\hat{\mathscr{H}}_{\mathrm{S}}t/\hbar}$ as

$$\hat{\mathbb{H}} = \int d^D\mathbf{r}\hat{\Psi}^{\dagger}\left(\mathbf{r},t\right)h\left(\mathbf{r}\right)\hat{\Psi}\left(\mathbf{r},t\right)+\frac{G_{\mathrm{B}}^{D}}{2}\int d^D\mathbf{r}\hat{\Psi}^{\dagger}\left(\mathbf{r},t\right)\hat{\Psi}^{\dagger}\left(\mathbf{r},t\right)\hat{\Psi}\left(\mathbf{r},t\right)\hat{\Psi}\left(\mathbf{r},t\right). \tag{2.87}$$

The Heisenberg equation of motion of the field operator $\hat{\Psi}\left(\mathbf{r}',t\right)$ is given by

$$\begin{aligned}
& i\hbar\frac{\partial}{\partial t}\hat{\Psi}\left(\mathbf{r}',t\right) = \left[\hat{\Psi}\left(\mathbf{r}',t\right),\hat{\mathbb{H}}\right] = \hat{\Psi}\left(\mathbf{r}',t\right)\hat{\mathbb{H}}-\hat{\mathbb{H}}\hat{\Psi}\left(\mathbf{r}',t\right), \qquad (2.88)\\
& = \hat{\Psi}\left(\mathbf{r}',t\right)\hat{\mathbb{H}}-\int d^D\mathbf{r}\hat{\Psi}^{\dagger}\left(\mathbf{r},t\right)h\left(\mathbf{r}\right)\hat{\Psi}\left(\mathbf{r},t\right)\hat{\Psi}\left(\mathbf{r}',t\right)\\
& -\frac{G_{\mathrm{B}}^{D}}{2}\int d^D\mathbf{r}\hat{\Psi}^{\dagger}\left(\mathbf{r},t\right)\hat{\Psi}^{\dagger}\left(\mathbf{r},t\right)\hat{\Psi}\left(\mathbf{r},t\right)\hat{\Psi}\left(\mathbf{r},t\right)\hat{\Psi}\left(\mathbf{r}',t\right),\\
& = \hat{\Psi}\left(\mathbf{r}',t\right)\hat{\mathbb{H}}-\int d^D\mathbf{r}\left[\hat{\Psi}\left(\mathbf{r}',t\right)\hat{\Psi}^{\dagger}\left(\mathbf{r},t\right)-\delta\left(\mathbf{r}-\mathbf{r}'\right)\right]h\left(\mathbf{r}\right)\hat{\Psi}\left(\mathbf{r},t\right)\\
& -\frac{G_{\mathrm{B}}^{D}}{2}\int d^D\mathbf{r}\left[\hat{\Psi}\left(\mathbf{r}',t\right)\hat{\Psi}^{\dagger}\left(\mathbf{r},t\right)-2\delta\left(\mathbf{r}-\mathbf{r}'\right)\right]\hat{\Psi}^{\dagger}\left(\mathbf{r},t\right)\hat{\Psi}\left(\mathbf{r},t\right)\hat{\Psi}\left(\mathbf{r},t\right),\\
& = \hat{\Psi}\left(\mathbf{r}',t\right)\hat{\mathbb{H}}-\hat{\Psi}\left(\mathbf{r}',t\right)\hat{\mathbb{H}}+\int d^D\mathbf{r}\delta\left(\mathbf{r}-\mathbf{r}'\right)h\left(\mathbf{r}\right)\hat{\Psi}\left(\mathbf{r},t\right)\\
& +G_{\mathrm{B}}^{D}\int d^D\mathbf{r}\delta\left(\mathbf{r}-\mathbf{r}'\right)\hat{\Psi}^{\dagger}\left(\mathbf{r},t\right)\hat{\Psi}\left(\mathbf{r},t\right)\hat{\Psi}\left(\mathbf{r},t\right).
\end{aligned}$$

This then simplifies to

$$i\hbar\frac{\partial}{\partial t}\hat{\Psi}\left(\mathbf{r}',t\right)=\left[-\frac{\hbar^2\Delta}{2m_{\mathrm{B}}}+V(\mathbf{r}')+G_{\mathrm{B}}^{D}\hat{\Psi}^{\dagger}\left(\mathbf{r}',t\right)\hat{\Psi}\left(\mathbf{r}',t\right)\right]\hat{\Psi}\left(\mathbf{r}',t\right). \tag{2.89}$$

We can derive the Gross-Pitaevskii equation (GPE) for dilute Bose gases by decomposing the field operator $\hat{\Psi}(\mathbf{r},t)=\psi(\mathbf{r},t)+\delta\hat{\psi}(\mathbf{r},t)$, here $\psi(\mathbf{r},t)$ is a complex wave function, which corresponds to the macroscopic occupation of the ground state, and $\delta\hat{\psi}(\mathbf{r},t)$ describes the non-condensed fraction, which corresponds either to excited atoms due to thermal or quantum-mechanical fluctuations. The equation of motion for the condensate wave function is obtained by substituting the decomposed field operator into Eq. (2.89) and neglecting the non-condensate fraction $\delta\hat{\psi}(\mathbf{r},t)$, so we obtain

$$i\hbar\frac{\partial}{\partial t}\psi(\mathbf{r},t)=\left[-\frac{\hbar^2\Delta}{2m_{\mathrm{B}}}+V(\mathbf{r})+G_{\mathrm{B}}^{D}\parallel\psi(\mathbf{r},t)\parallel^2\right]\psi(\mathbf{r},t). \tag{2.90}$$

This is the time-dependent Gross-Pitaevskii equation, which has become the main tool for theoretical studies of Bose-Einstein condensates. Here, the term on the left-hand-side (LHS) corresponds to the time dependent dynamics of the system, the first term on the right-hand-side (RHS) represents the kinetic energy of the system, middle term on the RHS describes the potential of the system and the last term on the RHS defines the two-particle interaction in the system. We can also derive the underlying GPE for a condensate wave function by using the Hamilton principle of least action with the action functional [171, 176]

$$\mathscr{A}_{\mathrm{D}}=\int dt\int\mathscr{L}_{\mathrm{D}}\,d^{D}\mathbf{r}, \tag{2.91}$$

where the Lagrangian density reads for three spatial dimensions as

$$\begin{aligned}\mathscr{L}_{\mathrm{D}}=&\frac{i\hbar}{2}\left[\psi^{\star}(\mathbf{r},t)\frac{\partial\psi(\mathbf{r},t)}{\partial t}-\psi(\mathbf{r},t)\frac{\partial\psi^{\star}(\mathbf{r},t)}{\partial t}\right]-\frac{\hbar^2}{2m_{\mathrm{B}}}\nabla\psi^{\star}(\mathbf{r},t)\nabla\psi(\mathbf{r},t)\\&-V(\mathbf{r})\psi^{\star}(\mathbf{r},t)\psi(\mathbf{r},t)-\frac{G_{\mathrm{B}}^{D}}{2}\parallel\psi(\mathbf{r},t)\parallel^4.\end{aligned} \tag{2.92}$$

Here $\psi(\mathbf{r},t)$ describes the BEC wave function with the coordinates $\mathbf{r}=(x_1,x_2,x_3,.....,x_{\mathrm{D}})$. To this end, we consider the D-dimensional action

$$\mathscr{A}_{\mathrm{D}}=\int_{-\infty}^{\infty}\int_{-\infty}^{\infty}\mathscr{L}_{\mathrm{D}}\left(\psi^{\star}(\mathbf{r},t),\frac{\partial\psi^{\star}(\mathbf{r},t)}{\partial t},\frac{\partial\psi^{\star}(\mathbf{r},t)}{\partial\mathbf{r}};\psi(\mathbf{r},t),\frac{\partial\psi(\mathbf{r},t)}{\partial t},\frac{\partial\psi(\mathbf{r},t)}{\partial\mathbf{r}}\right)d^{D}\mathbf{r}dt \tag{2.93}$$

and determine the time-dependent D-dimensional Gross-Pitaevskii equation (DDGPE) according to the Euler-Lagrangian equation

$$\frac{\delta\mathscr{A}_{\mathrm{D}}[\psi^{\star},\psi]}{\delta\psi^{\star}(\mathbf{r},t)}=\frac{\partial\mathscr{L}_{\mathrm{D}}}{\partial\psi^{\star}(\mathbf{r},t)}-\frac{\partial}{\partial\mathbf{r}}\frac{\partial\mathscr{L}_{\mathrm{D}}}{\partial\frac{\partial\psi^{\star}(\mathbf{r},t)}{\partial\mathbf{r}}}-\frac{\partial}{\partial t}\frac{\partial\mathscr{L}_{\mathrm{D}}}{\partial\frac{\partial\psi^{\star}(\mathbf{r},t)}{\partial t}}=0. \tag{2.94}$$

By using the D-dimensional Lagrangian density (2.92), the DDGPE reads (2.90). Strictly speaking, the Gross-Pitaevskii equation (GPE) is only valid for $n_D a^D \ll 1$, where n_D is the density of particles and a is the s-wave scattering length, the validity range calculated by using Bogoliubov theory [177].

2.4.1 Variational method

We now study the condensate function $\psi(\mathbf{r},t)$ for the anisotropic harmonic oscillator $V(\mathbf{r}) = m_\mathrm{B}\sum_{i=1}^{D}\omega_i^2 x_i^2/2$. As (2.90) can not be solved exactly, we follow [178] and work out an approximative variational solution, which is reasonable for weak interactions. To this end we perform the following ansatz for the condensate wave function

$$\psi(\mathbf{r},t) = \frac{1}{\pi^{D/4}\tilde{A}(t)^{D/2}} \exp\left\{-\sum_{i=1}^{D}\left(\frac{1}{2A_i(t)^2}+\mathrm{i}B_i(t)\right)x_i^2\right\}. \tag{2.95}$$

Here, $A_i(t)$ corresponds to the width of the BEC and $B_i(t)$ is a time-dependent variational parameter, the normalization condition is $\int d^D\mathbf{r}|\psi(\mathbf{r},t)|^2 = 1$ and $\tilde{A} = (A_1 A_2 \ldots\ldots A_D)^{1/D}$. With this the Lagrangian Eq. (2.92) decomposes into four contributions

$$L_\mathrm{D} = L_\mathrm{time} + L_\mathrm{kin} + L_\mathrm{pot} + L_\mathrm{int}\,. \tag{2.96}$$

The kinetic energy part of the Lagrangian reads

$$L_\mathrm{kin} = -\frac{\hbar^2}{2m_\mathrm{B}}\int d^D\mathbf{r}\nabla\psi^\star(\mathbf{r},t)\nabla\psi(\mathbf{r},t) = -\sum_{i=1}^{D}\left\{\frac{\hbar^2}{4m_\mathrm{B}A_i(t)^2}+\frac{\hbar^2}{m_\mathrm{B}}A_i(t)^2 B_i^2(t)\right\}. \tag{2.97}$$

Accordingly, the interaction energy part of the Lagrangian yields

$$L_\mathrm{int} = -\frac{G_\mathrm{B}^\mathrm{D}}{2}\int d^D\mathbf{r}|\psi(\mathbf{r},t)|^4 = -\sum_{i=1}^{D}\frac{G_\mathrm{B}^D}{2(2\pi)^{D/2}\tilde{A}(t)^D}\,. \tag{2.98}$$

The Lagrangian function for potential energy can be calculated as

$$L_\mathrm{pot} = -\int d^D\mathbf{r}V(\mathbf{r})|\psi(\mathbf{r},t)|^2 = -\frac{m_\mathrm{B}}{4}\sum_{i=1}^{D}\omega_i^2 A_i(t)^2\,. \tag{2.99}$$

And finally, the time dependent part of the Lagrangian function is given by

$$L_\mathrm{time} = -\frac{i\hbar}{\pi^{D/2}\tilde{A}(t)^D}\sum_{i=1}^{D}\int d^D\mathbf{r}\left\{-\frac{\dot{A}_i(t)}{2A_i(t)}+\left[\frac{\dot{A}_i(t)}{A_i(t)^3}-\mathrm{i}\dot{B}_i(t)\right]x_i^2\right\}\exp\left\{-\sum_{i=1}^{D}\frac{x_i^2}{2A_i(t)^2}\right\}, \tag{2.100}$$

which can be simplified as

$$L_{\text{time}} = \frac{\hbar}{2}\sum_{i=1}^{D} A_i(t)^2 \dot{B}_i(t)\,. \tag{2.101}$$

With this, we get for the entire Lagrangian (2.96):

$$L_{\mathrm{D}} = \sum_{i=1}^{D}\left\{\frac{\hbar}{2}A_i(t)^2\dot{B}_i(t) - \frac{\hbar^2}{4m_{\mathrm{B}}A_i(t)^2} - \frac{\hbar^2}{m_{\mathrm{B}}}A_i(t)^2B_i^2(t) - \frac{m_{\mathrm{B}}}{4}\omega_i^2A_i(t)^2\right\} - \frac{G_{\mathrm{B}}^D}{2(2\pi)^{D/2}\tilde{A}(t)^D}\,. \tag{2.102}$$

We extermize the action for the variation functions $A_i(t)$ and $B_i(t)$, which leads to the Euler-Lagrange equations

$$\frac{\delta\mathscr{A}_{\mathrm{D}}}{\delta A_i(t)} = \frac{\partial L_{\mathrm{D}}}{\partial A_i(t)} - \frac{d}{dt}\frac{\partial L_{\mathrm{D}}}{\partial\dot{A}_i(t)} = 0, \tag{2.103}$$

$$\frac{\delta\mathscr{A}_{\mathrm{D}}}{\delta B_i(t)} = \frac{\partial L_{\mathrm{D}}}{\partial B_i(t)} - \frac{d}{dt}\frac{\partial L_{\mathrm{D}}}{\partial\dot{B}_i(t)} = 0\,.$$

By inserting the Lagrangian (2.102) we obtain

$$-\hbar A_i(t)\dot{B}_i(t) + \tfrac{2\hbar^2}{m_{\mathrm{B}}}A_i(t)B_i^2(t) + \tfrac{m_{\mathrm{B}}\omega_i^2}{2}A_i(t)^2 = \tfrac{\hbar^2}{2m_{\mathrm{B}}A_i(t)^3} + \tfrac{G_{\mathrm{B}}^D}{2(2\pi)^{D/2}\tilde{A}(t)^DA_i(t)}, \tag{2.104}$$

$$B_i(t) = -\tfrac{m_{\mathrm{B}}\dot{A}_i(t)}{2\hbar A_i(t)}\,. \tag{2.105}$$

By eliminating $B_i(t)$ from above equations, we obtain the dynamical equations of the variational parameters $A_i(t)$

$$\ddot{A}_i(t) + \omega_i^2A_i(t) = \frac{\hbar^2}{m_{\mathrm{B}}^2A_i(t)^3} + \frac{G_{\mathrm{B}}^D}{(2\pi)^{D/2}m_{\mathrm{B}}\tilde{A}(t)^DA_i(t)}\,. \tag{2.106}$$

These coupled equations correspond to the dynamics of the Bose-Einstein condensate in any dimension.

2.4.2 Thomas-Fermi approximation

In the last subsection, we noticed that the many-body system can be reduced to the question of finding a condensate wave function of the many-body system. The overall shape of this wave function can be determined by solving numerically the Gross-Pitaevskii equation (2.90). The Gross-Pitaevskii equation is a non-linear second order differential equation to which we do not have an exact solution. Therefore, it is worthwhile to discuss the simplest possible solution for the time-independent Gross-Pitaevskii equation in the presence of a harmonic trap. To this end, we use of the condensate wave function the ansatz $\psi(\mathbf{r},t) = \psi(\mathbf{r})e^{-i\mu t/\hbar}$, insert it into the time-dependent DDGPE (2.90), which yields the

D-dimensional time-independent Gross-Pitaevskii equation

$$\mu\,\psi(\mathbf{r}) = \left\{-\frac{\hbar^2}{2m_{\mathrm{B}}}\nabla^2 + V(\mathbf{r}) + G_{\mathrm{B}}^{D} \parallel \psi(\mathbf{r}) \parallel^2\right\}\psi(\mathbf{r})\,. \tag{2.107}$$

here, $V(\mathbf{r}) = m_{\mathrm{B}}\sum_{i=1}^{D}\omega_i^2 x_i^2/2$ is the anisotropic harmonic oscillator. If the effect of interactions is significantly large, the width of the BEC will become so large and the density profile so smooth that the kinetic energy term in the Gross-Pitaevskii equation can be ignored. This limit is called the Thomas-Fermi approximation and is well satisfied in most experiments [173]. In this limit the density profile is given by

$$n(\mathbf{r}) = \sqrt{\frac{1}{G_{\mathrm{B}}^{\mathrm{D}}}\left[\mu - V(\mathbf{r})\right]\Theta\left[\mu - V(\mathbf{r})\right]}\,, \tag{2.108}$$

where the Heaviside function Θ prevents the density becoming negative. Thus the density profile in the Thomas-Fermi approximation takes the form of an inverted parabola. The chemical potential can be fixed by the normalization condition $\int \parallel \psi(\mathbf{r}) \parallel^2 d\mathbf{r} = 1$. The characteristic radii (also called the Thomas-Fermi radii) R_i of the cloud are given by the relation

$$R_i^2 = \frac{2\mu}{m_{\mathrm{B}}\omega_i^2},\, i = 1, 2...., D, \tag{2.109}$$

and, thus, depend on the chemical potential.

2.5 A special case: one-dimensional regime

In this thesis, we focus on studying neutral atoms within a quasi one-dimensional trap geometry. A highly elongated quasi-1D regime can be reached by tightly confining the atoms in the radial direction, effectively freezing-out the transverse dynamics [6, 105–112]. In this section we calculate the quasi-1D Gross-Pitaevskii equation.

From the previous section, we know that the underlying Gross-Pitaevskii equation for a condensate wave function can be formulated as the Hamilton principle of least action with the action functional, where the Lagrangian density reads for three spatial dimensions

$$\begin{aligned}\mathscr{L}_{3\mathrm{D}} =& \frac{i\hbar}{2}\left[\psi^{\star}(\mathbf{r},t)\,\frac{\partial\psi(\mathbf{r},t)}{\partial t} - \psi(\mathbf{r},t)\,\frac{\partial\psi^{\star}(\mathbf{r},t)}{\partial t}\right] + \frac{\hbar^2}{2m_{\mathrm{B}}}\psi^{\star}(\mathbf{r},t)\triangle\psi(\mathbf{r},t)\\ &- V(\mathbf{r})\psi^{\star}(\mathbf{r},t)\,\psi(\mathbf{r},t) - \frac{G_{\mathrm{B}}^{3\mathrm{D}}}{2} \parallel \psi(\mathbf{r},t) \parallel^4\,.\end{aligned} \tag{2.110}$$

Here $\psi(\mathbf{r},t)$ describes the BEC wave function with the coordinates $\mathbf{r} = (x,\, y,\, z)$ and the two-particle interaction strength reads $G_{\mathrm{B}}^{3\mathrm{D}} = N_{\mathrm{B}}4\pi\hbar^2 a_{\mathrm{B}}^{3\mathrm{D}}/m_{\mathrm{B}}$, where N_{B} denotes the number of bosonic atoms, and $a_{\mathrm{B}}^{3\mathrm{D}}$ is the three-dimensional s-wave scattering length of bosons. For instance, a MOT yields a harmonic confinement $V(\mathbf{r}) = m_{\rm B}\omega_z^2 z^2/2 + m_{\rm B}\omega_{\rm r}^2\left(x^2+y^2\right)/2$, which has rotational symmetry with respect to the z-axis.

In the following we assume that the MOT provides a quasi one-dimensional setting due to $a_{\rm B}^{\rm 3D} \ll l_{\rm r} \ll l_{\rm z}$, here $l_{\rm r} = \sqrt{\hbar/m_{\rm B}\omega_{\rm r}}$ is the radial oscillator length and $l_{\rm z} = \sqrt{\hbar/m_{\rm B}\omega_{\rm z}}$ the oscillator length along the z-axis. Then we follow Ref. [119] and decompose the BEC wave-function $\psi(\mathbf{r},t) = \psi(z,t)\phi(\mathbf{r}_\perp,t)$ with $\mathbf{r}_\perp = (x,\, y)$ and

$$\phi(\mathbf{r}_\perp,t) = \frac{1}{\sqrt{\pi} l_{\rm r}} e^{-\frac{x^2+y^2}{2l_{\rm r}^2}} e^{-i\omega_{\rm r} t}\,. \tag{2.111}$$

Subsequently, we integrate out the two transversal dimensions of the three-dimensional Lagrangian according to

$$\mathscr{L}_{\rm 1D} = \int_{-\infty}^{\infty}\int_{-\infty}^{\infty} \mathscr{L}_{\rm 3D}\, dxdy\,. \tag{2.112}$$

After a straight-forward calculation the resulting quasi one-dimensional Lagrangian reads

$$\begin{aligned}\mathscr{L}_{\rm 1D} = &\frac{i\hbar}{2}\left[\psi^\star(z,t)\frac{\partial\psi(z,t)}{\partial t} - \psi(z,t)\frac{\partial\psi^\star(z,t)}{\partial t}\right] + \frac{\hbar^2}{2m_{\rm B}}\psi^\star(z,t)\frac{\partial^2\psi(z,t)}{\partial z^2}\\ &-V(z)\psi^\star(z,t)\,\psi(z,t) - \frac{G_{\rm B}^{\rm 1D}}{2}\parallel\psi(z,t)\parallel^4,\end{aligned} \tag{2.113}$$

where $V(z) = m_{\rm B}\omega_z^2 z^2/2$ represents the effective one-dimensional harmonic potential from the MOT, and the one-dimensional two-particle interaction strength is

$$G_{\rm B}^{\rm 1D} = 2N_{\rm B} a_{\rm B}^{\rm 3D}\hbar\omega_{\rm r}\,. \tag{2.114}$$

By using the one-dimensional Lagrangian density (2.113) and the Euler-Lagrangian equation (2.94), we write the 1DGPE

$$i\hbar\frac{\partial}{\partial t}\psi(z,t) = \left\{-\frac{\hbar^2}{2m_B}\frac{\partial^2}{\partial z^2} + \frac{m_{\rm B}\omega_z^2}{2}z^2 + G_{\rm B}^{\rm 1D}\parallel\psi(z,t)\parallel^2\right\}\psi(z,t)\,. \tag{2.115}$$

Depending on the value of $G_{\rm B}^{\rm 1D}$ and the transversal harmonic trap such a system can be divided into two regimes, one is called of the Tonks-Girardeau regime and the quasi one-dimensional regime.

2.5.1 Tonks-Girardeau regime

Normally, one-dimensional (1D) systems are obtained in cylindrically symmetric traps by considering strong confinement in the transverse direction and weak confinement along the longitudinal direction. The inter-particle scattering length from Eq. (2.114) can be expressed

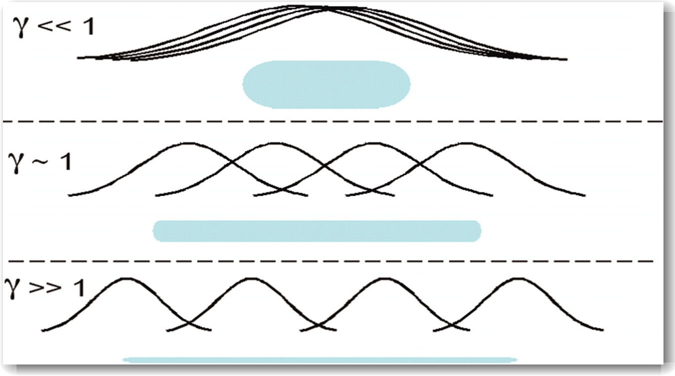

Figure 2.6: A cartoon figure of 1D atom distributions [117].

as

$$G_{\mathrm{B}}^{1\mathrm{D}} = \frac{2Na_{\mathrm{B}}^{3\mathrm{D}}\hbar^2}{m_{\mathrm{B}}l_{\mathrm{r}}^2}. \tag{2.116}$$

By using this relation, we define the so-called one-dimensional scattering length $a_{\mathrm{B}}^{1\mathrm{D}} = l_{\mathrm{r}}^2/a_{\mathrm{B}}^{3\mathrm{D}}$ [114], which is inversely proportional to the three-dimensional scattering length. The kinetic energy of the 1D-system reads $E_{\mathrm{kin}} = \hbar^2/2m_{\mathrm{B}}\xi^2 = \hbar^2 n_{1\mathrm{D}}^2/2m_{\mathrm{B}}$, where we used the relation $n_{1\mathrm{D}}(z) = \parallel \psi(z) \parallel^2$ and write the inverse coherence length as $n_{1\mathrm{D}}(0) = 1/\xi$. The kinetic energy can be compared to the interaction energy $E_{\mathrm{int}} = G_{\mathrm{B}}^{1\mathrm{D}}n_{1\mathrm{D}}$ of the ground state [114–117] as

$$\gamma = \frac{E_{\mathrm{int}}}{E_{\mathrm{kin}}} = 2\frac{m_{\mathrm{B}}G_{\mathrm{B}}^{1\mathrm{D}}}{\hbar^2 n_{1\mathrm{D}}}. \tag{2.117}$$

The behavior of the one-dimensional Bose gas can be described by using the γ parameter. For example, in the case of high densities the system is weakly interacting $\gamma \ll 1$, therefore the mean-field regime is well described by the GPE and Bose-Einstein condensation is possible [114–117]. On the other hand, when the longitudinal density is decreased $\gamma \gg 1$ the one-dimensional system enters the Tonks-Girardeau regime where the bosons exhibit fermionic properties as illustrated in Fig. 2.6 [117]. In the figure, three shaded drawings represent the atomic density in a one-dimensional tube. In the experiment, γ can be changed by transversely squeezing the tube. To describe the difference between the quasi and Tonks-Girardeau regimes, Petrov et al. introduced a complementary dimensionless quantity by comparing the longitudinal size of the trap to the one-dimensional scattering length $a_{\mathrm{B}}^{1\mathrm{D}}$ [179]:

$$\alpha = 2\frac{l_{\mathrm{z}}}{a_{\mathrm{B}}^{1\mathrm{D}}} = 2a_{\mathrm{B}}^{3\mathrm{D}}\frac{l_{\mathrm{z}}}{l_{\mathrm{r}}^2}. \tag{2.118}$$

The different possible regimes for a one-dimensional system at zero temperature are sketched in Fig. 2.7 [180]. Petrov et al. investigated at first the boundary between the Gaussian and the Thomas-Fermi BEC regime. From the condition that the chemical potential μ is much larger than the level spacing $\hbar\omega_{\mathrm{z}}$, i.e $\mu \gg \hbar\omega_{\mathrm{z}}$, in the trap they obtained the defining relation

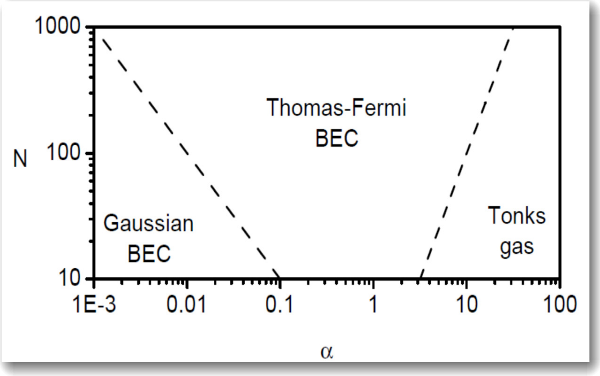

Figure 2.7: Depending on the parameter α and the atom number N for trapped one-dimensional gases three regions are possible [180]. The dashed lines indicate the cross-over regions between Gaussian BEC, Thomas-Fermi BEC, and Tonks-Girardeau gas.

$N\alpha \gg 1$ for the Thomas-Fermi regime as depicted in Fig. 2.7 [180]. If we let $\alpha \gg 1$ and the number of particles are small, then the trapped 1D gas is in the strongly interacting Tonks-Girardeau regime. In this regime bosons act as hard-core bosons, which have the properties of free fermions, therefore these bosons are described by a Fermi-Dirac distribution. Thus, for this scenario the chemical potential is equal to $\mu = N\hbar\omega_{\mathrm{z}}$, so by using the condition $\gamma = 1$, Petrov et al. specified between the Thomas-Fermi and the Tonks-Girardeau regime, which yields $N = \alpha^2$ as illustrated in Fig. 2.7 [180].

2.5.2 Quasi one-dimensional regime

In the previous subsection we discussed in detail the difference between the Tonks-Girardeau and the quasi one-dimensional regime. As we noticed the quasi one-dimensional regime can be divided further into two regimes namely: the Gaussian and the Thomas-Fermi regimes. In this subsection we argue that the difference between the Gaussian and the Thomas-Fermi regimes can be determined by calculating the equilibrium energy of the system by using the numerical simulation of the quasi-1D GPE (2.115). In order to make Eq. (2.115) dimensionless, we introduce the dimensionless time as $\tilde{t} = \omega_z t$, the dimensionless coordinate $\tilde{z} = z/l_{\mathrm{z}}$, and the dimensionless wave function $\tilde{\psi} = \psi\sqrt{l_{\mathrm{z}}}$. With this Eq. (2.115) can be written in the form

$$i\frac{\partial}{\partial \tilde{t}}\tilde{\psi}(\tilde{z},\tilde{t}) = \left\{-\frac{1}{2}\frac{\partial^2}{\partial \tilde{z}^2} + \frac{1}{2}\tilde{z}^2 + \tilde{G}_{\mathrm{B}}^{\mathrm{1D}} \parallel \tilde{\psi}(\tilde{z},\tilde{t}) \parallel^2\right\}\tilde{\psi}(\tilde{z},\tilde{t}), \tag{2.119}$$

where we have $\tilde{G}_{\mathrm{B}}^{\mathrm{1D}} = 2N_{\mathrm{B}}\omega_{\mathrm{r}}a_{\mathrm{B}}^{\mathrm{3D}}/(\omega_{\mathrm{z}}l_{\mathrm{z}})$. From here on, for this section, we will drop all tildes for simplicity. For the equilibrium case, by following the Gaussian ansatz (2.95), we

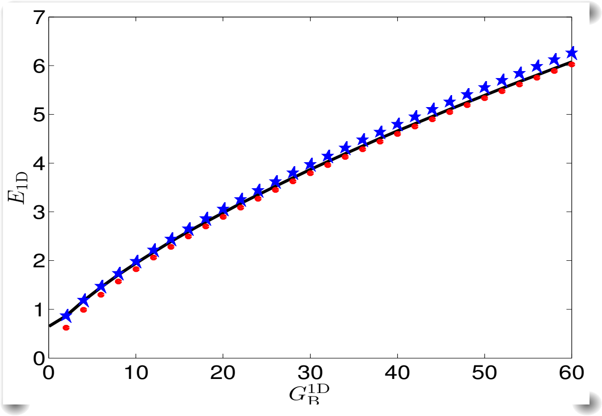

Figure 2.8: Quasi one-dimensional energy E_{1D} vs G_B^{1D}, solid black-line represents the numerical 1DGPE, blue stars represents the Gaussian variational solution (2.120) and the red circles correspond to the Thomas-Fermi approximation equilibrium energy (2.122).

write the dimensionless energy of the system

$$E_{1D} = \frac{1}{4A_1^2} + \frac{A_1^2}{4} + \frac{G_B^{1D}}{2\sqrt{2\pi}A_1}. \tag{2.120}$$

Here, A_1 is the width of the Bose-Einstein condensate, which can be determined by minimizing the energy function

$$\frac{A_1}{2} = \frac{1}{2A_1^3} + \frac{G_B^{1D}}{2\sqrt{2\pi}A_1^2}. \tag{2.121}$$

To investigate the Thomas-Fermi approximation for quasi one-dimensional case, we argue that, due to $G_B^{1D} \gg 1$, the TF approximation is valid qualitatively. Therefore we write the energy of the system by using the equation (2.108)

$$E_{1D} = \frac{A_1^2}{5} + \frac{3G_B^{1D}}{10\sqrt{2}A_1}. \tag{2.122}$$

Here, the width of the condensate turns out to be $A_1 = \left(3G_B^{1D}\right)^{1/3}/2^{5/6}$. In this thesis, we will focus our attention on the quasi one-dimensional Bose-Einstein condensate, therefore we provide now a comparison between previously described variational, Thomas-Fermi and numerical solution of the 1DGPE, where for the latter we used the split operator technique as described in Appendix A. To this end, we plot the energy of the system versus the two-particle interaction strength G_B^{1D}, as shown in Fig. 2.8. As we read off from Fig. 2.8, for small values of G_B^{1D}, the numerical solution of 1DGPE (2.119) agrees quite well with the Gaussian variational solution and for larger values of G_B^{1D} it agrees with the Thomas-Fermi approximated solution.

2.5.3 Nonlinear waves: solitons

The dynamics of nonlinear systems displays many distinctive features from solitons to shock-waves. Solitons were first observed in the year 1834 by John Scott Russel at the Union canal in Scotland as traveling water waves. Gray/dark solitons have a characteristic property that they can pass through one another without any change of shape, amplitude, or speed. There are various types of nonlinear partial differential equations that support soliton solutions. Solitons were discovered as solutions to the Korteweg-de Vries equation [181], the Sine-Gordon equation [182], and including the Gross-Piteavskii equation [183, 184] which will be investigated within this thesis. To review the study of the solitons, we rewrite the dimensionless quasi one-dimensional Gross-Piteavskii equation in the homogeneous case for the one soliton case:

$$i\frac{\partial}{\partial t}\psi_{1\mathrm{Sol}}\left(z,t\right)=\left\{-\frac{1}{2}\frac{\partial^2}{\partial z^2}+G_{\mathrm{B}}^{1\mathrm{D}}\parallel\psi_{1\mathrm{Sol}}\left(z,t\right)\parallel^2\right\}\psi_{1\mathrm{Sol}}\left(z,t\right), \tag{2.123}$$

where, $\psi_{1\mathrm{Sol}}$ is the one-soliton wave function. On the RHS the first term corresponds to the dispersion of the system for the massive particles, and the second term on the RHS is a nonlinear interaction term. In the case of nonlinear matter waves, bright solitons are expected only for an attractive inter-particle interaction $G_{\mathrm{B}}^{1\mathrm{D}}<0$ [185, 186], whereas gray/dark solitons are predicted for repulsive interactions $G_{\mathrm{B}}^{1\mathrm{D}}>0$ [66, 125–129, 187]. The shape of the soliton does not change due to the balance between the inter-particle interaction and the dispersion. In the repulsive case $G_{\mathrm{B}}^{1\mathrm{D}}>0$, solution of the homogeneous quasi 1DGPE leads to gray/dark solitons [121],

$$\psi_{1\mathrm{Sol}}\left(z,t\right)=\sqrt{n}\left(i\frac{v}{c}+\sqrt{1-\frac{v^2}{c^2}}\tanh\left\{\sqrt{n}\sqrt{1-\frac{v^2}{c^2}}\left[z-z_0\left(t\right)\right]\right\}\right)e^{-i\mu t}. \tag{2.124}$$

Here $z_0\left(t\right)=z_0-vt$ is the dimensionless time dependent soliton center, z_0 is an arbitrary dimensionless real constant describing the initial location of the gray/dark soliton, v is the velocity of the soliton, and n is the dimensionless background density of the BEC, $\mu=G_{\mathrm{B}}^{1\mathrm{D}}n$ defines the dimensionless chemical potential, and c represents the dimensionless speed of sound $c=\sqrt{G_{\mathrm{B}}^{1\mathrm{D}}n}=\sqrt{\mu}$. The corresponding one-soliton time independent density is

$$n_{1\mathrm{Sol}}\left(z\right)=n\left\{\frac{v^2}{c^2}+\left(1-\frac{v^2}{c^2}\right)\tanh^2\left(\sqrt{n}\sqrt{1-\frac{v^2}{c^2}}z\right)\right\}. \tag{2.125}$$

The minimum of the density depends on the speed of the soliton

$$n_{\mathrm{min}}=n\frac{v^2}{c^2}. \tag{2.126}$$

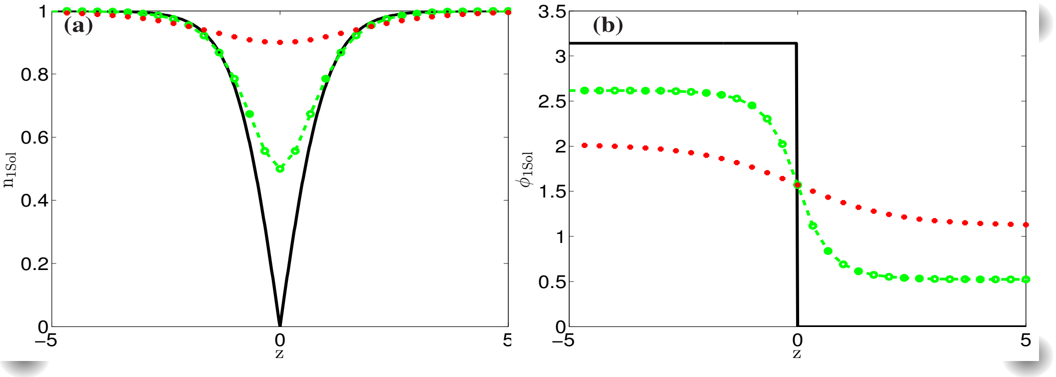

Figure 2.9: a) Density and b) phase profile of a gray/dark soliton for various speeds. Here black-solid line represents $v/c = 0$, green-dashed-circles describes $v/c = 0.5$ and the red-circles depicts $v/c = 0.9$.

Here, we emphasize two limiting cases, a complete black soliton is called a dark soliton with $v/c = 0$, i.e. it has always a node of zero density with phase slip of π, on the other hand the gray soliton $0 < v/c < 1$ has a smaller node as compared to the dark solitons, with a phase slip less than π and it moves faster than the dark soliton as shown in Fig. 2.9. The number of particles in one soliton is

$$N_{1\mathrm{Sol}} = \int_{-\infty}^{\infty} dz \left[n - n_{1\mathrm{Sol}}(z)\right] = 2\sqrt{n}\sqrt{1 - \frac{v^2}{c^2}}\,. \tag{2.127}$$

And the total energy of one soliton can be calculated as

$$\begin{aligned} E_{1\mathrm{Sol}} &= \int_{-\infty}^{\infty} dz \left\{ \frac{1}{2}\left|\frac{\partial \psi_{1\mathrm{Sol}}(z)}{\partial z}\right|^2 + \frac{G_{\mathrm{B}}^{1\mathrm{D}}}{2}\left[n - n_{1\mathrm{Sol}}(z)\right]^2 \right\}, \\ &= \frac{4}{3} n^{3/2} \left(1 - \frac{v^2}{c^2}\right)^{3/2} . \end{aligned} \tag{2.128}$$

From the energy of the one soliton, we conclude the important feature, that a stationary soliton has a maximum soliton energy, while at the velocity $v = c$ the soliton has a vanishing energy. This observation leads to the idea that the soliton has a negative effective mass. Indeed, for small velocities we write the energy (2.128) of a gray solitons as

$$E_{1\mathrm{Sol}} \approx \frac{4}{3} n^{3/2} \left(1 - \frac{3}{2}\frac{v^2}{c^2}\right) . \tag{2.129}$$

From the above equation follows that the dimensionless negative mass of one gray soliton is $m_{1\mathrm{Sol}} = -2n^{3/2}$ [188].

Chapter 3

Bose-Einstein condensate in harmonic and dimple trap

In this chapter, we investigate a quasi one-dimensional Bose-Einstein condensate in a harmonic trap with an additional dimple trap (dT) in the center. Within a zero-temperature Gross-Pitaevskii mean-field description we provide a one-dimensional physical intuitive model, which we solve by both a time-independent variational approach and numerical calculations. This chapter is organized as follows: in Sec. 3.1, we start with a model which describes the dynamical evolution of a quasi-1D Bose-Einstein condensate (BEC) in a magneto-optical trap with an additional red/blue-detuned dimple trap in the center. Afterwards in Sec. 3.2, we justify a Thomas-Fermi approximation for the condensate wave function and compare it with numerical results. With this we show that the dT induces a bump or a dip upon the condensate wave function depending on whether dT laser beam is red- or blue-detuned. Subsequently, in Sec. 3.3, we discuss the dynamics of the dT induced bump/dip-imprint upon the condensate wave function for two quench scenarios. After having released the trap, the resulting time-of-flight expansion shows that the dT induced imprint remains conserved for a red-detuned dT but decreases for a blue-detuned dT. Furthermore, when the initial red/blue-detuned dT is switched off, we observe the emergence of white shock-waves or gray/dark bi-soliton trains. Finally, Sec. 3.4 summarizes our findings for the proposed quasi-1D harmonically confined BEC with an additional dimple trap in the center in view of a possible experimental realization.

3.1 Quasi 1D model

We start with the fact that the underlying Gross-Pitaevskii equation for a condensate wave function can be formulated as the Hamilton principle of least action with the action functional

$$\mathscr{A}_{\mathrm{3D}} = \int dt \int \mathscr{L}_{\mathrm{3D}}\, d^3 r,$$

where the three spatial dimensions Lagrangian density reads from (2.110)

$$\begin{aligned}\mathscr{L}_{\mathrm{3D}} = & \frac{i\hbar}{2}\left[\psi^{\star}(\mathbf{r},t)\frac{\partial\psi(\mathbf{r},t)}{\partial t} - \psi(\mathbf{r},t)\frac{\partial\psi^{\star}(\mathbf{r},t)}{\partial t}\right] + \frac{\hbar^2}{2m_{\mathrm{B}}}\psi^{\star}(\mathbf{r},t)\triangle\psi(\mathbf{r},t) \\ & - V(\mathbf{r})\psi^{\star}(\mathbf{r},t)\,\psi(\mathbf{r},t) - \mathrm{U}_{\mathrm{dT}}^{\mathrm{3D}}(\mathbf{r})\,\psi^{\star}(\mathbf{r},t)\,\psi(\mathbf{r},t) - \frac{G_{\mathrm{B}}^{\mathrm{3D}}}{2}\parallel\psi(\mathbf{r},t)\parallel^4 .\end{aligned} \tag{3.1}$$

Here $\psi(\mathbf{r},t)$ describes the BEC wave function with the coordinates $\mathbf{r} = (x,\, y,\, z)$ and the two-particle interaction strength reads $G_{\mathrm{B}}^{\mathrm{3D}} = N_{\mathrm{B}}4\pi\hbar^2 a_{\mathrm{B}}/m_{\mathrm{B}}$, where N_{B} denotes the number of bosonic atoms. In case of ^{87}Rb atoms, the s-wave scattering length is $a_{\mathrm{B}} = 94.7\ \mathrm{a}_0$ with the Bohr radius a_0. We assume that the bosons are confined by a harmonic potential with an additional dT potential in the center. For instance, a MOT yields a harmonic confinement $V(\mathbf{r}) = m_{\mathrm{B}}\omega_{\mathrm{z}}^2 z^2/2 + m_{\mathrm{B}}\omega_{\mathrm{r}}^2\left(x^2+y^2\right)/2$, which has rotational symmetry with respect to the z-axis. In the following, we consider the experimentally realistic trap frequencies $\omega_{\mathrm{r}} = 2\pi\times 160\,\mathrm{Hz} \gg \omega_{\mathrm{z}} = 2\pi\times 6.8\,\mathrm{Hz}$ [30], so we have a cigar-shaped condensate, where the oscillator lengths amount to the values $l_{\mathrm{r}} = 0.84\,\mu\mathrm{m} \ll l_{\mathrm{z}} = 4.12\,\mu\mathrm{m}$.

An additional three-dimensional narrow Gaussian laser beam polarizes the neutral atoms and, thus, yields according to (2.18) the dT potential $\mathrm{U}_{\mathrm{dT}}^{\mathrm{3D}} = \mathrm{U}_0 I(\mathbf{r})$, where within the rotating-wave approximation the amplitude U_0 is given by [163, 164, 189, 190]

$$\mathrm{U}_0 = \frac{3\pi c^2\Gamma}{2\omega_{\mathrm{A}}^3\Delta} . \tag{3.2}$$

Here the damping rate Γ is defined by from (2.22), $\Delta = \omega - \omega_{\mathrm{A}}$ represents the detuning of the laser, where ω is the laser frequency and ω_{A} stands for the frequency of the D_1- or D_2-line of ^{87}Rb atoms, which are the transitions $5^2S_{1/2} \to 5^2P_{1/2}$ or $5^2S_{1/2} \to 5^2P_{3/2}$ with the wave lengths $\lambda_{\mathrm{D1}} = 794.76\,\mathrm{nm}$ and $\lambda_{\mathrm{D2}} = 780.03\,\mathrm{nm}$, respectively. The intensity profile of the Gaussian laser beam, which is assumed to move in y-direction, is determined via

$$I(\mathbf{r}) = \frac{2P}{\pi W_{\mathrm{x}}(y)\,W_{\mathrm{z}}(y)}e^{-\left[\frac{2x^2}{W_{\mathrm{x}}^2(y)}+\frac{2z^2}{W_{\mathrm{z}}^2(y)}\right]} , \tag{3.3}$$

where P denotes its power. Furthermore, $W_{\mathrm{x/z}}(y) = W_{0\mathrm{x/z}}\sqrt{1+y^2/y_{\mathrm{Rx/z}}^2}$ defines the beam radius in x- and z-direction, where the intensity decreases to $1/e^2$ of its peak value, and the Rayleigh lengths $y_{\mathrm{Rx/z}} = \pi W_{0\mathrm{x/z}}^2/\lambda$ with wave length $\lambda = 2\pi c/\omega$ define the distances where the beam radius increases by a factor of $\sqrt{2}$ [189]. We use for the Gaussian laser beam width along the x-axis $W_{0\mathrm{x}} = 1.1\,\mu\mathrm{m}$ and along the z-axis $W_{0\mathrm{z}} = 3.2\,\mu\mathrm{m}$, which are about ten times smaller than the corresponding ones used in Ref. [30]. The corresponding Rayleigh lengths for the red-detuned laser light with $\lambda = 840\,\mathrm{nm}$ [30] yield $y_{\mathrm{Rx}} = 4.526\,\mu\mathrm{m}$ and $y_{\mathrm{Rz}} = 38.29\,\mu\mathrm{m}$ and for the blue-detuned laser light with $\lambda = 772\,\mathrm{nm}$ [191] we get $y_{\mathrm{Rx}} = 4.92\,\mu\mathrm{m}$ and $y_{\mathrm{Rz}} = 41.6\,\mu\mathrm{m}$. Note that near the origin the dT potential $\mathrm{U}_{\mathrm{dT}}^{\mathrm{3D}} = \mathrm{U}_0 I(\mathbf{r})$

turns out to be approximately harmonic

$$\mathrm{U_{dip}}\left(x,y,z\right) = -\mathrm{U_1} + \frac{1}{2}m_\mathrm{B}\Omega_\mathrm{x}^2 x^2 + \frac{1}{2}m_\mathrm{B}\Omega_\mathrm{z}^2 z^2 + \frac{1}{2}m_\mathrm{B}\Omega_\mathrm{y}^2 y^2 \tag{3.4}$$

with the depth $\mathrm{U_1} = 2P\mathrm{U_0}/\pi\sqrt{W_\mathrm{0x}W_\mathrm{0z}}$ and the dipole trap frequencies

$$\frac{\Omega_\mathrm{x}}{2\pi} = \sqrt{\frac{4\mathrm{U_0}}{m_\mathrm{B}W_\mathrm{0x}^2}}\;, \frac{\Omega_\mathrm{y}}{2\pi} = \sqrt{\frac{2\mathrm{U_0}}{m_\mathrm{B}y_\mathrm{R}^2}}\;, \frac{\Omega_\mathrm{z}}{2\pi} = \sqrt{\frac{4\mathrm{U_0}}{m_\mathrm{B}W_\mathrm{0z}^2}}, \tag{3.5}$$

where the Rayleigh range for this elliptical Gaussian beam is given by $y_R = y_{Rx}y_{Rz}/\sqrt{\left(y_{Rx}^2+y_{Rz}^2\right)/2}$. Due to the fact $y_\mathrm{Rx/z} \gg l_\mathrm{r}$, we can approximate the widths of the beam in x- and z-direction according to $W_\mathrm{x/z}(y) \approx W_\mathrm{0x/z}$. This simplifies the dimple trap potential to

$$\mathrm{U_{dT}^{3D}}\left(\mathbf{r}\right) = \frac{2\mathrm{U_0}P}{\pi W_\mathrm{0x}W_\mathrm{0z}}e^{-\left(\frac{2x^2}{W_\mathrm{0x}^2}+\frac{2z^2}{W_\mathrm{0z}^2}\right)}. \tag{3.6}$$

As the MOT provides a quasi one-dimensional setting due to $a_\mathrm{B} \ll l_\mathrm{r} \ll l_\mathrm{z}$, we can follow Ref. [119], and decompose the BEC wave-function $\psi(\mathbf{r},t) = \psi(z,t)\phi(\mathbf{r}_\perp,t)$ with $\mathbf{r}_\perp = (x,\, y)$ and

$$\phi\left(\mathbf{r}_\perp,t\right) = \frac{e^{-\frac{x^2+y^2}{2l_\mathrm{r}^2}}}{\sqrt{\pi}l_\mathrm{r}}e^{-i\omega_\mathrm{r}t}. \tag{3.7}$$

Subsequently, we integrate out the two transversal dimensions of the three-dimensional Lagrangian (3.1) according to

$$\mathscr{L}_\mathrm{1D} = \int_{-\infty}^{\infty}\int_{-\infty}^{\infty}\mathscr{L}_\mathrm{3D}\,dxdy. \tag{3.8}$$

After a straight-forward calculation the resulting quasi one-dimensional Lagrangian reads

$$\begin{aligned}\mathscr{L}_\mathrm{1D} =& \frac{i\hbar}{2}\left[\psi^\star\left(z,t\right)\frac{\partial\psi\left(z,t\right)}{\partial t} - \psi\left(z,t\right)\frac{\partial\psi^\star\left(z,t\right)}{\partial t}\right] + \frac{\hbar^2}{2m_\mathrm{B}}\psi^\star\left(z,t\right)\frac{\partial^2\psi\left(z,t\right)}{\partial z^2}\\ &-V(z)\psi^\star\left(z,t\right)\psi\left(z,t\right) - \mathrm{U}e^{-\frac{2z^2}{W_\mathrm{0z}^2}}\psi^\star\left(z,t\right)\psi\left(z,t\right) - \frac{G_\mathrm{B}}{2}\parallel\psi\left(z,t\right)\parallel^4,\end{aligned} \tag{3.9}$$

where $V\left(z\right) = m_\mathrm{B}\omega_z^2 z^2/2$ represents an effective one-dimensional harmonic potential from the MOT, and the one-dimensional two-particle interaction strength is

$$G_\mathrm{B} = 2N_\mathrm{B}a_\mathrm{B}\hbar\omega_\mathrm{r}. \tag{3.10}$$

Furthermore, the one-dimensional dT depth turns out to be

$$\mathrm{U} = \frac{2\mathrm{U}_0 P}{\pi W_{0\mathrm{z}} \sqrt{W_{0\mathrm{x}}^2 + 2l_\mathrm{r}^2}}, \tag{3.11}$$

which depends on the power of the laser beam P as well as via (3.2) on the detuning $\Delta = \omega - \omega_\mathrm{A}$ of the laser wave length λ. Note that the latter not only changes the absolute value of the dT depth but also its sign. For red detuning, i.e. when the laser frequency is smaller than the atomic frequency, the dT is negative and atoms are sucked into the dT potential. In the opposite case of blue detuning the atoms are repelled from the dT potential. Thus, the dT induces an imprint on the BEC wave function, which can be either a bump for red detuning or a dip for blue detuning. In the following we will analyze this interesting effect in more detail. To this end we consider the 1D action

$$\mathscr{A}_{1\mathrm{D}} = \int_{-\infty}^{\infty} \int_{-\infty}^{\infty} \mathscr{L}_{1\mathrm{D}} \left(\psi^\star(z,t), \frac{\partial \psi^\star(z,t)}{\partial t}, \frac{\partial \psi^\star(z,t)}{\partial z}; \psi(z,t), \frac{\partial \psi(z,t)}{\partial t}, \frac{\partial \psi(z,t)}{\partial z} \right) dz dt \tag{3.12}$$

and determine the time dependent one-dimensional Gross-Pitaevskii equation (1DGPE) according to the Euler-Lagrangian equation

$$\frac{\delta \mathscr{A}_{1\mathrm{D}}[\psi^\star, \psi]}{\delta \psi^\star(z,t)} = \frac{\partial \mathscr{L}_{1\mathrm{D}}}{\partial \psi^\star(z,t)} - \frac{\partial}{\partial z} \frac{\partial \mathscr{L}_{1\mathrm{D}}}{\partial \frac{\partial \psi^\star(z,t)}{\partial z}} - \frac{\partial}{\partial t} \frac{\partial \mathscr{L}_{1\mathrm{D}}}{\partial \frac{\partial \psi^\star(z,t)}{\partial t}} = 0. \tag{3.13}$$

By using the one-dimensional Lagrangian density (3.9) the 1DGPE reads

$$i\hbar \frac{\partial}{\partial t} \psi(z,t) = \left\{ -\frac{\hbar^2}{2m_B} \frac{\partial^2}{\partial z^2} + \frac{m_\mathrm{B} \omega_z^2}{2} z^2 + \mathrm{U} e^{-\frac{2z^2}{W_{0\mathrm{z}}^2}} + G_\mathrm{B} \parallel \psi(z,t) \parallel^2 \right\} \psi(z,t). \tag{3.14}$$

On the right-hand side the first term represents the kinetic energy of the atoms with mass m_B, the second term describes the harmonic MOT potential, the third term stands for the dT potential, and the last term represents the two-particle interaction. In order to make Eq. (3.14) dimensionless, we introduce the dimensionless time as $\tilde{t} = \omega_z t$, the dimensionless coordinate $\tilde{z} = z/l_\mathrm{z}$, and the dimensionless wave function $\tilde{\psi} = \psi \sqrt{l_\mathrm{z}}$. With this Eq. (3.14) can be written in the form

$$i \frac{\partial}{\partial \tilde{t}} \tilde{\psi}(\tilde{z},\tilde{t}) = \left\{ -\frac{1}{2} \frac{\partial^2}{\partial \tilde{z}^2} + \frac{1}{2} \tilde{z}^2 + \tilde{\mathrm{U}} e^{-\frac{\tilde{z}^2}{\tilde{w}^2}} + \tilde{G}_\mathrm{B} \parallel \tilde{\psi}(\tilde{z},\tilde{t}) \parallel^2 \right\} \tilde{\psi}(\tilde{z},\tilde{t}), \tag{3.15}$$

where we have $\tilde{G}_\mathrm{B} = 2N_\mathrm{B} \omega_\mathrm{r} a_\mathrm{B} / (\omega_\mathrm{z} l_\mathrm{z})$ and $\tilde{\mathrm{U}} = \mathrm{U}/(\hbar \omega_\mathrm{z})$. For the above mentioned experimental parameters and $N_\mathrm{B} = 20 \times 10^4$ atoms of ^{87}Rb, we obtain the dimensionless coupling strength $\tilde{G}_\mathrm{B} = 11435.9$. Furthermore, the typical dT depth $|\mathrm{U}|/k_\mathrm{B} = 210\,\mathrm{nK}$ yields the di-

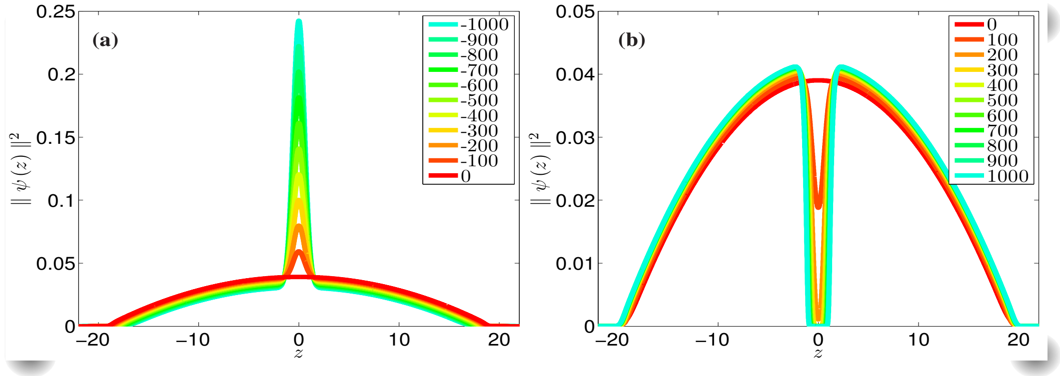

Figure 3.1: Numerical density profile of BEC for the experimental coupling constant value $G_{\mathrm{B}} = 11435.9$ and for the dT depth U which increases from top to bottom according to the inlets. For (a) negative values of U, the bump in the condensate wave function decreases, whereas for (b) positive values the corresponding dip increases.

mensionless value $\left|\tilde{\mathrm{U}}\right| = 643.83$, and $\tilde{w} = W_{0\mathrm{z}}/\left(\sqrt{2}l_{\mathrm{z}}\right) = 0.548$ represents the ratio of the width of the dT potential along the z-axis and the longitudinal harmonic oscillator length. From here on, we will drop all tildes for simplicity.

In order to clarify that we are in the regime where the mean-field theory is valid, we divide our argument into two parts. Firstly, in order to distinguish between the weakly interacting quasi-1D and the strongly interacting Tonks-Girardeau regime, Petrov et al. [114] introduced a dimensionless quantity $\alpha = \left(2a_{\mathrm{B}}l_{\mathrm{z}}\right)/l_{\mathrm{r}}^2$ as mentioned in Eq. (2.118). By using the above mentioned experimental parameters, we get the dimensionless quantity $\alpha = 0.057$, so according to Fig. 2.7 we are far in the weakly interacting regime, where the Gross-Pitaevskii mean-field theory is applicable. Secondly, the ratio of atoms $N_{\mathrm{QF}}^{\mathrm{1D}}$, which are depleted due to quantum fluctuations, with respect to the number of particles $N_{\mathrm{B}} = 20 \times 10^4$ can be calculated according to Eq. (B.10) of Appendix B

$$\frac{N_{\mathrm{QF}}^{\mathrm{1D}}}{N_{\mathrm{B}}} = \frac{3^{1/3}}{4}\left(a_{\mathrm{B}}^4 N_{\mathrm{B}} \Xi^2\right)^{1/3} = 0.022, \tag{3.16}$$

where $\Xi = l_{\mathrm{z}}/l_{\mathrm{r}}$ is the ratio of the axial and the longitudinal harmonic oscillator lengths. Thus the quantum fluctuations are, indeed, negligible.

3.2 Dimple trap induced bump/dip-imprint upon stationary condensate wave function

In order to determine the dT induced imprint on the condensate wave function in equilibrium, we solve the 1DGPE (3.15) in imaginary time numerically by using the split-operator method [192, 193]. In this way we find that the dT-imprint leads to a bump/hole in the BEC density

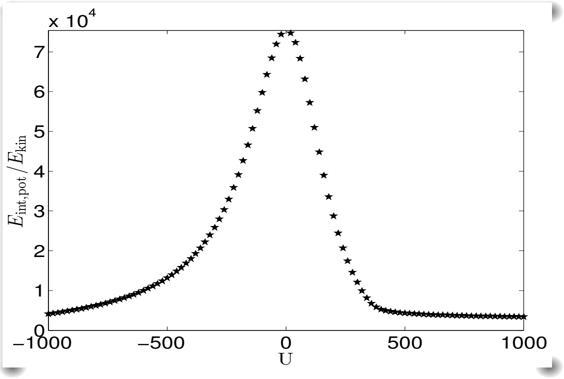

Figure 3.2: Ratio $E_{\mathrm{int,pot}}/E_{\mathrm{kin}}$ versus U from solving 1DGPE (3.15).

at the trap center for negative/positive values of U as shown in Fig. 3.1. For stronger red-detuned dT depth values the bump increases further, but for stronger blue-detuned dT the dip in the BEC density gets deeper and deeper until no more BEC atoms remain in the trap center. After this qualitative overview on the numerical results, we now work out an analytic approach for describing this red/blue-detuned dT induced bump/dip on the BEC density in a more quantitative way. To this end we present two arguments why the seminal Thomas-Fermi (TF) approximation is also applicable in our context.

At first we provide a rough estimate in the case of an absent dT, i.e. U$= 0$, so the BEC density is characterized by the TF profile $\psi(z) = \sqrt{\left(\mu - z^2/2\right)/G_{\mathrm{B}}}\Theta\left(\mu - z^2/2\right)$, where the Heaviside function Θ prevents the density to become negative. Thus, the Tomas-Fermi radius $\sqrt{2\mu}$ follows from the dimensionless chemical potential μ, which is determined by normalization to be $\mu = \frac{1}{2}\left(\frac{3}{2}\right)^{2/3}(G_{\mathrm{B}})^{2/3}$. As the red/blue-detuned dT is supposed to be inserted at the trap center, we then calculate the dimensionless BEC coherence length ξ at the trap center. It is defined by comparing the kinetic energy $1/2\xi^2$ with the interaction energy $G_{\mathrm{B}}n(0)$ in the trap center, which is given by μ. For the above mentioned experimental parameters this yields the dimensionless BEC coherence length $\xi = 1/\sqrt{2\mu} = 0.038$, which is about 14.4 times smaller than the dT width $w = 0.548$. This indicates that the dT induced imprint upon the BEC wave-function occurs on a length scale which is much larger than its coherence length, so the TF approximation seems to be reasonable even in the presence of the red/blue-detuned dT.

In view of a more quantitative justification for the applicability of the Thomas-Fermi approximation, Fig. 3.2 presents the numerical result how the ratio of the sum of interaction and potential energy $E_{\mathrm{int,pot}} = E_{\mathrm{pot}} + E_{\mathrm{int}}$ versus the kinetic energy E_{kin} of the condensate wave function changes with increasing or decreasing the red/blue-detuned dT depth U. We read off that the inequality $\left(E_{\mathrm{pot}} + E_{\mathrm{int}}\right)/E_{\mathrm{kin}} \gg 1$ holds within the whole region of interest for U, so the TF approximation seems to be, indeed, valid. Note that the maximal value of this energy ratio occurs for U$= 0$ and amounts to 7.5×10^4, which is of the order of the number of particles.

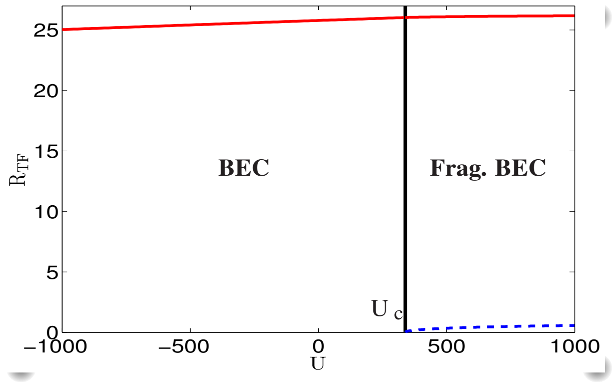

Figure 3.3: Outer Thomas-Fermi radius R_{TF1} (red solid) and inner Thomas-Fermi radius R_{TF2} (blue dashed) versus dimple trap depth U. BEC fragments into two parts above $\mathrm{U_c} \approx 339.5$.

Therefore, we investigate in the following the TF approximation in more detail for non-zero red/blue-detuned dT depth U. To this end we use for the condensate wave function the ansatz $\psi(z,t) = \psi(z)e^{-i\mu t}$, insert it into the 1DGPE (3.15), and neglect the kinetic energy term, which yields the density profile

$$\psi(z) = \sqrt{\frac{1}{G_{\mathrm{B}}}\left(\mu - \frac{z^2}{2} - \mathrm{U}e^{-\frac{z^2}{w^2}}\right)}\,\Theta\left(\mu - \frac{z^2}{2} - \mathrm{U}e^{-\frac{z^2}{w^2}}\right). \tag{3.17}$$

In view of the normalization $\int_{-\infty}^{+\infty} \parallel \psi(z) \parallel^2 dz = 1$, which fixes the chemical potential μ, we have to determine the Thomas-Fermi radii R_{TF} from the condition that the condensate wave function vanishes:

$$\mu = \frac{R_{\mathrm{TF}}^2}{2} + \mathrm{U}e^{-\frac{R_{\mathrm{TF}}^2}{w^2}}. \tag{3.18}$$

As can be read off from Fig. 3.1 (b) the number of solutions of Eq. (3.18) changes for increasing dT depth at a critical value $\mathrm{U_c}$ which we determine as follows. We put $\mu_{\mathrm{c}} = \mathrm{U_c}$ and utilize the normalization condition $2\int_0^{R_{\mathrm{TF}}} \parallel \psi(z) \parallel^2 dz = 1$ with assuming one TF radius $R_{\mathrm{TF}} \approx \sqrt{2\mu}$. This yields the implicit equation

$$\mathrm{U_c} = \frac{1}{2}\left(\frac{3}{2}\right)^{\frac{2}{3}} \left(G_{\mathrm{B}} + \sqrt{\pi}w\mathrm{U_c}\right)^{\frac{2}{3}}. \tag{3.19}$$

This produces the result $\mathrm{U_c} \approx 339.5$ for the experimental coupling constant $G_{\mathrm{B}} = 11435.9$, which compares well with the value $\mathrm{U_c} \approx 342$ determined from solving 1DGPE (3.15). In the case that U is smaller than $\mathrm{U_c}$ Eq. (3.18) defines only the cloud radius R_{TF1}. But for the case $\mathrm{U} > \mathrm{U_c}$ the dT drills a hole in the center of the ^{87}Rb condensate, so it fragments into two parts. Thus, we have then, apart from the outer cloud radius R_{TF1}, also an inner cloud

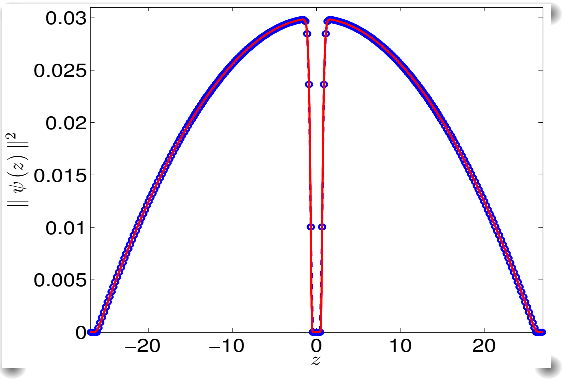

Figure 3.4: Condensate density for $\mathrm{U} = 1000$ from solving 1DGPE (3.15) in imaginary time numerically (red) and from TF approximation (3.17) (blue-circles).

radius R_{TF2}. With this the normalization condition $2\int_{R_{\mathrm{TF2}}}^{R_{\mathrm{TF1}}} \parallel \psi(z) \parallel^2 dz = 1$ yields

$$\mu\left(R_{\mathrm{TF1}} - R_{\mathrm{TF2}}\right) - \frac{1}{6}\left(R^3_{\mathrm{TF1}} - R^3_{\mathrm{TF2}}\right) = \frac{G_{\mathrm{B}}}{2} + \frac{\sqrt{\pi} w \mathrm{U}}{2}\left[\mathrm{Erf}\left(\frac{R_{\mathrm{TF1}}}{w}\right) - \mathrm{Erf}\left(\frac{R_{\mathrm{TF2}}}{w}\right)\right], \tag{3.20}$$

where $\mathrm{Erf}(y) = \frac{2}{\sqrt{\pi}}\int_0^y e^{-x^2} dx$ denotes the error function. In case of $\mathrm{U} \leq \mathrm{U_c}$ the inner cloud radius R_{TF2} vanishes and the cloud radius is approximated via $R_{\mathrm{TF1}} \approx \sqrt{2\mu}$ due to Eq. (3.18) as it is much larger than the dimple trap width w. Thus, by using the approximation $\mathrm{Erf}\left(R_{\mathrm{TF1}}/w\right) \approx 1$ for $R_{\mathrm{TF1}}/w \gg 0$, the chemical potential is determined explicitly from

$$\mu \approx \frac{1}{2}\left(\frac{3}{2}\right)^{2/3}\left(G_{\mathrm{B}} + \sqrt{\pi} w \mathrm{U}\right)^{2/3}, \quad \mathrm{U} \leq \mathrm{U_c}\,. \tag{3.21}$$

Provided that $\mathrm{U} \geq \mathrm{U_c}$, the inner cloud radius R_{TF2} has to be taken into account according to Fig. 3.1 and, due to the fact that $R^2_{\mathrm{TF2}} \ll \mathrm{U}$, we get from Eq. (3.18) the approximation $\mu \approx \mathrm{U} e^{-\frac{R^2_{\mathrm{TF2}}}{w^2}}$, which reduces to

$$R_{\mathrm{TF2}} \approx w\sqrt{\log\left(\frac{\mathrm{U}}{\mu}\right)}. \tag{3.22}$$

Thus, we conclude that R_{TF2} vanishes, indeed, at $\mathrm{U_c}$ according to Eq. (3.19) and Eq. (3.21). With this we obtain from Eq. (3.20) that the chemical potential follows from solving

$$\begin{aligned} 3\left[\sqrt{\pi} w \mathrm{U} + G_{\mathrm{B}} + 2w\mu\sqrt{\log\left(\frac{\mathrm{U}}{\mu}\right)}\right] &\approx 3\sqrt{\pi} w \mathrm{U} \mathrm{Erf}\left(\sqrt{\log\left(\frac{\mathrm{U}}{\mu}\right)}\right) \\ &+ w^3 \log^{\frac{3}{2}}\left(\frac{\mathrm{U}}{\mu}\right) + 4\sqrt{2}\mu^{3/2}, \, \mathrm{U} \geq \mathrm{U_c}\,. \end{aligned} \tag{3.23}$$

Figure 3.3 shows the resulting outer and inner Thomas-Fermi radius as a function of the dT depth U. We read off that $R_{\mathrm{TF1}} \approx \sqrt{2\mu}$ remains approximately constant for $\mathrm{U} \geq \mathrm{U_c}$, so

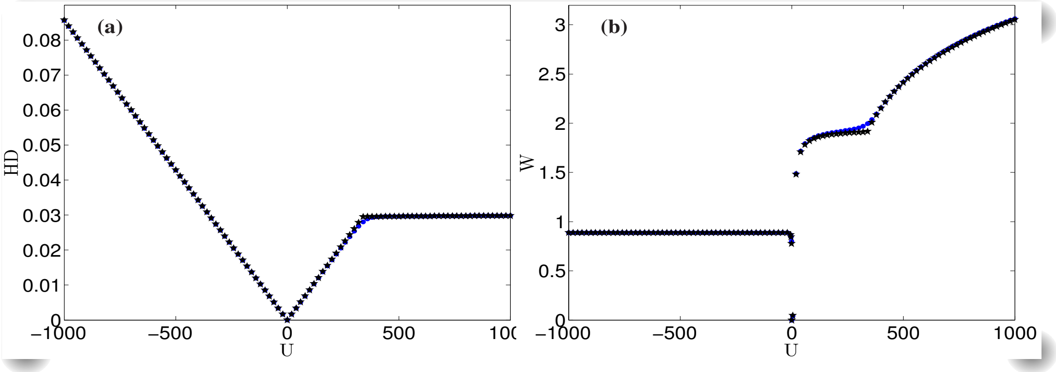

Figure 3.5: (a) Height/depth and (b) width of the dT induced bump/dip according to Eqs. (3.24)–(3.26), versus the red/blue-detuned dT depth U for the experimental BEC coupling constant $G_{\mathrm{B}} = 11435.9$ calculated numerically by solving 1DGPE (3.15) in imaginary time (blue circles) and analytically (black stars) from the TF condensate wave function (3.17).

we conclude that the chemical potential μ is locked to its critical value $\mu_c \approx \mathrm{U_c} = 339.5$. Furthermore, we note that the inner Thomas-Fermi radius R_{TF2} increases up to about $5.4w$ for the considered range of U.

Figure 3.4 compares the resulting TF condensate wave function (3.17) with a numerical solution of the 1DGPE (3.15) in imaginary time at U= 1000 and we read off that both agree quite well. Thus, our TF approximation describes the equilibrium properties of the condensate wave function in the presence of the red/blue-detuned dT even quantitatively correct. In view of a more detailed comparison, we characterize the red/blue-detuned dT induced imprint upon the condensate wave function $\psi(z)$ by the following two quantities. The first one is the height/depth (HD) of the dT induced imprint

$$\mathrm{HD} = \begin{cases} \parallel \psi(0) \parallel_{\mathrm{U}}^2 - \parallel \psi(0) \parallel_{\mathrm{U}=0}^2 & \mathrm{U} \leq 0 \\ \\ \mathrm{Max}\left(\parallel \psi(z) \parallel_{\mathrm{U}}^2\right) - \parallel \psi(0) \parallel_{\mathrm{U}}^2 & \mathrm{U} \geq 0 \end{cases} \tag{3.24}$$

and the second one is the red/blue-detuned dT induced imprint width W, which we define as follows. For $\mathrm{U} \leq 0$ we use the full width half maximum

$$\parallel \psi(\mathrm{W}/2) \parallel_{\mathrm{U}}^2 = \frac{\parallel \psi(0) \parallel_{\mathrm{U}}^2 + \parallel \psi(0) \parallel_{\mathrm{U}=0}^2}{2} \qquad \mathrm{U} \leq 0\,, \tag{3.25}$$

whereas for $\mathrm{U} > 0$ we define the equivalent width [194]:

$$\mathrm{W} = \frac{2I_0 z_{\mathrm{Max}} - \int_{-z_{\mathrm{Max}}}^{z_{\mathrm{Max}}} \parallel \psi(z) \parallel_{\mathrm{U}}^2 dz}{I_0 - \parallel \psi(0) \parallel_{\mathrm{U}}^2} \qquad \mathrm{U} > 0\,, \tag{3.26}$$

where we have $I_0 = \mathrm{Max}\left(\parallel \psi(z) \parallel_{\mathrm{U}}^2\right)$. Figure 3.5 (a) shows the red/blue-detuned dT induced

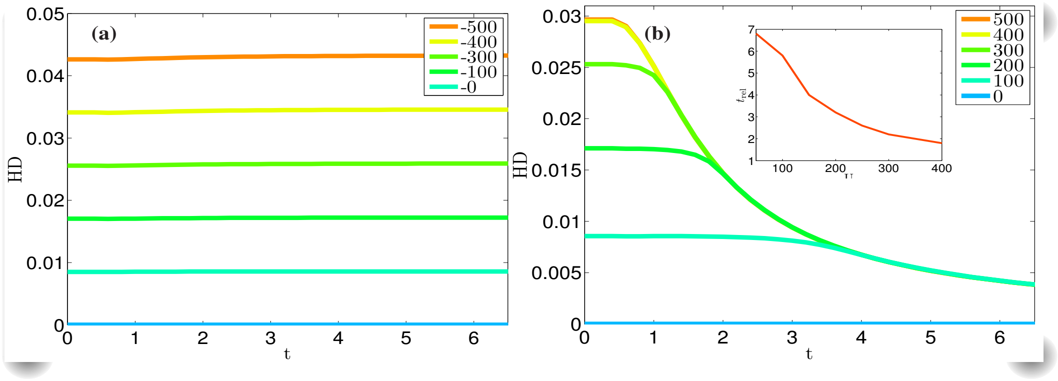

Figure 3.6: (a) Height/depth of the dT induced imprint after having released the harmonic trap versus time for (a) increasing negative and (b) decreasing positive values of dT depth U from top to bottom. Inlet: relaxation time t_{rel} decreases with increasing U.

imprint height/depth as a function of U. At first, we read off that for $\mathrm{U} = 0$, i.e. when we have not switched on the dT, that the bump/dip vanishes. Furthermore, in the range $\mathrm{U} \leq \mathrm{U_c}$ we observe that the height/depth of the dT induced imprint bump/dip changes linearly with U according to

$$\mathrm{HD} \approx \frac{|\mathrm{U}|}{G_{\mathrm{B}}} . \tag{3.27}$$

In case of $\mathrm{U} > \mathrm{U_c}$ the height/depth of the dT induced imprint has approximately the constant value $\mathrm{HDc} = \mathrm{U_c}/G_{\mathrm{B}} \approx 0.029$ as follows from the TF wave function (3.17) and the above mentioned locking of the chemical potential to its critical value. Note that this constant value only slightly deviates from the corresponding numerical value $\mathrm{HDc} = 0.03$.

Correspondingly, Figure 3.5 (b) depicts the dimple trap induced width W as a function of U. From our TF approximation we obtain for the width transcendental formulas, which read in case of $\mathrm{U} \leq 0$

$$\frac{\mathrm{W}^2}{4} + 2\mathrm{U}e^{-\frac{\mathrm{W}^2}{4w^2}} - \mathrm{U} + \frac{1}{2}\left(\frac{3}{2}\right)^{2/3}\left[(G_{\mathrm{B}})^{2/3} - \left(G_{\mathrm{B}} + \sqrt{\pi}w\mathrm{U}\right)^{2/3}\right] = 0 , \tag{3.28}$$

and for $\mathrm{U} > w^2/2$

$$\mathrm{W} = \frac{2w^3\sqrt{\log\left(\frac{2\mathrm{U}}{w^2}\right)}\left[2\log\left(\frac{2\mathrm{U}}{w^2}\right) + 3\right] - 6\sqrt{\pi}w\mathrm{U}\mathrm{Erf}\left(\sqrt{\log\left(\frac{2\mathrm{U}}{w^2}\right)}\right)}{3\left[w^2 + w^2\log\left(\frac{2\mathrm{U}}{w^2}\right) - 2\mathrm{U}\right]} . \tag{3.29}$$

As shown in Fig. 3.5 (b), for a red-detuned dT depth, the width remains approximately constant and is determined by the FWHM of the dimple Gaussian. Just before $\mathrm{U} = 0$ the width W starts to decrease to zero. For a blue-detuned dT the width of the dip continuously in-

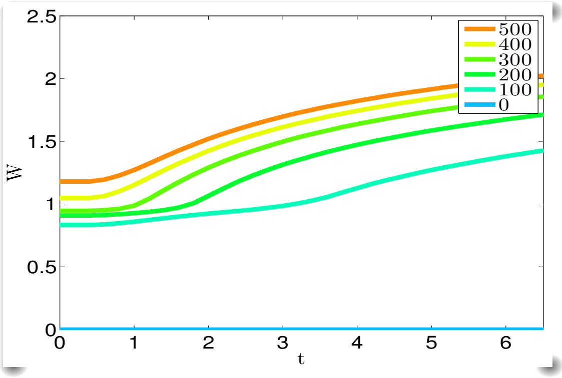

Figure 3.7: Width of the dT induced imprint after having released the trap versus time for decreasing positive values of dT depth U from top to bottom.

creases with an intermediate plateau at U_c with the value $Wc \approx 1.91$, which agrees well with the numerically obtained one $Wc \approx 1.99$. After the critical blue-detuned laser beam strength U_c the width of the imprint of the dT on the condensate increases drastically according to Fig. 3.5 (b), as more and more BEC atoms move away from the center of the condensate.

Note that the Thomas-Fermi approximation would break down when the dimensionless healing length ξ in the trap center would be larger than the dimensionless dimple trap width w. This is the case for several previous studies treating experimentally relevant localized dimples, which can well be modeled by Dirac delta potentials [195, 196].

3.3 Dimple trap induced imprint upon condensate dynamics

In the following we investigate two quench scenarios numerically in more detail. The first one is the standard time-of-flight (TOF) expansion after having switched off the harmonic trap when the amplitude of the red/blue-detuned dT is still present. In the second case we consider the inverted situation that the red/blue-detuned dT is suddenly switched off within a remaining harmonic confinement. The latter turns out to give rise to the emergence of white shock-waves or bi-solitons trains, i.e. two trains of more than one soliton each, respectively.

3.3.1 Time-of-flight expansion

Time-of-flight (TOF) absorption pictures represent an important diagnostic tool to analyze dilute quantum gases since the field's inception. By suddenly turning off the magnetic trap, the atom cloud expands with a dynamics which is determined by both the momentum distribution of the atoms at the instance, when the confining potential is switched off, and by inter-atomic interactions [197, 198]. We have investigated the time-of-flight expansion dynamics of the BEC in the presence of the dT by solving numerically the 1DGPE (3.15) and by analyzing the resulting evolution of the condensate wave function. It turns out that, despite the continuous broadening of the condensate density, its dT induced imprint remains qualitatively preserved both for red- and blue-detuned dT. Therefore, we focus a more quantitative discussion upon the dynamics of the corresponding dT induced imprint height/depth and width.

For a red-detuned dT, it turns out that the bump height even remains constant in time. This is shown explicitly in Fig. 3.6 (a), which roughly preserves its initial value at $t = 0$. This is due to the fact that a fraction of atoms remains trapped in the dimple trap while the rest of the cloud expands. This physical picture also explains the bump width, we even find that no significant changes do occur neither in time nor for varying U, therefore we do not present a corresponding figure. Note that the latter finding originates from Fig. 3.5 (b), where the width is shown to be roughly constant for all dT depths in the red-detuned case.

Instead, in case of a blue-detuned dT, the dip decays after a characteristic time scale as shown in Fig. 3.6 (b). Defining that relaxation time t_{rel} according to $\text{HD}\left(t_{\text{rel}}\right) = \text{HD}\left(0\right)/2$, the inlet reveals that the dip relaxes with a shorter time scale for increasing blue-detuned dT depth U. These results are explained by the fact that an increasing blue-detuned dT potential pushes the expanding cloud even faster apart. This physical picture is confirmed by the dynamics of the dT induced imprint width shown in Fig. 3.7. At the beginning of TOF it remains at first constant and then increases gradually. This change of W occurs on the scale of the relaxation time of HD, which is depicted in the inlet of Fig. 3.6 (b).

3.3.2 Wave packets versus solitons

Due to their quantum coherence, BECs exhibit rich and complex dynamic patterns, which range from the celebrated matter-wave interference of two colliding condensates [123, 124] over Faraday waves [199, 200] to the particle-like excitations of solitons [66, 125–129, 187]. For our 1D model of a BEC with a harmonic and a dimple trap in the center, we investigated the dynamics of the condensate wave function which emerges after having switched off the dT. To this end, Fig. 3.8 depicts the resulting density profile of density $n = |\psi|^2$ and phase $\phi = \tan^{-1}\left(\psi_{\text{Im}}/\psi_{\text{Re}}\right)$ of the condensate wave function ψ at different instants of time. Both for an initial red- and blue-detuned dT, we observe that two excitations of the condensate are created at the dT position, which travel in opposite direction with the same center-of-mass speed, are reflected at the trap boundaries, and then collide at the dT position. Furthermore, we find that these excitations qualitatively preserve their shape despite the collision and that the BEC wave function reveals characteristic phase slips between $-\pi/2$ and $\pi/2$. All these findings are not yet conclusive to decide whether these excitations represent wave packets in the absence of dispersion or solitons. Therefore, we investigate their dynamics in more

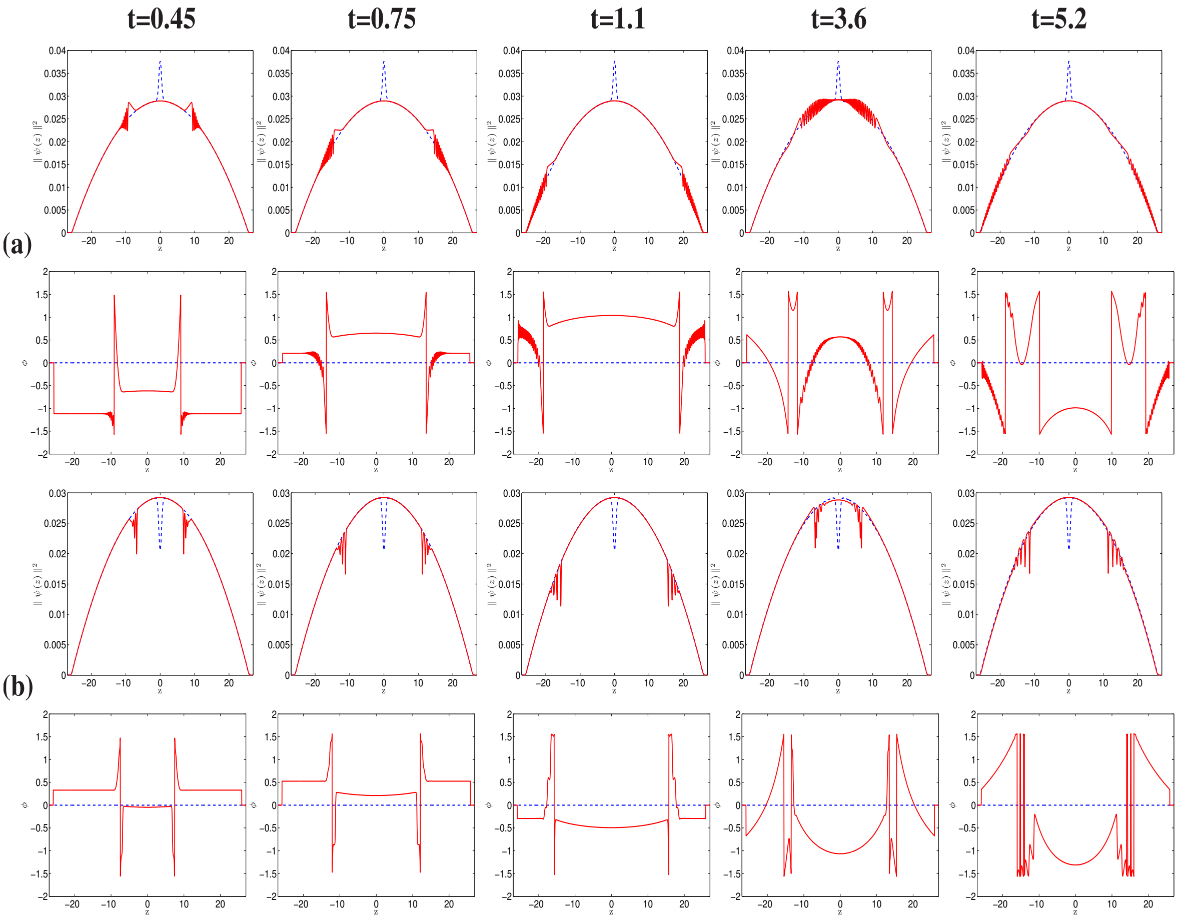

Figure 3.8: Density (phase) profile of BEC after having switched off the red/blue-detuned dT: in blue-dashed line at t=0, and in red-solid line at t=0.45 (1st column), t=0.75 (2nd column), t=1.1 (3rd column), t=3.6 (4th column), and t=5.2 (5th column) for (a) U=-100 and (b) U=100.

detail by determining their center-of-mass motion via

$$\bar{z}_{\mathrm{L,R}}(t) = \frac{\int_{-\infty,0}^{0,\infty} z \left(\| \psi(z,t) \|_{\mathrm{U}}^2 - \| \psi(z,t) \|_{\mathrm{U}=0}^2 \right) dz}{\int_{-\infty,0}^{0,\infty} \left(\| \psi(z,t) \|_{\mathrm{U}}^2 - \| \psi(z,t) \|_{\mathrm{U}=0}^2 \right) dz}, \tag{3.30}$$

which are plotted in Fig. 3.9. Note that the mean positions $\bar{z}_{\mathrm{L}}$ and $\bar{z}_{\mathrm{R}}$ of the excitations are uncertain in the region where they collide. Nevertheless Fig. 3.9 demonstrates that the excitations oscillate with the frequency $\Omega = 2\pi \times 4.87$ Hz irrespective of sign and size of U. As we have assumed the trap frequency $\omega_z = 2\pi \times 6.8$ Hz, we obtain the ratio $\Omega/\omega_z \approx 0.72$, which is quite close to $\Omega/\omega_z = 1/\sqrt{2} \approx 0.707$.

Despite these similarities of the cases of an initial red- and blue-detuned dT, we observe one significant difference. Whereas the oscillation amplitudes of the excitations do not depend on the initial value U < 0 according to Fig. 3.9 (a), we find decreasing oscillation amplitudes of the excitations with increasing the initial value U > 0 in Fig. 3.9 (b). The

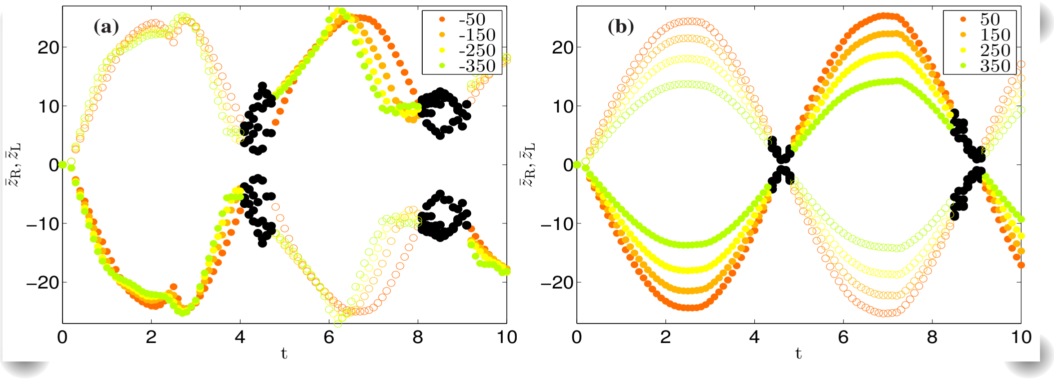

Figure 3.9: Center of mass positions of excitations $\bar{z}_L$ (filled circles) and $\bar{z}_R$ (empty circles) according to Eq. (3.30) versus time after having switched off the dT with increasing absolute value of the depth |U| from top to bottom, for (a) red-detuning and (b) blue-detuning. Black filled circles represent the region of colliding excitations, where mean positions are not perfectly detectable.

latter amplitude dependence on the initial condition is characteristic for gray/dark solitons according to Ref. [187]. Indeed, for an increasing dT potential the gray soliton acquires a larger depth, which corresponds to a smaller velocity, so its oscillation amplitude is reduced. This particle-like interpretation of the excitations is also confirmed by the other theoretical prediction of Ref. [187] that gray/dark solitons oscillate in a harmonic confinement with the frequency $\Omega/\omega_z = 1/\sqrt{2}$, which was already confirmed in the Hamburg experiment of Ref. [66] and in the Heidelberg experiment of Ref. [97] and is also seen in Fig. 3.9 (b).

Conversely, for an initial red-detuned dT the excitations can not be identified with bright solitons as the dynamics is governed by a GPE with a repulsive two-particle interaction. Here the excitations have to be interpreted as wave packets which move without any dispersion as follows from a Bogoliubov dispersion relation and the smallness of the coherence length. Thus, for $U < 0$ the excitations propagate like sound waves in the BEC [123] and, within a TF approximation, their center-of-mass motion is described by the evolution equation [201]

$$\frac{dz(t)}{dt} = \sqrt{\mu - \frac{z^2(t)}{2}}\,. \tag{3.31}$$

Solving (3.31) with the initial condition $z(0) = 0$ yields the result $z(t) = \sqrt{2\mu}\sin t/\sqrt{2}$. Thus, we read off that the oscillation amplitude coincides with the TF radius and that the dimensionless oscillation frequency turns out to be $1/\sqrt{2}$ in agreement with Fig. 3.9 (a).

Thus, we conclude that switching off the red/blue-detuned dT leads to physically different situations. For an initial red-detuned dT, we generate wave packets which correspond to bright shock waves [202], whereas for the corresponding blue-detuned case bi-soliton trains emerge [91, 125, 203], due to the collision of the two fragmented parts of the condensate.

Note that gray bi-solitons trains are generated for a partially fragmented BEC, i.e. $\mathrm{U} < \mathrm{U_c}$. On the other hand the dark bi-solitons trains turn out to be only generated for $\mathrm{U} \geq \mathrm{U_c}$, where initially in equilibrium the BEC is well fragmented into two parts.

3.4 Summary and conclusion

In this chapter we studied within a quasi 1D model both analytically and numerically how a dimple trap in the center of a harmonically trapped BEC affects the condensate wave function. At first, we showed for the equilibrium properties of the system that the Thomas-Fermi approximation agrees quantitatively with numerical solutions of the underlying 1D Gross-Pitaevskii equation. For an increasing red-detuned dT depth, it turns out for the induced bump that the height decreases linearly, whereas the width remains approximately constant. In contrast to that we found for an increasing blue-detuned dT that depth and width of the induced dip initially increase. Beyond a critical value $\mathrm{U_c}$, the BEC even fragments into two parts and, if U is increased beyond $\mathrm{U_c}$, the dT induced imprint yields a condensate wave function whose width increases further, although the dip height/depth remains constant. Afterwards, we investigated the dT induced bump/dip upon the condensate dynamics for two quench scenarios.

At first, we considered the release of the harmonic confinement, which leads to a time-of-flight expansion and found that the dT induced imprint remains conserved for a red-detuned dT but decreases in the blue-detuned case. This result suggests that it might be experimentally easier to observe the bump for a red-detuned dT. A more realistic description of the experiment needs to consider the loss of condensate atoms by adding damping terms to the 1DGPE (3.15), which are of the form $i\Upsilon_2 \parallel \psi(z,t) \parallel^2$ and $i\Upsilon_3 \parallel \psi(z,t) \parallel^4$, where the positive constants Υ_2 and Υ_3 denote two- and three-body loss rates, respectively. We note that these additional terms may have nontrivial effects on the dT properties [204].

In addition, we analyzed the condensate dynamics after having switched off the red/blue-detuned dT. This case turned out to be an interesting laboratory in order to study the physical similarities and differences of white shock-waves and gray/dark bi-soliton trains, which emerge for an initial red- and blue-detuned dT, respectively. The astonishing observation, that the oscillation frequencies of both the white shock-waves and the bi-soliton trains coincide, is presumably an artifact of the harmonic confinement. Thus, it might be rewarding to further investigate these different dynamical features also in anharmonic confinements [205–207]. Additionally, we have also found that the generation of gray/dark bi-soliton trains is a generic phenomenon on collisions of partially/fully fragmented BEC, respectively, and the partially/fully fragmented BEC is strongly depending upon the equilibrium values of the dimple trap depth.

Chapter 4

Sculpting quasi one-dimensional Bose-Einstein condensate

In this chapter we explore how to tune the dynamics of a quasi-one-dimensional harmonically trapped Bose-Einstein condensate (BEC) due to an additional red- and blue-detuned Hermite-Gaussian dimple trap (HGdT). We organize this chapter as follows. We derive the underlying quasi one-dimensional Gross-Pitaevskii equation (1DGPE) in Sec. 4.1, where we also outline the system geometry and relate our simulation parameters to tunable experimental parameters. Afterwards in Sec. 4.2, for the equilibrium properties of the system, we compare a Thomas-Fermi approximate solution with numerical results and show that the HGdT imprint upon the condensate wave function strongly depends upon whether the HGdT is red- or blue-detuned. Later, the time-of-flight (TOF) dynamics of the red/blue-detuned HGdT imprint upon the condensate wave function is discussed in detail in Sec. 4.3. We obtain that for red-detuning the HGdT imprint does not decay, but for the blue-detuning HGdT imprint decreases during TOF. In Sec. 4.4, we discuss the formation of shock-waves/gray(dark) pair-soliton bi-trains in the harmonic trap, after having switched off the red/blue-detuned HGdT potential. There, we also find out that the generation of gray/dark pair-solitons bi-trains represents a generic phenomenon of collisions of moderately/fully fragmented BEC, respectively, where the latter is strongly depending upon the equilibrium values of the red/blue-detuned HGdT depth. Finally, Sec. 4.5 provides a summary and conclusions.

4.1 Modified quasi 1D model

We consider a one-component BEC with time-dependent two-particle interactions described by the three-dimensional GPE

$$i\hbar\frac{\partial}{\partial t}\psi(\mathbf{r},t)=\left\{-\frac{\hbar^2}{2m_B}\nabla^2+V(\mathbf{r})+\mathrm{U}_{\mathrm{dT}}^{3\mathrm{D}}+\mathrm{G}_{\mathrm{B}}^{3\mathrm{D}}\parallel\psi(\mathbf{r},t)\parallel^2\right\}\psi(\mathbf{r},t)\,, \tag{4.1}$$

where $\psi(\mathbf{r},t)$ denotes the macroscopic condensate wave function for the ^{87}Rb BEC with the spatial coordinates $\mathbf{r}=(x,\ y,\ z)$. Here m_B stands for the mass of the ^{87}Rb atom, $\mathrm{G}_\mathrm{B}^{3\mathrm{D}}=N_\mathrm{B}4\pi\hbar^2 a_\mathrm{B}/m_\mathrm{B}$ represents the three-dimensional ^{87}Rb coupling constant, where $N_\mathrm{B}=20\times 10^4$ denotes the number of ^{87}Rb atoms, and the s-wave scattering length is $a_\mathrm{B}=94.7\ \mathrm{a}_0$ with the Bohr radius a_0. Furthermore, $V(\mathbf{r})=m_\mathrm{B}\omega_\mathrm{z}^2 z^2/2+m_\mathrm{B}\omega_\mathrm{r}^2\left(x^2+y^2\right)/2$ describes a three-dimensional harmonic confinement, which has rotational symmetry with respect to the z-axis. The oscillator lengths for experimental parameters are $l_\mathrm{z}=\sqrt{\hbar/m_\mathrm{B}\omega_\mathrm{z}}=4.12\,\mu\mathrm{m}$ and $l_\mathrm{r}=\sqrt{\hbar/m_\mathrm{B}\omega_\mathrm{r}}=0.84\,\mu\mathrm{m}$ for the trap frequencies $\omega_\mathrm{z}=2\pi\times 6.8\,\mathrm{Hz}$ and $\omega_\mathrm{r}=2\pi\times 160\,\mathrm{Hz}$, respectively.

An additional three-dimensional narrow Hermite-Gaussian laser beam polarizes the neutral atoms which yields the HGdT potential $\mathrm{U}_\mathrm{dT}^{3\mathrm{D}}=\mathrm{U}_0 I_{nm}(\mathbf{r})$ according to (2.18). Within the rotating-wave approximation its amplitude is $\mathrm{U}_0=3\pi c^2\Gamma/\left(2\omega_\mathrm{A}^3\Delta\right)$ [163, 164, 189, 190], where Γ denotes the damping rate due to energy loss via radiation (2.22), which is depends on the dipole matrix element between ground and excited state. Furthermore, $\Delta=\omega-\omega_\mathrm{A}$ represents the detuning of the laser, here ω is the laser frequency and ω_A stands for the atomic frequency. And $I_{nm}(\mathbf{r})$ describes the intensity profile of the TEM_{nm} Hermite-Gaussian laser beam, which is assumed to propagate in y-direction and is determined via

$$I_{nm}(\mathbf{r})=\frac{2P}{2^{n+m}n!m!\pi}H_n\left(\frac{\sqrt{2}x}{W_\mathrm{x}(y)}\right)^2 H_m\left(\frac{\sqrt{2}z}{W_\mathrm{z}(y)}\right)^2\frac{e^{-\left[\frac{2x^2}{W_\mathrm{x}^2(y)}+\frac{2z^2}{W_\mathrm{z}^2(y)}\right]}}{W_\mathrm{x}(y)\,W_\mathrm{z}(y)}, \tag{4.2}$$

with $P=\int\int \mathrm{I}_{nm}(\mathbf{r})\,dxdz$ denoting the total intensity. Furthermore $W_\mathrm{x/z}(y)$ denotes the Gaussian beam radius in x- and z-direction, where the intensity decreases to $1/e^2$ of its peak value, $y_{Rx/z}=\pi W_{0x/z}^2/\lambda$ represents the so-called Rayleigh-lengths, which are defined as the distance from the focus $W_\mathrm{0x/z}$ position where the beam radius increases by a factor of $\sqrt{2}$ [189]. Here $H_n(x)$ and $H_m(z)$ are Hermite polynomials of order n and m in x- and z-direction, respectively. In the following we restrict ourselves to a HGdT potential for a BEC, which is based on a Hermite-Gaussian TEM_{01} laser beam mode and thus carries a dark spot in the center of the profile:

$$I_{01}(\mathbf{r})=\frac{8Pz^2}{\pi W_\mathrm{x}(y)\,W_\mathrm{z}^3(y)}e^{-\left[\frac{2x^2}{W_\mathrm{x}^2(y)}+\frac{2z^2}{W_\mathrm{z}^2(y)}\right]}. \tag{4.3}$$

For the TEM_{01} laser beam, we use the width along the x-axis $W_\mathrm{0x}=1.1\,\mu\mathrm{m}$ and along the z-axis $W_\mathrm{0z}=3.2\,\mu\mathrm{m}$. Therefore, the Rayleigh lengths for the red-detuned laser light with $\lambda=840\,\mathrm{nm}$ [30] yield $y_\mathrm{Rx}=4.526\,\mu\mathrm{m}$ and $y_\mathrm{Rz}=38.29\,\mu\mathrm{m}$ as well as for the blue detuned laser light with $\lambda=772\,\mathrm{nm}$ [191] we get $y_\mathrm{Rx}=4.92\,\mu\mathrm{m}$ and $y_\mathrm{Rz}=41.6\,\mu\mathrm{m}$. With keeping in mind the fact that $y_{\mathrm{Rx}/z}\gg l_\mathrm{r}$, we can approximate the widths of the HG laser beam in x- and z-direction according to $W_{\mathrm{x}/z}(y)\approx W_{0\mathrm{x}/z}$. This simplifies the HGdT potential to

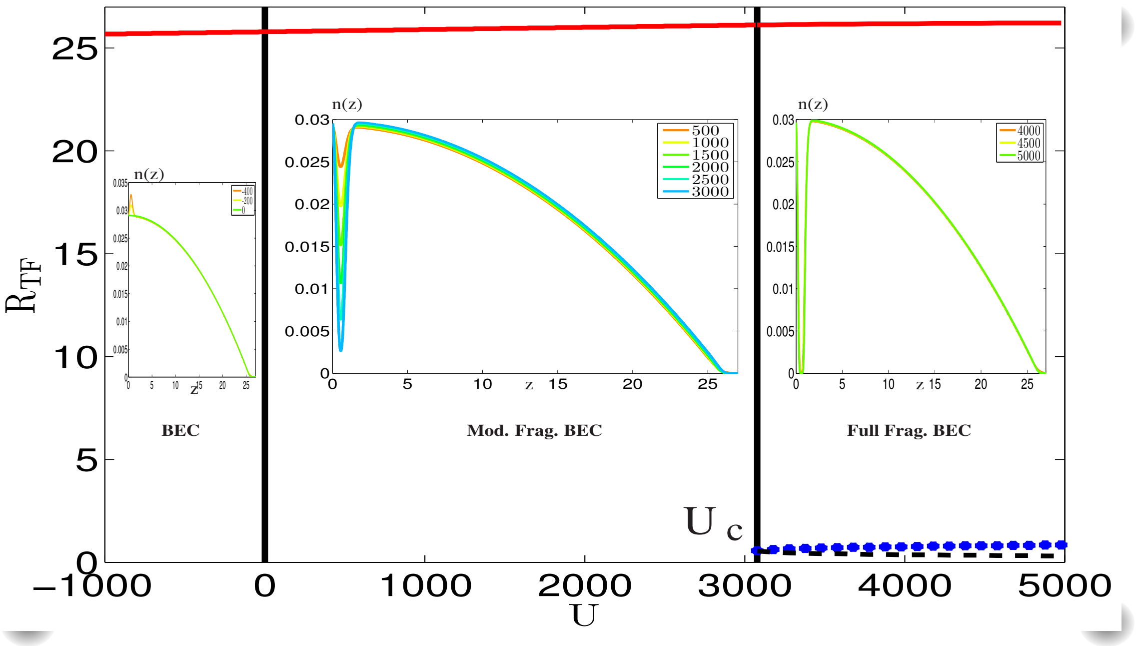

Figure 4.1: Outer Thomas-Fermi radius $\mathrm{R_{TF1}}$ (red solid), central Thomas-Fermi radius $\mathrm{R_{TF2}}$ (blue circles) and inner Thomas-Fermi radius $\mathrm{R_{TF3}}$ (dashed black) as a function of HGdT depth U for the coupling constant value $\mathrm{G_B} = 11435.9$. Below the critical value HGdT depth $\mathrm{U} < \mathrm{U_c}$, the BEC is moderately (Mod.) fragmented (Frag.), with one exceptional case at U=0, where the BEC is completely confined in one-dimensional harmonic trap. The BEC fully fragments into three parts above the critical value $\mathrm{U_c} \approx 3079$, as can be seen in the specific regional inset density plots.

$$\mathrm{U_{dT}^{3D}}(\mathbf{r}) = \frac{8U_0 P z^2}{\pi W_{0\mathrm{x}} W_{0\mathrm{z}}^3} e^{-\left(\frac{2x^2}{W_{0\mathrm{x}}^2}+\frac{2z^2}{W_{0\mathrm{z}}^2}\right)}. \tag{4.4}$$

As we have an effective one-dimensional setting due to $\omega_\mathrm{z} \ll \omega_\mathrm{r}$, which implies $l_\mathrm{z} > l_\mathrm{r}$, and $y_{\mathrm{Rx/z}} \gg l_\mathrm{r}$, we factorize the BEC wave-function via Eq. (3.7). We follow Ref. [119] and integrate out the two transversal dimensions of the three-dimensional GPE. After some algebra, the resulting quasi one-dimensional GPE reads

$$i\hbar\frac{\partial}{\partial t}\psi(z,t) = \left\{-\frac{\hbar^2}{2m_B}\frac{\partial^2}{\partial z^2} + V(z) + \mathrm{U}z^2 e^{-\frac{2z^2}{W_{0\mathrm{z}}^2}} + \mathrm{G_B} \parallel \psi(z,t) \parallel^2\right\}\psi(z,t), \tag{4.5}$$

where $V(z) = m_\mathrm{B}\omega_z^2 z^2/2$ represents an effective one-dimensional harmonic potential from the MOT, and the one-dimensional two-particle interaction strength turns out to be Eq. (3.10). Furthermore, the one-dimensional HGdT depth results in

$$\mathrm{U} = \frac{8\mathrm{U}_0 P}{\pi W_{0\mathrm{z}}^3 \sqrt{W_{0\mathrm{x}}^2 + 2l_\mathrm{r}^2}}, \tag{4.6}$$

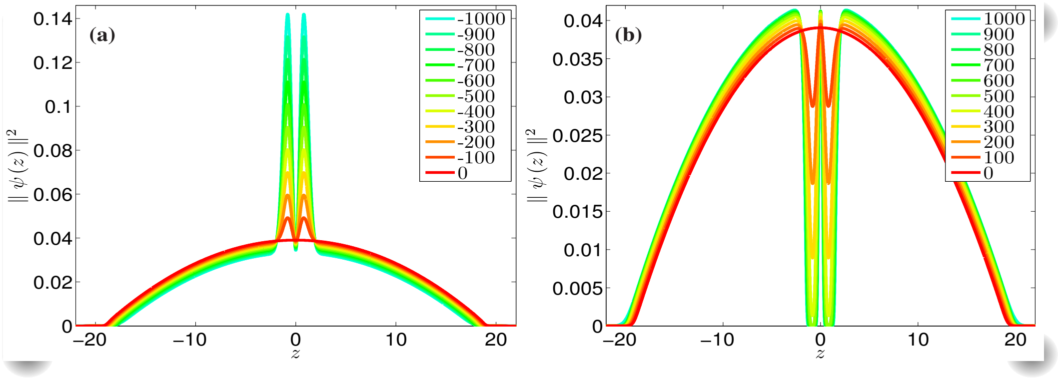

Figure 4.2: Numerical density profile of BEC for the experimental coupling constant value $G_B = 11435.9$ and for the dT depth U which decreases from top to bottom according to the inlets. For (a) negative values of U, the bumps in the condensate wave function decreases, whereas for (b) positive values the corresponding dips increases.

In order to make the 1DGPE in (4.5) dimensionless, we introduce the dimensionless time as $\tilde{t} = \omega_z t$, the dimensionless coordinate $\tilde{z} = z/l_z$, and the dimensionless wave function $\tilde{\psi} = \psi\sqrt{l_z}$. With this Eq. (4.5) can be written in dimensionless form

$$i\frac{\partial}{\partial \tilde{t}}\tilde{\psi}(\tilde{z},\tilde{t}) = \left\{-\frac{1}{2}\frac{\partial^2}{\partial \tilde{z}^2} + \frac{1}{2}\tilde{z}^2 + \tilde{\mathrm{U}}\tilde{z}^2 e^{-\frac{\tilde{z}^2}{\tilde{w}^2}} + \tilde{\mathrm{G}}_{\mathrm{B}} \parallel \tilde{\psi}(\tilde{z},\tilde{t}) \parallel^2\right\}\tilde{\psi}(\tilde{z},\tilde{t}), \tag{4.7}$$

here $\tilde{\mathrm{G}}_{\mathrm{B}} = 2N_{\mathrm{B}}\omega_r a_{\mathrm{B}}/\omega_z l_z$, and $\tilde{\mathrm{U}} = 8\mathrm{U}_0 P l_z/\left(\pi\omega_z W_{0z}^3\sqrt{W_{0x}^2 + 2l_r^2}\right)$ are the dimensionless two-particle coupling strength and the dimensionless HGdT depth, respectively. The above mentioned experimental values yield the dimensionless coupling strength $\tilde{\mathrm{G}}_{\mathrm{B}} = 11435.9$ and $\tilde{w} = W_{0z}/\left(\sqrt{2}l_z\right) = 0.548$ represents the ratio of the width of the HGdT potential and the harmonic oscillator length along the z-axis. Furthermore, the typical depth of the dipole potential trap ranges from micro-kelvin to nano-kelvin [46, 208], which yields $\tilde{\mathrm{U}}$ to be of the order of up to few thousands. From here on, we will drop all tildes for simplicity.

4.2 Stationary condensate wave function

In order to determine the equilibrium properties of the red/blue-detuned HGdT potential imprint on the condensate wave function, we solve the quasi 1DGPE (4.7) numerically by using the split-operator method in imaginary time [192, 193]. The HGdT imprint induces two bumps/dips at the center of the BEC density for red/blue-detuned HGdT as shown in the insets of Fig. 4.1. For stronger red-detuned HGdT depth values the two bumps increase further, but for stronger blue-detuned HGdT depth the two dips in the BEC density get deeper and deeper until the BEC fragments into three parts as shown in the inset of Fig. 4.1. To investigate this scenario in more detail, we argue that, due to $\mathrm{G}_{\mathrm{B}} \gg 1$, the TF approximation is valid, as the inequality $\mathrm{E}_{\mathrm{int,pot}}/\mathrm{E}_{\mathrm{kin}} \gg 1$ holds within the whole region of interest for the

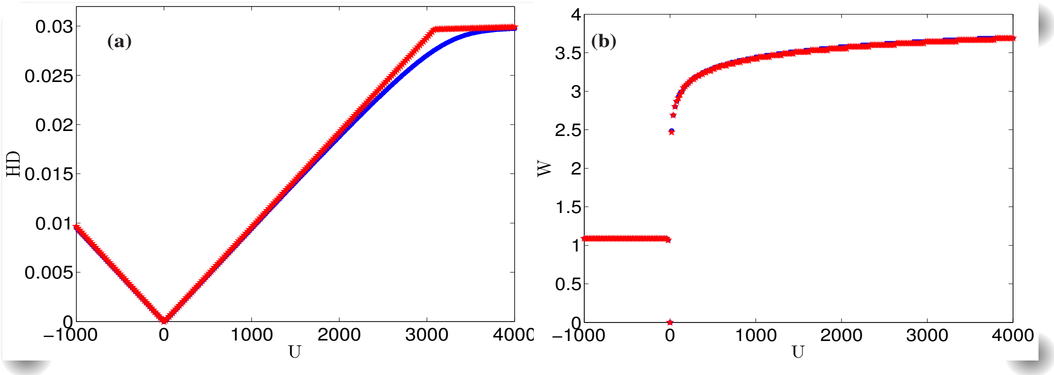

Figure 4.3: (a) Height/depth and (b) width of red/blue-detuned HGdT induced bumps/dips according to Eq. (4.11) and $\mathrm{W} = 2z_{\mathrm{Max}}$, respectively, versus red/blue-detuned HGdT depth U for the experimental BEC coupling constant $\mathrm{G_B} = 11435.9$ determined numerically by solving the quasi 1DGPE (4.7) in dimensionless imaginary time (blue circles) and analytically (red stars) from the TF wave function (4.8).

HGdT depth U [152].

Therefore we perform for the condensate wave function the ansatz $\psi(z,t) = \psi(z)e^{-i\mu t}$, insert it into the modified quasi 1DGPE (4.7), and neglect the kinetic energy term, yielding the density profile

$$\psi(z) = \sqrt{\frac{\mu}{\mathrm{G_B}}\left(1 - \frac{z^2}{2\mu} - \frac{\mathrm{U}z^2}{\mu}e^{-\frac{z^2}{w^2}}\right)}\Theta\left(1 - \frac{z^2}{2\mu} - \frac{\mathrm{U}z^2}{\mu}e^{-\frac{z^2}{w^2}}\right) . \tag{4.8}$$

In view of the normalization $2\int_0^\infty \parallel \psi(z) \parallel^2 dz = 1$, which fixes the chemical potential μ, we determine the Thomas-Fermi radii $\mathrm{R_{TF}}$ from the condition that the condensate wave function vanishes:

$$\mu = \frac{\mathrm{R_{TF}^2}}{2} + \mathrm{R_{TF}^2}\mathrm{U}e^{-\frac{\mathrm{R_{TF}^2}}{w^2}} . \tag{4.9}$$

As can be read off from the inset of the Fig. 4.1 the number of solutions of Eq. (4.8) changes for increasing red/blue-detuned HGdT depth U. In the case, when U is smaller than $\mathrm{U_c}$, Eq. (4.8) defines only the BEC cloud radius $\mathrm{R_{TF1}}$. But for the case $\mathrm{U} > \mathrm{U_c}$, the blue-detuned HGdT drills two holes at the center of the ^{87}Rb condensate, so the BEC fragments into three parts as shown in Fig. 4.1 and Fig. 4.2. Thus, we have then, apart from the outer condensate radius $\mathrm{R_{TF1}}$, also two inner condensate radii $\mathrm{R_{TF2}}$ and $\mathrm{R_{TF3}}$. With this the normalization condition $2\int_0^{\mathrm{R_{TF3}}} \parallel \psi(z) \parallel^2 dz + 2\int_{\mathrm{R_{TF2}}}^{\mathrm{R_{TF1}}} \parallel \psi(z) \parallel^2 dz = 1$ yields

$$\begin{aligned}\mu\left(\mathrm{R_{TF1}} - \mathrm{R_{TF2}} + \mathrm{R_{TF3}}\right) - \frac{1}{6}\left(\mathrm{R_{TF1}^3} - \mathrm{R_{TF2}^3} + \mathrm{R_{TF3}^3}\right) + \frac{w^2\mathrm{U}}{2}\Bigg(\mathrm{R_{TF1}}e^{-\frac{\mathrm{R_{TF1}^2}}{w^2}} - \mathrm{R_{TF2}}e^{-\frac{\mathrm{R_{TF2}^2}}{w^2}} \\ + \mathrm{R_{TF3}}e^{-\frac{\mathrm{R_{TF3}^2}}{w^2}}\Bigg) = \frac{w^3\sqrt{\pi}\mathrm{U}}{4}\left[\mathrm{Erf}\left(\frac{\mathrm{R_{TF1}}}{w}\right) - \mathrm{Erf}\left(\frac{\mathrm{R_{TF2}}}{w}\right) + \mathrm{Erf}\left(\frac{\mathrm{R_{TF3}}}{w}\right)\right] ,\end{aligned} \tag{4.10}$$

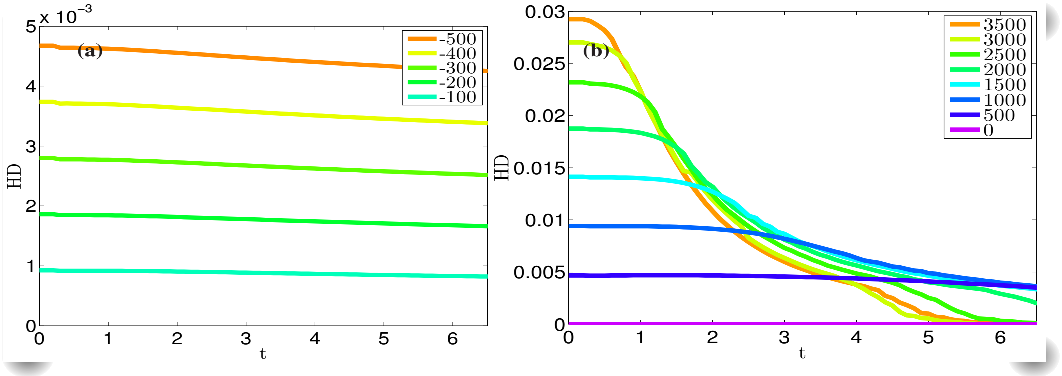

Figure 4.4: Height/depth versus dimensionless time during TOF for different (a) red-detuned and (b) blue-detuned HGdT depths U.

where $\mathrm{Erf}(y) = \frac{2}{\sqrt{\pi}} \int_0^y e^{-x^2} dx$ denotes the error function. In case of $\mathrm{U} < \mathrm{U_c}$, the BEC's inner two radii $\mathrm{R_{TF2}}$ and $\mathrm{R_{TF3}}$ vanish and the BEC outer radius is approximated via $\mathrm{R_{TF1}} \approx \sqrt{2\mu}$ due to Eq. (4.9). Thus, for $\mathrm{U} < \mathrm{U_c}$ the chemical potential is determined explicitly from (4.10): $\mu \approx 3^{2/3}/2^{7/2} \left(2\mathrm{G_B} + \sqrt{\pi} w^3 \mathrm{U}\right)^{2/3}$. Provided that $\mathrm{U} > \mathrm{U_c}$, two inner cloud radii $\mathrm{R_{TF2}}$ and $\mathrm{R_{TF3}}$ have to be taken into account according to Fig. 4.1. We observe that the Thomas-Fermi value of the critical red/blue-detuned HGdT depth $\mathrm{U_c} \approx 3079$ is close to the numerical one $\mathrm{U_c} \approx 3090$. Figure 4.1 also shows the resulting outer and inner Thomas-Fermi radius as a function of the red/blue-detuned HGdT depth U. Here, the two inner radii behave symmetric, e.g., for $\mathrm{U} > 3079$ the $\mathrm{R_{TF2}}$ is increasing and $\mathrm{R_{TF3}}$ is decreasing correspondingly, however after $\mathrm{U} \gtrsim 4500$, they both become approximately constant as shown in Fig. 4.1. We also read off that $\mathrm{R_{TF1}} \approx \sqrt{2\mu}$ remains approximately constant for $\mathrm{U} > \mathrm{U_c}$, so we conclude that the chemical potential μ is then sealed to its critical value $\mu_c \approx 341.28$.

In the perspective of a quantitative comparison between the analytical and the numerical calculation, we characterize the red/blue-detuned HGdT induced imprint upon the condensate wave function by the following two quantities. The first one is the red/blue-detuned HGdT induced imprint height/depth

$$\mathrm{HD} = \begin{cases} \mathrm{Max}\left(\parallel \Psi(z) \parallel^2\right) - \parallel \Psi(0) \parallel^2 & \mathrm{U} \leq 0 \\ \\ \parallel \Psi(0) \parallel^2 - \mathrm{Min}\left(\parallel \Psi(z) \parallel^2_{z \to 0}\right) & \mathrm{U} > 0 \end{cases} \tag{4.11}$$

and the second one is the red/blue-detuned HGdT induced imprint width $\mathrm{W} = 2z_{\mathrm{Max}}$, where z_{Max} denotes the coordinate of maximal density. To find out a one-to-one resemblance between analytical and numerical calculation of HD and W, we determine the solution of the dimensionless 1DGPE (4.7) and compare it with the TF solution of Eq. (4.8), as shown in Fig. 4.3. The case $\mathrm{U} = 0$, i.e., when the HGdT potential is switched off, corresponds to a BEC in a quasi one-dimensional harmonic trap. Furthermore, in the range $\mathrm{U} < \mathrm{U_c}$ we observe that the red/blue-detuned HGdT induced imprint height/depth changes linearly with the optical dipole trap depth U according to

$$\mathrm{HD} \approx \frac{w^2|\mathrm{U}|e^{T(-e/2|\mathrm{U}|)-1}}{\mathrm{G_B}} \qquad \mathrm{U} \neq 0\,, w \neq 0\,, \tag{4.12}$$

where $T = xe^x$ abbreviates the productlog function. In case of $\mathrm{U} > \mathrm{U_c}$ the blue-detuned HGdT induced imprint depth yields the constant value $\mathrm{HD_c} \approx 0.0296$ due to Eq. (4.12), which slightly deviates from the corresponding numerical value $\mathrm{HD_c} = 0.027$. Similarly, the red/blue-detuned HGdT induced imprint width follows from $\mathrm{W} = 2w\sqrt{1 - T\left(-e/2|\mathrm{U}|\right)}$ according to the TF approximation, which reduces at the critical blue-detuned optical dipole depth to $\mathrm{W_c} \approx 3.60$ whereas the corresponding numerical value is $\mathrm{W_c} \approx 3.64$, as shown in Fig. 4.3.

4.3 Time-of-flight dynamics of red/blue-detuned Hermite-Gaussian dimple trap induced imprint

The time-of-flight (TOF) expansion has been used to measure various BEC properties. By suddenly turning off the magnetic trap, when the HGdT is still present, the atom cloud is allowed to expand in all directions. This expansion proceeds according to the momenta of the atoms at the initial time $t = 0$ and an additional tiny acceleration results from inter-particle interactions. The red-detuned HGdT induced two bumps remain approximately constant during the temporal evolution as shown in Fig. 4.4(a). But the blue-detuned HGdT induced two dips at the center of the condensate start decaying with a characteristic time scale after having switched off the trap as shown in Fig. 4.4(b). Furthermore, the dips of the HGdT induced imprint start decaying faster with increasing blue-detuned HGdT depth for smaller time as shown in Fig. 4.4(b). Note that the relative speed of the bumps or dips from each other turns out to vanish.

Furthermore, we investigate the possible occurrence of matter wave stripes at the top of the condensate during the evolution of the moderately/fully fragmented BEC cloud by plotting the density distribution of the released cloud during non-ballistic expansion as shown in Fig. 4.5. According to Fig. 4.5(a) we do not observe matter wave stripes for the red-detuned HGdT induced imprint, but Fig. 4.5(b-d) shows that they occur for the blue-detuned HGdT induced imprint. For small blue-detuned HGdT depth, the generation of matter wave stripes can be seen at a later time, as compared to higher blue-detuned HGdT depth, as shown in Fig. 4.5(b-d). The matter wave stripes are directly visible for $\mathrm{U} < \mathrm{U_c}$, as can be explained as follows. In Fig. 4.5(b), the height of the blue-detuned HGdT induced two dips is smaller as compared to Fig. 4.5(c), therefore they need more time to drill a hole in the condensate during TOF. For the HGdT potential depth U=1500, the BEC fragments into three parts at the dimensionless time $t = 2.4$, afterwards the three fragmented condensates start to interact as separate identities with the HGdT potential, which leads to the formation of characteristic matter wave stripes. The similar phenomenon happens in Fig. 4.5(c), but in this example the initial HGdT potential depth U=2500 is larger than the previous one in Fig. 4.5(b), so the BEC becomes fragmented at the earlier time $t = 1.3$. In the example of Fig. 4.5(d), when $\mathrm{U} > \mathrm{U_c}$, the BEC is already initially, i.e. at time $t = 0$, fragmented according to Fig. 4.1. Therefore the matter wave stripes can be seen just after $t > 0$, but the stripes are not as visible as in the two previous cases, although these stripes are quite visible in the BEC density plot Fig. 4.6 at time $t = 1.7$.

4.4 White shock-waves and gray/dark pair-solitons bi-trains

In this section, we show that matter-wave self-interferences emerge, once the red/blue-detuned HGdT potential is suddenly switched off, within the remaining harmonic confinement, as this leads to white shock-waves and gray/dark pair-solitons bi-trains, respectively as shown in Fig. 4.7(a-d). A shock-wave is a special kind of propagating disturbance in the BEC, whose amplitude, unlike for solitons, decreases relatively quickly with large distance. Furthermore, gray/dark solitons have a characteristic property that they can pass through one another without any change of shape, amplitude, or speed. We can see from Fig. 4.7(b-d) that the pair-solitons bi-trains do, indeed, pass through one another and that they are reflected from the end of the trapping potential.

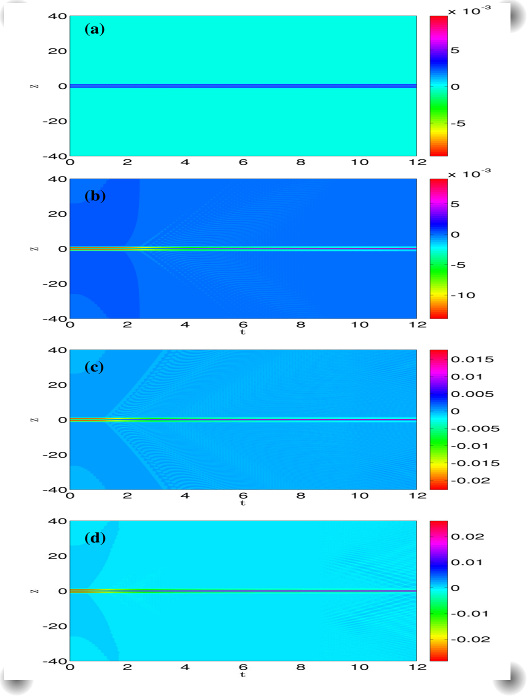

Figure 4.5: Time-of-flight evolution of depleted density $\| \psi(z,t) \|^2_{\mathrm{DD}} = \| \psi(z,t) \|^2_{\mathrm{U}} - \| \psi(z,t) \|^2_{\mathrm{U}=0}$ from solving the modified quasi 1DGPE equation for different values of $|\mathrm{U}|$: (a) $\mathrm{U} = -500$, (b) $\mathrm{U} = 1500$, (c) $\mathrm{U} = 2500$, and (d) $\mathrm{U} = 3500$.

Once the red/blue-detuned HGdT potential is switched off, the system quasi instantaneously adjusts its energy to the new equilibrium, paving the way for the creation of white shock-waves and bi-trains of gray/dark pair-solitons, respectively. The total normalized energy $\mathrm{E}(t) = \mathrm{E}(t)/\mathrm{Max}\{\mathrm{E}(t)\}$ as shown in Fig. 4.7(i-l) changes quite quickly from its initial value to a new equilibrium value, thus generating the white shock-waves or the pair-solitons bi-trains. For an initial red- and blue-detuned HGdT depth, we observe that

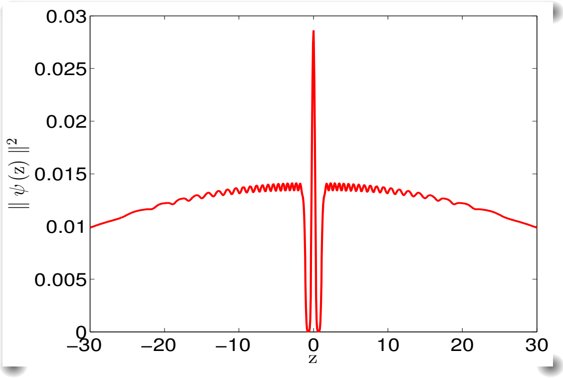

Figure 4.6: The BEC density during the time-of-flight at time $t = 1.7$ for U $= 3500$.

two excitations of the condensate are created at the position of the red/blue-detuned HGdT potential, which travel in the opposite direction with the same center-of-mass speed, are reflected back from the harmonic trap boundaries, and then collide at the red/blue-detuned HGdT potential position as shown in Fig. 4.7(a-d).

We have performed calculations for different red-detuned HGdT potential depths U < 0 and in all cases we observe the formation of the shock-wave structures as shown in Fig. 4.7(a). The density of atoms around the shocks is mostly enhanced in comparison with the density far away from these perturbations. And for the blue-detuned HGdT potential trap, we detect gray/dark pair-solitons bi-trains, traveling in opposite directions with the same speed as shown in Fig. 4.7(b-d). The creation of these calibrated gray/dark pair-solitonic bi-trains are generic collision phenomena of moderately/fully fragmented BEC, which is strongly depending upon the equilibrium values of the red/blue-detuned HGdT potential depth, respectively.

The dynamics of one soliton in a BEC cloud is well described by $\ddot{z} = (-1/2)\partial V_{\text{ext}}/\partial z$, where V_{ext} is the dimensionless confining potential and z denotes the position of the gray/dark soliton [104]. In the case of harmonic confinement with a potential $V_{\text{ext}} = z^2/2$ the solution of this evolution equation leads to an oscillation of the soliton described by $z(t) = \mathrm{R}_{\mathrm{TF1}} \sin\left(t/\sqrt{2}\right)$. Thus the frequency of the oscillating soliton and the frequency of the dipole oscillation of the Bose-Einstein condensate in the trap differ by the factor $\sqrt{2}$ [104]. In our system, pair-solitons bi-trains generally oscillate with the average frequency $\Omega = 2\pi \times 4.80$ Hz irrespective of the sign and the size of U as shown in Fig. 4.7. With this, we get the ratio $\Omega/\omega_z \approx 0.705$, which is quite close to the dimensionless soliton frequency $1/\sqrt{2} \approx 0.707$ in a harmonic trap as presented in Ref. [104]. Note that previously the generation of solitons was studied theoretically by investigating the collision of two condensates [127] and experimentally for different quasi one-dimensional trap geometries [97, 129]. Although in the latter experiments only one potential maximum occurs instead of two as in our work, so there single solitons and not pairs of solitons as here are observed, the basic physics is the same.

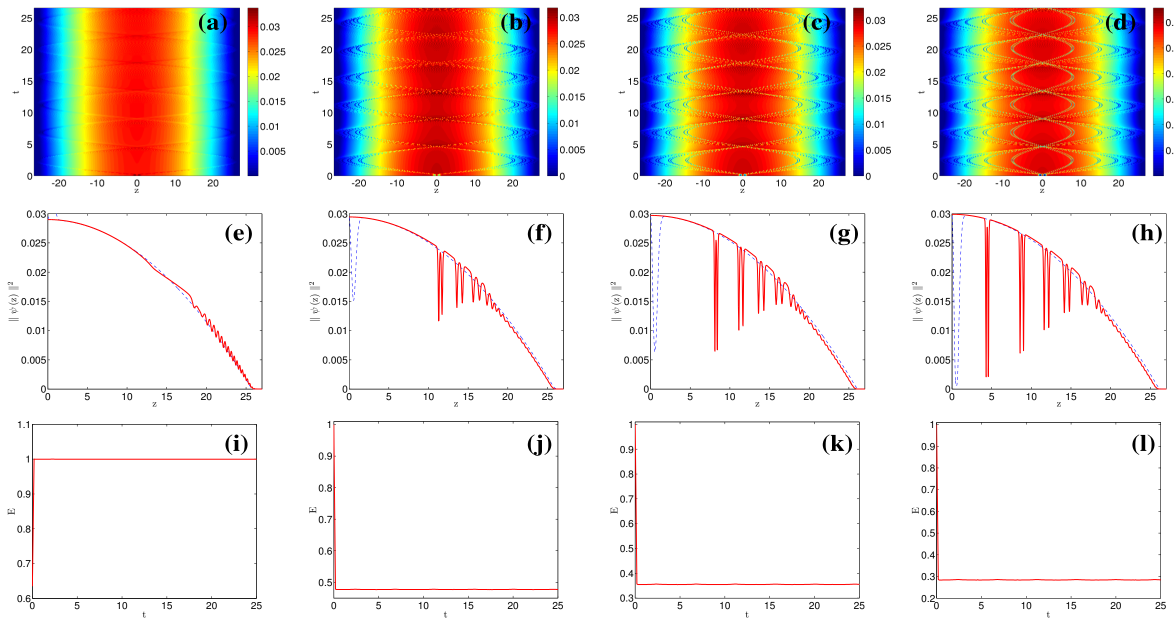

Figure 4.7: Coherent matter-waves evolution in the BEC density, when red/blue-detuned HGdT potential is switched off, versus time and position for different values of (a) $\mathrm{U} = -500$, (b) $\mathrm{U} = 1500$, (c) $\mathrm{U} = 2500$, and (d) $\mathrm{U} = 3500$. Graphs (e-h) show the BEC density at time $t = 5.3$, and in graphs (i-l) we plotted the corresponding dimensionless energies $\mathrm{E}(t) = \mathrm{E}(t) / \mathrm{Max}\{\mathrm{E}(t)\}$ versus dimensionless time for the HGdT depths U of the graphs (a-d).

We also observe an intriguing substructure of each soliton, which we call pair-soliton. Normally, we find that there are solitons which always move in pairs, and the mean distance between each other is less than the neighboring solitons as shown in Fig. 4.7(b-d) and Fig. 4.7(f-h). Numerically, we have observed that the averaged distance between pair-solitons is less for dark solitons as compared to the gray solitons as shown in Fig. 4.7(f-h). We also observe that, in general, a minimal time of about 4.6 ms is required to generate white shock-waves/pair-solitons bi-trains as shown in Fig. 4.7. The number of white shock-waves are not effected by the red-detuned HGdT potential depth, but the number of interference fringes increases. On the other hand, we observe that the number of gray/dark pair-solitons depends on the depth of the blue-detuned HGdT potential as shown in Fig. 4.8, the highest number of pair-solitons in every train is 7. For the blue-detuned HGdT depth $\mathrm{U} < \mathrm{U_c}$, the number of pair-solitons grows linearly in the condensate and after the critical value $\mathrm{U_c}$, the number of pair-solitons remains approximately constant.

Note that in case of the collision of two condensates in Ref. [127], it turned out that the number of observable solitons depends sensitively on the initial phase difference of both condensates. Thus, if the two condensates have an initial phase difference of $0(\pi)$, the number of solitons is even(odd). In our case, we have a single BEC fragmenting into three parts, which have the same phase, therefore we observe an even number of pair-solitons in the condensate

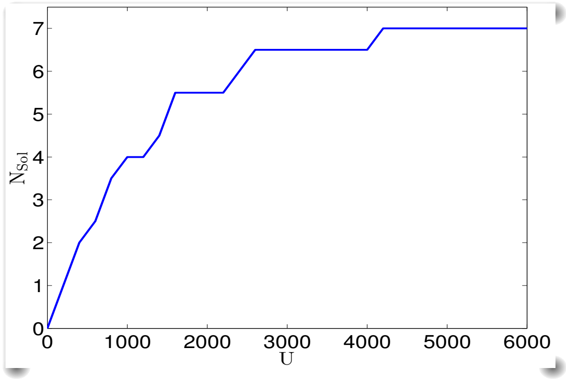

Figure 4.8: Number of pair-solitons N_{Sol} in each solitonic train versus HGdT potential depth U.

in agreement with Ref. [127]. Indeed, Fig. 4.8 shows the number of pair-solitons in each solitonic train, so the total number of pair-solitons in the whole condensate is twice as large. But, in Fig. 4.8 it turns out that the number of pair-solitons depends crucially on the depth of the red/blue-detuned HGdT potential. Furthermore, we remark by adjusting the position of the red/blue-detuned HGdT potential near to the outer Thomas-Fermi radius R_{TF1}, at the same time gray and dark pair-solitons can be generated in the BEC.

4.5 Summary and conclusion

We have developed a simple quasi 1D model both analytically and numerically to calculate the statics and dynamics of the red/blue-detuned HGdT imprint upon the ^{87}Rb condensate. First of all, we showed a quantitative comparison between the Thomas-Fermi approximation and numerical solutions for the underlying 1D Gross-Pitaevskii equation for the equilibrium properties of the proposed system. Later we discussed that the HGdT potential imprint upon the condensate wave function strongly depends upon whether the effective HGdT is red- or blue-detuned. With this we found out that the HGdT imprint generates two bumps/dips at the center of the BEC density of the red/blue-detuned HGdT. Later we discussed that the red-detuned HGdT induced two bumps did not decay when we switched off the harmonic trap but the blue-detuned HGdT induced two dips decay. During the time of flight, we saw the emergence of matter-wave interference stripes in the condensate, which arise as the BEC decomposes into a fraction at rest in the center and two moving condensates at the borders. We have used the quasi one-dimensional time-dependent GPE to analyze the creation of gray/dark pair-solitons bi-trains within the moderately/fully fragmented BEC, which is strongly depending upon the HGdT potential depth. The Hermite-Gaussian dimple trap geometry maybe more applicable to soliton interferometry rather than the Gaussian barrier adopted in Refs. [152, 209], because one can shape solitons. Additionally, we also showed that the number of pair-solitons in the system is depending on the initial HGdT potential depth U. During the generation of pair-solitons it was astonishing to find that the special shape of the newly generated solitons in the harmonically trapped BEC is sculptured by the external potential and the generation of gray/dark pair-solitons bi-trains is a generic phenomenon of collisions of moderately/fully fragmented BEC. With this we conclude that it maybe possible in the future to frame complex shapes of solitons in the harmonically trapped BEC by imposing a unique geometrical configuration for the external potential.

The ability of sculpting a quasi one-dimensional harmonic trapped Bose-Einstein condensate by a HGdT has many exciting prospects. For instance, it can be used to generate a truly continuous atom laser, which has many applications in atom interferometry [210, 211]. To construct such an atom laser one needs a device that continuously converts a source of condensed atoms into a laser-like beam. In Sec. 4.4, we saw in the time-of-flight picture for the case $U > U_c$ that a BEC reservoir occurs at the center of the trap. By suitably tuning the HGdT depth a fraction of this fragmented condensate could be coupled out, serving as a source for an atomic beam.

Chapter 5

Bose-Einstein condensate in gravito-optical surface trap

Motivated by the crucial relevance of gravito-optical surface traps (GOST) in atomic waveguides [212–214] and atomic chips [215–218], in this chapter we study the special case of a quasi one-dimensional Bose-Einstein condensate which is trapped orthogonal to the prism surface along the vertical axis as shown in Fig. 5.1. In our proposed model the downward pull of gravity is compensated by an exponentially decaying evanescent wave (EW), which can be thought of as a mirror as it repels the atoms upward against gravity as shown in Fig. 5.2. In order to deal with the hard-wall boundary condition, we apply the mirror solution analogy to the BEC context, and obtain analytical results, which agree with those from numerically solving the underlying one-dimensional Gross-Pitaevskii equation (1DGPE). Later on, as an interesting application, we compare our numerical simulation results for a time-of-flight dynamics with the Innsbruck experiment for a quasi-2D BEC in a GOST [82]. Surprisingly, our proposed quasi one-dimensional model agrees even quantitatively with the Innsbruck experiment. Although this Innsbruck experiment uses a 2D pancake shaped BEC,

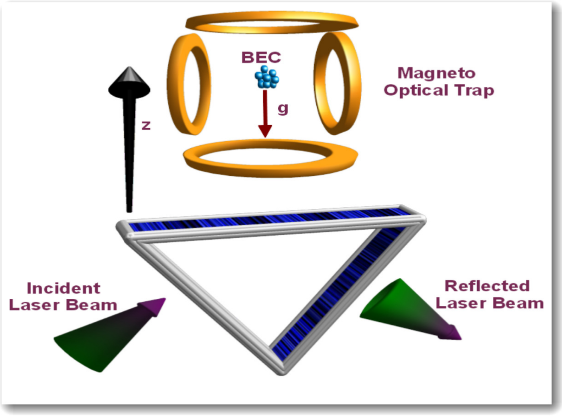

Figure 5.1: The systematic diagram of the GOST experiment.

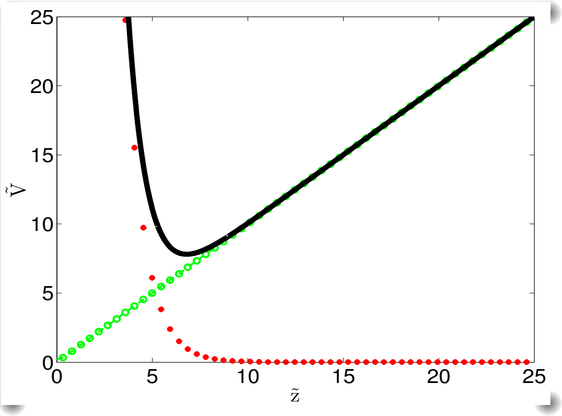

Figure 5.2: Anharmonic GOST potential (solid line) from Eq. (5.2) in dimensionless units, which are explained at the end of the Sec. 5.1. It consists of a superposition of an exponentially decaying optical potential (red circles) due to an evanescent light field above a mirror and a linear gravitational potential (green circles). When the atoms are cold enough, they stay in the vicinity of the potential minimum.

when performing the time-of-flight expansion vertically the transversely confining beam is kept constant, so our quasi-1D model for a BEC should apply in this case. The underlying fundamental model for such a quasi-1D BEC is reviewed in Sec. 5.1. Further, we provide estimates for experimentally realistic parameters, which we use in our quantitative analysis. Afterwards, we work out approximate solutions for the 1DGPE wave function in the ground state of the system. To this end, Sec. 5.2 performs a modified Gaussian variational ansatz for weak interactions, which corresponds to a small number of atoms. For a larger number of atoms, the interaction strength becomes so strong that the Thomas-Fermi solution turns out to be valid, as described in Sec. 5.3. Then, in Sec. 5.4, we outline our numerical method and compare numerical results with the previous analytical solutions. In Sec. 5.5, we deal with the time-of-flight expansion of the BEC when the EW is removed, showing quantitative agreement with previous experimental results. In Sec. 5.6 we discuss further dynamical properties of the BEC in a GOST after switching off the evanescent laser field in the presence of the hard-wall mirror. Lastly, we summarize our findings and end with brief concluding remarks.

5.1 Model

For our 1D model of the BEC in a GOST, we assume that we have a dilute Bose gas and that the radial frequency is much larger than the axial frequency, i.e. the BEC is cigar-shaped. With this assumption, we arrive at the 1DGPE [219, 220]

$$i\hbar\frac{\partial}{\partial t}\psi(z,t)=\left\{-\frac{\hbar^2}{2m_\mathrm{B}}\frac{\partial^2}{\partial z^2}+V(z)+\mathrm{G_B}|\psi(z,t)|^2\right\}\psi(z,t). \qquad (5.1)$$

On the right-hand side of the equation, the first term represents the kinetic energy of the atoms with mass m_{B}, while the last term describes the two-particle interaction, where its strength $\mathrm{G_B} = 2N_{\mathrm{B}}a_{\mathrm{B}}\hbar\omega_r$ is related to the s-wave scattering length a_{B} according to (2.114), and the particle number N_{B}, whereas ω_r denotes the radial trapping frequency. The anharmonic potential energy $V(z)$ in Eq. (5.1) is produced by both gravity and the exponentially decaying evanescent wave as shown in Fig. 5.2 [221]:

$$V(z) = V_0 e^{-\kappa z} + m_{\mathrm{B}} g z. \tag{5.2}$$

Here, g is the gravitational acceleration and the constant $V_0 = \Gamma\lambda_0^3 I_0/(8\pi^2 c\delta_3)$ [1] denotes the strength of the evanescent field, where Γ is the natural linewidth of ^{133}Cs atoms, $\lambda_0 =$ 852 nm is the wavelength of the optical transition, I_0 stands for the peak intensity of the EW, and δ_3 corresponds to the detuning frequency of the hyperfine sub-level $F = 3$ of the ^{133}Cs atom [79, 80, 82]. Furthermore, according to Eq. (2.37) the decay length is denoted by $1/\kappa = \Lambda/2 = \lambda/4\pi\sqrt{n^2\sin^2\theta - 1}$, where λ is the wavelength of the EW, n stands for the refractive index of the medium and θ is the angle of incidence. The potential Eq. (5.2) has a minimum at $z_0^{\mathrm{min}} = (1/\kappa)\ln(V_0\kappa/m_{\mathrm{B}}\mathrm{g})$ with the axial frequency $\omega_z = \sqrt{\mathrm{g}\kappa}$. Note that this potential yields a hard-wall condition with $V(z \leq 0) = \infty$, because the atoms cannot penetrate the prism, as it is a macroscopic object.

In order to have a concrete set-up in mind for our analysis, we adapt parameter values from the GOST experiments [79, 82]. For the EW, we consider the inverse decay length to be $\kappa = 2/\Lambda = 1.43 \times 10^6\ \mathrm{m}^{-1}$, i.e. $\Lambda \approx 1.4\,\mu$m. Additionally, we assume an axial frequency of $\omega_z \approx 2\pi \times 600$ Hz. For our atoms in the $F = 3$ state, the strength of the EW is given by $V_0 \approx 100 \times k_B\ \mu$K, where k_B is the Boltzmann constant. This potential value is within an order of magnitude of the Innsbruck experiments [79, 82]. In view of the quasi-1D model, we must satisfy the condition $\omega_{\mathrm{z}} \ll \omega_{\mathrm{r}}$, so we assume $\omega_r = 2\pi \times 3$ kHz, which corresponds to the radial oscillator length $l_{\mathrm{r}} = 0.158\ \mu$m. The experiment uses a magnetic field for Feshbach resonance, such that the s-wave scattering length amounts to $a_{\mathrm{B}} = 440\ \mathrm{a}_0$ with the Bohr radius a_0. As both $\omega_{\mathrm{z}} \ll \omega_{\mathrm{r}}$ and $l_{\mathrm{r}} > a_{\mathrm{B}}$ are fulfilled, we have, indeed, a quasi one-dimensional setting.

In order to explain that we are in the regime where the mean-field theory is valid, we argue as follows. Firstly, in order to distinguish between the weakly interacting quasi-1D and the strongly interacting Tonks-Girardeau regime, Petrov et al. [114] introduced a dimensionless quantity $\alpha = (2a_{\mathrm{B}}l_{\mathrm{z}})/l_{\mathrm{r}}^2$ as discussed in Eq. (2.118). By using above mentioned experimental parameters, we get the dimensionless quantity $\alpha = 0.65$, therefore according to Fig. 2.7 we are far in the weakly interacting regime, where the Gross-Pitaevskii mean-field theory is applicable. Secondly, the ratio of the quantum depleted atoms with respect to the

---

[1] We rewrite Eq. (2.18) with using $c = \lambda_{\mathrm{A}} f_{\mathrm{A}}$, i.e. $U_{\mathrm{dip}} = \frac{3\Gamma c^2}{16\pi^2 f_{\mathrm{A}}^3 \Delta} I(z) = \frac{3\Gamma\lambda_{\mathrm{A}}^3}{16\pi^2 c\Delta} I(z)$, and $I(z) = I_0 e^{-\kappa z}$.

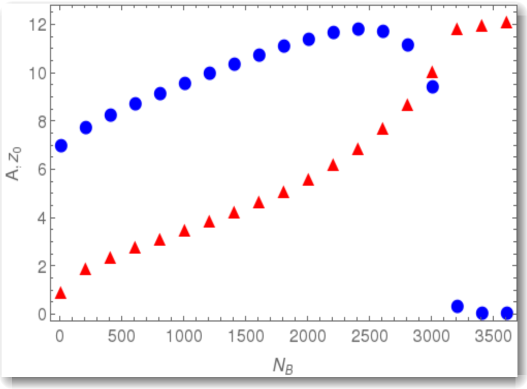

Figure 5.3: Width A (triangles) and mean position z_0 (circles) as a function of the number of atoms N_B. Note that the mean position gives meaningless values for $N_\mathrm{B} > 3000$. Thus, the variational ansatz is only successful for quite a small number of particles.

number of particles can be calculated according to Eq. (B.10)

$$\frac{N_\mathrm{QF}^\mathrm{1D}}{N_\mathrm{B}} = \frac{3^{1/3}}{4}\left(a_\mathrm{B}^4 N_\mathrm{B} \Xi^2\right)^{1/3} = 0.0002. \tag{5.3}$$

Here $\Xi = l_z/l_r$ is the ratio of the axial and the longitudinal harmonic oscillator lengths and we consider $N_\mathrm{B} = 10^4$ as a special case. Thus equation (5.3) shows that quantum fluctuations are negligible for our proposed model.

When the atoms are close to the dielectric surface of the prism, we would have to add an additional potential contribution due to the van-der-Waals interaction. Here we have to distinguish two special cases depending on the distance of the BEC from the surface. The regime, where the BEC is close to the dielectric surface, i.e. $z \ll \lambda/2\pi$, is called the Lennard-Jones regime [168, 169]. In the case where the BEC is far away from the surface, i.e. $z \gg \lambda/2\pi$, the regime is called Casimir-Polder regime. In the latter case the Casimir-Polder potential can be described within a two-level approximation of the Cesium atoms according to $V_\mathrm{CP} = -C_4/z^4$, where the Casimir-Polder coefficient is $C_4 = 1.78 \times 10^{-55}\mathrm{Jm}^4$ [166, 170, 222]. As the BEC does not penetrate very far into the repulsive EW, it is hardly influenced by the van-der-Waals potential, which follows from the above values of the GOST experiment. Indeed, for the wavelength $\lambda = 839$ nm [82] and the distance being estimated by the minimal distance of the BEC from the surface $z_0^\mathrm{min} = 4.761$ μm, we are in the Casimir-Polder regime. Thus, the value of the Casimir-Polder potential is of the order $V_\mathrm{CP} = 24.9 \times$ $\mathrm{k_B}$ pK, which is negligible in comparison with the EW potential $V_0 \approx 100 \times k_B$ μK.

In view of the forthcoming discussion we use dimensionless parameters as follows. First we introduce the dimensionless spatial coordinate $\tilde{z} = \kappa z$. Further, we multiply all terms in

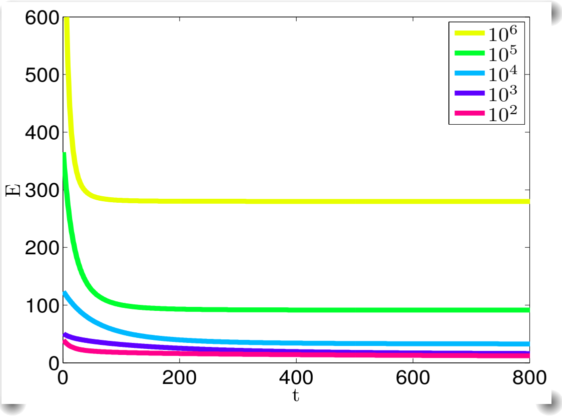

Figure 5.4: Energy of the BEC as a function of imaginary time for a decreasing number of particles from the top to the bottom.

Eq. (5.1) by $\kappa/(m_\mathrm{B}g)$, yielding the dimensionless GPE,

$$i\frac{\partial}{\partial\tilde{t}}\tilde{\psi}(\tilde{z},\tilde{t}) = \left\{-\frac{\tilde{k}}{2}\frac{\partial^2}{\partial\tilde{z}^2} + \tilde{z} + \tilde{V}_0 e^{-\tilde{z}} + \tilde{G}_\mathrm{B}|\tilde{\psi}(\tilde{z},\tilde{t})|^2\right\}\tilde{\psi}(\tilde{z},\tilde{t}), \tag{5.4}$$

where the dimensionless kinetic energy constant reads $\tilde{k} = (\hbar^2\kappa^3)/(gm_\mathrm{B}^2)$, the dimensionless time $\tilde{t} = t(m_\mathrm{B}g)/(\hbar\kappa)$ and the two-particle dimensionless interaction strength $\tilde{G}_\mathrm{B} = 2N_\mathrm{B}\tilde{\omega}_r\tilde{a}_\mathrm{B}$ with $\tilde{a}_\mathrm{B} = a_\mathrm{B}\kappa$ being a dimensionless s-wave scattering length. Additionally, we measure energies in units of the gravitational energy $m_\mathrm{B}g/\kappa$ and get $\tilde{\omega}_z = \hbar\kappa\omega_z/gm_\mathrm{B}$ as a dimensionless frequency, and $\tilde{V}_0 = \kappa V_0/gm_\mathrm{B}$ as a dimensionless strength of the evanescent field.

According to these chosen parameters, the dimensionless quantities have the following values. The dimensionless strength of the EW is $\tilde{V}_0 = 905.7$, the dimensionless kinetic energy amounts to $\tilde{k} = 0.066$, the dimensionless s-wave scattering length is given by $\tilde{a}_\mathrm{B} = 0.033$, the dimensionless radial frequency yields $\tilde{\omega}_r = 1.303$, and, finally, the resulting dimensionless two-particle interaction strength is $\tilde{G}_\mathrm{B} = 0.086N_\mathrm{B}$. From here on, we will drop the tildes for simplicity.

5.2 Variational solution

For the number of particles $N_\mathrm{B} < 3000$, the effective interaction strength is quite small. In this limit the BEC has only a reduced extension, so the anharmonic confinement $V(z)$ approximately corresponds to a harmonic potential well around its minimum $z_0^\mathrm{min} \approx 6.809$. Therefore, it is reasonable to propose a Gaussian-like ansatz for the wave function in the static case. In order to meet the hard-wall condition, however, we modify the Gaussian

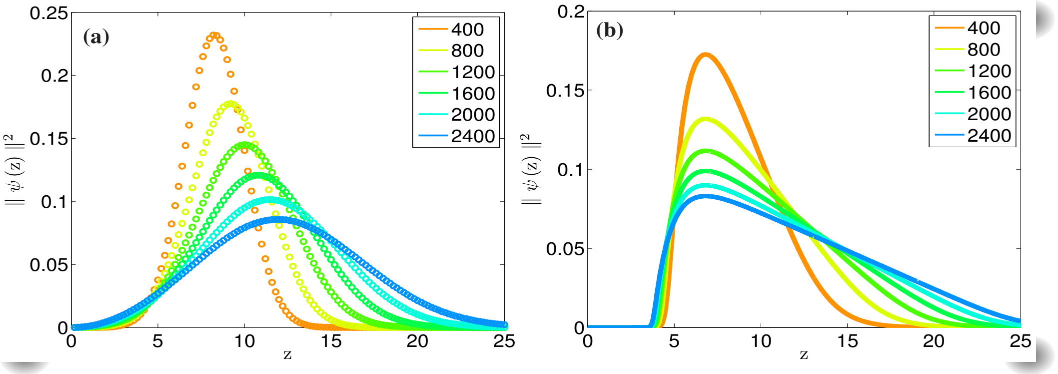

Figure 5.5: Probability density plots from (a) Gaussian ansatz (5.6) and (b) numerical calculations for an increasing number of atoms from the top to the bottom.

function such that it has the form of a so-called mirror solution [223, 224],

$$\psi(z) \propto \exp\left[\frac{-(z-z_0)^2}{2A^2}\right] - \exp\left[\frac{-(z+z_0)^2}{2A^2}\right], \tag{5.5}$$

where z_0 is the mean position and A represents the width. In this way it is guaranteed that the wave function meets the hard-wall boundary condition $\psi(0) = 0$. In order to find the variational parameters z_0 and A, we minimize the energy of this ansatz following the idea of Perez et al. [178, 225]. In order to get the simple expression for the corresponding energy, we introduce the parameter $\gamma = z_0/A$ and normalize the wave function (5.5) to obtain

$$\psi(z) = \frac{\exp\left(-\frac{z^2}{2A^2}\right) \operatorname{Sinh}\left(\frac{\gamma z}{A}\right)}{\sqrt{\frac{A}{4}\sqrt{\pi}[\exp(\gamma^2) - 1]}}. \tag{5.6}$$

From this ansatz, we obtain the Gross-Pitaevskii energy

$$\begin{aligned} E &= \frac{V_0\{e^{\frac{1}{4}(A-2\gamma)^2}\left[\operatorname{Erfc}\left(\frac{A}{2}-\gamma\right)+e^{2A\gamma}\operatorname{Erfc}\left(\frac{A}{2}+\gamma\right)\right]-2e^{\frac{A^2}{4}}\operatorname{Erfc}\left(\frac{A}{2}\right)\}}{2\left(e^{\gamma^2}-1\right)} + \frac{2Ae^{\gamma^2}\gamma\operatorname{Erf}(\gamma)}{2\left(e^{\gamma^2}-1\right)} \\ &\quad + \frac{\left(2\gamma^2+e^{\gamma^2}-1\right)k}{4A^2\left(e^{\gamma^2}-1\right)} + \frac{\mathrm{G_B}}{2\sqrt{2\pi}A}\left[2\left(e^{\frac{\gamma^2}{2}}+1\right)^{-2}+1\right]. \end{aligned} \tag{5.7}$$

where $\operatorname{Erf}(y) = \frac{2}{\sqrt{\pi}}\int_0^y e^{-x^2}dx = 1 - \operatorname{Erfc}(y)$ denotes the error function. Although, this expression cannot be minimized analytically, we can use numerical techniques to extremize it with respect to the parameters γ and A based on the values of k, $\mathrm{G_B}$, and V_0 given in Sec. 5.1. We can see from Fig. 5.3 that our variational approach turns out to be valid only for quite small number of atoms. Indeed, the extremization process fails when the condensate has more than around 3000 atoms, as then the mean position becomes zero as shown in Fig. 5.3. Note that BEC experiments with such small particle numbers are possible, see for instance

Refs. [226, 227].

5.3 Thomas-Fermi solution

For a large enough number of atoms, the effective interaction term and the potential term are much larger than the kinetic term. In such a case, an approximate Thomas-Fermi (TF) solution is found by neglecting the much smaller kinetic term. Thus, the time-independent GP reduces to

$$\mu \approx z + V_0 e^{-z} + \mathrm{G_B} |\psi(z)|^2. \tag{5.8}$$

In order to determine the chemical potential, we use the normalization condition, which reads in the dimensionless scheme as $\int |\psi|^2 dz = 1$. Thus, we get

$$1 = \frac{\mu}{\mathrm{G_B}} \int_{z_1}^{z_2} \left(1 - \frac{z}{\mu} - \frac{V_0}{\mu} e^{-z} \right) dz, \tag{5.9}$$

where z_1 and z_2 denote the zeros of the integrand. For larger z the decaying exponential vanishes, and so we have $z_2 \approx \mu$. Examining the smaller root, we see that for small values of z and moderate values of μ, z/μ is quite small, thus a reasonable approximation for this root is $z_1 \approx \log(V_0/\mu)$. This motivates us to divide the TF solution into two parts: first, the soft-wall TF solution, where $V_0 > \mu$, so that z_1 is larger than zero. Second, the hard-wall TF solution in the case $V_0 < \mu$, where the lower integration limit z_1 would be less than zero, so the soft-wall TF wave function would fail. The latter case necessitates to use the mirror principle in order to guarantee the hard-wall boundary condition.

5.3.1 Soft-wall mirror solution

With the integration boundaries $z_1 \approx \log(V_0/\mu)$ and $z_2 \approx \mu$ known to be a good approximation, we carry out the integration in Eq. (5.9), yielding

$$2\mathrm{G_B} \approx \mu^2 \left\{ 1 - \frac{2}{\mu} \left[\log\left(\frac{V_0}{\mu} \right) + 1 \right] \right\}, \tag{5.10}$$

where we have neglected the small terms $(V_0/\mu)e^{-\mu}$ and $\log(V_0/\mu)^2/(2\mu)$. Thus, to leading order, we have $\mu \approx \sqrt{2\mathrm{G_B}}$ with a subsequent logarithmic correction. For small changes of the chemical potential, the natural log term in Eq. (5.10) does not change significantly. Therefore in Eq. (5.10) we can substitute $\sqrt{2\mathrm{G_B}}$ for μ in the natural log. Solving the resulting quadratic equation and neglecting small terms in the square root, we obtain the improved approximation

$$\mu \approx \sqrt{2\mathrm{G_B}} + 1 + \log\left(V_0 / \sqrt{2\mathrm{G_B}} \right). \tag{5.11}$$

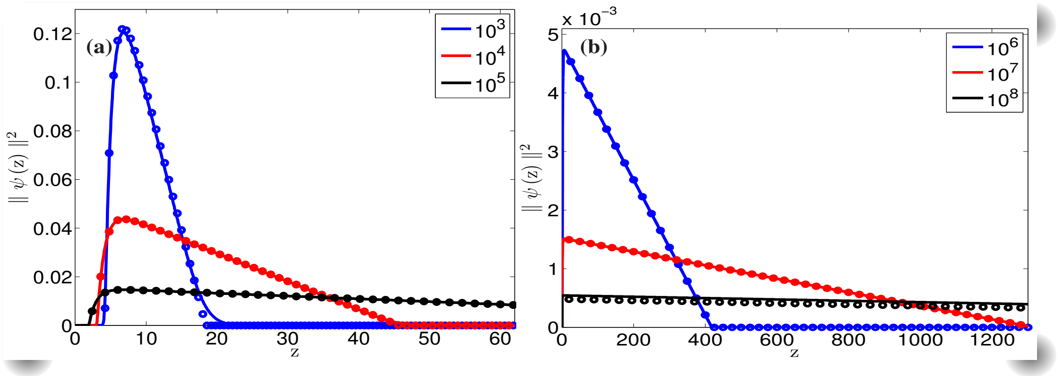

Figure 5.6: Comparison of numerical results from GPE (solid lines) with TF approximation (circles), (a) $N_\mathrm{B} = 10^3$, $N_\mathrm{B} = 10^4$, and $N_\mathrm{B} = 10^5$. (b) $N_\mathrm{B} = 10^6$, $N_\mathrm{B} = 10^7$, and $N_\mathrm{B} = 10^8$ from top to bottom, respectively.

Thus, assuming that $V_0 > \sqrt{2\mathrm{G_B}}$, we obtain the following soft-wall TF solution for $z_1 < z < z_2$.

$$\psi(z) = \sqrt{\frac{\mu}{\mathrm{G_B}}\left(1 - \frac{z}{\mu} - \frac{V_0}{\mu}e^{-z}\right)}, \tag{5.12}$$

where μ is given by Eq. (5.11). The function is set to zero for $z < z_1 \approx \log(V_0/\sqrt{2G})$ and $z > z_2 \approx \mu$, because the probability density cannot be less than zero.

5.3.2 Hard-wall mirror solution

For particle numbers $N_\mathrm{B} > 2.35 \times 10^5$ the soft-wall TF solution is not valid anymore as $z_1 \approx \log(V_0/\sqrt{2\mathrm{G_B}})$ becomes negative. In order to extend this approximate solution to the case where $V_0 < \mu$, we must work out the corresponding hard-wall TF solution. With the help of the mirror analogy [223, 224], we obtain the approximate TF wave function

$$\psi(z) = \begin{cases} \sqrt{\frac{1}{M}}\left[\sqrt{\left(\frac{\mu}{\mathrm{G_B}}\right)\left(1 - \frac{z}{\mu} - \frac{V_0}{\mu}e^{-z}\right)} - \sqrt{\left(\frac{\mu}{\mathrm{G_B}}\right)\left(1 + \frac{z}{\mu} - \frac{V_0}{\mu}e^{+z}\right)}\,\right] & \text{for } 0 < z < |z_1| \\ \sqrt{\frac{1}{M}\left(\frac{\mu}{\mathrm{G_B}}\right)\left(1 - \frac{z}{\mu} - \frac{V_0}{\mu}e^{-z}\right)} & \text{for } |z_1| < z < z_2. \end{cases} \tag{5.13}$$

Here, M denotes the normalization constant which is determined from $\int |\psi|^2 dz = 1$. Note that an analytical derivation of M is not possible, therefore, we performed the respective integration numerically.

5.4 Numerical method and results

In order to demonstrate the validity of the proposed analytical results, we numerically find the ground state of the wave function by propagating the GPE in imaginary time, with the

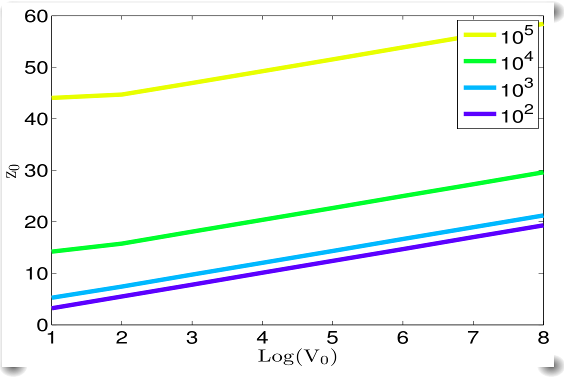

Figure 5.7: Mean position of the BEC versus EW strength V_0 for decreasing number of atoms from the top to the bottom.

help of the split operator technique as describe in Appendix A. For the above mentioned experimental parameters and with the value of N_{B} ranging from 10^2 to 10^8 atoms, the ground-state energy of the BEC in a GOST does, indeed, quickly converge as shown in Fig. 5.4.

With this technique in mind, we compare our analytical results from Sec. 5.2 and 5.3 to numerical results and show how the BEC wave function in a GOST changes with increasing the number of atoms. For a smaller number of atoms, the variational Gaussian ansatz is more suitable as shown in Fig. 5.5, whereas for a larger number of atoms the Thomas-Fermi approximation turns out to be quite accurate as shown in Fig. 5.6. The variational Gaussian ansatz roughly reproduces the mean, but it is rather symmetrical, unlike the numerical results as the number of atoms approach 2400, see Fig. 5.5. Qualitatively, the BEC width is proportional to the number of atoms in a GOST. However, due to the EW decaying exponential potential, the BEC cannot expand in the negative z-direction, so the BEC wave function takes up a triangular shape for N_{B} larger than 10^3 as shown in Fig. 5.6. The agreement between numerical and analytical TF results is much better for larger number of atoms. Note that the BEC wave function is quite wide for 10^8 atoms in Fig. 5.6.

The van-der-Waal forces with the surface can demolish the BEC, so it is necessary to have a larger EW potential. Therefore, keeping in mind recent developments in the laser field technology, it is possible to increase the EW strength V_0 by increasing the laser power [46]. Thus, we explore now the parameter space of our model. Irrespective of the number of atoms, the mean position of the BEC in GOST increases only moderately with V_0. For the soft-wall case $V_0 > \mu$ as shown in Fig. 5.7, the maximum of the wave function occurs at $\log(V_0)$, but for the hard-wall case $V_0 < \mu$ the maximum of the BEC wave function exists at $\left|\log(V_0/\sqrt{2G_{\mathrm{B}}})\right|$. Thus, due to the interaction term, for a large number of atoms, the maximum of the wave function no longer remains within the minimum of the trapping potential $z_0^{\min} \approx \log(V_0)$.

The BEC wave function in a GOST becomes asymmetric for larger interaction strengths. Therefore we quantify the BEC width based on the standard deviation $\sigma = \sqrt{< z^2 > - < z >^2}$, where $< \bullet >= \int \bullet |\psi(z)|^2 dz$ denotes the expectation value. As shown in Fig. 5.8, the BEC

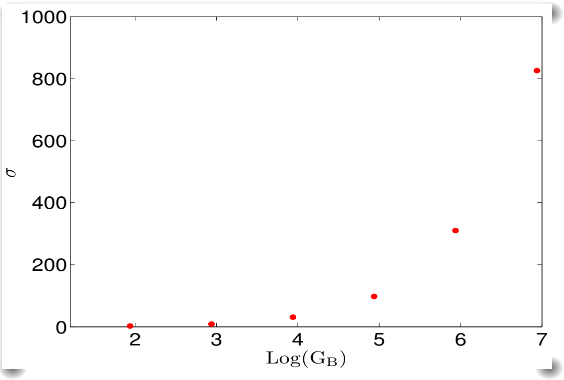

Figure 5.8: Standard deviation σ of BEC wave function increases with inter-particle interaction strength $\mathrm{G_B}$ for EW strength $V_0 = 906$.

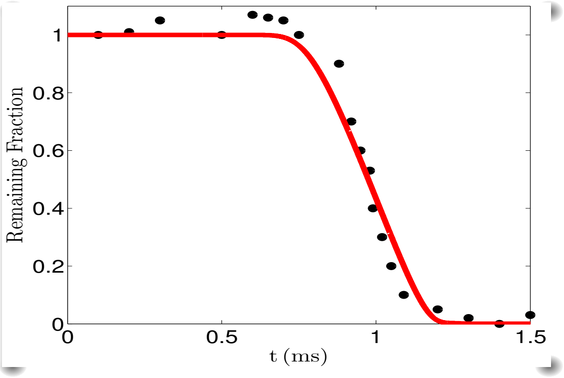

Figure 5.9: Fraction of remaining atoms in time-of-flight during a vertical expansion for $V_0 = 453$. Initially, total number of atoms is $N_\mathrm{B} = 2400$. Here the circles stem from the Innsbruck experimental [82], whereas the solid line shows our numerical results.

standard deviation grows extremely rapidly with increasing number of atoms N_B. However, on the other hand, changing V_0 only slightly affects the standard deviation σ.

5.5 Time-of-flight expansion

The standard observation of a BEC is based on suddenly turning off the trapping potential and allowing the atoms to expand non-ballistically. The resulting time-of-flight (TOF) measurements are performed either by acquiring the absorption signal of the probe laser beam through the falling and expanding BEC cloud, or by measuring the fluorescence of the atoms which are excited by a resonant probe light [85].

In the Innsbruck experiment, the remaining number of atoms is measured after allowing atoms from the GOST to expand vertically by suddenly turning off the EW [82]. Note that some particles are lost due to thermalization processes which occur when the particles hit the prism or due to the van-der-Waal forces with the surface. Although this Innsbruck experiment uses a 2D pancake shaped BEC, when performing this vertical expansion the

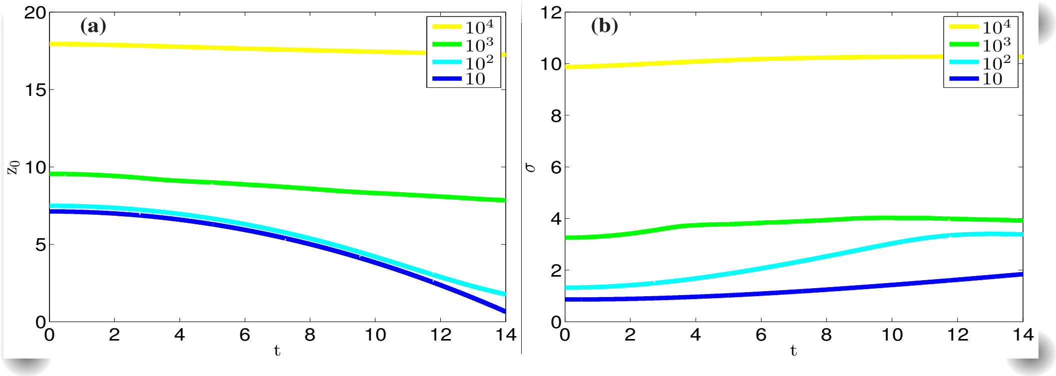

Figure 5.10: (a) Mean position z_0 and (b) standard deviation σ of BEC density in the time-of-flight expansion for decreasing number of atoms from the top to the bottom for $V_0 = 906$.

transversally confining beam is kept constant, so our quasi-1D model for BEC should apply in this case. Using the experimental parameters in Ref. [82], we numerically reproduce their vertical expansion curve (their Figure 2), as shown in Fig. 5.9 [2]. To this end, we use $N_{\mathrm{B}} = 2400$ atoms and $V_0 = 453$, yielding an initial condensate wave function with dimensionless standard deviation $\sigma = 0.86$ and the dimensionless mean position $z_0 = 6.40$. We propagate this wave function without the hard-wall boundary condition. Then we approximate the fraction of remaining atoms by $\int_0^\infty |\psi(z,t)|^2 dz$, as atoms in the BEC wave function extending past $z = 0$ are lost by sticking to the surface. While the interaction term is quite small in the Innsbruck experiment, the standard deviation of the BEC is small and remains roughly constant during the time-of-flight, so the loss of atoms does not affect time-of-flight expansion significantly for $t < 0.7$ ms as shown in Fig. 5.9.

We also simulated the TOF expansion without the prism at $z = 0$ for different particle numbers N_{B}. We see that the mean position of the BEC drops due to gravity as shown in Fig. 5.10 with different rates, which strongly depend upon the number of confined atoms. At the same time the BEC width, which is proportional to the standard deviation, increases according to Fig. 5.10.

5.6 Dynamics of BEC on hard-wall mirror

Concerning the dynamics of the BEC in a GOST, we consider two cases. First we describe the dynamics of the BEC with $N_{\mathrm{B}} = 2 \times 10^4$ after switching off the evanescent potential and letting the BEC atoms fall on a hard-wall mirror. The latter could be experimentally realized by a blue-detuned far-off-resonant sheet of light, and is modeled theoretically via the boundary condition $V(0) \to \infty$ at $t > 0$. Thus, the BEC of $N_{\mathrm{B}} = 1800$ atoms has the

---

[2] Here, we used the experimental value of the transversal frequency $\omega_{\mathrm{r}} = 10$ Hz from Ref. [82] to get the two-particle interaction strength and the dimensionless time $\tilde{t} = t(m_{\mathrm{B}}g)/(\hbar\kappa)$.

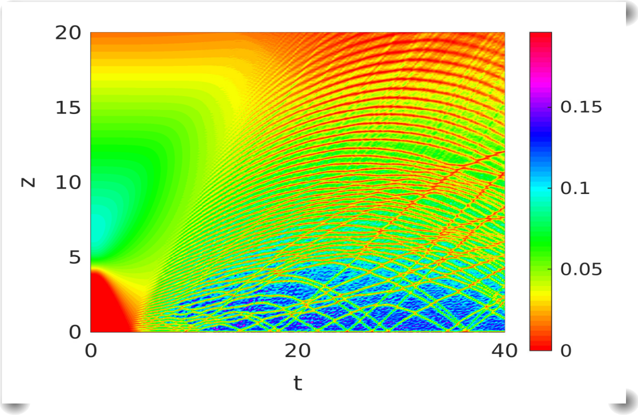

Figure 5.11: Dynamics of BEC in presence of gravity with hard wall at $z = 0$ for $N_{\mathrm{B}} = 1800$ number of atoms. Here the color scale represents the density of the BEC.

dimensionless mean position $z_0 = 10.7$ and the dimensionless standard deviation $\sigma = 4.28$ at time $t = 0$. We observe the matter-wave interference pattern formed upon releasing the condensate from GOST as shown in Fig. 5.11, as atoms impinging on the 'hard-wall' at the origin 'bounce' back. For short times the atoms remain near the hard-wall surface, so the BEC dynamics is characterized by the reflection of atoms from the hard-wall mirror. But for larger times those atoms, which are far away from the hard-wall mirror, are reflected above the hard-wall mirror due to collisions among themselves as depicted in Fig. 5.11. The number of atoms $N_{\mathrm{B}} = 1800$ is so large that the BEC is staying quite close to the mirror, so we have not seen any total reflection of the BEC wave packet.

In order to see the latter scenario, we need a small number of $N_{\mathrm{B}} = 30$ particles far away from the hard-wall mirror. This is realized by the EW potential $V_0 e^{-(z-20)}$, which could be implemented by trapping atoms in a MOT above the surface, so that, once the EW trap is switched off, the atoms have enough momenta when they hit the hard-wall mirror as shown in Fig. 5.12. Similar to experiments of photonic bouncing balls [228] and plasmonic paddle balls [229], the BEC shows significant self-interference patterns, for example in the time intervals t =24-34 and 83-91 as analyzed in Fig. 5.12, which originate from the interference of incoming and reflecting BEC wave packets. It is worth mentioning that a smaller initial width of the BEC wave packet would lead to finer revivals and a larger initial width of the BEC would lead to larger interference regions as depicted in Fig. 5.13. The evolution of a BEC falling under gravity and bouncing off a hard-wall mirror formed by a far-detuned sheet of light was already observed experimentally by Bongs et al. in both the soft-wall and the hard-wall regime [230]. In the soft-wall regime, they have recorded that the BEC is reflected up to three times off the optical mirror in the lossy environment. Due to a large two-particle coupling strength, which in turn results in a condensate with a larger width, this group also observed a splitting of the BEC into two parts close to the upper turning point of the BEC. This effect is heuristically modeled by a GPE dynamics with assuming that the

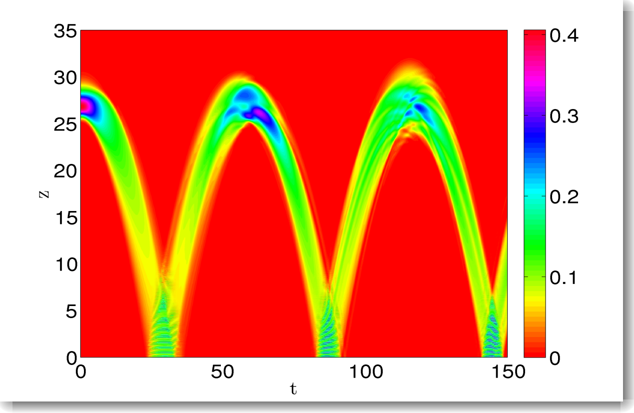

Figure 5.12: Numerical results for the BEC density $|\psi(z,t)|^2$ with initial dimensionless mean position $z_0 = 27.2$ and dimensionless standard deviation $\sigma = 0.99$ for $N_\mathrm{B} = 30$ number of atoms. BEC experiences full periodic revivals, however incoming and reflecting BEC wave packets lead to larger matter-wave interference regions at time intervals t =24-34 and 83-91. Here the color scale represents the density of the BEC.

two-particle interaction strength decreases exponentially in time in Ref. [230]. In our case we restricted ourselves to the evolution of the BEC with a constant coupling constant, so we did not observe any splitting of the BEC in our simulation, but we do observe the BEC for longer time intervals in Fig. 5.12. In our simulation, we observed more than three reflections of the atomic cloud in a lossless environment. The center-of-mass of the BEC wave packet shows periodic revivals at dimensionless time $t_\mathrm{RT} \approx 58.2$ as depicted in Fig. 5.12. Quantitatively, the classical particle revival time can be measured in dimensionless time as $t_\mathrm{RT} = 2t = 2\sqrt{2z_0/k} = 56.9$ [3].

In Fig. 5.13, we investigate complex dynamic patterns of the BEC after having switched off the evanescent potential and letting the BEC atoms fall on a hard-wall mirror for different number of particles. For $N_\mathrm{B} = 500$, in Fig. 5.13(a), BEC atoms which are located nearby to the hard-wall mirror, can collide with the mirror and bounce back for a time lesser than $t < 20$. And those atoms which are far away from the mirror, are reflected above the hard-wall mirror due to collisions among themselves as already predicted in Fig. 5.11. As we explored in Fig. 5.5 and Fig. 5.6 that the mean position of the BEC decreases with increasing number of particles, therefore these atoms does not have enough momenta and they cannot reflect back, thus they collide with other falling of atoms due to the gravity and finally lead a web-of-interference pattern between the interval $20 < t < 60$. For larger number of BEC particles as shown in Fig. 5.13(b-c) this web-of-interference can be seen for smaller time intervals and for larger heights, for instance as compared to the case discussed in Fig. 5.13(a). And for very large number of particles like $N_\mathrm{B} = 5000$, as displayed in Fig. 5.13(d), the BEC atoms have less momenta since they are quite close to the hard-wall mirror, therefore we have not

---

[3] Here, in dimensional units, we determine the classical particle revival time by using equation of projectile $z(t) = z_0 + v_0 t - gt^2/2$.

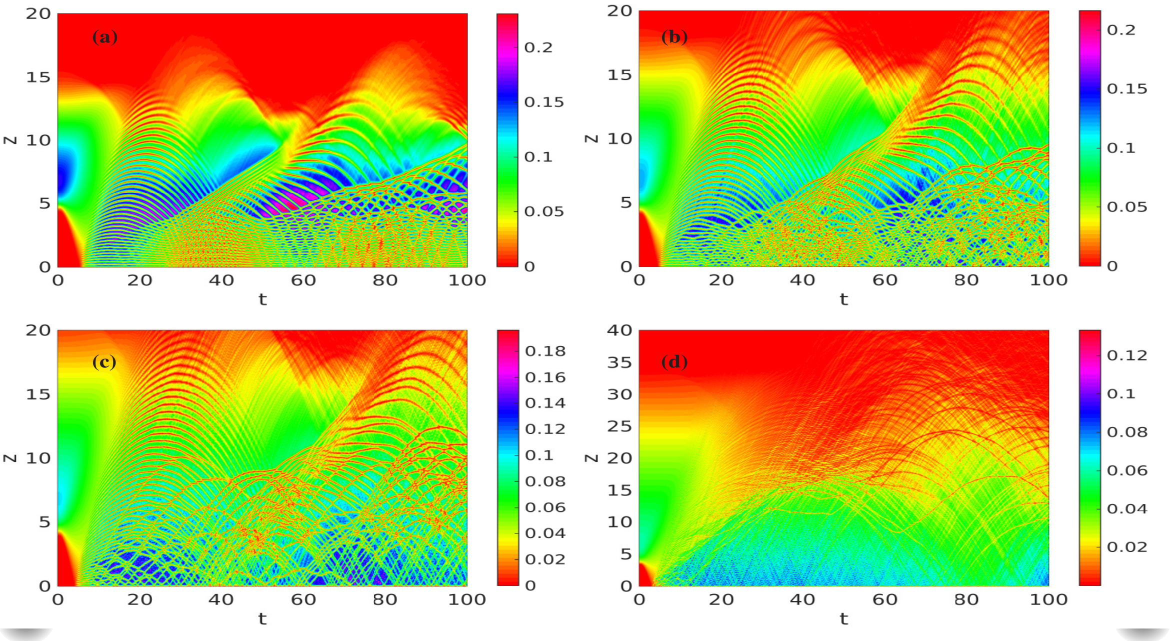

Figure 5.13: Numerical results for the BEC density $|\psi(z,t)|^2$ after having switched off the evanescent potential and letting the BEC atoms fall on a hard-wall mirror for different number of particles (a) $N_\mathrm{B} = 500$, (b) $N_\mathrm{B} = 1000$ (c) $N_\mathrm{B} = 1500$ and (d) $N_\mathrm{B} = 5000$. Here the color scale representing the density of the depleted density of the BEC.

observe clear self-interference patterns.

5.7 Summary and conclusion

In summary, in this chapter we studied the behavior of a Cs BEC in a quasi-1D gravito-optical surface trap. We have developed approximate solutions to the GP equation for both small and large numbers of atoms. In the former, we have used the variational ansatz technique, while in the latter we have used the Thomas-Fermi approximation. Later on, we compared the analytical approach with numerical results, which agreed quite well for a wide range of atom numbers N_B.

Furthermore, we have numerically reproduced the experimental result of Ref. [82], where a 2D BEC is confined in the radial direction, but is allowed to expand in the vertical direction freely. This indicates that our analysis could be extended beyond the 1D case. Our model suggests that for a small particle number N_B the BEC retains its Gaussian shape in the expansion and falls due to gravity. As suggested by Fig. 5.10, for larger number of atoms, the standard deviation does not expand as fast as compared to small number of particles, therefore we conclude that the initial number of the particles pays a significant role in the expansion of the BEC cloud. Afterwards, we investigated the dynamics of the BEC in the presence of gravity and a hard-wall boundary condition, where we observed self-interferences and revivals of the wave packet. The observation of the bouncing of the BEC can be used to characterize and determine mirror properties such as roughness and steepness. All our results can be applied to develop atomic interferometers for a BEC.

Chapter 6

Numerical study of localized impurity in a Bose-Einstein condensate

Inspired by the recent experiments [147–149, 231], we propose and analyze a quasi one-dimensional model of a hybrid system which consists of a single ^{133}Cs impurity in a ^{87}Rb Bose-Einstein condensate. To this end, we start with defining the quasi-1D model in Sec. 6.1 and we derive two coupled quasi one-dimensional differential equations (1DDEs) for the condensate and the impurity wave function. As a result the effective one-dimensional interspecies coupling strength depends not only on the three-dimensional s-wave scattering length, but also on the transversal trap frequencies of cesium and rubidium, respectively. In the same section, we plot the phase diagram, and specify the regions where the impurity is localized at the trap center or expelled to the condensate boarder. Afterwards in Sec. 6.2, we show that the impurity imprint upon the condensate wave function strongly depends upon whether the effective impurity-BEC coupling strength is attractive or repulsive. And within the mean-field regime, we calculate the effective mass of the impurity, which yields a quadratic behavior for small attractive/repulsive interspecies coupling strength. Subsequently, Sec. 6.3 discusses the dynamics of the impurity imprint upon the condensate wave function for two quench scenarios. After having released the trap, the resulting time-of-flight expansion shows that the impurity imprint marginally decreases for an attractive s-wave coupling but considerably decreases for a repulsive s-wave scattering. Furthermore, we investigate the emergence of white shock-waves or gray/dark bi-solitons when the initial negative or positive interspecies coupling constant is switched off. Finally, Section. 6.4 summarizes our findings for the proposed quasi 1D model system in view of a possible experimental realization.

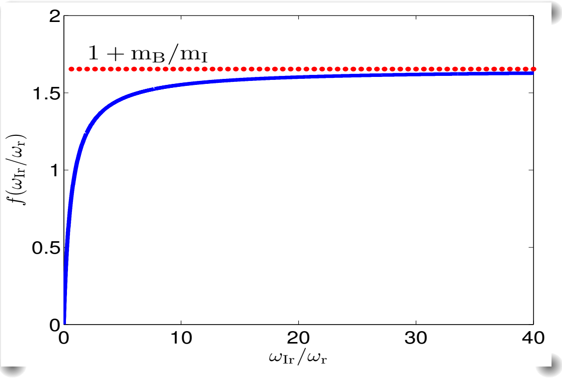

Figure 6.1: Geometric function $f\left(\omega_\mathrm{Ir}/\omega_\mathrm{r}\right)$ reaches its maximum value at $1+m_\mathrm{B}/m_\mathrm{I}$.

6.1 Quasi 1D model

We start with the fact that the underlying equations for describing an impurity immersed in a BEC can be formulated in terms of the Hamilton principle of least action with the action functional $\mathscr{A}_{3\mathrm{D}} = \int dt \int d^3r \mathscr{L}_{3\mathrm{D}}$, where the Lagrangian density reads for three-dimensions

$$\mathscr{L}_{3\mathrm{D}} = \sum_{j=\mathrm{B,I}} N_\mathrm{j}\left\{\frac{i\hbar}{2}\left(\psi_\mathrm{j}^\star(\mathbf{r},t)\frac{\partial\psi_\mathrm{j}(\mathbf{r},t)}{\partial t} - \psi_\mathrm{j}(\mathbf{r},t)\frac{\partial\psi_\mathrm{j}^\star(\mathbf{r},t)}{\partial t}\right) + \frac{\hbar^2}{2m_\mathrm{j}}\psi_\mathrm{j}^\star(\mathbf{r},t)\triangle\psi_\mathrm{j}(\mathbf{r},t)\right.$$
$$\left. - V_\mathrm{j}(\mathbf{r})\psi_\mathrm{j}^\star(\mathbf{r},t)\psi_\mathrm{j}(\mathbf{r},t) - \frac{N_\mathrm{j}g_\mathrm{j}^{3\mathrm{D}}}{2}\parallel\psi_\mathrm{j}(\mathbf{r},t)\parallel^4\right\} - N_\mathrm{B}N_\mathrm{I}g_{\mathrm{IB}}^{3\mathrm{D}}\parallel\psi_\mathrm{I}(\mathbf{r},t)\parallel^2\parallel\psi_\mathrm{B}(\mathbf{r},t)\parallel^2 . \tag{6.1}$$

Here $\psi_\mathrm{B}(\mathbf{r},t)$ and $\psi_\mathrm{I}(\mathbf{r},t)$ describe the BEC and the impurity wave function with $\mathbf{r}=(x,\ y,\ z)$, $V_\mathrm{B}(\mathbf{r}) = m_\mathrm{B}\omega_\mathrm{z}^2z^2/2 + m_\mathrm{B}\omega_\mathrm{r}^2\left(x^2+y^2\right)/2$ and $V_\mathrm{I}(\mathbf{r}) = m_\mathrm{I}\omega_\mathrm{Iz}^2z^2/2 + m_\mathrm{I}\omega_\mathrm{Ir}^2\left(x^2+y^2\right)/2$ denote the three-dimensional harmonic potential for the bosons and the ^{133}Cs impurity. The three-dimensional ^{87}Rb coupling constant reads $g_\mathrm{B}^{3\mathrm{D}} = 4\pi\hbar^2 a_\mathrm{B}/m_\mathrm{B}$, where the s-wave scattering length is $a_\mathrm{B} = 94.7\ \mathrm{a}_0$ with the Bohr radius a_0, while the three-dimensional ^{133}Cs coupling constant reads $g_\mathrm{I}^{3\mathrm{D}} = 0$, because there is only one single ^{133}Cs impurity atom present in the system, i.e. $N_\mathrm{I} = 1$. The three-dimensional effective Rb-Cs coupling constant is $g_\mathrm{IB}^{3\mathrm{D}} = 2\pi\hbar^2 a_\mathrm{IB}/m_\mathrm{IB}$, where $m_\mathrm{IB} = m_\mathrm{I}m_\mathrm{B}/\left(m_\mathrm{I}+m_\mathrm{B}\right)$ is the reduced mass of the two species and $a_\mathrm{IB} = 650\ \mathrm{a}_0$ represents the effective Rb-Cs s-wave scattering length [147]. We assume an effective one-dimensional setting with $\omega_\mathrm{z} \ll \omega_\mathrm{r}$, so we decompose the BEC wave function $\psi_\mathrm{B}(\mathbf{r},t) = \psi_\mathrm{B}(z,t)\phi_\mathrm{B}(\mathbf{r}_\perp,t)$ with $\mathbf{r}_\perp = (x,\ y)$ and

$$\phi_\mathrm{B}(\mathbf{r}_\perp,t) = \frac{1}{\sqrt{\pi}l_\mathrm{r}}e^{-\frac{x^2+y^2}{2l_\mathrm{r}^2}}e^{-i\omega_\mathrm{r}t} . \tag{6.2}$$

Furthermore, we assume that the single impurity in the center of the BEC is trapped by a harmonic potential with $\omega_\mathrm{Iz} \ll \omega_\mathrm{Ir}$. Thus, we perform a similar decomposition of the

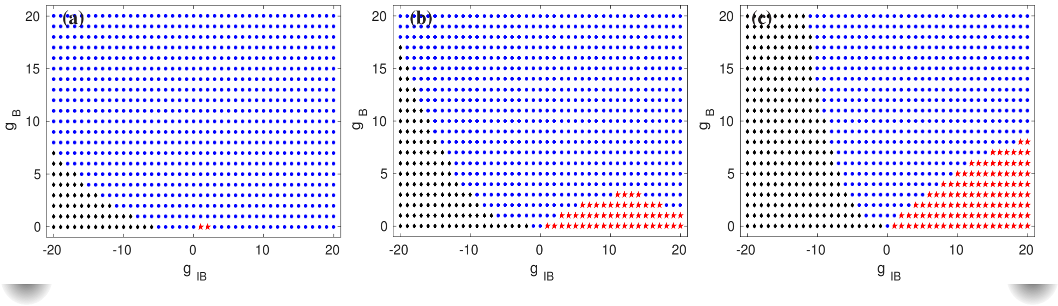

Figure 6.2: Equilibrium phase diagram spanned by g_{B} and g_{IB} for (a) $N_{\mathrm{B}} = 20$ (b) $N_{\mathrm{B}} = 200$ and (c) $N_{\mathrm{B}} = 800$. Impurity is localized at trap center (blue) or expelled to the condensate border (red) together with unstable region (black).

impurity wave function $\psi_{\mathrm{I}}(\mathbf{r},t) = \psi_{\mathrm{I}}(z,t)\phi_{\mathrm{I}}(\mathbf{r}_{\perp},t)$ with

$$\phi_{\mathrm{I}}(\mathbf{r}_{\perp},t) = \frac{1}{\sqrt{\pi}l_{\mathrm{rI}}} e^{-\frac{x^2+y^2}{2l_{\mathrm{rI}}^2}} e^{-i\omega_{\mathrm{rI}}t} . \tag{6.3}$$

Here $l_{\mathrm{r}} = \sqrt{\hbar/(m_{\mathrm{B}}\omega_{\mathrm{r}})}$ and $l_{\mathrm{Ir}} = \sqrt{\hbar/(m_{\mathrm{I}}\omega_{\mathrm{Ir}})}$ denote the oscillator lengths in radial direction for BEC and impurity. For the experimentally realistic trap frequencies $\omega_{\mathrm{r}} = \omega_{\mathrm{Ir}} = 2\pi \times 0.179$ kHz $\gg \omega_{\mathrm{z}} = \omega_{\mathrm{Iz}} = 2\pi \times 0.050$ kHz [148] these radial oscillator lengths amount to the values $l_{\mathrm{r}} = 15190.8\,a_0$ and $l_{\mathrm{Ir}} = 12279.0\,a_0$ for BEC and impurity, respectively. As they are much larger than both a_{IB} and a_{B}, we are indeed within the quasi 1D regime. Therefore, we can follow Sec. 2.5 and integrate out the two transversal dimensions of our three-dimensional Lagrangian according to $\mathscr{L}_{1\mathrm{D}} = \int_{-\infty}^{\infty}\int_{-\infty}^{\infty}\mathscr{L}_{3\mathrm{D}}\,dxdy$. After some algebra, the resulting quasi one-dimensional Lagrangian reads

$$\begin{aligned}\mathscr{L}_{1\mathrm{D}} = \sum_{j=\mathrm{B,I}} N_{\mathrm{j}} \Bigg\{ \frac{i\hbar}{2}\left(\psi_{\mathrm{j}}^{\star}(z,t)\frac{\partial\psi_{\mathrm{j}}(z,t)}{\partial t} - \psi_{\mathrm{j}}(z,t)\frac{\partial\psi_{\mathrm{j}}^{\star}(z,t)}{\partial t}\right) + \frac{\hbar^2}{2m_{\mathrm{j}}}\psi_{\mathrm{j}}^{\star}(z,t)\,\triangle\,\psi_{\mathrm{j}}(z,t) \\ - V_{\mathrm{j}}(z)\psi_{\mathrm{j}}^{\star}(z,t)\,\psi_{\mathrm{j}}(z,t) - \frac{N_{\mathrm{j}}g_{\mathrm{j}}}{2}\parallel\psi_{\mathrm{j}}(z,t)\parallel^4\Bigg\} - N_{\mathrm{B}}N_{\mathrm{I}}g_{\mathrm{IB}}\parallel\psi_{\mathrm{I}}(z,t)\parallel^2\parallel\psi_{\mathrm{B}}(z,t)\parallel^2 .\end{aligned} \tag{6.4}$$

where $V_{\mathrm{B,I}}(z) = m_{\mathrm{B,I}}\omega_{\mathrm{z,Iz}}^2 z^2/2$ represents the one-dimensional harmonic potential for the BEC and for the impurity, the one-dimensional intraspecies coupling strength is

$$g_{\mathrm{B}} = 2a_{\mathrm{B}}\hbar\omega_{\mathrm{r}}, \tag{6.5}$$

whereas for interspecies coupling one obtains

$$g_{\mathrm{IB}} = 2a_{\mathrm{IB}}\hbar\omega_{\mathrm{r}} f\left(\frac{\omega_{\mathrm{Ir}}}{\omega_{\mathrm{r}}}\right). \tag{6.6}$$

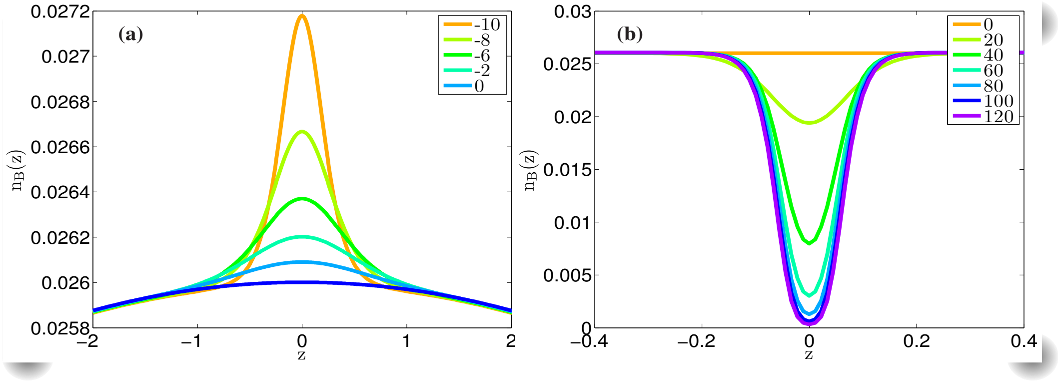

Figure 6.3: Numerical density profile of the BEC for the two-particle Rb-Rb coupling constant value $G_{\mathrm{B}} = 16000$ and for interspecies coupling constants g_{IB} which increases from top to bottom according to the inlets. For increasing negative values of g_{IB} the impurity-induced bump (a) in the condensate wave function decreases, whereas for positive values the corresponding dip (b) increases.

Here the geometric function

$$f\left(\frac{\omega_{\mathrm{Ir}}}{\omega_{\mathrm{r}}}\right) = \frac{1+(m_{\mathrm{B}}/m_{\mathrm{I}})}{1+(m_{\mathrm{B}}\omega_{\mathrm{r}})/(m_{\mathrm{I}}\omega_{\mathrm{Ir}})} \tag{6.7}$$

depends on the ratio of the trap frequencies as depicted in Fig. 6.1. Thus, $f(\omega_{\mathrm{Ir}}/\omega_{\mathrm{r}})$ is monotonously increasing, equals to one for the present case $\omega_{\mathrm{Ir}} = \omega_{\mathrm{r}}$, and reaches its maximum value at $1+m_{\mathrm{B}}/m_{\mathrm{I}}$ for the frequency ratio of about $\omega_{\mathrm{Ir}}/\omega_{\mathrm{r}} \geq 20$. In order to vary the impurity-BEC coupling strength there are, in principle, two possibilities according to Eq. (6.7): either the ratio of the radial trap frequencies is tuned as shown in Fig. 6.1, or the interspecies s-wave scattering length a_{IB} is modified with the use of a Feshbach resonance [147, 232, 233].

The two coupled time dependent differential equations follow from the action $\mathscr{A}_{1\mathrm{D}} = \int_{-\infty}^{\infty}\int_{-\infty}^{\infty}\mathscr{L}_{1\mathrm{D}}dzdt$ and by using the Euler-Lagrangian equation (2.94). Inserting the one-dimensional Lagrangian density (6.4), after some algebra we can write the two coupled 1DDEs as

$$i\hbar\frac{\partial}{\partial t}\psi_{\mathrm{B}}(z,t) = \left\{-\frac{\hbar^2}{2m_{\mathrm{B}}}\frac{\partial^2}{\partial z^2} + \frac{m_{\mathrm{B}}\omega_{\mathrm{z}}^2}{2}z^2 + G_{\mathrm{IB}} \parallel \psi_{\mathrm{I}}(z,t) \parallel^2 + G_{\mathrm{B}} \parallel \psi_{\mathrm{B}}(z,t) \parallel^2\right\}\psi_{\mathrm{B}}(z,t), \tag{6.8}$$

$$i\hbar\frac{\partial}{\partial t}\psi_{\mathrm{I}}(z,t) = \left\{-\frac{\hbar^2}{2m_{\mathrm{I}}}\frac{\partial^2}{\partial z^2} + \frac{m_{\mathrm{I}}\omega_{\mathrm{Iz}}^2}{2}z^2 + G_{\mathrm{BI}} \parallel \psi_{\mathrm{B}}(z,t) \parallel^2\right\}\psi_{\mathrm{I}}(z,t). \tag{6.9}$$

On the right-hand side of Eq. (6.8) and Eq. (6.9) the first term represents the kinetic energy of the BEC(impurity) atoms with mass $m_{\mathrm{B}}(m_{\mathrm{I}})$, the second term describes the potential energy term, the third term stands for the impurity-BEC coupling, and the last term in (6.8)

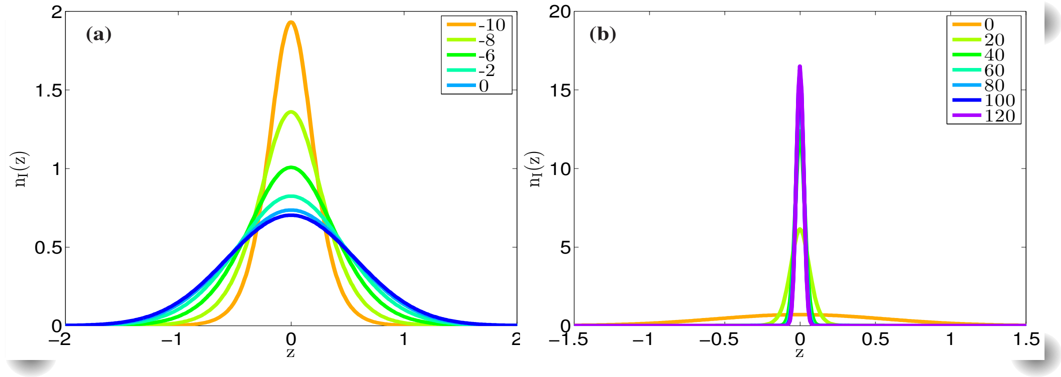

Figure 6.4: Numerical density profile of the impurity for the two-particle Rb-Rb coupling constant value $G_{\mathrm{B}} = 16000$ and for interspecies coupling constants g_{IB} which increases from top to bottom according to the inlets. For increasing negative (a) values of g_{IB} the impurity wave function decreases, whereas for positive (b) values the corresponding impurity wave function increases.

represents the Rb-Rb two-particle interaction. Here $G_{\mathrm{B}} = N_{\mathrm{B}} g_{\mathrm{B}}$ represents the two-particle Rb-Rb coupling strength, $G_{\mathrm{IB}} = g_{\mathrm{IB}}$ and $G_{\mathrm{BI}} = N_{\mathrm{B}} g_{\mathrm{IB}}$ describe the two-particle Rb-Cs coupling strengths for impurity to BEC and for BEC to impurity, respectively. In order to make Eqs. (6.8) and (6.9) dimensionless we introduce the dimensionless time as $\tilde{t} = \omega_z t$, the dimensionless coordinate $\tilde{z} = z/l_z$, and the dimensionless wave function $\tilde{\psi} = \psi\sqrt{l_z}$ with the oscillator length $l_z = \sqrt{\hbar/(m_{\mathrm{B}}\omega_z)}$. With this Eqs. (6.8) and (6.9) can be rewritten in the form

$$i\frac{\partial}{\partial \tilde{t}}\tilde{\psi}_{\mathrm{B}}(\tilde{z},\tilde{t}) = \left\{-\frac{1}{2}\frac{\partial^2}{\partial \tilde{z}^2} + \frac{\tilde{z}^2}{2} + \tilde{G}_{\mathrm{IB}} \parallel \tilde{\psi}_{\mathrm{I}}(\tilde{z},\tilde{t}) \parallel^2 + \tilde{G}_{\mathrm{B}} \parallel \tilde{\psi}_{\mathrm{B}}(\tilde{z},\tilde{t}) \parallel^2\right\} \tilde{\psi}_{\mathrm{B}}(\tilde{z},\tilde{t}), \tag{6.10}$$

$$i\frac{\partial}{\partial \tilde{t}}\tilde{\psi}_{\mathrm{I}}(\tilde{z},\tilde{t}) = \left\{-\frac{\tilde{k}^2}{2}\frac{\partial^2}{\partial \tilde{z}^2} + \frac{\tilde{z}^2}{2\tilde{k}^2} + \tilde{G}_{\mathrm{BI}} \parallel \tilde{\psi}_{\mathrm{B}}(\tilde{z},\tilde{t}) \parallel^2\right\} \tilde{\psi}_{\mathrm{I}}(\tilde{z},\tilde{t}), \tag{6.11}$$

where we have $\tilde{G}_{\mathrm{B}} = N_{\mathrm{B}}\tilde{g}_{\mathrm{B}}$, $\tilde{G}_{\mathrm{IB}} = \tilde{g}_{\mathrm{IB}}$ and $\tilde{G}_{\mathrm{BI}} = N_{\mathrm{B}}\tilde{g}_{\mathrm{IB}}$ with $\tilde{g}_{\mathrm{B}} = g_{\mathrm{B}}/(\hbar\omega_z l_z)$ and $\tilde{g}_{\mathrm{IB}} = g_{\mathrm{IB}}/(\hbar\omega_z l_z)$. Here $\tilde{k} = l_{\mathrm{Iz}}/l_z$ defines the ratio of the two oscillator lengths. Thus, we can summarize that Eq. (6.10) is nothing but a standard Gross-Piteavskii equation with an additional potential stemming from the impurity, whereas Eq. (6.11) is a typical Schrödinger wave equation with a potential originating from the BEC. From here on, we will drop the tildes for simplicity.

Typically, a mixture of two species can occur in two different states, either it is miscible, i.e. both species overlap, or it is immiscible, i.e. the two species do not overlap [234]. In our case the equilibrium phase diagram is spanned by the coupling strengths g_{B} and g_{IB} and contains a region, where the impurity is localized at the center, and another one, where the impurity is expelled to be localized at the border of the condensate. Note that a similar equilibrium phase diagram was studied for the homogeneous case with attractive interspecies

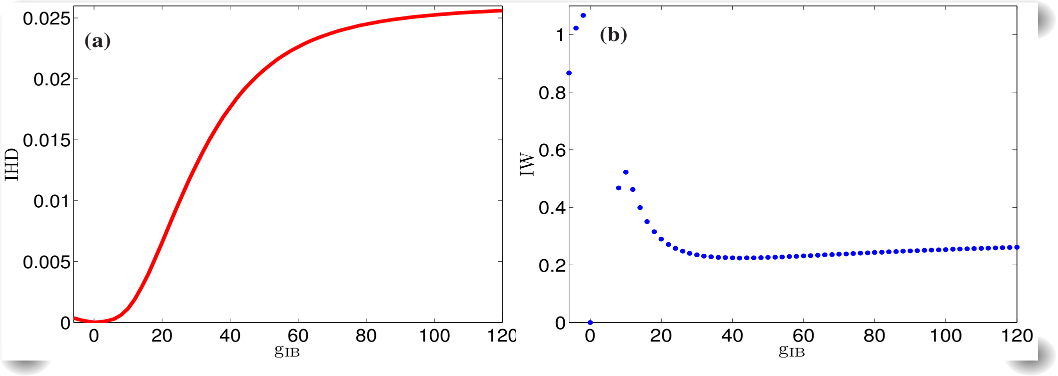

Figure 6.5: (a) Height/depth and (b) width of impurity bump/dip according to Eqs. (6.16)–(6.18) versus impurity-BEC coupling constant g_{IB} for the BEC coupling constant $G_{\mathrm{B}} = 16000$ calculated numerically by solving 1DDEs (6.10) and (6.11).

s-wave scattering lengths in Ref. [235]. In order to investigate the physical regions of interest for our proposed model, we solve the two coupled 1DDEs (6.10) and (6.11) in imaginary time numerically by using the split-operator method [192, 193], which yields the equilibrium phase diagram Fig. 6.2. The blue region shows where the impurity is localized at the center of the BEC, the red region depicts that the impurity is displaced from the center to the border of the condensate, and finally, the black region represents the unstable region where impurity and condensate do not coexist. The above mentioned experimental parameters yield the dimensionless intraspecies and interspecies coupling strengths $g_{\mathrm{B}} = 0.023$ and $g_{\mathrm{IB}} = 0.16$, respectively, which correspond to the red region of Fig. 6.2(c) for $N_{\mathrm{B}} = 800$ ^{87}Rb atoms. As we are interested into the localization of the impurity at the center of the BEC, however, we use from now on, different dimensionless values of intraspecies and interspecies coupling strengths, which stem from the blue region in the equilibrium phase diagram of Fig. 6.2. In particular, we consider that the BEC consists of $N_{\mathrm{B}} = 800$ ^{87}Rb atoms, for the dimensionless intraspecies couplings constant we assume $G_{\mathrm{B}} = 16000$, and the ratio of the two oscillator lengths $k = l_{\mathrm{Iz}}/l_{\mathrm{z}}$ turns out to have the value $\sqrt{87/133} = 0.808$.

In order to argue that we are in the regime where the mean-field theory is valid, we divide our argument into two parts. Firstly, in order to differentiate between the weakly interacting quasi-1D and the strongly interacting Tonks-Girardeau regime, Petrov et al. [114] introduced a dimensionless quantity $\alpha = (2a_{\mathrm{B}}l_{\mathrm{z}})/l_{\mathrm{r}}^2 = 0.023$ as pointed out in Eq. (2.118). Therefore, we are far in the weakly interacting regime, where the Gross-Pitaevskii mean-field theory is appropriate as shown in Fig. 2.7. Secondly, it is physically reasonable to assume that the impurity in our proposed model does not affect the mean-field description of our system. Therefore, we restrict the following calculation of the validity range of the mean-field analysis to a BEC without any impurity.

We determine how quantum and thermal fluctuations within the Bogoliubov theory restrict the validity range of our mean-field description. The ratio of one-dimensional quantum

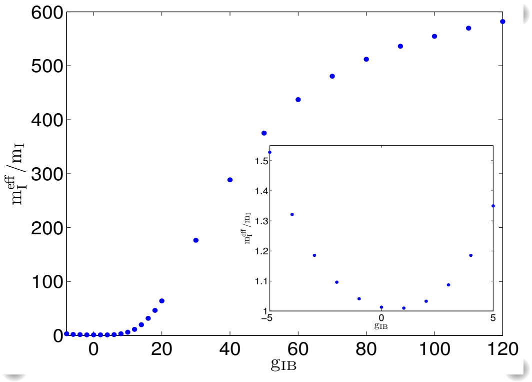

Figure 6.6: Effective mass of ^{133}Cs impurity versus impurity-BEC coupling strength g_{IB}. Inlet shows that effective mass increases quadratically for small impurity-BEC coupling strength g_{IB}.

fluctuations depleted atoms with respect to the number of particles $N_{\mathrm{B}} = 800$ can be written as calculated in Appendix B of Eq. (B.10)

$$\frac{N_{\mathrm{QF}}^{\mathrm{1D}}}{N_{\mathrm{B}}} = \frac{3^{1/3}}{4}\left(a_{\mathrm{B}}^4 N_{\mathrm{B}} \Xi^2\right)^{1/3} = 0.0038, \tag{6.12}$$

so that the quantum fluctuations are, indeed, negligible. Here $\Xi = l_{\mathrm{z}}/l_{\mathrm{r}}$ denotes the ratio of the axial and the longitudinal harmonic oscillator lengths. Correspondingly, the one-dimensional thermal depleted number of atoms $N_{\mathrm{TF}}^{\mathrm{1D}}$ with respect to the number of particles follows from Bogoliubov theory (B.16)

$$\frac{N_{\mathrm{TF}}^{\mathrm{1D}}}{N_{\mathrm{B}}} = \gamma \left(\frac{T}{T_{\mathrm{c}}}\right)^2, \tag{6.13}$$

with the dimensionless prefactor from Eq. (B.17)

$$\gamma = \frac{5^{2/5}\pi^2}{2^{3/2}\times 3^{3/5}}\left(\frac{N_{\mathrm{B}}^{1/3}}{\xi\left(3\right)^{8/3}} a_{\mathrm{B}}^2 \Xi^{4/3}\right)^{1/5}. \tag{6.14}$$

For our system parameters we obtain $\gamma = 0.0593$ and the critical temperature from Eq. (2.76) is $T_{\mathrm{c}} = \hbar\left[\omega_r^2 \omega_{\mathrm{z}} N_{\mathrm{B}}/\xi\left(3\right)\right]^{1/3}/k_{\mathrm{B}} = 49.0\,\mathrm{nK}$. Thus, choosing a reasonable ratio of the thermal depleted term $N_{\mathrm{TF}}^{\mathrm{1D}}/N_{\mathrm{B}} = 0.001$, we estimate the temperature of the system to be

$$T = T_{\mathrm{c}}\sqrt{\frac{1}{\eta}\frac{N_{\mathrm{TF}}^{\mathrm{1D}}}{N_{\mathrm{B}}}} = 6.35\ \mathrm{nK} \tag{6.15}$$

With this we conclude that, if the temperature of the system is lower than $T = 6.35$ nK, the thermal fluctuations are not affecting the Bose-Einstein condensate.

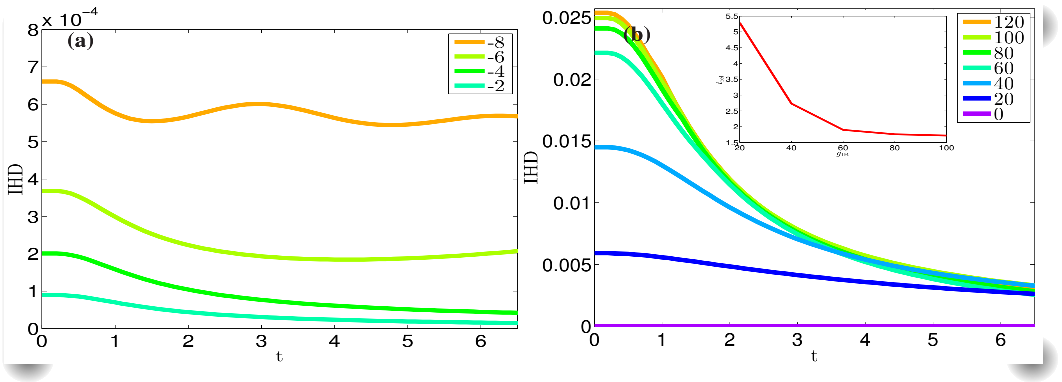

Figure 6.7: Impurity imprint height/depth after having released the trap versus time for (a) increasing negative and (b) decreasing positive values of impurity-BEC coupling constant g_{IB} from top to bottom. Inlet: relaxation time t_{rel} decreases with increasing g_{IB}.

6.2 Impurity imprint upon stationary condensate wave function

In order to determine the impurity imprint on the condensate wave function in equilibrium we solve the two coupled 1DDEs (6.10), (6.11) numerically in imaginary time. In this way we find that the impurity leads to a bump/hole in the BEC density at the trap center for negative/positive values of g_{IB} as shown in Fig. 6.3. For increasing the attractive/repulsive interspecies coupling strength the bump/dip upon the condensate decreases/increases. For the repulsive interspecies coupling strength, the impurity drills a dip in the BEC density which gets deeper and deeper until no more BEC atoms remain in the trap center and, finally, the BEC fully fragments into two parts as depicted in Fig. 6.3(b) at the characteristic value $g_{\mathrm{IBc}} = 110$. The width/height of the impurity wave function decreases/increases for increasing interspecies coupling constant $|g_{\mathrm{IB}}|$, respectively, as demonstrated in Fig. 6.4.

In view of a more detailed comparison, we categorize the impurity imprint upon the condensate wave function $\psi_{\mathrm{B}}(z)$ by the following two quantities. The first one is the impurity height/depth

$$\mathrm{IHD} = \begin{cases} \parallel \psi_{\mathrm{B}}(0) \parallel^2_{g_{\mathrm{IB}}} - \parallel \psi_{\mathrm{B}}(0) \parallel^2_{g_{\mathrm{IB}}=0} & g_{\mathrm{IB}} \leq 0 \\ \mathrm{Max}\left(\parallel \psi_{\mathrm{B}}(z) \parallel^2_{g_{\mathrm{IB}}}\right) - \parallel \psi_{\mathrm{B}}(0) \parallel^2_{g_{\mathrm{IB}}} & g_{\mathrm{IB}} \geq 0 \end{cases} \tag{6.16}$$

and the second one is the impurity width IW, which we define as follows. For $g_{\mathrm{IB}} \leq 0$ we use the full width half maximum

$$\parallel \psi(\mathrm{IW}/2) \parallel^2_{g_{\mathrm{IB}}} = \frac{\parallel \psi_{\mathrm{B}}(0) \parallel^2_{g_{\mathrm{IB}}} + \parallel \psi_{\mathrm{B}}(0) \parallel^2_{g_{\mathrm{IB}}=0}}{2} \quad g_{\mathrm{IB}} \leq 0, \tag{6.17}$$

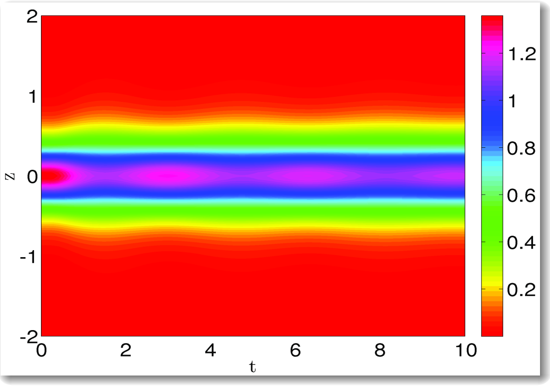

Figure 6.8: Dynamics of impurity density represented in color scale after having switched off the harmonic trap for initial g_{IB}=-8 for the BEC coupling strength $G_{\mathrm{B}} = 16000$.

whereas for $g_{\mathrm{IB}} \geq 0$ we define the equivalent width [194]:

$$\mathrm{IW} = \frac{2I_0 z_{\mathrm{Max}} - \int_{-z_{\mathrm{Max}}}^{z_{\mathrm{Max}}} \parallel \psi_{\mathrm{B}}(z) \parallel_{g_{\mathrm{IB}}}^2 dz}{I_0 - \parallel \psi_{\mathrm{B}}(0) \parallel_{g_{\mathrm{IB}}}^2} \qquad g_{\mathrm{IB}} \geq 0\,, \tag{6.18}$$

where we have $I_0 = \mathrm{Max}\left(\parallel \psi_{\mathrm{B}}(z) \parallel_{g_{\mathrm{IB}}}^2\right)$. In Fig. 6.5(a) we plot the IHD for $g_{\mathrm{IB}} > -10$, while $g_{\mathrm{IB}} < -10$ is not a valid region for $g_{\mathrm{B}} = 20$ according to Fig. 6.2(c). From Figure 6.5(a) we read off that for $g_{\mathrm{IB}} = 0$, i.e. when there is no impurity present, the impurity height/depth vanishes. The IHD quadratically increases for the repulsive interspecies coupling strength $0 < g_{\mathrm{IB}} < 60$ and partially fragments the BEC until it reaches its marginally saturated value IHDc ≈ 0.025 for the characteristic interspecies coupling strength $g_{\mathrm{IBc}} = 110$. In the case of $g_{\mathrm{IB}} > g_{\mathrm{IBc}}$, the impurity fully fragments the BEC into two parts as depicted in Fig. 6.3(b). The impurity imprint width increases abruptly just before/after $g_{\mathrm{IB}} = 0$ for attractive/repulsive interspecies coupling strength, respectively, as shown in Fig. 6.5(b). For an increasing repulsive impurity-BEC coupling strength the impurity width then decreases until it reaches the interspecies coupling strength $g_{\mathrm{IB}} = 30$, later on it marginally increases until the characteristic interspecies coupling strength $g_{\mathrm{IBc}} = 110$, where we have IWc ≈ 0.23.

The effective mass of the impurity is defined as $m_{\mathrm{I}}^{\mathrm{eff}} = \hbar / \left(l_{\mathrm{Iz}}^2 \omega_z\right)$, where the impurity oscillator length $l_{\mathrm{Iz}} = \sqrt{2}\sigma$ follows from the standard deviation $\sigma = \sqrt{<z^2> - <z>^2}$, with $<\bullet> = \int \bullet |\psi_{\mathrm{I}}(z)|^2 dz$ denoting the expectation value. Figure 6.6 shows the ratio of the effective mass of the ^{133}Cs impurity with respect to the bare mass m_{I}, which increases quadratically for interspecies coupling strength $-5 < g_{\mathrm{IB}} < 5$ as shown in the inlet of Fig. 6.6, and becomes marginally saturated for interspecies coupling strength $g_{\mathrm{IB}} > g_{\mathrm{IBc}}$. Note that our results for the effective mass of the impurity are restricted to the mean-field regime. In order to go beyond and include the impact of quantum fluctuations, one would need to investigate polaron physics [150, 151, 236, 237].

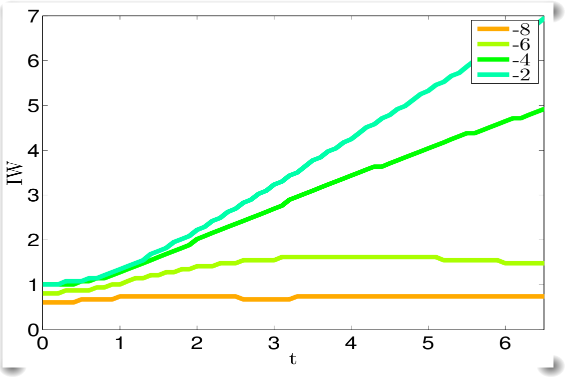

Figure 6.9: Impurity imprint width after having released the trap versus time for increasing values of impurity-BEC coupling constant g_{IB} from top to bottom.

6.3 Impurity imprint upon condensate dynamics

In an experiment, any imprint of the impurity upon the condensate wave function could only be detected dynamically. Thus, it is of high interest to study theoretically whether the impurity imprint, which we have found and analyzed for the stationary case in the previous section, remains present also during the dynamical evolution of the condensate wave function. To this end, we explore two quench scenarios numerically in more detail. The first one is the standard time-of-flight (TOF) expansion after having switched off the external trap when the interspecies interaction is still present. In the second case we consider the inverted situation that the impurity-BEC interaction is suddenly switched off within a remaining harmonic confinement, which turns out to give rise to the emergence of wave packets or bi-solitons depending on whether the initial interspecies interaction strength is attractive or repulsive.

6.3.1 Time-of-flight expansion

Time-of-flight (TOF) absorption pictures represent an important diagnostic tool to analyze dilute quantum gases. By suddenly turning off the magnetic trap, the atom cloud expands non-ballistically with a dynamics which is determined by both the momentum distribution of the atoms at the instance, when the confining potential is switched off, and by inter-atomic interactions [197, 198]. We have investigated the time-of-flight expansion dynamics of the BEC with impurity by solving numerically the two coupled 1DDEs (6.10), (6.11) and analyzing the resulting evolution of both the condensate and the impurity wave function. It turns out that, despite the continuous broadening of the condensate density, its impurity imprint remains qualitatively preserved both for attractive and repulsive interspecies interaction strengths, respectively. Therefore, we focus a more quantitative discussion upon the dynamics of the corresponding impurity height/depth and width. For an attractive Rb-Cs coupling strength, it turns out that the impurity imprint even remains approximately constant in the time-of-flight, as is shown explicitly in Fig. 6.7 (a) for the IHD, which marginally decreases for $t \gg 0$. As shown in Fig. 6.7 (a) for smaller attractive interspecies coupling strength, we observe the crumbling breathing of the impurity upon IHD as discussed recently for the Bose-Hubbard model [238]. For the attractive interspecies coupling strength $g_{\mathrm{IB}} = -8$ the dynamics of the impunity density is displayed in Fig. 6.8, which clearly reflects the crumbling breathing of the impurity at the center of the BEC. In case of the IW, we find that the IW starts increasing marginally for smaller values of attractive interspecies coupling strength and increases linearly for smaller attractive interspecies coupling strength g_{IB} as shown in Fig. 6.9.

In case of a repulsive interspecies interaction, the IHD decays with a characteristic time scale as depicted in Fig. 6.7(b). Defining that relaxation time t_{rel} according to $\mathrm{IHD}(t_{\mathrm{rel}}) = \mathrm{IHD}(0)/2$, the inlet reveals that the impurity imprint depth relaxes with a shorter time scale for increasing repulsive impurity-BEC coupling strength as shown in Fig. 6.7(b). This physical picture is confirmed by the dynamics of the time-of-flight evolution of the depleted density as shown in Fig. 6.10. At the beginning of TOF the impurity-imprint remains at first constant, then the imprint width expands and the imprint height decays gradually as shown in Fig. 6.10. In Fig. 6.10 we plotted the time-of-flight of the depleted density of the BEC for two cases. For the repulsive interspecies coupling strength $g_{\mathrm{IB}} = 20$ we observe that the impurity imprint decays marginally from its equilibrium value as shown in Fig. 6.7(b) and the impurity remains localized at the center as shown in Fig. 6.10(a). On the other hand, for the larger value of the repulsive interspecies coupling strength $g_{\mathrm{IB}} = 80$, the impurity imprint decays from its equilibrium value as shown in Fig. 6.7(b) and at the same time the impurity is expelled from the center of the BEC as shown in Fig. 6.10(b). With this we conclude that for a small enough repulsive interspecies coupling strengths the impurity survives in the center of the BEC for larger times.

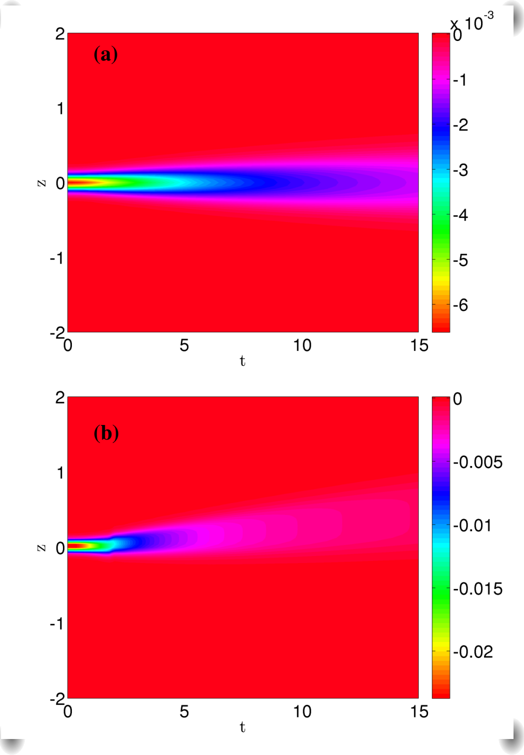

Figure 6.10: Coherent matter-wave TOF evolution of depleted density $\| \psi_{\mathrm{B}}(z,t) \|^2_{\mathrm{DD}} = \| \psi_{\mathrm{B}}(z,t) \|^2_{g_{\mathrm{IB}}} - \| \psi_{\mathrm{B}}(z,t) \|^2_{g_{\mathrm{IB}}=0}$ after having switched off the trap for the BEC coupling constant $G_{\mathrm{B}} = 16000$: (a) $g_{\mathrm{IB}} = 20$ and (b) $g_{\mathrm{IB}} = 80$. Here the color scale represents the density of the depleted density of the BEC.

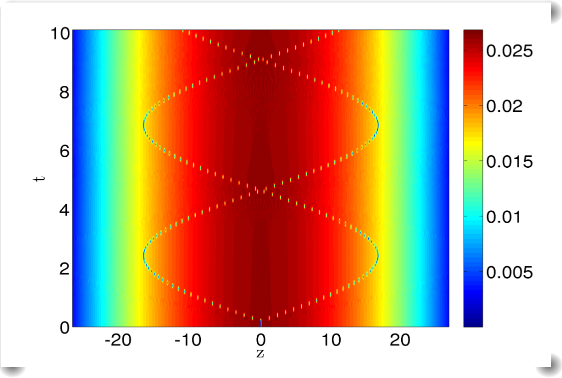

Figure 6.11: Density profile of BEC represented in color scale after having switched off the impurity-BEC coupling constant for initial g_{IB}=120 and for the BEC coupling constant $G_{\mathrm{B}} = 16000$.

6.3.2 Wave packets versus solitons

For our proposed quasi 1D model of a BEC with an impurity we investigated the dynamics of the condensate wave function which emerges after having switched off the interspecies coupling strength. Both for an initial attractive and repulsive interspecies coupling strength g_{IB} we observe that two excitations of the condensate are created at the impurity position, which travel in opposite direction with the same center-of-mass speed, are reflected at the trap boundaries and then collide at the impurity position as shown exemplarily in Fig. 6.11 for the initial g_{IB}=120 and $G_{\mathrm{B}} = 16000$. These excitations qualitatively retain their shape despite the collision at the impurity position. All these findings are not yet conclusive to decide whether these excitations represent wave packets in the absence of dispersion or solitons. Therefore, we investigate their dynamics in more detail, by determining their center-of-mass motion via [152]

$$\bar{z}_{\mathrm{L,R}}\left(t\right) = \frac{\int_{-\infty,0}^{0,\infty} z \left(\parallel \psi_{\mathrm{B}}\left(z,t\right) \parallel_{g_{\mathrm{IB}}}^{2} - \parallel \psi_{\mathrm{B}}\left(z,t\right) \parallel_{g_{\mathrm{IB}}=0}^{2} \right) dz}{\int_{-\infty,0}^{0,\infty} \left(\parallel \psi_{\mathrm{B}}\left(z,t\right) \parallel_{g_{\mathrm{IB}}}^{2} - \parallel \psi_{\mathrm{B}}\left(z,t\right) \parallel_{g_{\mathrm{IB}}=0}^{2} \right) dz}, \tag{6.19}$$

which are plotted in Fig. 6.12. Note that the mean positions $\bar{z}_{\mathrm{L}}$ and $\bar{z}_{\mathrm{R}}$ of the excitations are uncertain in the region where they collide. Nevertheless Fig. 6.12 demonstrates that the excitations oscillate with the frequency $\omega = 2\pi \times 35.7$ Hz irrespective of sign and size of g_{IB}. As we have assumed the trap frequency $\omega_z = 2\pi \times 50$ Hz, we obtain the ratio $\omega/\omega_z \approx 0.714$, which is quite close to $\omega/\omega_z = 1/\sqrt{2} \approx 0.707$. Despite these similarities of the cases of an initial attractive and repulsive interspecies coupling constant g_{IB}, we observe one significant difference. Whereas the oscillation amplitudes of the excitations do not depend on the value of the initial $g_{\mathrm{IB}} < 0$ according to Fig. 6.12(a), we find decreasing oscillation amplitudes of the excitations with increasing the initial $g_{\mathrm{IB}} > 0$ in Fig. 6.12(b). Such an amplitude dependence on the initial condition is characteristic for gray/dark solitons according to Ref. [187]. This particle-like interpretation of the excitations agrees with the other theoretical prediction

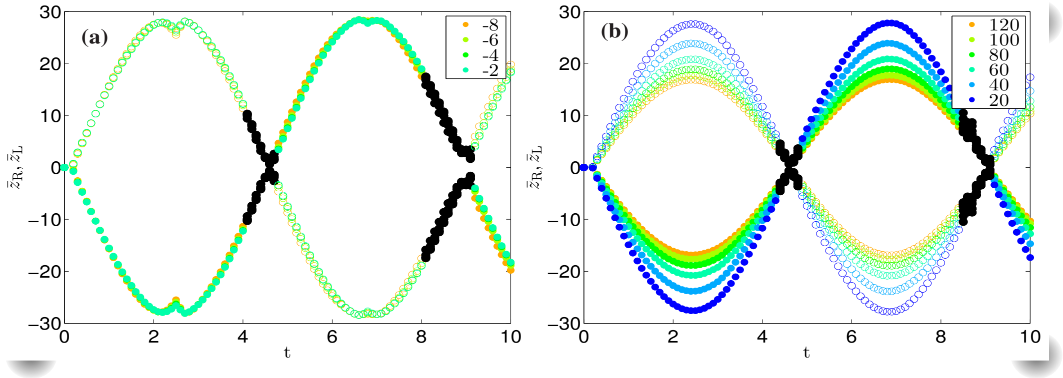

Figure 6.12: Center of mass positions of excitations $\bar{z}_L$ (filled circles) and $\bar{z}_R$ (empty circles) according to Eq. (6.19) versus time after having switched off (a) negative decreasing and (b) positive increasing values of g_{IB} from top to bottom. Black filled circles represent the region of colliding excitations, where mean positions are not perfectly detectable.

of Ref. [187] that gray/dark solitons oscillate in a harmonic confinement with the frequency $\omega/\omega_z = 1/\sqrt{2}$, which was already confirmed in the Hamburg experiment of Ref. [66] and in the Heidelberg experiment of Ref. [97] and is also seen in Fig. 6.12. Conversely, for an initial attractive interspecies coupling constant the excitations can not be identified with bright solitons as the dynamics is governed by a GPE with a repulsive two-particle interaction. Here the excitations have to be interpreted as wave packets which move without any dispersion, thus, for $g_{IB} < 0$ the excitations propagate like sound waves in the BEC [152, 153, 239].

Thus, we conclude that switching off the interspecies coupling constant leads for $g_{IB} < 0$ and $g_{IB} > 0$ to physically different situations. For an initial attractive RbCs coupling constant we generate wave packets which correspond to white shock-waves [202], whereas for the corresponding repulsive case bi-solitons emerge [91, 203], which are due to the collision of the two partially/fully fragmented parts of the condensate. Note that it can be shown in our proposed system that gray bi-solitons are generated for a partially fragmented BEC, i.e. the impurity-BEC coupling strength $g_{IB} < g_{IBc}$. On the other hand the dark bi-solitons turn out to be only generated for $g_{IB} > g_{IBc}$, where the BEC is fully fragmented into two parts at equilibrium. In Section 3.3, we have observed that bi-solitons trains are generated in the traditional harmonic trap with an additional dimple trap [152]. Similar to the situation described in sections 3.3 and 4.4, we found out that the oscillation frequencies of both the white shock-waves and the soliton coincide and attribute it to be an artifact of the harmonic confinement. We emphasize that beside many practical applications of the impurity-BEC system, someone can also generate solitons by considering an impurity as a drilling appliance to fragment the BEC, which allows to study soliton physics in the condensate.

6.4 Summary and conclusion

In the present work we studied within a quasi 1D model numerically how a single impurity in the center of a trapped BEC affects the condensate wave function. At first, we investigated the equilibrium properties of that hybrid system by numerically solving the underlying two coupled 1DDEs (6.10) and (6.11) with the imaginary-time propagation method. For an increasing attractive/repulsive Rb-Cs interaction strength it turns out that the impurity imprint bump/dip decreases/increases quadratically and reaches its marginally saturated value after $g_{\mathrm{IBc}} = 110$. Later we found that the impurity imprint width increases abruptly for increasing the attractive/repulsive Rb-Cs interaction strength, but for the repulsive case it reaches a marginally saturated value for $g_{\mathrm{IB}} > g_{\mathrm{IBc}}$. Beyond the characteristic value g_{IBc}, the BEC fragments into two parts and, if g_{IB} is increased beyond g_{IBc}, the impurity yields a condensate wave function whose impurity width increases further, although the impurity height/depth remains constant. Afterwards, we investigated the impurity imprint upon the condensate dynamics for two quench scenarios.

At first, we considered the release of the harmonic confinement, which leads to a time-of-flight expansion and found that the impurity imprint upon the condensate decays slowly for small valves of the attractive/repulsive interspecies coupling strength. This result suggests that it might be experimentally easier to observe the impurity imprint for small attractive/repulsive coupling constant g_{IB}. We also observed the decaying breathing of the impurity at the center of the condensate for small attractive Rb-Cs coupling strength. Additionally, we found for stronger repulsive interspecies coupling strength that the ^{87}Rb atoms repel the single ^{133}Cs impurity from the center. In an experiment one has to take into account that inelastic collisions lead to two- and three-body losses of the condensate atoms [220, 240]. As such inelastic collisions are enhanced for a higher BEC density, they play a vital role for an attractive interspecies coupling, when the condensate density has a bump at the impurity position, but are negligible in the repulsive case with the dip in the wave function.

In addition, we analyzed the condensate dynamics after having switched off the interspecies coupling strength. This case turned out to be an interesting laboratory in order to study the physical similarities and differences of bright shock waves and gray/dark bi-solitons, which emerge for an initial negative and positive interspecies coupling constant g_{IB}, respectively. We consider the astonishing observation, that the oscillation frequencies of both the shock waves and the soliton coincide, to be an artifact of the harmonic confinement. Additionally, we also found that the generation of gray/dark bi-solitons is a generic phenomenon on collisions of partially/fully fragmented BEC, respectively, which is strongly depending upon the equilibrium values of the impurity wave function height and width.

Chapter 7

Summary and conclusion

We fabricated our thesis into four parts which roughly follow on from one to another. **Part I** gave fundamental basic calculation of the optical dipole trap (ODT) and an essential summary of describing a Bose-Einstein condensate (BEC) within the mean-field theory. **Part II** covered the physics of the creation of complex coherent matter waves in a harmonically trapped BEC, which we sculpted by assuming a specific geometrical configuration of the external ODT and by changing the intensity as well as the detuning of the laser. **Part III** presented results for the dynamics of matter waves by shaping a quasi one-dimensional BEC from Gaussian to triangular shape for an increasing number of atoms in a nonlinear gravito-optical surface trap including a quantitative comparison with experimental measurements. And **part IV** demonstrated the shaping of a BEC cloud with a single impurity atom at the center of the trap by changing the interspecies coupling strength in order to produce matter waves.

Part I

Part I of this thesis, which consisted of chapters 1 and 2, presented a necessary basic theoretical background on the ODT and a primary description of the BEC within the mean-field theory. In chapter 1 we discussed in Sec. 1.1 the historical importance and the background of Bose-Einstein condensation. Later, in Sec. 1.2, we described the physical mechanism behind an ODT, and outlined the advantage of the ODT in contrast to a magneto-optical trap (MOT), which can only trap atoms with a certain internal state [29, 30]. Furthermore, we defined the so called dimple trap (dT) or Hermite-Gaussian dimple trap (HGdT), which is nothing but a small tight optical dipole trap [31–33]. In Sec. 1.3, we outlined the historical importance of the gravito-optical surface trapping. Subsequently, in Sec. 1.4, we discussed the possibility to control and manipulate a BEC by changing the respective system parameters. In Sec. 1.5, we briefly reviewed the interaction of the BEC with an impurity, which can consist of a different atom or alike atom but in a different internal hyperfine state.

In chapter 2, we outlined the physical background of an ODT in Sec. 2.1 and derived the relations for both the optical dipole potential and the scattering rate, by using the classical Abraham–Lorentz model as well as a semiclassical calculation, both yielding surprisingly the same results. Furthermore, we described how to trap atoms near to dielectric surfaces with the help of the evanescent wave (EW) potential in Sec. 2.2, and determined its field strength (2.36). Later, in Sec. 2.3 we derived the semiclassical free energy (2.60) and the number of particles (2.61) for bosons in D-dimensions, as a special case we calculated the critical temperature for a three-dimensional and for a one-dimensional system for both homogeneous and trapped cases. And we studied the Mermin–Wagner theorem, which states that the BEC transition is not achievable for the 1D homogeneous case, but for the one-dimensional harmonic trap a finite BEC critical temperature is possible. Further, we derived the Gross–Pitaevskii equation (GPE) (2.90) for D-dimensions in Sec. 2.4. Afterwards, by using the Gaussian variational ansatz (2.95), we obtained the equations of motion (2.106) for the widths of the Bose-Einstein condensate for the D-dimensional harmonic trap, in the same section we also described the approximative Thomas-Fermi (TF) solution (2.108). At the end of this chapter in Sec. 2.5, we discussed the quasi one-dimensional Gross–Pitaevskii equation (1DGPE) (2.119) as a special case, where we compared a Gaussian variational ansatz, the Thomas-Fermi solution, and the numerical solution by solving the 1DGPE as shown in Fig. 2.8. We observed that for small inter-particle interaction the BEC has a Gaussian density profile, whereas for large inter-particle interaction value the BEC reveals a TF density profile as depicted in Fig. 2.8. And finally, we illustrated the difference of black and gray solitons in Fig. 2.9.

Part II

Part II consisted of chapters 3 and 4 and covered the physics creating complex coherent matter waves in a harmonically trapped BEC, which we sculpted by assuming a specific geometrical configuration of the external ODT [152, 153].

In chapter 3 we started in Sec. 3.1 with a model, which explained the dynamical evolution of a quasi 1DBEC in a magneto-optical trap with an additional red/blue-detuned dimple trap in the center. In particular, by using the one-dimensional Lagrangian density (3.9) we obtained the 1DGPE (3.15). Afterwards in Sec. 3.2, we explained that, for the equilibrium properties of the system, the Thomas-Fermi approximation (3.17) agrees quantitatively with the numerical solution of the underlying quasi 1DGPE as shown in Fig. 3.4. With this we showed that the dT induces a bump or a dip upon the condensate wave function depending on whether the dT laser beam is red- or blue-detuned. For an increasing red-detuned dT depth, it turned out for the induced bump that the height decreases linearly, whereas the width remains approximately constant as depicted in Fig. 3.5. In contrast to that we found for an increasing blue-detuned dT that both depth and width of the induced dip initially increase, and beyond a critical value U_c the BEC even fragments into two parts. If U is increased beyond U_c, the dT induced imprint yields a condensate wave function whose width increases further, although the dip depth remains constant as illustrated in Fig. 3.5.

Subsequently, in Sec. 3.3, we discussed the dynamics of the dT induced bump/dip-imprint upon the condensate wave function for two quench scenarios. In the first one, where we released the harmonic trap but kept the dT, the resulting time-of-flight expansion showed in Fig. 3.6 that the dT induced imprint remains conserved for a red-detuned dT but decreases for a blue-detuned dT. In addition, we analyzed the condensate dynamics after having switched off the red/blue-detuned dT but not the harmonic trap. This case turned out to be an interesting laboratory in order to study the physical similarities and differences of white shock-waves and gray/dark bi-soliton trains, which emerge for an initial red- and blue-detuned dT, respectively. We observed astonishingly that the oscillation frequencies of both white shock-waves and bi-soliton trains coincide according to Fig. 3.9. Additionally, we also found that the generation of gray/dark bi-soliton trains is a generic phenomenon of collisions of partially/fully fragmented BEC and the partially/fully fragmented BEC is strongly depending upon the equilibrium values of the dimple trap depth.

After having found the intuitive and interesting physics of gray/dark bi-soliton trains, by sculpting a BEC with an additional red/blue-detuned dimple trap at the center of the BEC, we asked ourselves, whether we can create different shapes of matter waves by framing a harmonically trapped BEC with an external Hermite-Gaussian TEM_{01} laser mode of ODTs. To investigate this scenario in more detail in chapter 4, we started with deriving the underlying quasi 1DGPE (4.5) in Sec. 4.1, where we also outlined the system geometry and related our simulation parameters to tunable experimental parameters. Afterwards in Sec. 4.2, for the equilibrium properties of the system, we compared an approximative TF solution (4.8) with numerical results and showed in Fig. 4.3 that the HGdT imprint upon the condensate wave function strongly depends upon whether the HGdT is red or blue-detuned. With this we found out that the HGdT imprint generates two bumps/dips at the center of the BEC density, where the imprint height/depth depends on the chosen red/blue-detuned HGdT strength. Later, the TOF dynamics of the red/blue-detuned HGdT imprint upon the condensate wave function was discussed in Sec. 4.3, where we switched off the harmonic trap by keeping the HGdT. Here we obtained for the red-detuning that the HGdT imprint does not decay, but for the blue-detuning HGdT imprint decreases during TOF as depicted in Fig. 4.4. In Sec. 4.4, we discussed in Fig. 4.7 the formation of shock-waves/gray(dark) pair-soliton bi-trains in the harmonic trap after having switched off the red/blue-detuned HGdT potential. There, we also found that the generation of gray/dark pair-solitons bi-trains represents a generic phenomenon of collisions of moderately/fully fragmented BEC, respectively. Then, we showed that the number of pair-solitons in the system crucially depends on the initial HGdT potential depth U as shown in Fig. 4.8.

The Hermite-Gaussian dimple trap geometry is probably more applicable to soliton interferometry rather than the Gaussian barrier adopted in Refs. [152, 209], because one can shape solitons. With this we conclude that it may be possible in the future to frame complex shapes of solitons in the harmonically trapped BEC by imposing a unique geometrical configuration for the external potential.

The ability of sculpting a quasi one-dimensional harmonic trapped Bose-Einstein condensate by a HGdT has also other exciting prospects. For instance, it can be used to generate a truly continuous atom laser, which has many applications in atom interferometry [210, 211]. To construct such an atom laser one needs a device that continuously converts a source of condensed atoms into a laser-like beam. In Sec. 4.4, we saw in the time-of-flight picture for the case $\mathrm{U} > \mathrm{U_c}$ that a BEC reservoir occurs at the center of the trap. By suitably tuning the HGdT depth a fraction of this fragmented condensate could be coupled out, serving as a source for an atomic beam.

Part III

Motivated by the crucial relevance of gravito-optical surface traps in atomic waveguides [212–214] and atomic chips [215–218], **part III** of this thesis analyzed a quasi-1D BEC in the vicinity of a surface as shown in Fig. 5.1 [154]. **Part III** consisted of chapter 5, where we sculpted the BEC near to the dielectric surface with the nonlinear trap geometry of a gravito-optical surface trap as depicted in Fig. 5.2. The underlying fundamental model for such a quasi-1D BEC is reviewed in Sec. 5.1. Further, we provided estimates for the experimentally realistic parameters of a ^{133}Cs BEC, which we used in our quantitative analysis. Afterwards, we developed approximate solutions for the 1DGPE wave function in the ground state of the system by satisfying the hard-wall boundary condition of the dielectric surface with the mirror principle. Traditionally, the mirror analogy is used to solve linear differential equations in elctromagnetics and quantum mechanics. According to our knowledge, this is the first time where the mirror analogy is used to solve the nonlinear Gross–Pitaevskii equation in the following two cases. In Sec. 5.2 we used the mirror analogy in order to perform a modified Gaussian variational ansatz (5.6) for weak interactions, which corresponds to a small number of ^{133}Cs atoms. For a larger number of ^{133}Cs atoms, the interaction strength becomes so strong that the Thomas-Fermi solution (5.13) turns out to be valid, whose mirror analogy leads to a triangular shape of the condensate wave function according to Sec. 5.3. Then, in Sec. 5.4, we outlined our numerical methods and compared them to the analytical solutions obtained in the previous section in Fig. 5.5 and Fig. 5.6. We found that the numerical and analytical solutions agreed quite well with each other.

Additionally, in Sec. 5.5, we described the time-of-flight expansion of the BEC when the EW is switched off. We numerically calculated the fraction of remaining atoms in the time-of-flight picture and, surprisingly, reproduced quantitatively the experimental result of Ref. [82] as demonstrated in Fig. 5.9. Although this Innsbruck experiment uses a quasi

2D pancake shaped BEC, when performing the time-of-flight expansion vertically, the transversely confining beam is kept constant, so our quasi-1D model for BEC applied also in this case. In Sec. 5.6, we investigated the dynamics of the BEC in the presence of gravity and a hard-wall mirror, which is formed by a far-detuned sheet of light, where we observed self-interferences in Fig. 5.11 and revivals of the wave packet in Fig. 5.12. The evolution of a BEC falling under gravity and bouncing off a hard-wall mirror was already observed in the Hanover experiment by Bongs et al. [230], therefore we compared qualitatively their results with our numerical simulation. Due to a large two-particle coupling strength, which in turn results in a condensate with a larger width, the Hanover experimental group observed that the bouncing of the BEC was escorted with an additional splitting of the BEC into two parts close to the upper turning point of the BEC, which we did not detect. The observation of the bouncing of the BEC can be used to characterize and determine mirror properties such as roughness and steepness. All results in this part of the thesis can be applied to develop atomic interferometers for a BEC in a gravito-optical surface trap or to the formation of a Bose–Einstein condensate on a microelectronic chip.

Part IV

In the last **part IV** of this thesis, we sculpted a harmonically trapped quasi one-dimensional BEC with a single impurity to generate calibrated matter waves [155]. Inspired by the recent experiments of Refs. [147–149], we proposed and analyzed a quasi one-dimensional model of a hybrid system, which consisted of a ^{133}Cs impurity in a ^{87}Rb Bose-Einstein condensate in chapter 6. To this end, we started with defining the hybrid species quasi-1D model in Sec. 6.1 and derived a set of two coupled equations, namely a Gross-Pitaevskii equation (6.8) for the condensate wave function and a Schrödinger equation (6.9) for the impurity wave function. Due to integrating out the transversal degrees of freedom the effective one-dimensional interspecies coupling strength (6.6) depends not only on the three-dimensional s-wave scattering length, but also on the transversal trap frequencies of cesium and rubidium, respectively. In the same section, we specified within the equilibrium phase diagram, which is spanned by the intraspecies coupling strength g_{B} and interspecies coupling strength g_{IB}, the regions where the impurity is localized at the BEC center or expelled to the condensate border according to Fig. 6.2. Afterwards in Sec. 6.2, we showed that the impurity imprint upon the BEC strongly depends upon whether the impurity-BEC coupling strength is attractive or repulsive as depicted in Fig. 6.3. At first, we demonstrated for the equilibrium properties of the hybrid system that the impurity fragmented the BEC at the center of the trap by using the numerical simulation of the underlying two coupled 1DDEs (6.10) and (6.11). For an increasing attractive/repulsive Rb-Cs interaction strength it turned out that the impurity imprint bump/dip increases quadratically for repulsive interspecies interaction strength and reaches its marginally saturated value beyond a critical value g_{IBc}. Beyond a critical value g_{IBc}, the BEC fragmented into two parts and, if g_{IB} is increased beyond g_{IBc}, the impurity imprint width increases further, although impurity imprint height/depth remain constant as shown in Fig. 6.5. And within the mean-field regime, we calculated the effective mass of the impurity in Fig. 6.6, which yielded a quadratic behavior for small attractive and repulsive interspecies coupling strengths.

Afterwards, in Sec. 6.3, we discussed the dynamics of the impurity imprint upon the condensate wave function for two quench scenarios. After having released the trap for a fixed interspecies coupling strength, the resulting TOF expansion showed that the impurity imprint marginally decreases for an attractive s-wave coupling but considerably decreases for a repulsive s-wave scattering as depicted in Fig. 6.7. This result suggested that it might be experimentally easier to observe the impurity imprint for small attractive/repulsive coupling constant g_{IB}. In Fig. 6.8 we also observed the decaying breathing of the impurity at the center of the condensate for small attractive Rb-Cs coupling strength. Additionally, we found for stronger repulsive interspecies coupling strength in Fig. 6.10 that the ^{87}Rb atoms repel the single ^{133}Cs impurity from the center. In an experiment one has to take into account that inelastic collisions lead to two- and three-body losses of the condensate atoms [220, 240]. As such inelastic collisions are enhanced for a higher BEC density, they play a vital role for an attractive interspecies coupling, when the condensate density has a bump at the impurity position, but are negligible in the repulsive case with the dip in the condensate wave function. Furthermore, we investigated the emergence of white shock-waves or gray/dark bi-solitons in Fig. 6.12 when the initial attractive or repulsive interspecies coupling strength is switched off but the harmonic trap is still kept. Similar to the situation described in chapters 3 and 4, we found out that the oscillation frequencies of both the white shock-waves and the soliton coincide and attribute it to be an artifact of the harmonic confinement. Additionally, we concluded that the generation of gray/dark bi-solitons is a generic phenomenon of collisions of partially/fully fragmented BEC, respectively, and that the partially/fully fragmented BEC is strongly depending upon the equilibrium values of the impurity wave function height and width.

All these results can be used to describe ultra-cold atoms at low dimensions, which have applications in atomic chips, in nonlinear optics, and in quantum communication. On the other hand, also some fundamental questions of quantum mechanics can be addressed with remarkable precision. For instance, by implementing a single impurity atom within a BEC one can study to which extent a single impurity can act as a local, nondestructive probe for a strongly correlated quantum many-body state.

Bibliography

[1] E. Cornell, J. Res. Natl. Inst. Stand. Technol. **101**, 419 (1996).

[2] M. H. Anderson, J. R. Ensher, M. R. Matthews, C. E. Wieman, and E. A. Cornell, Science **269**, 198 (1995).

[3] S. Bose, Z. Physik **26**, 178 (1924).

[4] A. Einstein, Sitzber. Kgl. Preuss. Akad. Wiss. (1924).

[5] A. Chodos, APS News **13**, 06 (2004).

[6] C. J. Pethick and H. Smith, *Bose-Einstein Condensation in Dilute Gases*, 2nd ed. (Cambridge University Press, Cambridge, 2008).

[7] S. Chu, Rev. Mod. Phys. **70**, 685 (1998).

[8] C. N. Cohen-Tannoudji, Rev. Mod. Phys. **70**, 707 (1998).

[9] W. D. Phillips, Rev. Mod. Phys. **70**, 721 (1998).

[10] J. Kasprzak, M. Richard, S. Kundermann, A. Baas , P. Jeambrun, J. J. Keeling, F. M. Marchetti, M. H. Szymanska, R. Andre, J. L. Staehli , V. Savona, P. B. Littlewood, B. Deveaud, and L. S. Dang, Nature (London) **443**, 409 (2006).

[11] C. M. Savage, *Bose-Einstein Condensation: From Atomic Physics to Quantum Fluids: Proceedings of the 13th Physics Summer School*, 1st ed. (World Scientific, Singapore, 2000).

[12] K. B. Davis, M. O. Mewes, M. R. Andrews, N. J. van Druten, D. S. Durfee, D. M. Kurn, and W. Ketterle, Phys. Rev. Lett. **75**, 3969 (1995).

[13] C. C. Bradley, C. A. Sackett, and R. G. Hulet, Phys. Rev. Lett. **78**, 985 (1997).

[14] D. G. Fried, T. C. Killian, L. Willmann, D. Landhuis, S. C. Moss, D. Kleppner, and T. J. Greytak, Phys. Rev. Lett. **81**, 3811 (1998).

[15] G. Modugno, G. Ferrari, G. Roati, R. J. Brecha, A. Simoni, and M. Inguscio, Science **294**, 1320 (2001).

[16] T. Weber, J. Herbig, M. Mark, H.-C. Nägerl, and R. Grimm, Science **299**, 232 (2003).

[17] S. Kraft, F. Vogt, O. Appel, F. Riehle, and U. Sterr, Phys. Rev. Lett. **103**, 130401 (2009).

[18] S. Stellmer, M. K. Tey, B. Huang, R. Grimm, and F. Schreck, Phys. Rev. Lett. **103**, 200401 (2009).

[19] Y. N. M. de Escobar, P. G. Mickelson, M. Yan, B. J. DeSalvo, S. B. Nagel, and T. C. Killian, Phys. Rev. Lett. **103**, 200402 (2009).

[20] Y. Takasu, K. Maki, K. Komori, T. Takano, K. Honda, M. Kumakura, T. Yabuzaki, and Y. Takahashi, Phys. Rev. Lett. **91**, 040404 (2003).

[21] A. Robert, O. Sirjean, A. Browaeys, J. Poupard, S. Nowak, D. Boiron, C. I. Westbrook, and A. Aspect, Science **292**, 461 (2001).

[22] F. P. D. Santos, J. Léonard, J. Wang, C. Barrelet, F. Perales, E. Rasel, C. Unnikrishnan, M. Leduc, and C. Cohen-Tannoudji, Phys. Rev. Lett. **86**, 3459 (2001).

[23] A. Griesmaier, J. Werner, S. Hensler, J. Stuhler, and T. Pfau, Phys. Rev. Lett. **94**, 160401 (2005).

[24] K. Aikawa, A. Frisch, M. Mark, S. Baier, A. Rietzler, R. Grimm, and F. Ferlaino, Phys. Rev. Lett. **108**, 210401 (2012).

[25] M. Lu, N. Q. Burdick, S. H. Youn, and B. L. Lev, Phys. Rev. Lett. **107**, 190401 (2011).

[26] K. G. Lagoudakis, B. Pietka, M. Wouters, R. André, and B. Deveaud-Plédran, Phys. Rev. Lett. **105**, 120403 (2010).

[27] S. O. Demokritov, V. E. Demidov, O. Dzyapko, G. A. Melkov, A. A. Serga, B. Hillebrands, and A. N. Slavin, Nature (London) **443**, 430 (2006).

[28] S. Chu, J. E. Bjorkholm, A. Ashkin, and A. Cable, Phys. Rev. Lett. **57**, 314 (1986).

[29] R. Grimm, M. Weidemüller, and Y. Ovchinnikov, Adv. At. Mol. Opt. Phys. **42**, 95 (2000).

[30] M. C. Garrett, A. Ratnapala, E. D. van Ooijen, C. J. Vale, K. Weegink, S. K. Schnelle, O. Vainio, N. R. Heckenberg, H. Rubinsztein-Dunlop, and M. J. Davis, Phys. Rev. A **83**, 013630 (2011).

[31] Z.-Y. Ma, C. J. Foot, and S. L. Cornish, J. Phys. B: At., Mol. Opt. Phys. **37**, 3187 (2004).

[32] D. Comparat, A. Fioretti, G. Stern, E. Dimova, B. L. Tolra, and P. Pillet, Phys. Rev. A **73**, 043410 (2006).

[33] D. Jacob, E. Mimoun, L. D. Sarlo, M. Weitz, J. Dalibard, and F. Gerbier, New J. Phys. **13**, 065022 (2011).

[34] J. Stenger, S. Inouye, D. M. Stamper-Kurn, H.-J. Miesner, A. P. Chikkatur, and W. Ketterle, Nature (London) **396**, 345 (1998).

[35] S. Stellmer, B. Pasquiou, R. Grimm, and F. Schreck, Phys. Rev. Lett. **110**, 263003 (2013).

[36] N. Davidson, H. Jin Lee, C. S. Adams, M. Kasevich, and S. Chu, Phys. Rev. Lett. **74**, 1311 (1995).

[37] J.D. Weinstein, R. deCarvalho, T. Guillet, B. Friedrich, and J. M. Doyle, Nature (London) **395**, 148 (1998).

[38] A. Ashkin, Phys. Rev. Lett. **24**, 156 (1970).

[39] D. M. Stamper-Kurn, M. R. Andrews, A. P. Chikkatur, S. Inouye, H.-J. Miesner, J. Stenger, and W. Ketterle, Phys. Rev. Lett. **80**, 2027 (1998).

[40] R. González-Férez, M. Iñarrea, J. P. Salas, and P. Schmelcher, Phys. Rev. E **90**, 062919 (2014).

[41] X. Xu, V. G. Minogin, K. Lee, Y. Wang, and W. Jhe, Phys. Rev. A **60**, 4796 (1999).

[42] Y. Song, D. Milam, and W. T. Hill, Opt. Lett. **24**, 1805 (1999).

[43] X. Xu, K. Kim, W. Jhe, and N. Kwon, Phys. Rev. A **63**, 063401 (2001).

[44] K. Bongs, S. Burger, S. Dettmer, D. Hellweg, J. Arlt, W. Ertmer, and K. Sengstock, Phys. Rev. A **63**, 031602 (2001).

[45] H.-R. Noh, X. Xu, and W. Jhe, Adv. At., Mol., Opt. Phys. **48**, 153 (2002).

[46] J. Yin, Phys. Rep. **430**, 1 (2006).

[47] G. M. Gallatin and P. L. Gould, J. Opt. Soc. Am. B **8**, 502 (1991).

[48] J. Söding, R. Grimm, and Y. Ovchinnikov, Opt. Commun. **119**, 652 (1995).

[49] T. Kuga, Y. Torii, N. Shiokawa, T. Hirano, Y. Shimizu, and H. Sasada, Phys. Rev. Lett. **78**, 4713 (1997).

[50] S. Kuppens, M. Rauner, M. Schiffer, K. Sengstock, W. Ertmer, F. E. van Dorsselaer, and G. Nienhuis, Phys. Rev. A **58**, 3068 (1998).

[51] J. Yin and Y. Zhu, Opt. Commun. **152**, 421 (1998).

[52] S. A. Webster, G. Hechenblaikner, S. A. Hopkins, J. Arlt, and C. J. Foot, J. Phys. B: At., Mol. Opt. Phys. **33**, 4149 (2000).

[53] H. Metcalf and P. van der Straten, Phys. Rep. **244**, 203 (1994).

[54] M. D. Barrett, J. A. Sauer, and M. S. Chapman, Phys. Rev. Lett. **87**, 010404 (2001).

[55] T. L. Gustavson, A. P. Chikkatur, A. E. Leanhardt, A. Görlitz, S. Gupta, D. E. Pritchard, and W. Ketterle, Phys. Rev. Lett. **88**, 020401 (2001).

[56] A. M. Kaufman, B. J. Lester, and C. A. Regal, Phys. Rev. X **2**, 041014 (2012).

[57] E. Vetsch, D. Reitz, G. Sagué, R. Schmidt, S. T. Dawkins, and A. Rauschenbeutel, Phys. Rev. Lett. **104**, 203603 (2010).

[58] R. J. Cook and R. K. Hill, Opt. Commun. **43**, 258 (1982).

[59] V. I. Balykin, V. G. Minogin, and V. S. Letokhov, Rep. Prog. Phys. **63**, 1429 (2000).

[60] V. Balykin and V. Letokhov, Opt. Commun. **64**, 151 (1987).

[61] V. I. Balykin, V. S. Letokhov, Y. B. Ovchinnikov, A. I. Sidorov, and S. V. Shul'ga, Opt. Lett. **13**, 958 (1988).

[62] M. A. Kasevich, D. S. Weiss, and S. Chu, Opt. Lett. **15**, 607 (1990).

[63] C. G. Aminoff, A. M. Steane, P. Bouyer, P. Desbiolles, J. Dalibard, and C. Cohen-Tannoudji, Phys. Rev. Lett. **71**, 3083 (1993).

[64] T. Esslinger, M. Weidemüller, A. Hemmerich, and T. W. Hänsch, Opt. Lett. **18**, 450 (1993).

[65] R. Kaiser, Y. Lévy, N. Vansteenkiste, A. Aspect, W. Seifert, D. Leipold, and J. Mlynek, Opt. Commun. **104**, 234 (1994).

[66] C. Becker, S. Stellmer, P. Soltan-Panahi, S. Dorscher, M. Baumert, E.M. Richter, J. Kronjager, K. Bongs, and K. Sengstock, Nature Phys. **4**, 496 (2008).

[67] S. Stock, Z. Hadzibabic, B. Battelier, M. Cheneau, and J. Dalibard, Phys. Rev. Lett. **95**, 190403 (2005).

[68] J. I. Gillen, W. S. Bakr, A. Peng, P. Unterwaditzer, S. Fölling, and M. Greiner, Phys. Rev. A **80**, 021602 (2009).

[69] E. Vetsch, S. Dawkins, R. Mitsch, D. Reitz, P. Schneeweiss, and A. Rauschenbeutel, IEEE J. Quant. Elect. **18**, 1763 (2012).

[70] G. J. Liston, S. M. Tan, and D. F. Walls, Appl. Phys. B **60**, 211 (1995).

[71] H. Wallis, J. Dalibard, and C. Cohen-Tannoudji, Appl. Phys. B **54**, 407 (1992).

[72] H. Wallis, J. Opt. B: Quantum Semiclass. Opt. **8**, 727 (1996).

[73] K.-P. Marzlin and J. Audretsch, Phys. Rev. A **53**, 4352 (1996).

[74] F. Saif, I. Bialynicki-Birula, M. Fortunato, and W. P. Schleich, Phys. Rev. A **58**, 4779 (1998).

[75] F. Saif, Phys. Rep. **419**, 207 (2005).

[76] F. Saif and I. Rehman, Phys. Rev. A **75**, 043610 (2007).

[77] J. Akram, K. Naseer, and F. Saif, J. Russ. Las. Res. **30**, 157 (2009).

[78] V. V. Nesvizhevsky, H. G. Borner, A. K. Petukhov, H. Abele, S. Baeszler, F. J. Ruesz, T. Stoferle, A. Westphal, A. M. Gagarski, G. A. Petrov, and A. V. Strelkov, Nature (London) **415**, 297 (2002).

[79] Y. B. Ovchinnikov, I. Manek, and R. Grimm, Phys. Rev. Lett. **79**, 2225 (1997).

[80] M. Hammes, D. Rychtarik, V. Druzhinina, U. Moslener, I. Manek-Hönninger, and R. Grimm, J. Mod. Opt. **47**, 2755 (2000).

[81] P. Domokos and H. Ritsch, Europhys. Lett. **54**, 306 (2001).

[82] D. Rychtarik, B. Engeser, H.-C. Nägerl, and R. Grimm, Phys. Rev. Lett. **92**, 173003 (2004).

[83] Y. Colombe, D. Kadio, M. Olshanii, B. Mercier, V. Lorent, and H. Perrin, J. Opt. B: Quan. Sem. Opt. **5**, S155 (2003).

[84] Y. Colombe, B. Mercier, H. Perrin, and V. Lorent, Phys. Rev. A **72**, 061601 (2005).

[85] H. Perrin, Y. Colombe, B. Mercier, V. Lorent, and C. Henkel, J. Phys. B: At., Mol. Opt. Phys. **39**, 4649 (2006).

[86] P. Kevrekidis, D. Frantzeskakis, and R. Carretero-González, *Emergent Nonlinear Phenomena in Bose-Einstein Condensates*, 1st ed. (Springer, Berlin, 2008).

[87] L. Pitaevskii and A. Stringari, *Bose-Einstein Condensation*, 1st ed. (Clarendon Press, Oxford, 2003).

[88] R. Dodd, J. Eilbeck, J. Gibbon, and H. Morris, *Solitons and Nonlinear Wave Equations*, 1st ed. (Academic, New York, 1983).

[89] C. Sulem and P. Sulem, *The Nonlinear Schrodinger Equation*, 1st ed. (Springer, 1999).

[90] M. Ablowitz, B. Prinari, and A. Trubatch, *Discrete and Continuous Nonlinear Schrodinger Systems*, 1st ed. (Cambridge University, Cambridge, 2004).

[91] K. E. Strecker, G. B. Partridge, A. G. Truscott, and R. G. Hulet, Nature (London) **417**, 150 (2002).

[92] S. L. Rolston and W. D. Phillips, Nature (London) **416**, 219 (2002).

[93] P. Meystre, J. Phys. B: At., Mol. Opt. Phys. **38**, S617 (2005).

[94] P. G. Drazin and R. Johnson, *Solitons: An Introduction*, 2nd ed. (Cambridge University Press, Cambridge, 1983).

[95] R. Dum, J. I. Cirac, M. Lewenstein, and P. Zoller, Phys. Rev. Lett. **80**, 2972 (1998).

[96] J. Denschlag, J. E. Simsarian, D. L. Feder, C. W. Clark, L. A. Collins, J. Cubizolles, L. Deng, E. W. Hagley, K. Helmerson, W. P. Reinhardt, S. L. Rolston, B. I. Schneider, and W. D. Phillips, Science **287**, 97 (2000).

[97] A. Weller, J. P. Ronzheimer, C. Gross, J. Esteve, M. K. Oberthaler, D. J. Frantzeskakis, G. Theocharis, and P. G. Kevrekidis, Phys. Rev. Lett. **101**, 130401 (2008).

[98] T. Yefsah, A. T. Sommer, M. J. H. Ku, L. W. Cheuk, W. Ji, W. S. Bakr, and M. W. Zwierlein, Nature (London) **499**, 426 (2013).

[99] G. Huang, M. G. Velarde, and V. A. Makarov, Phys. Rev. A **64**, 013617 (2001).

[100] S. Stellmer, C. Becker, P. Soltan-Panahi, E.-M. Richter, S. Dörscher, M. Baumert, J. Kronjäger, K. Bongs, and K. Sengstock, Phys. Rev. Lett. **101**, 120406 (2008).

[101] L. Khaykovich, F. Schreck, G. Ferrari, T. Bourdel, J. Cubizolles, L. D. Carr, Y. Castin, and C. Salomon, Science **296**, 1290 (2002).

[102] K. E. Strecker, G. B. Partridge, A. G. Truscott, and R. G. Hulet, New J. Phys. **5**, 73 (2003).

[103] S. L. Cornish, S. T. Thompson, and C. E. Wieman, Phys. Rev. Lett. **96**, 170401 (2006).

[104] T. Busch and J. R. Anglin, Phys. Rev. Lett. **87**, 010401 (2001).

[105] A. Görlitz, J. M. Vogels, A. E. Leanhardt, C. Raman, T. L. Gustavson, J. R. Abo-Shaeer, A. P. Chikkatur, S. Gupta, S. Inouye, T. Rosenband, and W. Ketterle, Phys. Rev. Lett. **87**, 130402 (2001).

[106] H. Moritz, T. Stöferle, M. Köhl, and T. Esslinger, Phys. Rev. Lett. **91**, 250402 (2003).

[107] D. Hellweg, L. Cacciapuoti, M. Kottke, T. Schulte, K. Sengstock, W. Ertmer, and J. J. Arlt, Phys. Rev. Lett. **91**, 010406 (2003).

[108] B. L. Tolra, K. M. O'Hara, J. H. Huckans, W. D. Phillips, S. L. Rolston, and J. V. Porto, Phys. Rev. Lett. **92**, 190401 (2004).

[109] T. Kinoshita, T. Wenger, and D. S. Weiss, Phys. Rev. Lett. **95**, 190406 (2005).

[110] C.-S. Chuu, F. Schreck, T. P. Meyrath, J. L. Hanssen, G. N. Price, and M. G. Raizen, Phys. Rev. Lett. **95**, 260403 (2005).

[111] S. Hofferberth, I. Lesanovsky, B. Fischer, T. Schumm, and J. Schmiedmayer, Nature (London) **449**, 324 (2007).

[112] M. Eckart, R. Walser, and W. P. Schleich, New J. Phys. **10**, 045024 (2008).

[113] M. Olshanii, Phys. Rev. Lett. **81**, 938 (1998).

[114] D. S. Petrov, G. V. Shlyapnikov, and J. T. M. Walraven, Phys. Rev. Lett. **85**, 3745 (2000).

[115] T. Bergeman, M. G. Moore, and M. Olshanii, Phys. Rev. Lett. **91**, 163201 (2003).

[116] B. Paredes, A. Widera, V. Murg, O. Mandel, S. Fölling, I. Cirac, G. V. Shlyapnikov, T. W. Hänsch, and I. Bloch, Nature (London) **429**, 277 (2004).

[117] T. Kinoshita, T. Wenger, and D. S. Weiss, Science **305**, 1125 (2004).

[118] E. Haller, M. Gustavsson, M. J. Mark, J. G. Danzl, R. Hart, G. Pupillo, and H.-C. Nagel, S. B.gerl, Science **325**, 1224 (2009).

[119] A. M. Kamchatnov, J. Exp. Theor. Phys. **98**, 908 (2003).

[120] A. Radouani, Phys. Rev. A **70**, 013602 (2004).

[121] D. J. Frantzeskakis, J. Phys. A: Math. Theor **43**, 213001 (2010).

[122] J. Cuevas, P. G. Kevrekidis, B. A. Malomed, P. Dyke, and R. G. Hulet, New J. Phys. **15**, 063006 (2013).

[123] M. R. Andrews, C. G. Townsend, H.-J. Miesner, D. S. Durfee, D. M. Kurn, and W. Ketterle, Science **275**, 637 (1997).

[124] Z. Dutton, M. Budde, C. Slowe, and L. V. Hau, Science **293**, 663 (2001).

[125] W. P. Reinhardt and C. W. Clark, J. Phys. B: At., Mol. Opt. Phys. **30**, L785 (1997).

[126] Y. S. Kivshar and B. Luther-Davies, Phys. Rep. **298**, 81 (1998).

[127] T. F. Scott, R. J. Ballagh, and K. Burnett, J. Phys. B: At., Mol. Opt. Phys. **31**, L329 (1998).

[128] J. Ruostekoski, B. Kneer, W. P. Schleich, and G. Rempe, Phys. Rev. A **63**, 043613 (2001).

[129] I. Shomroni, E. Lahoud, S. Levy, and J. Steinhauer, Nature Phys. **5**, 193 (2009).

[130] S. Burger, K. Bongs, S. Dettmer, W. Ertmer, K. Sengstock, A. Sanpera, G. V. Shlyapnikov, and M. Lewenstein, Phys. Rev. Lett. **83**, 5198 (1999).

[131] L. D. Carr, J. Brand, S. Burger, and A. Sanpera, Phys. Rev. A **63**, 051601 (2001).

[132] T. Gericke, P. Wurtz, D. Reitz, T. Langen, and H. Ott, Nature Phys. **4**, 949 (2008).

[133] W. S. Bakr, J. I. Gillen, A. Peng, S. Folling, and M. Greiner, Nature (London) **462**, 74 (2009).

[134] J. F. Sherson, C. Weitenberg, M. Endres, M. Cheneau, I. Bloch, and S. Kuhr, Nature (London) **467**, 68 (2010).

[135] F. Serwane, G. Zürn, T. Lompe, T. B. Ottenstein, A. N. Wenz, and S. Jochim, Science **332**, 336 (2011).

[136] A. V. Gorshkov, M. Hermele, V. Gurarie, C. Xu, P. S. Julienne, J. Ye, P. Zoller, E. Demler, M. D. Lukin, and A. M. Rey, Nature Phys. **6**, 289 (2010).

[137] A. Schirotzek, C.-H. Wu, A. Sommer, and M. W. Zwierlein, Phys. Rev. Lett. **102**, 230402 (2009).

[138] S. Palzer, C. Zipkes, C. Sias, and M. Köhl, Phys. Rev. Lett. **103**, 150601 (2009).

[139] C. Zipkes, S. Palzer, C. Sias, and M. Köhl, Nature (London) **464**, 388 (2010).

[140] S. Schmid, A. Härter, and J. H. Denschlag, Phys. Rev. Lett. **105**, 133202 (2010).

[141] A. Micheli, A. J. Daley, D. Jaksch, and P. Zoller, Phys. Rev. Lett. **93**, 140408 (2004).

[142] A. Klein and M. Fleischhauer, Phys. Rev. A **71**, 033605 (2005).

[143] A. J. Daley, P. O. Fedichev, and P. Zoller, Phys. Rev. A **69**, 022306 (2004).

[144] A. Klein, M. Bruderer, S. R. Clark, and D. Jaksch, New J. Phys. **9**, 411 (2007).

[145] H. T. Ng and S. Bose, Phys. Rev. A **78**, 023610 (2008).

[146] J.B. Balewski, A.T. Krupp, A. Gaj, D. Peter, H.P. Buchler, R. Low, S. Hofferberth, and T. Pfau, Nature (London) **502**, 664 (2013).

[147] A. D. Lercher, T. Takekoshi, M. Debatin, B. Schuster, R. Rameshan, F. Ferlaino, R. Grimm, and H.-C. Nägerl, Eur. Phys. J. D **65**, 3 (2011).

[148] N. Spethmann, F. Kindermann, S. John, C. Weber, D. Meschede, and A. Widera, Appl. Phys. B **106**, 513 (2012).

[149] N. Spethmann, F. Kindermann, S. John, C. Weber, D. Meschede, and A. Widera, Phys. Rev. Lett. **109**, 235301 (2012).

[150] W. Casteels, J. Tempere, and J. T. Devreese, Phys. Rev. A **84**, 063612 (2011).

[151] D. H. Santamore and E. Timmermans, New J. Phys. **13**, 103029 (2011).

[152] J. Akram and A. Pelster, ArXiv:1508.05482 (2015).

[153] J. Akram and A. Pelster, Phys. Rev. A **93**, 023606 (2016).

[154] J. Akram, B. Girodias, and A. Pelster, J. Phys. B: At., Mol. Opt. Phys. **49**, 075302 (2016).

[155] J. Akram and A. Pelster, Phys. Rev. A **93**, 033610 (2016).

[156] W. Silfvast, *Laser fundamentals*, 2nd ed. (Cambridge University Press, Cambridge, 2004).

[157] D. Griffiths, *Introduction to Electrodynamics*, 4th ed. (Pearson Addison-Wesley, Boston, 2013).

[158] J. D. Jackson, *Classical Electrodynamics*, 3rd ed. (Wiley, New York, 2007).

[159] D. A. Steck, *Quantum and Atom Optics*, 1st ed. (University of Oregon, Oregon, 2013).

[160] M. Perkovac, Physics Essays **16**, 162 (2003).

[161] G. Grynberg, A. Aspect, C. Fabre, and C. Cohen-Tannoudji, *Introduction to Quantum Optics: From the Semi-classical Approach to Quantized Light*, 1st ed. (Cambridge University Press, Cambridge, 2010).

[162] J. Bosse, *Private communication* (2015).

[163] L. Allen and J. H. Eberly, *Optical Resonance and Two-Level Atoms*, 3rd ed. (Wiley, New York, 1987).

[164] M. O. Scully and M. S. Zubairy, *Quantum Optics*, 1st ed. (Cambridge University Press, 1997).

[165] R. Boyd, *Nonlinear Optics*, 3rd ed., Nonlinear Optics Series (Elsevier Science, Amsterdam, 2008).

[166] A. Landragin, J.-Y. Courtois, G. Labeyrie, N. Vansteenkiste, C. I. Westbrook, and A. Aspect, Phys. Rev. Lett. **77**, 1464 (1996).

[167] J. M. Wylie and J. E. Sipe, Phys. Rev. A **30**, 1185 (1984).

[168] J. E. Lennard-Jones, Trans. Faraday Soc. **28**, 333 (1932).

[169] J.-Y. Courtois, J.-M. Courty, and J. C. Mertz, Phys. Rev. A **53**, 1862 (1996).

[170] H. B. G. Casimir and D. Polder, Phys. Rev. **73**, 360 (1948).

[171] A. Pelster, *Bose-Einstein-Kondensation* (Lecture Notes, University Duisburg-Essen, 2004).

[172] J. E. Robinson, Phys. Rev. **83**, 678 (1951).

[173] F. Dalfovo, S. Giorgini, L. P. Pitaevskii, and S. Stringari, Rev. Mod. Phys. **71**, 463 (1999).

[174] N. D. Mermin and H. Wagner, Phys. Rev. Lett. **17**, 1133 (1966).

[175] B. Klünder and A. Pelster, Eur. Phys. J. B **68**, 457 (2009).

[176] H. Kleinert, *Path Integrals in Quantum Mechanics, Statistics, Polymer Physics, and Financial Markets*, 5th ed. (World Scientific Publishing Company, London, 2009).

[177] T. D. Lee, K. Huang, and C. N. Yang, Phys. Rev. **106**, 1135 (1957).

[178] V. M. Pérez-García, H. Michinel, J. I. Cirac, M. Lewenstein, and P. Zoller, Phys. Rev. Lett. **77**, 5320 (1996).

[179] J. Reichel and J. H. Thywissen, J. Phys. IV France **116**, 265 (2004).

[180] D. S. Petrov, D. M. Gangardt, and G. V. Shlyapnikov, J. Phys. IV France **116**, 3 (2004).

[181] N. J. Zabusky and M. D. Kruskal, Phys. Rev. Lett. **15**, 240 (1965).

[182] S. Mandelstam, Phys. Rev. D **11**, 3026 (1975).

[183] V. E. Zakharov and A. B. Shabat, Sov. Phys.-JETP (Engl. Transl.) **34**, 62 (1972).

[184] A. C. Scott, F. Chu, and D. McLaughlin, Proc. IEEE **61**, 1443 (1973).

[185] W. Zhang, D. F. Walls, and B. C. Sanders, Phys. Rev. Lett. **72**, 60 (1994).

[186] A. D. Jackson, G. M. Kavoulakis, and C. J. Pethick, Phys. Rev. A **58**, 2417 (1998).

[187] T. Busch and J. R. Anglin, Phys. Rev. Lett. **84**, 2298 (2000).

[188] P. O. Fedichev, A. E. Muryshev, and G. V. Shlyapnikov, Phys. Rev. A **60**, 3220 (1999).

[189] B. Saleh and M. Teich, *Fundamentals of Photonics*, 2nd ed. (Wiley, New York, 2007).

[190] P. Milonni and J. Eberly, *Laser Physics*, 2nd ed. (Wiley, 2010).

[191] P. Xu, X. He, J. Wang, and M. Zhan, Opt. Lett. **35**, 2164 (2010).

[192] J. Javanainen and J. Ruostekoski, J. Phys. A: Math. Gen. **39**, L179 (2006).

[193] D. Vudragović, I. Vidanović, A. Balaź, P. Muruganandam, and S. K. Adhikari, Comput. Phys. Commun. **183**, 2021 (2012).

[194] B. Carroll and D. Ostlie, *An Introduction to Modern Astrophysics*, 2nd ed. (Pearson Addison-Wesley, Boston, 2007).

[195] H. Uncu, D. Tarhan, E. Demiralp, and O. E. Müstecaplıoğlu, Phys. Rev. A **76**, 013618 (2007).

[196] J. Goold, D. O'Donoghue, and T. Busch, J. Phys. B: At., Mol. Opt. Phys. **41**, 215301 (2008).

[197] M.-O. Mewes, M. R. Andrews, N. J. van Druten, D. M. Kurn, D. S. Durfee, and W. Ketterle, Phys. Rev. Lett. **77**, 416 (1996).

[198] S. Inouye, T. Pfau, S. Gupta, A. P. Chikkatur, A. Görlitz, D. E. Pritchard, and W. Ketterle, Nature (London) **402**, 641 (1999).

[199] P. Engels, C. Atherton, and M. A. Hoefer, Phys. Rev. Lett. **98**, 095301 (2007).

[200] A. Balaž and A. I. Nicolin, Phys. Rev. A **85**, 023613 (2012).

[201] B. Damski, Phys. Rev. A **69**, 043610 (2004).

[202] B. Damski, Phys. Rev. A **73**, 043601 (2006).

[203] U. Al Khawaja, H. T. C. Stoof, R. G. Hulet, K. E. Strecker, and G. B. Partridge, Phys. Rev. Lett. **89**, 200404 (2002).

[204] W. Bao and D. Jaksch, SIAM J. Num. Anal. **41**, 1406 (2003).

[205] V. Bretin, S. Stock, Y. Seurin, and J. Dalibard, Phys. Rev. Lett. **92**, 050403 (2004).

[206] S. Kling and A. Pelster, Phys. Rev. A **76**, 023609 (2007).

[207] S. Kling and A. Pelster, Laser Physics **19**, 1072 (2009).

[208] K. Bongs and K. Sengstock, Rep. Prog. Phys. **67**, 907 (2004).

[209] J. H. V. Nguyen, P. Dyke, D. Luo, B. A. Malomed, and R. G. Hulet, Nature Phys. **10**, 918 (2014).

[210] A. D. Cronin, J. Schmiedmayer, and D. E. Pritchard, Rev. Mod. Phys. **81**, 1051 (2009).

[211] B. G. Kleine, J. Will, W. Ertmer, C. Klempt, and J. Arlt, Appl. Phys. B **100**, 117 (2010).

[212] G. L. Gattobigio, A. Couvert, B. Georgeot, and D. Guéry-Odelin, New J. Phys. **12**, 085013 (2010).

[213] V. S. Melezhik and P. Schmelcher, Phys. Rev. A **84**, 042712 (2011).

[214] S. Saeidian, V. S. Melezhik, and P. Schmelcher, Phys. Rev. A **86**, 062713 (2012).

[215] Y.-J. Wang, D. Z. Anderson, V. M. Bright, E. A. Cornell, Q. Diot, T. Kishimoto, M. Prentiss, R. A. Saravanan, S. R. Segal, and S. Wu, Phys. Rev. Lett. **94**, 090405 (2005).

[216] S. Jöllenbeck, J. Mahnke, R. Randoll, W. Ertmer, J. Arlt, and C. Klempt, Phys. Rev. A **83**, 043406 (2011).

[217] J. Petrovic, I. Herrera, P. Lombardi, F. Schäfer, and F. S. Cataliotti, New J. Phys. **15**, 043002 (2013).

[218] B. Jian and W. A. van Wijngaarden, J. Phys. B: At., Mol. Opt. Phys. **47**, 215301 (2014).

[219] A. Kamchatnov, J. Exp. Theor. Phys. **98**, 908 (2004).

[220] R. Carretero-González, D. J. Frantzeskakis, and P. G. Kevrekidis, Nonlinearity **21**, R139 (2008).

[221] P. C. Hohenberg, Phys. Rev. **158**, 383 (1967).

[222] J. M. Obrecht, R. J. Wild, M. Antezza, L. P. Pitaevskii, S. Stringari, and E. A. Cornell, Phys. Rev. Lett. **98**, 063201 (2007).

[223] R. W. Robinett, Eur. J. Phys. **27**, 281 (2006).

[224] M. Belloni and R. Robinett, Phys. Rep. **540**, 25 (2014).

[225] V. M. Pérez-García, H. Michinel, J. I. Cirac, M. Lewenstein, and P. Zoller, Phys. Rev. A **56**, 1424 (1997).

[226] J. M. Gerton, D. Strekalov, I. Prodan, and R. G. Hulet, Nature (London) **408**, 692 (2000).

[227] Y. Colombe, T. Steinmetz, G. Dubois, F. Linke, D. Hunger, and J. Reichel, Nature (London) **450**, 272 (2007).

[228] G. Della Valle, M. Savoini, M. Ornigotti, P. Laporta, V. Foglietti, M. Finazzi, L. Duò, and S. Longhi, Phys. Rev. Lett. **102**, 180402 (2009).

[229] W. Liu, D. N. Neshev, A. E. Miroshnichenko, I. V. Shadrivov, and Y. S. Kivshar, Phys. Rev. A **84**, 063805 (2011).

[230] K. Bongs, S. Burger, G. Birkl, K. Sengstock, W. Ertmer, K. Rzazewski, A. Sanpera, and M. Lewenstein, Phys. Rev. Lett. **83**, 3577 (1999).

[231] M. Hohmann, F. Kindermann, B. Gänger, T. Lausch, D. Mayer, F. Schmidt, and A. Widera, arXiv: **1508.02646** (2015).

[232] K. Pilch, A. D. Lange, A. Prantner, G. Kerner, F. Ferlaino, H.-C. Nägerl, and R. Grimm, Phys. Rev. A **79**, 042718 (2009).

[233] T. Takekoshi, M. Debatin, R. Rameshan, F. Ferlaino, R. Grimm, H.-C. Nägerl, C. R. Le Sueur, J. M. Hutson, P. S. Julienne, S. Kotochigova, and E. Tiemann, Phys. Rev. A **85**, 032506 (2012).

[234] H. Pu and N. P. Bigelow, Phys. Rev. Lett. **80**, 1130 (1998).

[235] R. M. Kalas and D. Blume, Phys. Rev. A **73**, 043608 (2006).

[236] J. Tempere, W. Casteels, M. K. Oberthaler, S. Knoop, E. Timmermans, and J. T. Devreese, Phys. Rev. B **80**, 184504 (2009).

[237] F. Grusdt and E. Demler, ArXiv:1510.04934 (2015).

[238] S. Peotta, D. Rossini, M. Polini, F. Minardi, and R. Fazio, Phys. Rev. Lett. **110**, 015302 (2013).

[239] M. R. Andrews, D. M. Kurn, H.-J. Miesner, D. S. Durfee, C. G. Townsend, S. Inouye, and W. Ketterle, Phys. Rev. Lett. **79**, 553 (1997).

[240] S. L. Cornish, N. R. Claussen, J. L. Roberts, E. A. Cornell, and C. E. Wieman, Phys. Rev. Lett. **85**, 1795 (2000).

[241] P. Bader, S. Blanes, and F. Casas, J. Chem. Phys. **139**, 124117 (2013).

[242] M. Feit, J. Fleck, and A. Steiger, J. Comput. Phys. **47**, 412 (1982).

Appendix A

Split-step algorithm

To show the validity of our proposed theoretical models, we numerically solve GPE with the help of the split operator technique [192, 193, 241]. We first discuss the case of the dimensionless time-dependent Schrödinger wave equation, for the time being in one spatial dimension

$$\mathrm{i}\frac{\partial}{\partial t}\psi(z,t)=\hat{H}\psi(z,t)\,. \tag{A.1}$$

Here, the Hamiltonian $\hat{H}=\hat{P}+\hat{V}$, decomposes into the kinetic energy term $\hat{P}=-\frac{1}{2}\frac{\partial^2}{\partial z^2}$ and the potential energy term $\hat{V}(z)$. With this the time evolution of the wave function within a time step from t to $t+h$ can be written as

$$\psi(z,t+h)=e^{-\mathrm{i}h\hat{H}/\hbar}\psi(z,t)\,. \tag{A.2}$$

However, the operators $\hat{P}$ and $\hat{V}$ do not commute, so we conclude $\exp\left[-\mathrm{i}h\left(\hat{P}+\hat{V}\right)\right]\neq\exp\left[-\mathrm{i}h\hat{P}\right]\exp\left[-\mathrm{i}h\hat{V}\right]$. To avoid this, we use the split-step method which is based on the idea to approximate the exponential of the sum of noncommuting operators $\hat{A}$ and $\hat{B}$ according to

$$e^{\tau\left(\hat{A}+\hat{B}\right)}\simeq e^{\tau\beta_n\hat{B}}e^{\tau\alpha_n\hat{A}}\cdots e^{\tau\beta_1\hat{B}}e^{\tau\alpha_1\hat{A}} \tag{A.3}$$

with the conditions $\sum_{i=1}^{n}\alpha_i=\sum_{i=1}^{n}\beta_i=1$. In above equation, by matching left-hand side with right-hand side of the equation for a certain order in τ, we obtain multivariate polynomial equations determining α_n and β_n. The simplest nontrivial split-operator method found in this way is the original split operator algorithm, which yields an accuracy of third order [242]. The general operator-algebra argument does not distinguish between the operators $\hat{A}$ and $\hat{B}$, but the choices for the nonzero coefficients $\alpha_1=\alpha_2=1/2$, $\beta_1=1$, $\beta_2=0$ and $\beta_1=\beta_2=1/2, \alpha_2=1, \alpha_1=0$ do both [192]. With this we can write the split-step representation as

$$\begin{aligned}\exp\left\{-\mathrm{i}h\left[-\frac{1}{2}\frac{\partial^2}{\partial z^2}+\hat{V}(x)\right]\right\}\simeq{}&\exp\left\{\mathrm{i}h\left(\frac{1}{4}\frac{\partial^2}{\partial z^2}\right)\right\}\exp\left\{-\mathrm{i}h\hat{V}(z)\right\}\\&\times\exp\left\{\mathrm{i}h\left(\frac{1}{4}\frac{\partial^2}{\partial z^2}\right)\right\}+O\left(h^3\right)\,.\end{aligned} \tag{A.4}$$

In order to implement the resulting discrete time evolution of the wave function, according to (A.4) it is useful to implement a fast Fourier transformation with Matlab for the propagation steps involving $\hat{T} = -\frac{1}{4}\frac{\partial^2}{\partial z^2}$. This algorithm preserves the normalization of the wave function.

By reforming the same steps also for the Gross–Pitaevskii equation (GPE), the split-operator method yields for the condensate wave function

$$\begin{aligned} \psi(z,t+h) \simeq \exp\left\{\mathrm{i}h\left(\frac{1}{4}\frac{\partial^2}{\partial z^2}\right)\right\} \exp\left\{-\mathrm{i}h\left(\hat{V}(z) + G_{\mathrm{B}}^{1\mathrm{D}} \parallel \psi(z,t) \parallel^2\right)\right\} \\ \times \exp\left\{\mathrm{i}h\left(\frac{1}{4}\frac{\partial^2}{\partial z^2}\right)\right\} \psi(z,t) + O\left(h^3\right) . \end{aligned} \tag{A.5}$$

Here, $G_{\mathrm{B}}^{1\mathrm{D}}$ defines the two-particle interaction strength. This represents an approximated numerical method but it has quite promising results. The middle part of this equation involving $\hat{D} = \hat{V}(z) + G_{\mathrm{B}}^{1\mathrm{D}} \parallel \psi(z,t) \parallel^2$ can be computed directly using the condensate wave function at time t, but to compute the exponential involving $\hat{T} = -\frac{1}{4}\frac{\partial^2}{\partial z^2}$, we use again the Fourier transformation according to

$$\psi(z,t+h) \simeq F^{-1}\left[e^{-\mathrm{i}h\frac{k^2}{4}} F\left[e^{-\mathrm{i}h\hat{D}} F^{-1}\left\{e^{-\mathrm{i}h\frac{k^2}{4}} F\left[\psi(z,t)\right]\right\}\right]\right] . \tag{A.6}$$

Note that the split-operator algorithms for the GPE work the same way in more than one spatial dimension.

Appendix B

Quantum and thermal fluctuations

B.1 Quantum fluctuations

In this appendix, we investigate how quantum and thermal fluctuations affect ground-state occupancy according to the Thomas-Fermi-Bogoliubov theory [171]. These calculations allow to estimate the validity range of a Gross-Pitaevskii mean-field description for a Bose-Einstein condensate.

B.1.1 Three dimensions

By using the Thomas-Fermi-Bogoliubov theory, we obtain for the quantum depletion of a three-dimensional BEC [171]

$$n_{0\mathrm{B}}^{3\mathrm{D}}(\mathbf{r}) = n_{\mathrm{B}}^{3\mathrm{D}}(\mathbf{r}) - \frac{8}{3\sqrt{\pi}} \left[N_{\mathrm{B}} a_{\mathrm{B}} n_{\mathrm{B}}^{3\mathrm{D}}(\mathbf{r})\right]^{3/2}. \tag{B.1}$$

Here the density $n_{0\mathrm{B}}^{3\mathrm{D}}(\mathbf{r}) = \parallel \psi(\mathbf{r}) \parallel^2$ is determined by the three-dimensional Gross-Piteavskii equation (2.90)

$$\mu^{3\mathrm{D}}\psi(\mathbf{r},t) = \left\{-\frac{\hbar^2}{2m_B}\frac{\partial^2}{\partial \mathbf{r}^2} + \frac{m_{\mathrm{B}}\omega_{\mathrm{z}}^2}{2}z^2 + \frac{m_{\mathrm{B}}\omega_{\mathrm{r}}^2}{2}\left(x^2+y^2\right) + G_{\mathrm{B}}^{3\mathrm{D}} \parallel \psi(\mathbf{r},t) \parallel^2\right\}\psi(\mathbf{r},t). \tag{B.2}$$

By using the Thomas-Fermi approximation, the BEC density profile is given by

$$n^{3\mathrm{D}}(\mathbf{r}) = \frac{\mu^{3\mathrm{D}}}{G_{\mathrm{B}}^{3\mathrm{D}}}\left\{1 - \frac{z^2}{R_{\mathrm{z}}^2} - \frac{\left(x^2+y^2\right)}{R_{\mathrm{r}}^2}\right\}. \tag{B.3}$$

Here, $R_{\mathrm{z}}^2 = 2\mu^{3\mathrm{D}}/m_{\mathrm{B}}\omega_{\mathrm{z}}^2$ and $R_{\mathrm{r}}^2 = 2\mu^{3\mathrm{D}}/m_{\mathrm{B}}\omega_r^2$ denote the Thomas-Fermi radius along the z-axis and along the radial axis, respectively. So the three-dimensional quantum depletion follows from integrating the three-dimensional quantum fluctuation term $n_{\mathrm{QF}}^{3\mathrm{D}}(\mathbf{r}) = n_{\mathrm{B}}^{3\mathrm{D}}(\mathbf{r}) - n_{0\mathrm{B}}^{3\mathrm{D}}(\mathbf{r})$ according to

$$\begin{aligned} N_{\mathrm{QF}}^{3\mathrm{D}} &= \int n_{\mathrm{QF}}^{3\mathrm{D}}(\mathbf{r})\,d\mathbf{r} = \frac{8}{3\sqrt{\pi}}\left(N_{\mathrm{B}}a_{\mathrm{B}}\right)^{3/2}\int\left\{n_{\mathrm{B}}^{3\mathrm{D}}(\mathbf{r})\right\}^{3/2}d\mathbf{r} \\ &= \frac{8}{3\sqrt{\pi}}\left(\frac{\mu^{3\mathrm{D}}}{G_{\mathrm{B}}^{3\mathrm{D}}}N_{\mathrm{B}}a_{\mathrm{B}}\right)^{3/2}\int_{-R_{\mathrm{z}}}^{R_{\mathrm{z}}}\int_0^{R_r\sqrt{1-\frac{z^2}{R_{\mathrm{z}}^2}}}\int_0^{2\pi} r\left\{1-\frac{z^2}{R_{\mathrm{z}}^2}-\frac{r^2}{R_{\mathrm{r}}^2}\right\}^{3/2}d\phi\,dr \\ &= \frac{8}{3\sqrt{\pi}}\left(\frac{\mu^{3\mathrm{D}}}{G_{\mathrm{B}}^{3\mathrm{D}}}N_{\mathrm{B}}a_{\mathrm{B}}\right)^{3/2}2\pi\left(\frac{1}{16}\pi R_{\mathrm{r}}^2R_{\mathrm{z}}\right) = \frac{R_{\mathrm{r}}^2R_{\mathrm{z}}}{3}\left(\frac{\mu^{3\mathrm{D}}}{G_{\mathrm{B}}^{3\mathrm{D}}}N_{\mathrm{B}}\pi a_{\mathrm{B}}\right)^{3/2}. \end{aligned} \tag{B.4}$$

By using the normalization constant $\int n_{\mathrm{B}}^{3\mathrm{D}}(\mathbf{r})\,d\mathbf{r} = 1$, we determine the three-dimensional chemical potential as

$$\mu^{3\mathrm{D}} = \left(\frac{15}{\pi}\right)^{2/5}\frac{\left(G_{\mathrm{B}}^{3\mathrm{D}}\right)^{2/5}\left(m_{\mathrm{B}}\right)^{3/5}\omega_r^{4/5}\omega_{\mathrm{z}}^{2/5}}{2^{9/5}}. \tag{B.5}$$

Defining the oscillator lengths $l_{\mathrm{r}} = \sqrt{\hbar/(m_{\mathrm{B}}\omega_{\mathrm{r}})}$ and $l_{\mathrm{z}} = \sqrt{\hbar/(m_{\mathrm{B}}\omega_{\mathrm{z}})}$ in radial and axial direction, receptively, we obtain for the relative three-dimensional quantum depletion

$$\frac{N_{\mathrm{QF}}^{3\mathrm{D}}}{N_{\mathrm{B}}} = \frac{5^{6/5}3^{1/5}}{2^{9/2}}\left(\frac{a_{\mathrm{B}}^6N_{\mathrm{B}}}{l_{\mathrm{r}}^4l_{\mathrm{z}}^2}\right)^{1/5}. \tag{B.6}$$

B.1.2 Quasi one dimension

Now we assume an effective one-dimensional setting with $\omega_{\mathrm{z}} \ll \omega_{\mathrm{r}}$, so we decompose the BEC wave-function $\psi_{\mathrm{B}}(\mathbf{r},t) = \psi_{\mathrm{B}}(z,t)\phi_{\mathrm{B}}(\mathbf{r}_\perp,t)$, where $\phi_{\mathrm{B}}(\mathbf{r}_\perp,t)$ is defined in Eq. (2.111). We integrate out the transversal dimensions of equation (B.1) to get the depleted density in quasi one-dimension:

$$n_{0\mathrm{B}}^{1\mathrm{D}}(z) = n_{\mathrm{B}}^{1\mathrm{D}}(z) - \frac{16}{9\pi l_{\mathrm{r}}}\left[N_{\mathrm{B}}a_{\mathrm{B}}n_{\mathrm{B}}^{1\mathrm{D}}(z)\right]^{3/2}. \tag{B.7}$$

We know that $n_{\mathrm{B}}^{1\mathrm{D}}(z) = \mu^{1\mathrm{D}}\left(1-z^2/R_{\mathrm{z}}^2\right)/G_{\mathrm{B}}^{1\mathrm{D}}$ with $R_{\mathrm{z}}^2 = 2\mu^{1\mathrm{D}}/m_{\mathrm{B}}\omega_{\mathrm{z}}^2$ represents the one-dimensional Thomas-Fermi density with the one-dimensional two-particle interaction strength $G_{\mathrm{B}}^{1\mathrm{D}}$ in (2.114). The one-dimensional quantum fluctuations depleted number of atoms can be calculated as

$$
\begin{aligned}
N_{\mathrm{QF}}^{1\mathrm{D}} &= \int n_{\mathrm{QF}}^{1\mathrm{D}}(z)\,dz = \frac{16}{9\pi l_{\mathrm{r}}}\left(N_{\mathrm{B}}a_{\mathrm{B}}\right)^{3/2}\int\left[n_{\mathrm{B}}^{1\mathrm{D}}(z)\right]^{3/2}dz, \\
&= \frac{16}{9\pi l_{\mathrm{r}}}\left(\frac{\mu^{1\mathrm{D}}}{G_{\mathrm{B}}^{1\mathrm{D}}}N_{\mathrm{B}}a_{\mathrm{B}}\right)^{3/2}\frac{3\pi R_{\mathrm{z}}}{8} = \frac{2R_{\mathrm{z}}}{3l_{\mathrm{r}}}\left(\frac{\mu^{1\mathrm{D}}}{G_{\mathrm{B}}^{1\mathrm{D}}}N_{\mathrm{B}}a_{\mathrm{B}}\right)^{3/2}.
\end{aligned}
\tag{B.8}
$$

By using the normalization constant $\int n_{\mathrm{B}}^{1\mathrm{D}}(\mathbf{r})\,d\mathbf{r} = 1$, we determine the one-dimensional chemical potential as

$$
\mu^{1\mathrm{D}} = \frac{1}{2}\left(\frac{3}{2}G_{\mathrm{B}}^{1\mathrm{D}}m_{\mathrm{B}}\omega_{\mathrm{z}}\right)^{2/3}. \tag{B.9}
$$

With this we obtain for the one-dimensional quantum relative depletion as

$$
\frac{N_{\mathrm{QF}}^{1\mathrm{D}}}{N_{\mathrm{B}}} = \frac{3^{1/3}}{4}\left(\frac{a_{\mathrm{B}}^{4}N_{\mathrm{B}}}{l_{\mathrm{r}}^{2}l_{\mathrm{z}}^{2}}\right)^{1/3}. \tag{B.10}
$$

B.2 Thermal fluctuations

By using the Thomas-Fermi-Bogoliubov theory, we write the leading three-dimensional thermal depleted density as [171]

$$
n_{\mathrm{TF}}^{3\mathrm{D}}(\mathbf{r}) = \frac{m_{\mathrm{B}}\left(k_{\mathrm{B}}T\right)^{2}}{12\hbar^{3}c(\mathbf{r})} \tag{B.11}
$$

with the local sound velocity $c(\mathbf{r}) = \sqrt{G_{\mathrm{B}}^{3\mathrm{D}}n^{3\mathrm{D}}(\mathbf{r})/m_{\mathrm{B}}}$. By inserting the three-dimensional density Eq. (B.3), we get

$$
n_{\mathrm{TF}}^{3\mathrm{D}}(\mathbf{r}) = \frac{m_{\mathrm{B}}^{3/2}\left(k_{\mathrm{B}}T\right)^{2}}{12\hbar^{3}\sqrt{\mu^{3\mathrm{D}}\left\{1-\frac{z^{2}}{R_{\mathrm{z}}^{2}}-\frac{\left(x^{2}+y^{2}\right)}{R_{\mathrm{r}}^{2}}\right\}}}. \tag{B.12}
$$

Integrating out the two transversal dimensions, the one-dimensional thermal depletion reads

$$
n_{\mathrm{TF}}^{1\mathrm{D}}(z) = \frac{m_{\mathrm{B}}^{3/2}\pi\left(k_{\mathrm{B}}T\right)^{2}}{6\hbar^{3}\sqrt{\mu^{3\mathrm{D}}}}R_{\mathrm{r}}^{2}\sqrt{1-\frac{z^{2}}{R_{\mathrm{z}}^{2}}}. \tag{B.13}
$$

With this we count the number of thermally excited atoms to be

$$
\begin{aligned}
N_{\mathrm{TF}}^{\mathrm{1D}} = \int n_{\mathrm{TF}}^{\mathrm{1D}}(z)\,dz = \frac{m_{\mathrm{B}}^{3/2}\pi\left(k_{\mathrm{B}}T\right)^2}{6\hbar^3\sqrt{\mu^{\mathrm{3D}}}}R_{\mathrm{r}}^2\int_{-R_{\mathrm{z}}}^{R_{\mathrm{z}}}\sqrt{1-\frac{z^2}{R_{\mathrm{z}}^2}}dz, \\
= \frac{m_{\mathrm{B}}^{3/2}\pi\left(k_{\mathrm{B}}T\right)^2}{6\hbar^3\sqrt{\mu^{\mathrm{3D}}}}R_{\mathrm{r}}^2\left(\frac{\pi R_{\mathrm{z}}}{2}\right) = \frac{m_{\mathrm{B}}^{3/2}\pi^2\left(k_{\mathrm{B}}T\right)^2}{12\hbar^3\sqrt{\mu^{\mathrm{3D}}}}R_{\mathrm{r}}^2R_{\mathrm{z}}.
\end{aligned}
\tag{B.14}
$$

By using the two-body contact interaction strength $G_{\mathrm{B}}^{\mathrm{3D}} = N_{\mathrm{B}}4\pi\hbar^2 a_{\mathrm{B}}/m_{\mathrm{B}}$ and the three-dimensional chemical potential (B.5), the one-dimensional thermal depletion reads

$$
N_{\mathrm{TF}}^{\mathrm{1D}} = \frac{5^{2/5}\pi^2}{2^{3/2}\times 3^{3/5}}\frac{\left(k_{\mathrm{B}}T\right)^2 m_{\mathrm{B}}^{1/5}\left(N_{\mathrm{B}}a_{\mathrm{B}}\right)^{2/5}}{\hbar^{11/5}}\left(\frac{1}{\omega_r^2\omega_{\mathrm{z}}}\right)^{3/5}. \tag{B.15}
$$

By assuming relation (2.76), we define the three-dimensional critical temperature as $T_{\mathrm{c}} = \hbar\left[\left(\omega_r^2\omega_{\mathrm{z}}N_{\mathrm{B}}\right)/\xi\left(3\right)\right]^{1/3}/k_{\mathrm{B}}$. Thus, the one-dimensional relative thermal depletion is according to Thomas-Fermi-Bogoliubov theory of the form

$$
\frac{N_{\mathrm{TF}}^{\mathrm{1D}}}{N_{\mathrm{B}}} = \eta\left(\frac{T}{T_{\mathrm{c}}}\right)^2, \tag{B.16}
$$

with the dimensionless prefactor

$$
\gamma = \frac{5^{2/5}\pi^2}{2^{3/2}\times 3^{3/5}}\left\{\frac{N_{\mathrm{B}}^{1/3}}{\xi\left(3\right)^{8/3}}\frac{a_{\mathrm{B}}^2}{l_{\mathrm{r}}^{4/3}l_{\mathrm{z}}^{2/3}}\right\}^{1/5}. \tag{B.17}
$$

List of Figures

Index